

Atomic Layer Deposition and Metal Organic Chemical Vapour Deposition of Materials for Photovoltaic Applications

**Thesis submitted in accordance with the requirements of the
University of Liverpool for the degree of Doctor in Philosophy by
Sarah Louise Hindley**

January 2014

Abstract

In this thesis, the development of thin films and nanostructures prepared with chemical vapour techniques are investigated for applications in photovoltaics. The deposition of both p-type and n-type oxides are investigated as a means of preparing all oxide p-n junctions. Both CVD and ALD precursors and processes have been developed. Zinc oxide nanowires are of interest as an n-type absorber layer with high surface area. In this thesis, the crystal structures of DEZn and DMZn were revisited and a new understanding of conventional zinc CVD precursors is presented. For DEZn a single structure was isolated and characterised with single crystal XRD. In the case of DMZn two temperature dependant structures were identified: namely α and β at 200K and 150K respectively. The DMZn precursor was subsequently exploited in a series of adduct-based precursors of the notation [DMZn.L] (where L = 1,2-dimethoxyethane, 1,4-dioxane and 1,4-thioxane). The crystal structures of these precursors were determined, and they were subsequently used to grow ZnO and sulphur doped ZnO across a range of CVD growth conditions. The microstructure and electronic properties of the nanowires have been characterised with electron microscopy, x-ray diffraction, Raman spectroscopy and photoluminescence. The II:VI ratio and substrate temperatures were both confirmed as playing a significant role in determining the microstructure of the nanowires. It has been demonstrated that the use of [DMZn.L] can avoid the pre-reaction between DMZn and oxygen. The studies with the thioxane adduct suggests the involvement of the ligand and hence sulphur incorporation in the nanowires.

Two copper precursors were selected as the basis of p-type copper oxide film studies. The first Cu(hfac)(COD) has been used previously to deposit copper oxide

by conventional CVD. In this thesis it is demonstrated for the first time that a pulsed LI-ALD approach can be exploited to deposit CuO with ozone as the co-reagent. An unexpected outcome of the research was the successful growth of electrically conductive copper metal films with a sheet resistance of $0.83\Omega/\square$ when the precursor was thermally decomposed. The second copper precursor, namely $\text{CpCu}(\text{}^t\text{BuNC})$ was used in atomic layer deposition to successfully deposit CuO or Cu_2O with oxygen plasma and water respectively. Having identified that the β -diketonate compound yielded copper, the cyclopentadienyl based precursor was investigated as a route for the deposition of conductive copper metal films. Both thermal decomposition and a hydrogen plasma ALD process have been shown to deposit copper. With the plasma process, deposition of copper was demonstrated as low as 75°C with a sheet resistance of only $0.55\Omega/\square$.

This thesis has demonstrated novel deposition routes for p- and n-type oxide materials which have potential future applications in thin film or nanostructured photovoltaic technology.

Contents

Chapter 1Introduction	1
1.1 Project Aim.....	1
1.2 Band Theory	4
1.3 Fermi-Level	8
1.4 Band-gap Energy	13
1.5 Carrier Concentration and Mobility	16
1.6 The p-n junction	17
1.7 Substrate	28
1.8 Transparent Conducting Oxide.....	30
1.9 Film Deposition Techniques	33
1.10 Precursors	42
1.11 Summary	49
Chapter 2Literature Review	50
2.1 Zinc.....	50
2.2 Copper	71
Chapter 3Experimental Methods	100
3.1 Chemical Characterisation	100
3.2 Thin Film Deposition	108
3.3 Thin Film Characterisation.....	112
Chapter 4Zinc Results and Discussion	125
4.1 Overview	125
4.2 Dialkylzinc Precursor Characterisation.....	125
4.3 Dialkylzinc Adduct Precursor Synthesis.....	132
4.4 Dialkylzinc Adduct Precursor Characterisation	133
4.5 Zinc Oxide Growth.....	145
4.6 Zinc Oxide Analysis	147
4.7 Conclusions	159
4.8 Experimental Details	160
Chapter 5Copper Results and Discussion.....	163
5.1 Overview	163
5.2 Deposition of Metallic Copper Films	169
5.3 Deposition of Cupric Oxide-CuO.....	192

5.4	Deposition of Cuprous Oxide-Cu ₂ O.....	196
5.5	Conclusions	200
5.6	Experimental	201
Chapter 6Conclusions and Recommendations for Future Work	204
Chapter 7References	207

Acknowledgements

I would like to express my deepest thanks and gratitude to Professor Paul Chalker for providing me with the opportunity to join his group. His continued support, guidance and patience, coupled with his immense knowledge of materials science, have made the past four years a very successful and enjoyable time.

SAFC Hitech very kindly provided the financial sponsorship and allowed me the time to complete the required experimental work. A special mention to Paul Williams who helped me to secure the funding, believed in me and continued to support me to the end.

For assistance with the experimental work and useful discussions the list is endless; to the chemists, Tony Jones, Helen Aspinall, John Basca, Aggi Steiner from the University of Liverpool, and work-colleagues at SAFC Hitech, Barry, Raj, Peter, Andy, Louis, John, Steve and Shaun, many thanks. To the physicist, Matt-your time, knowledge, and assistance with publications has been invaluable to me, and to the 'engineer' Paul for always assisting with reactor modifications and the general maintenance of the clean room...as well as asking the difficult questions! I would also like to thank, Tim Joyce (for help with XPS and AFM), Simon Romani, Tobias Heil, Kerry Abrams and especially Karl Dawson (for SEM and TEM), Joseph Roberts (four point probe) and Peter King (Raman).

On a personal note, it would not have been possible for me to complete this doctorate without the support of my loving husband John, my parents, Paul and Sue, my sister Michelle and all my dear friends, thank you for believing in me, and encouraging me when needed. I finally got there!

Publications

- 1. Metal Organic Chemical Vapour Deposition of Vertically Aligned ZnO Nanowires Using Oxygen Donor Adducts**
Hindley, S.; Jones, A. C.; Ashraf, S.; Bacsa, J.; Steiner, A.; Chalker, P.; Beahan, P.; Williams, P.; Odedra, R.
Journal of Nanoscience and Nanotechnology (2011), 11(9), 8294-8301.
- 2. The Solid-State Structures of Dimethylzinc and Diethylzinc**
Bacsa, J.; Hanke, F.; Hindley, S.; Odedra, R.; Darling, G.; Jones, A.; Steiner, A.
Angewandte Chemie, International Edition (2011), 50(49), 11685-11687, S11685/1-S11685/20.
- 3. MOCVD of Vertically Aligned ZnO Nanowires Using Bidentate Ether Adducts of Dimethylzinc**
Ashraf, S.; Jones, A.; Bacsa, J.; Steiner, A.; Chalker, P.; Beahan, P.; Hindley, S.; Odedra, R.; Williams, P.; Heys, P.
Chemical Vapor Deposition (2011), 17(1-2-3), 45-53.
- 4. Dimethylzinc Adduct Chemistry Revisited: MOCVD of Vertically Aligned ZnO Nanowires Using the Dimethylzinc.1,4-dioxane Adduct**
Kanjolia, R.; Jones, A.; Ashraf, S.; Bacsa, J.; Black, K.; Chalker, P.; Beahan, P.; Hindley, S.; Odedra, R.; Williams, P.; et al
Journal of Crystal Growth (2011), 315(1), 292-296.
- 5. Influence of Co-reagent on the Atomic Layer Deposition of Copper Thin Films**
Kanjolia, R.; Hindley, S.; Abrams, K.; Heil, T.; Chalker, P.; Williams, P.
Poster presented at ALD 2013, San Diego, California,
July 28th-31st 2013
- 6. Molybdenum(IV) Amide Precursors and Use Thereof in Atomic Layer Deposition**
Heys, P.; Odedra, R.; Hindley, S.
Assignee: Sigma-Aldrich Co. LLC, USA
Patent Information: Mar 01, 2012, WO 2012027575, A1
Application: Aug 25, 2011, WO 2011-US49155
Priority: Aug 27, 2010, US 2010-377692P
- 7. Atomic Layer Deposition of Ti-HfO₂ Dielectrics**
Werner, M.; King, P.; Hindley, S.; Romani, S.; Mather, S.; Chalker, P.; Williams, P.; van den Berg, J.
J. Vac. Sci. Technol. A 31, 01A102 (2013).

8. Physical and Electrical Characterisation of Ce-HfO₂ Thin Films Deposited by Thermal ALD

King, P.; Sedghi, N.; Hall, S.; Mitrovic, I.; Chalker, P.; Werner, M.; Hindley, S
J. Vac. Sci. Technol. B 32, 03D103 (2014)

Prizes

9. Metal Organic Chemical Vapour Deposition of Vertically-Aligned ZnO Nanowires using Oxygen Donor Adducts

Hindley, S.; Jones, Anthony C.; Ashraf, Sobia.; Bacsa, John.; Steiner, Alexander.; Chalker, Paul R.; Beahan, Peter.; Williams, Paul A.; Odedra, Rajesh.

First prize: Oral Presentation

EuroCVD18, Kinsale, Co. Cork, Ireland 4-9 September 2011

10. Metal Organic Chemical Vapour Deposition ZnO Nanowires

3rd Prize, Poster Day, University of Liverpool, 2012

List of figures

Figure 1 Schematic view of band theory.....	5
Figure 2 Idealized band structure of a metal, insulator and semi-conductor	6
Figure 3 Schematic view of an n-type and p-type semiconductor	8
Figure 4 Band structures of differently doped semiconductors	9
Figure 5 Fermi-Dirac Function	10
Figure 6 Schematic band diagram, density of states, Fermi-Dirac distribution, and carrier concentrations for intrinsic, n-type and p-type semiconductors at thermal equilibrium	12
Figure 7 Energy-momentum diagram for a free electron.....	14
Figure 8 Energy-momentum diagrams for a semiconductor.....	15
Figure 9 Idealised p-n junction.....	17
Figure 10 A p-n junction energy diagram	18
Figure 11 Current and voltage characteristics of a p-n junction	19
Figure 12 Carrier generation and current flow at the junction	21
Figure 13 Schematic of PV cell.....	23
Figure 14 The crystal structure of silicon.....	29
Figure 15 A schematic showing film formation from PVD.....	34
Figure 16 A schematic showing film formation from CVD	36
Figure 17 A representation of an MOCVD process	36
Figure 18 A stainless steel bubbler	37
Figure 19 A growth curve for a saturative, self-limiting ALD process	39
Figure 20 ALD of hafnium oxide.....	40
Figure 21 ALD growth curve	41

Figure 22 A schematic showing conformal film formation from ALD	42
Figure 23 A generic TGA highlighting the key features used to understand thermal stability and volatility of precursors.....	47
Figure 24 Vapour pressure plot for naphthalene.....	48
Figure 25 Uses of zinc.....	50
Figure 26 Possible bonding modes possible for a zinc centre.....	53
Figure 27 Ball and stick representation of ZnO	58
Figure 28 Local density approximation of the band structure of bulk ZnO.....	60
Figure 29 SEM images of ZnO nanowires from dialkylzinc and oxygen.....	68
Figure 30 SEM images of ZnO nanowires grown using [MeZn(O ⁱ Pr)] and [MeZn(O ^t Bu)]	70
Figure 31 Face centred cubic structure of copper metal	72
Figure 32 A schematic of the Damascene process	74
Figure 33 Crystal structure of CuO and Cu ₂ O	76
Figure 34 Cu(hfac)(vtms).....	78
Figure 35 SEM image of a copper film obtained from [(ⁿ Bu ₃ P) ₂ CuO ₂ CCF ₃]	78
Figure 36 Basic Cu(II) β-diketonate CVD precursor	80
Figure 37 Cu(hfac) ₂	80
Figure 38 Proposed mechanism for copper deposition by CVD for Copper (II) β-diketonate precursors	81
Figure 39 Ester functionalised Cu(II) bis(β-diketoesterates) precursor	83
Figure 40 Structure of Cu(I) N,N ¹ -di-sec-butylacetamidinate	85
Figure 41 SEM micrographs of Cu films grown on SiO ₂ /Si(100) substrate with varying ALD cycles	86
Figure 42 Reaction between [Cu(dmap) ₂] and Et ₂ Zn.....	87

Figure 43 Structure of $[(^n\text{Bu}_3\text{P})_2\text{Cu}(\text{acac})]$	97
Figure 44 Overview of expected proton chemical shifts.....	102
Figure 45 Coupling patterns with relative intensities for ^1H NMR	103
Figure 46 Schematic for ICP-MS.....	104
Figure 47 A flow chart defining ICP-OES analysis.....	105
Figure 48 The vapour pressure system at SAFC Hitech.....	106
Figure 49 Aixtron reactor used for LI-CVD	108
Figure 50 OpAL ALD Reactor.....	110
Figure 51 Plasma unit of OpAL ALD reactor.....	111
Figure 52 X-Ray diffraction.....	112
Figure 53 Miller Indices.....	114
Figure 54 Raman scattering modes	115
Figure 55 A simplified schematic representation of an ellipsometer.....	123
Figure 56 X-ray crystal structure of Et_2Zn	126
Figure 57 Packing diagram of Et_2Zn	127
Figure 58 X-ray crystal structure of $\alpha\text{-Me}_2\text{Zn}$	128
Figure 59 Interactions between $\alpha\text{-Me}_2\text{Zn}$ molecules	128
Figure 60 Disorder of stacks in $\alpha\text{-Me}_2\text{Zn}$	129
Figure 61 Crystal packing diagrams of $\alpha\text{-Me}_2\text{Zn}$	129
Figure 62 X-ray crystal structure of $\beta\text{-Me}_2\text{Zn}$	130
Figure 63 Interactions between $\beta\text{-Me}_2\text{Zn}$ molecules.....	130
Figure 64 Crystal packing diagrams of $\beta\text{-Me}_2\text{Zn}$	131
Figure 65 ^1H NMR spectra of DMZn.THF	134
Figure 66 The oxidation product: $(\text{MeZnOMe})_4$	135

Figure 67 Dependence of the oxidation product formed in the presence of water and/or oxygen.....	136
Figure 68 [(MeZn) ₆ Zn(OMe) ₈]	137
Figure 69 Crystal structure of [DMZn.DMOE].....	138
Figure 70 Crystal structure of [DMZn.1,4-dioxane].....	139
Figure 71 Crystal structure of [DMZn.1,4-thioxane].....	140
Figure 72 Loose packing chains formed via ZnO and ZnS contacts	141
Figure 73 TGA data for DMZn.L and [(MeZn) ₆ Zn(OMe) ₈].	144
Figure 74 Variation of the ZnO growth rate with substrate temperature for [Me ₂ Zn(L)].....	146
Figure 75 Impact of substrate temperature on ZnO formation.....	147
Figure 76 SEM images for ZnO nanowires deposited using [DMZn.1,4dioxane]	149
Figure 77 SEM images of the deposition time dependence on morphology of ZnO deposited on Si(111)	151
Figure 78 SEM images analysing the impact of oxygen flow rate on the morphology of ZnO	152
Figure 79 XRD data for the ZnO NWs deposited from [DMZn.1,4-dioxane].....	154
Figure 80 Raman spectra of the ZnO NWs grown [DMZn.1,4-dioxane], [DMZn.DMOE] and [DMZn.1,4-thioxane].....	155
Figure 81 Room temperature photoluminescence data for ZnO NWs.....	156
Figure 82 Cu(hfac)(COD)	163
Figure 83 Reaction scheme for the synthesis of CpCu(^t BuNC).....	164
Figure 84 ¹ H NMR with a photograph insert of CpCu(^t BuNC).....	164
Figure 85 TGA of CpCu(^t BuNC).....	165
Figure 86 Vapour pressure of CpCu(^t BuNC).....	166

Figure 87 Isothermal TGA at 100°C	167
Figure 88 ¹ H NMR for CpCu(^t BuNC) after being held at 100°C for 16 hours.....	168
Figure 89 Isothermal TGA at 140°C for CpCu(^t BuNC)	168
Figure 90 Thermal decomposition growth rates for Cu(hfac)(COD) and CpCu(^t BuNC)	170
Figure 91 Copper film deposited from Cu(hfac)(COD).....	171
Figure 92 XRD for as-deposited films from CpCu(^t BuNC) and Cu(hfac)(COD) .	172
Figure 93 XRD trace of copper deposited from Cu(hfac)(COD) on glass via both thermal decomposition and with a tertiary butyl hydrazine coreagent	176
Figure 94 TEM images of the copper film grown with Cu(hfac)(COD) and tertiary butyl hydrazine.....	179
Figure 95 Diffraction pattern from TEM	179
Figure 96 Variation of growth rate for CpCu(^t BuNC) for pulsed CVD and hydrogen plasma-assisted ALD	181
Figure 97 Photographs showing copper deposition on glass, silicon and TiN substrates.....	181
Figure 98 XRD for as-deposited samples from CpCu(^t BuNC) and hydrogen plasma at 75°C.....	182
Figure 99 SEM study of the surface morphology of the Cu ALD film deposited on various substrates at 75°C	183
Figure 100 Cross section of a copper film grown at 75°C on silicon using CpCu(^t BuNC) and a hydrogen plasma.....	185
Figure 101 Copper films imaged at a high tilt angle on silicon and TiN.....	185
Figure 102 TEM of copper films deposited from CpCu(^t BuNC) and hydrogen plasma at 75°C	186

Figure 103 Atomic resolution TEM of copper films deposited from CpCu(^t BuNC) and hydrogen plasma.....	187
Figure 104 Diffraction pattern via TEM for the Copper film grown at 75°C using CpCu(^t BuNC) and hydrogen plasma.....	187
Figure 105 EELs spectra showing the characteristic copper metal peak	188
Figure 106 EELs spectra showing the lack of oxygen detected.....	188
Figure 107 TEM images for copper film deposited at 150°C from 5000 cycles CpCu(^t BuNC).....	189
Figure 108 Diffraction pattern from the deposition at 150°C of CpCu(^t BuNC) and hydrogen plasma, 5000 cycles	190
Figure 109 TEM images from the deposition of CpCu(^t BuNC) and hydrogen plasma at 175°C on a holey carbon grid at 200nm scale.....	190
Figure 110 TEM images from the deposition of CpCu(^t BuNC) and hydrogen plasma at 175°C on a holey carbon grid at 20nm scale.....	191
Figure 111 Statistical analysis of particle diameter	191
Figure 112 Diffraction pattern confirming both Cu and Cu ₂ O was deposited CpCu(^t BuNC) and hydrogen plasma at 175°C	192
Figure 113 A spot pattern confirming the Cu ₂ O zone axis from the deposited CpCu(^t BuNC) and hydrogen plasma at 175°C	192
Figure 114 Growth curve for the ALD of Cu(hfac)(COD) with ozone	193
Figure 115 Raman spectra for as-deposited films from Cu(hfac)(COD) and ozone between 125°C and 350°C. (C is denoting the peak for carbon incorporation).....	194
Figure 116 TEM images for the film deposited at 150°C with CpCu(^t BuNC) and oxygen plasma.....	195

Figure 117 TEM diffraction pattern for the film deposited using CpCu(^t BuNC) and oxygen plasma at 150°C	196
Figure 118 The growth rate for CpCu(^t BuNC) with water against the temperature range 175-350°C	197
Figure 119 XRD for the film deposited with CpCu(^t BuNC) and water at 175°C..	197
Figure 120 TEM images of deposited material from CpCu(^t BuNC) and water at 175°C	198
Figure 121 Identification of the Cu ₂ O zone axis from the FFT of a 4nm particle	199
Figure 122 The morphology of a film deposited from CpCu(^t BuNC) and water..	199

List of Tables

Table 1 Solar cell efficiencies	3
Table 2 Reported band gap energies for ZnO, CuO and Cu ₂ O	24
Table 3 Reported valence and conduction band offsets for Cu ₂ O/ZnO and CuO/ZnO systems	24
Table 4 Cell efficiencies recorded for ZnO/Cu ₂ O and Zn/CuO based upon method of deposition.....	27
Table 5 A selection of typical precursors used for various electronic applications .	45
Table 6 Nitrogen based adducted dimethylzinc compounds.....	55
Table 7 The beneficial properties of Zn	58
Table 8 Summary of the conditions used for the deposition of ZnO NWs	69
Table 9 Copper (II) β-diketonate CVD Precursors	80
Table 10 Evaporation and deposition temperature for selected Cu(II) β-diketonate precursors	82
Table 11 Ester functionalised Cu(II) β-diketonate precursors	83
Table 12 Controlling the copper oxide phase using either oxygen or a mixture of oxygen/water with Cu(hfa) ₂ .TMEDA.....	91
Table 13 Impact of altering oxygen partial pressure for a copper oxide film.....	93
Table 14 Cu(acac) ₂ used for copper oxide deposition on fibreglass at various substrate temperatures.....	95
Table 15 Key parameters for the crystal structures of diethyl and dimethyl zinc..	132
Table 16 Ligands used for DMZn.L adduct synthesis	133
Table 17 Crystallographic data for DMZn.L.....	142
Table 18 Selected bond lengths and angles for complexes of DMZn.L	143

Table 19 Growth conditions used to deposit ZnO by LI- MOCVD.....	145
Table 20 SEM images of temperature dependence of ZnO morphology	148
Table 21 Summary of oxygen flow rates and subsequent O ₂ :Zn ratio.....	152
Table 22 Summary of the deposition conditions and ZnO film morpholgy from [DMZn.L].....	153
Table 23 The composition of ZnO nanowires deposited by MOCVD from DMZn.L	158
Table 24 ¹ H NMR characterisation data for [DMZn.L]	161
Table 25 SEM images for films deposited from Cu(hfac)(COD) and CpCu(^t BuNC) without co-reagent.....	173
Table 26 Conditions used for the thermal decomposition of Cu(hfac)(COD)	175
Table 27 SEM images for films deposited using Cu(hfac)(COD) via thermal decomposition and with tertiary butyl hydrazine co-reagent.....	177
Table 28 Growth parameters used for copper metal deposition using CpCu(^t BuNC) and hydrogen plasma.....	180
Table 29 Copper and copper oxide deposition summary	200

Abbreviations and symbols

J_{max}	Maximum theoretical current density
m_n^*	Electron effective mass
m_p^*	Hole effective mass
μ	Electron mobility
\AA	Angstrom
AES	Atomic emission spectroscopy
AFM	Atomic force microscopy
ALD	Atomic layer deposition
ALE	Atomic layer epitaxy
AZO	Aluminium doped zinc oxide
b.p.	Boiling point
CBE	Chemical beam epitaxy
CMOS	Complementary metal oxide semiconductor
Cp	Cyclopentadienyl ($C_5H_5^-$)
CpCu(^t BuNC)	Cyclopentadienyl copper tertiary butyl isocyanide
Cu(hfac)(COD)	Copper hexafluoroacetylacetonato cyclo-octadiene
d	Atomic spacing (lattice parameter)
DEZn	Diethyl zinc
DMOE	1,2-dimethoxyethane
DMZn	Dimethyl zinc
DMZn.L	Adducted dimethyl zinc where L=ligand adduct
E	Energy
$E(\lambda)$	Photon energy
EELs	Electron energy loss spectroscopy
EDX	Energy dispersive x-ray spectroscopy
E_c	Conduction band edge energy
E_f	Fermi-level
E_g	Band gap energy
E_i	Intrinsic Fermi-level
E_v	Valance band energy
FCC	Face centred cubic
FFT	Fast fourier transform
FTO	Fluorine doped tin oxide
GZO	Gallium doped zinc oxide

h	Planck's constant ($6.626068 \times 10^{-34} \text{ m}^2 \text{ kg / s}$)
hfac	Hexafluoroacetylacetone
IC	Integrated circuit
ICPms	Inductively coupled plasma mass spectroscopy
ICPoes	Inductively coupled plasma optical emission spectroscopy
ITO	Indium doped tin oxide
k	Boltzmann's constant ($1.38 \times 10^{-23} \text{ JK}^{-1}$)
K	Propagation constant
L	Ligand
LASER	Light Amplification by Stimulated Emission of Radiation
LED	Light emitting diode
LICVD	Liquid injection chemical vapour deposition
m	Mass of electron
m.p.	Melting point
MBE	Molecular beam epitaxy
MOCVD	Metal organic chemical vapour deposition
MOMBE	Metal-organic molecular beam epitaxy
n	Order of diffraction
n_i	Intrinsic carrier density
N_c	Effective density of states in the conduction band
N_v	Effective density of states in the valence band
nm	Nanometer
NMR	Nuclear magnetic resonance
NW	Nanowire
p	Momentum
$P(\lambda)$	Spectral irradiance
PECVD	Plasma Enhanced chemical vapour deposition
PL	Photoluminescence
ppm	Parts per million
PV	Photovoltaic
PVD	Physical vapour deposition
q	Electron charge
QE	Quantum efficiency
$QE(\lambda)$	Ratio of the number of charge carriers the cell yields vs. number of photon illuminating the cell for a given unit of time
R-NC	Isocyanide
SEM	Scanning electron microscopy

T	Temperature (K)
^t Bu	Tertiary butyl
TCO	Transparent conducting oxide
TEM	Transmission electron microscopy
TFT	Thin film transistor
TGA	Thermogravemetric analysis
THF	Tetrahydrofuran
THP	Tetrahydropyran
XPS	X-ray photon spectroscopy
XRD	X-ray diffraction
θ	Incident angle of the incoming X-Rays
λ	Wavelength
ϕ	Flux of the spectrum illuminating the cell

Chapter 1 Introduction

1.1 Project Aim

The overall project aim was to develop and investigate the materials and structure for a more efficient, cost effective photovoltaic (PV) cell. In keeping with the recent emergence of a new field of PV, this thesis focuses on an all-oxide PV structure. An all-oxide PV approach was chosen due to the attractive properties of using less toxic and more abundant chemicals in manufacture, good chemical stability increasing the operating lifetime and having the ability to scale production for industrial manufacture leading to cost reductions. Metal oxides are already integrated into PV cells in the form of transparent conductive oxides (TCOs). The work here looks to the development of metal oxide materials as both n-type and p-type semiconductors forming a p-n junction PV cell. To fully investigate this, an introduction to the scientific theory, along with a review of the literature for previously manufactured solar cells is presented within this chapter. **Section 1.6.2** brings focus to the specifics of the target PV structure and introduces the material systems investigated. Furthermore, the benefits and novelty of the work undertaken are discussed before moving onto **Chapter 2** which provides a detailed literature review of the materials employed.

1.1.1 Solar Cells

1.1.1.1 Introduction

Solar energy for photovoltaic conversion into electricity is abundant, inexhaustible and clean; yet, it requires special techniques to gather it efficiently. Photovoltaic cells, also termed solar cells, operate by converting sunlight directly into electricity using the electronic properties of semi-conductor materials. Based upon quantum

theory, light is made up of packets of energy called photons where the energy of the photon is dependent on the frequency of light. This energy is sufficient to excite charge carriers (e.g. electrons and holes) in the semi-conductor material. It is these charge carriers that are pulled away to an external circuit by contacts with differing electronic properties in a photovoltaic device. The effectiveness of such a device depends upon the choice of light absorbing materials and the way in which it contacts with the external circuit. The photovoltaic effect was first reported by Edmund Becquerel in 1839 when he observed that when light struck a silver coated platinum electrode immersed in electrolyte an electric current was produced.¹

An electrolyte is a substance that conducts electric current as a result of dissociation into positively and negatively charged ions. These ions migrate toward, and are discharged at, the negative and positive terminals (cathode and anode respectively) of an electric circuit.² The PV effect was first studied in solids such as selenium in the 1870s.³ In the 1940s and early 1950s a method for producing highly pure crystalline silicon, the Czochralski method,⁴ led to a huge step forward in solar cell technology. The first silicon solar cell was reported by Chaplin, Fuller and Pearson in 1954 and converted sunlight with an efficiency of 6%.¹ In the 1970s much interest was placed on alternative sources of energy including solar cells due to the crisis in energy supply experienced by the western world. Interest focused on producing devices more cheaply and improving the efficiency. This interest has been maintained in a drive to secure sources of electricity which provide an alternative to fossil fuels. With advances in chemistry, materials science and the general understanding of solar cells, we are now in an age where solar cells are affordable and practical to consumers on private housing, yet, there is still a strive to provide more efficient solar cells.

1.1.1.2 Types of Solar Cell

There are many varied types of solar cell. All have their own advantages, disadvantages and efficiencies and these are documented in **Table 1**.

Cell Type	Advantages	Disadvantages	Efficiency
Monocrystalline silicon	Highly standardised and available on the market.	Most expensive. Waste of silicon in the production process.	25%
Monocrystalline GaAs	Increased temperature efficiency over silicon. Direct band gap	High material cost. Expensive to grow on costly lattice matched substrates e.g. Ge	29%
Polycrystalline silicon	Less expensive than monocrystalline Silicon (less energy and time needed for production)	Slightly less efficient than monocrystalline Silicon	20%
Thin Films PV Cells (e.g. a-Si, CdTe, CI(G)S (Cu-In-(Ga)-Se)	Low cost due to fast throughput over large areas via physical/chemical deposition. Varied substrates. Robust. Visually more pleasing.	Lower power conversion. Requiring larger areas of PV arrays and more material (cables, support structures) to produce the same amount of electricity. Some elements are toxic.	20% (CI(G)S) 18% (CdTe) 10% (a-Si)
Multi-stack thin film	High efficiency as each cell absorbs a certain wavelength, and then the stack can absorb more from the solar spectrum.	Multi material system can be costly. Increased skill in manufacturing.	44.7% ⁵
Dye-sensitised (Grätzel Cell)	Very well understood.	Platinum and ruthenium are expensive metals. Liquid electrolyte has temperature limitations. Thicker devices required. VOCs	12%
Excitonic (Organic/polymeric materials)	High absorption coefficient. Simple processing. Structurally flexible.	Still in development stages. Material and production cost low but devices have a short life span.	10%

Table 1 Solar cell efficiencies.⁶

The work discussed within the scope of this research involves the potential application of semiconductor materials in a p-n junction as a nanostructured solar cell. The following sections briefly describe the background scientific theory necessary to understand the motivation and objectives based upon the required attributes of a PV device.

1.2 Band Theory

The electrical properties of a solid are determined by the distribution of electrons. Band theory can be used to describe the electronic structure of conductors, insulators and semiconductors.

1.2.1 Conductors

A conductor is a material in which electric current (i.e. electrons) flow under the influence of an applied voltage. Metals are all conductors. Lithium (Li), is the lightest metal, and contains atoms held together in a three-dimensional crystal lattice. Bonding interactions among these atoms can be described by orbital overlap. One Li atom contributes one s orbital at certain energy. When we introduce a second atom, it overlaps the first and forms bonding and anti-bonding orbitals, three atoms would have three molecular orbitals, n atoms would give n molecular orbitals. As the number of atoms increases, the number of molecular orbitals covering a band of energies increases, and the energy spacing between them decreases as the band remains of finite width. For an infinite number of atoms, the orbitals are spaced so closely that they behave as though they are merged together into an energy band. **Figure 1** shows this 2s orbital overlap description schematically, however, metal bonding does include interactions with all valence s, p, d and f orbitals. Each group of orbitals interact to generate an energy band. The band formed from the overlap of

the s orbitals is called the s band. If the atoms have p orbitals available the same procedure applies and leads to a p band.

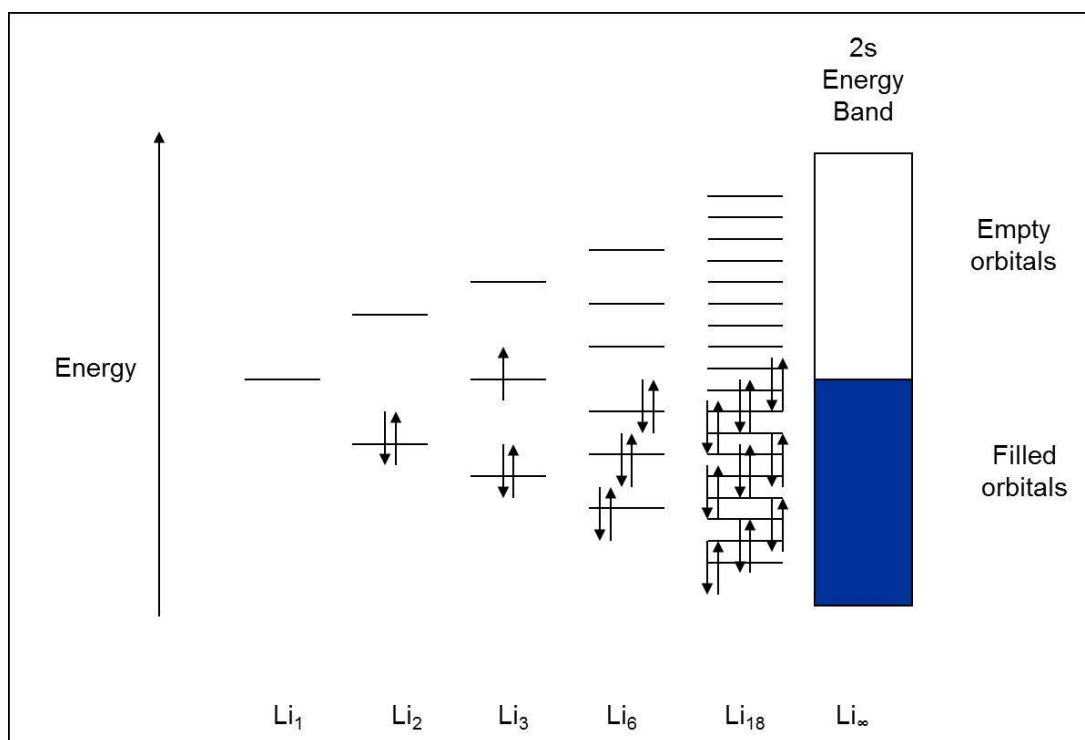


Figure 1 Schematic view of band theory for the energies of delocalised orbitals made from the 2s orbitals of lithium atoms. A metal containing n atoms of Lithium, has a continuous band of filled bonding and empty antibonding orbitals. (adapted from ⁷⁾)

In a metal, the orbitals of highest-energy are so close in energy to the unoccupied orbitals of lowest energy that very little energy is required to transfer an electron from an occupied to an unoccupied orbital. When an electrical potential is applied to a metal, the negative pole repels electrons. In energy terms, the occupied orbitals near the negative pole are pushed higher in energy than the unoccupied orbitals near the positive pole. As a result, electrons flow from the filled orbitals to the empty orbitals and an electrical current is generated. Partially filled atomic orbitals can also enable a metal to be conducting and this is highlighted in **Figure 2**.

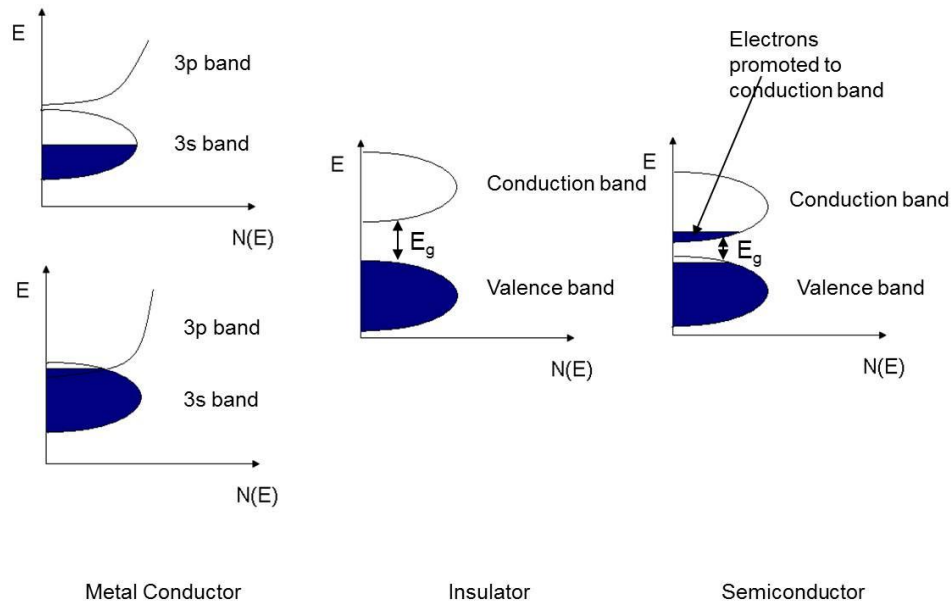


Figure 2 Idealized band structure of a metal, insulator and semi-conductor.⁸

1.2.2 Insulators

In an insulator the highest occupied band (the valence band) is filled and is energetically separated for the lowest unoccupied band (the conduction band) by a band gap (E_g). The band gap is large enough to prevent the thermal excitation of electrons into the conduction band. Electrical conduction is prevented because the electrons do not have vacant energy levels into which they migrate, and so cannot move through the material, **Figure 2**.

1.2.3 Semi-conductors

A semi-conductor has a similar overall band structure to that of an insulator, however, the difference being the size of the band gap (see **Figure 2**). In a semiconductor the band gap is small (1-3eV) enough to allow thermal excitation of electrons into the conduction band. Examples include the semiconductors, InP ($E_g = 1.42\text{eV}$) and CdTe ($E_g = 1.61\text{eV}$) at 0K, both used for solar cells.⁹ As with

molecular orbitals, the energy levels in a band are progressively filled from the lowest energy upwards. At zero Kelvin, the electrons occupy only the lowest energy levels available. The Fermi Level, E_f , refers to the highest occupied molecular orbital at absolute zero, and will be discussed further in **section 1.3**. Above zero Kelvin, electrons can be thermally excited to higher levels. Raising the temperature of the semiconductor increases the number of electrons promoted across the band gap. This is an important property of an intrinsic or un-doped semiconductor. The number of electrons in the conduction band must equal the number of holes in the valence band. (Note for a metal, increasing the temperature actually reduces the conductivity due to increased thermal motion in the lattice which limits the electron mobility due to increased collision between the lattice and electrons).

One method of increasing the number of charge carriers and enhancing the conductivity of a solid, is to add foreign atoms to an otherwise pure material, this is termed an extrinsic, or doped semiconductor. An extrinsic semiconductor has almost the same band structure as the pure material, but it has more levels in the band gap, allowing the excitation of electrons. If these dopants can trap electrons (e.g. gallium (Ga) atoms doped into silicon (Si)), they withdraw electrons from the filled band, leaving holes which allow the remaining electrons to move (E.g. $\text{Ga}=[\text{Ar}]3d^{10} 4s^2 4p^1$ in $\text{Si}=[\text{Ne}] 3s^2 3p^2$). This is a p-type semiconductor, because their low-energy bands have positive vacancies or 'holes'. Electrons move through the crystal by flowing from filled orbitals into these vacant orbitals. Alternatively, a dopant may carry excess electrons (E.g. arsenic (As) atoms doped into silicon, $\text{As}=[\text{Ar}]3d^{10} 4s^2 4p^3$ and $\text{Si}=[\text{Ne}] 3s^2 3p^2$), the additional valence electron can occupy an otherwise empty band giving n-type semi-conductivity, where n denotes the negative charge e.g. electrons of the carriers.⁷ This is shown schematically in **Figure 3**.

Semiconductors such as silicon are extremely sensitive to impurities. Replacing just 0.00001% of the Si atoms with a dopant can cause as much as a 100,000-fold increase in electrical conductivity.

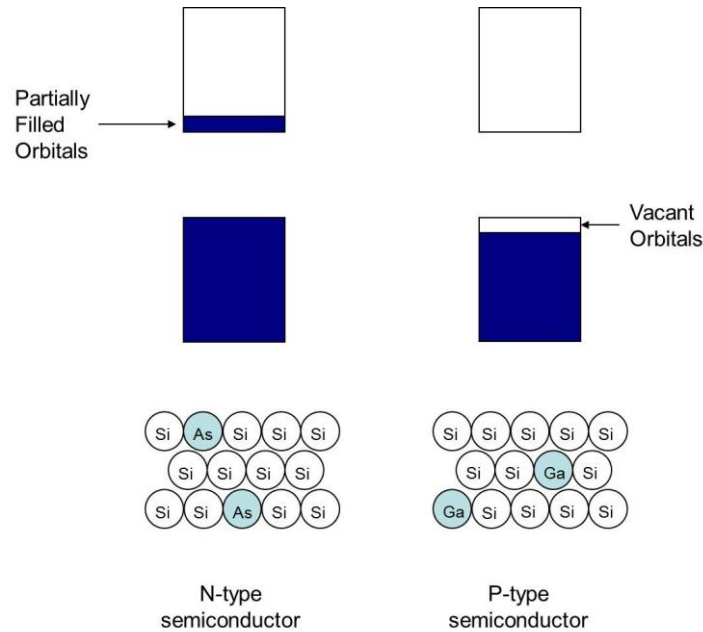


Figure 3 Schematic view of an n-type and p-type semiconductor. Each arsenic atom (As) contributes 5 valence electrons instead of four, which forces an electron to occupy the higher energy band. Each gallium atom (Ga) contributes three valence electrons instead of four, which leaves a vacancy in the lower-energy band.⁷

Current flows in a doped semiconductor the same way current flows in a metal. Only a small energy difference exists between the top of the filled band and the next available orbital, so the slightest applied potential allows electrons to move and current to flow.

1.3 Fermi-Level

The Fermi level can be described as a reference energy-level at which the probability of occupation by an electron is 50%. As the Fermi-level is only a reference level it can appear at different levels on a semiconductor energy-band diagram depending on the doping conditions. The band structure of the two

differently doped semiconductors (e.g. n-type and p-type) with respect to their Fermi levels can be seen in **Figure 4**.

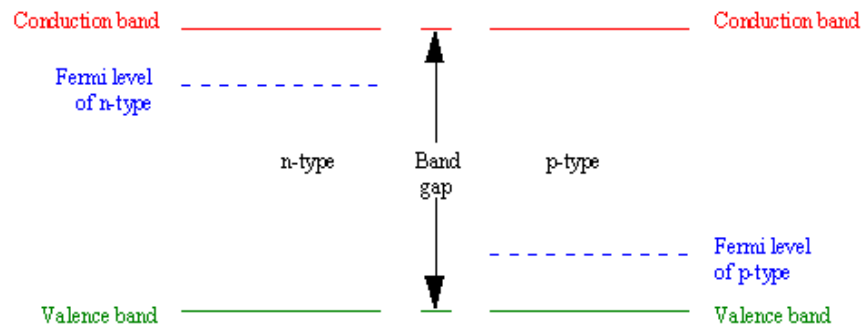


Figure 4 Band structures of differently doped semiconductors. ^{4, 10, 11}

The Fermi-Dirac function (equation 1) gives the probability of occupation of an energy-level at energy E as an inverse exponential function involving the difference in energy between the energy level under consideration, E and the Fermi-level, E_F :

Equation 1:
$$P_{fd}(E) = \frac{1}{1 + \exp\left(\frac{E - E_F}{kT}\right)}$$

Where k = Boltzmann's constant ($1.38 \times 10^{-23} \text{JK}^{-1}$) and T=temperature (K)

If we consider the energy level E to be at the Fermi-level then:

Equation 2:
$$P_{fd}(E_F) = \frac{1}{1 + \exp\left(\frac{E - E_F}{kT}\right)} = \frac{1}{2}$$

The probability of finding an electron at the Fermi-level is 50%. If $P_{fd}(E_F)$ is the probability of finding an electron at energy E, then $1 - P_{fd}(E_F)$ must be the probability of not finding an electron at energy E, or the probability of finding a hole at energy E. The calculation indicates the symmetry of the Fermi-Dirac function about the Fermi-Level.

1.3.1 Temperature Dependence

The temperature dependence of the function shows that at 0K all levels below the Fermi-Level are filled, and all levels above the Fermi-Level are empty.

When T=0K

If $E > E_F$ $P_{fd}(E) = \frac{1}{1 + \infty} = 0$

Or if $E < E_F$ $P_{fd}(E) = \frac{1}{1 + 0} = 1$

Increasing the temperature causes some levels above E_f to become filled and therefore, since the function is symmetrical, some levels below E_f empty. A plot of the probability as a function of energy for the Fermi-Dirac function is shown in **Figure 5** for several temperatures.

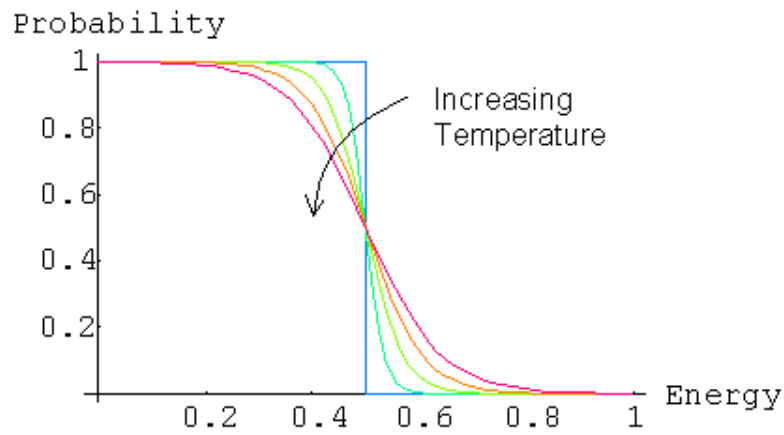


Figure 5 Fermi-Dirac Function. ¹²

1.3.2 Calculation of Fermi-Level

For an intrinsic semiconductor the Fermi-level lies very close to the middle of the band gap. The Fermi energy, E_i , is related to the intrinsic carrier density as shown in equation 3:

Equation 3: $n_i = N_c e^{(E_i - E_c)/kT} = N_v e^{(E_v - E_i)/kT}$

Where:

n_i is intrinsic carrier density

N_c is the effective density of states in the conduction band

N_v is the effective density of states in the conduction band

E_i is the intrinsic Fermi-level

E_c is the conduction band edge energy

E_v is the valence band edge energy

To eliminate the intrinsic Fermi energy from both of the above (equation 3), multiply both E_i and take the square root. This now provides an expression for the intrinsic carrier density as a function of the effective density of states in the conduction and valence band (and thus the band gap energy as $E_g=E_c-E_v$):

$$\text{Equation 4:} \quad n_i = \sqrt{N_C N_V} e^{-(E_c-E_v)/2kT}$$

Where: k =Boltzmann's constant ($1.38 \times 10^{-23} \text{JK}^{-1}$)

T =temperature (K)

By rearrangement of equations 3 and 4, to calculate the position that the Fermi-level occupies in an intrinsic, un-doped semiconductor:

$$\text{Equation 5:} \quad E_i = \frac{E_c+E_v}{2} + \frac{1}{2} kT \ln \left(\frac{N_V}{N_C} \right)$$

Knowing that the product of the electron and hole density (n and p respectively) is equal to the square of the intrinsic carrier density

$$\text{Equation 6:} \quad n \cdot p = N_C N_V e^{(E_v-E_c)/kT} = n_i^2$$

The intrinsic Fermi energy can also be expressed as a function of the effective masses of the electrons and holes in the semiconductor. Using the expressions for the effective density of states in the conduction and valence band (equation 5) and combining with 6:

$$\text{Equation 7:} \quad E_i = \frac{E_c+E_v}{2} + \frac{3}{4} kT \ln \frac{m_p^*}{m_n^*}$$

Where: m_p^* is the hole effective mass

m_n^* is the electron effective mass

In general the electron and hole effective masses are unequal and therefore the intrinsic Fermi-level does not lie in the exact middle of the band gap. The intrinsic Fermi-level would lie in the middle of the band gap if $T=0\text{K}$ as the part of the equation containing the effective masses disappears.

When impurities are introduced into the semiconductor crystals, energy levels are introduced that usually lie within the energy gap, depicted in **Figure 6**.

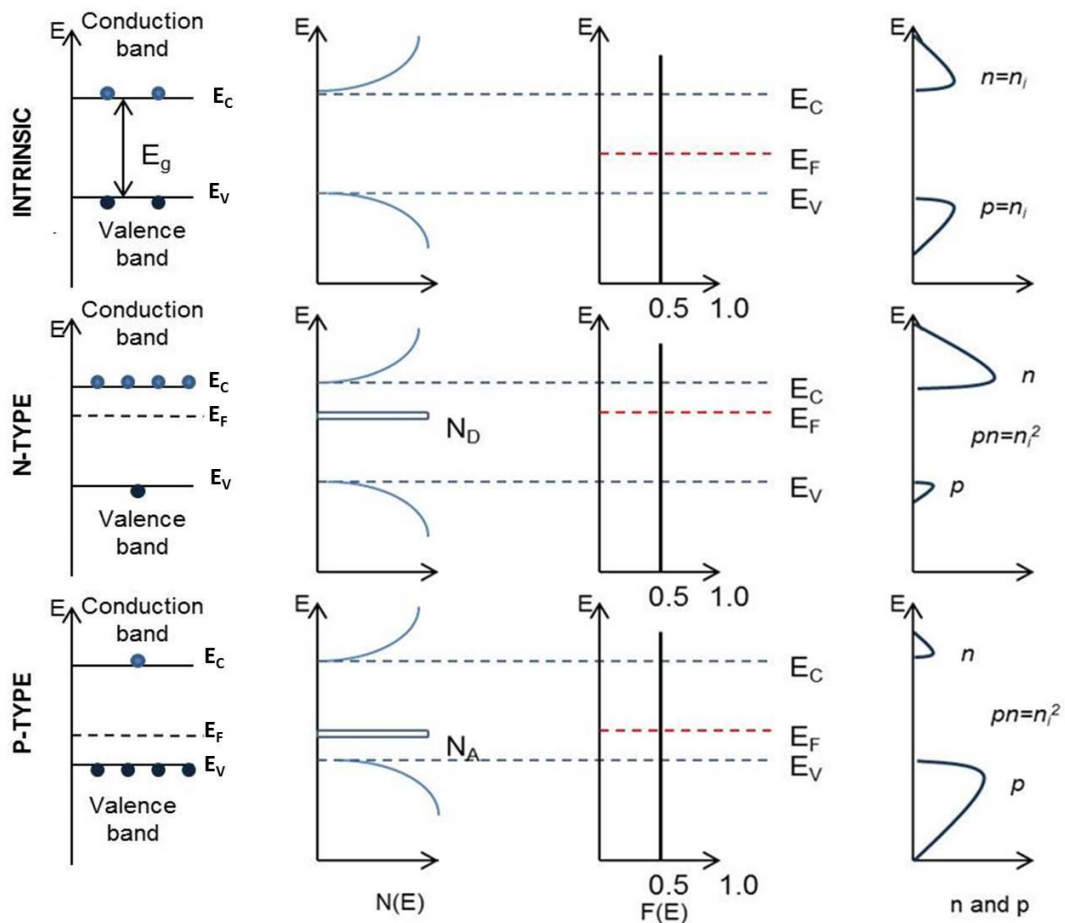


Figure 6 Schematic band diagram, density of states, Fermi-Dirac distribution, and carrier concentrations for intrinsic, n-type and p-type semiconductors at thermal equilibrium. ¹³

Increasing the temperature of an extrinsic semiconductor, increases the number of electron-hole pairs because more thermal energy is available to promote an electron from the valence to the conduction band. As the temperature is increased further, there will become a point where the number of thermally generated electron-hole pairs exceeds the number of deliberately introduced dopant carriers. At this point the semiconductor begins to lose its characteristic doping type and begins to act intrinsically. For a p-type material, the Fermi-level will move away from the position near the valence band edge, towards the middle of the energy gap. For an n-

type material, the Fermi-level moves away from the conduction band edge and towards the middle of the gap with increasing temperature.

1.4 Band-gap Energy

Particles under certain conditions can show wave-like behaviour, one example of this is when electrons (and holes) travelling through a crystal lattice are diffracted. To link particle to wave-like behaviour, we can use the de Broglie equation to calculate the wavelength, λ , of the electron. Electrons will only be diffracted if they satisfy the diffraction condition which is a function of their momentum. For the diffraction of waves (e.g. x-rays) the Bragg diffraction condition, equation 8, must be obeyed:

$$\text{Equation 8:} \quad n\lambda = 2d \sin \theta$$

Where: n = order of diffraction

λ =the wavelength of X-rays

d =atomic spacing (lattice parameter)

θ =incident angle of the incoming X-Rays

Assuming wave propagation is normal to a set of atomic planes, the angular dependence is neglected, when thinking about the diffraction of particles (e.g. electrons), the angle free diffraction equation becomes:

$$\text{Equation 9:} \quad n\lambda = 2d$$

At values of λ given in equation 9, standing waves will be set-up between the atomic planes. Since the wavelength of the electron is directly related to its momentum, electrons with this momentum cannot propagate through the crystal lattice and the velocity is zero. These conditions account for forbidden energy bands. If there was a completely free electron, its energy is related to its momentum by:

Equation 10: $E = \frac{p^2}{2m}$

Where: E=energy

p=momentum

m=mass of electron

Writing the momentum in terms of the particles de Broglie wavelength:

Equation 11: $p = \frac{h}{\lambda}$

Where: h=Planck's constant

Knowing that the propagation constant of a wave is denoted by k, where

Equation 12: $k = \frac{2\pi}{\lambda}$

The energy-momentum equation can now become:

Equation 13: $E = \frac{\hbar^2 k^2}{2m}$

Where: $\hbar^2 = h^2/4\pi^2$

Equation 13 now relates the energy of a particle, E, with the propagation constant, k, and this is shown graphically in **Figure 7**.

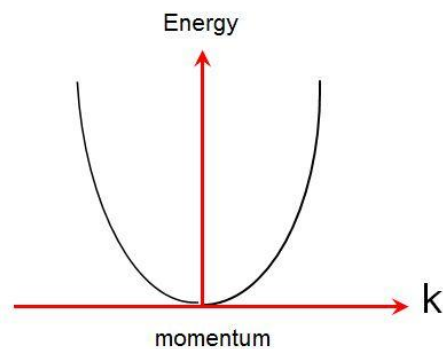


Figure 7 Energy-momentum diagram for a free electron. ^{12, 14}

The E-k curve is parabolic and all values of energy (and momentum) are allowed. To find the mass of the particle, (given in the E-k diagram the mass is inversely proportional to the curvature of the E-k curve),

Equation 14:
$$E = \frac{\hbar^2 k^2}{2m}$$

Equation 15:
$$\frac{dE}{dk} = \frac{\hbar^2 k}{m}$$

Equation 16:
$$\frac{d^2E}{dk^2} = \frac{\hbar^2}{m}$$

Although this was generated assuming free electrons, the equation still holds for electrons (or holes) in crystals, so more generally the effective mass of the particle (electron or hole), m^* , can be calculated using:

Equation 17:
$$m^* = \frac{\hbar^2}{d^2E/dk^2}$$

As explained earlier, the band-gap energy is defined as the difference in energy between the valence and conduction bands for insulators and semiconductors. The band-gap can be further categorized as direct or indirect. **Figure 8** shows two hypothetical energy-momentum diagrams for a direct and indirect band-gap semiconductor.

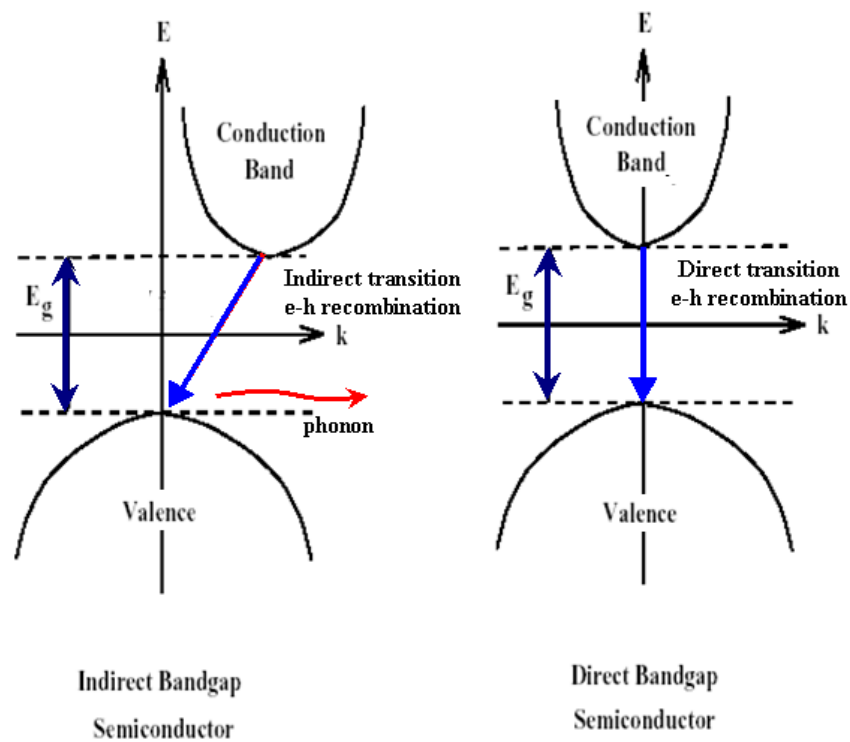


Figure 8 Energy-momentum diagrams for a semiconductor. ¹⁵

For an indirect band gap semiconductor, note that there is a maximum in the valence band curve at $k=0$, and a minimum in the conduction band curve at a different k value. If an electron sitting near the conduction band minimum (where its energy is lowest) is to recombine with a hole sitting near the valence band maximum, then the electron must lose some momentum in making this transition. To ensure the overall momentum is conserved a phonon is released. Conversely, for a direct band gap semiconductor when $k=0$ the conduction band is at a minimum and the valence band is at a maximum. This means that an electron and hole pair can recombine and there is no change in momentum required.

III-V semiconductors (e.g. GaAs) are direct band-gap materials with efficient photon producers which makes them suitable for use in LEDs and LASERS, whilst bulk silicon is a highly inefficient photon producer and is an indirect band gap material.

1.5 Carrier Concentration and Mobility

The conductivity of a semi-conductor is determined by both the carrier concentration and the electron mobility (μ). The carrier concentration is the number of electrons or holes per unit area and the electron mobility is simply the ratio of the drift velocity and the electric field, and relates to the ease of movement of the carriers under the effect of an electric field. Both these features are highly influenced by temperature; at higher temperature, higher lattice vibrations allow energy to transfer between the lattice and carriers thus leading to scattering and reduced mobility. At higher temperatures for an intrinsic semiconductor, more electron-hole pairs are generated so the conductivity increases, eventually, the semiconductor breaks down.

1.6 The p-n junction

The p-n junction is of great importance both in modern electronic applications and in understanding other semi-conductor devices. When a p-type and n-type material are placed in contact with one another, it allows current to flow easily in one direction only (forward biased) and not in the other (reverse biased), creating a diode. This non-reversing behaviour comes from the charge transport process in the two types of material. **Figure 9** shows a schematic of an idealised p-n junction.

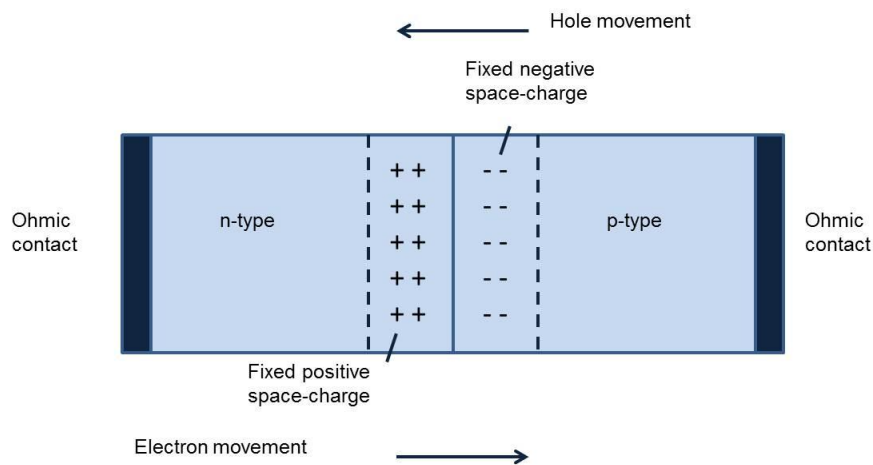


Figure 9 Idealised p-n junction. ¹²

A p-type material (rich in holes) has formed a junction with an n-type material (rich in electrons), with the solid line in **Figure 9** representing the junction. The holes and the electrons ideally would like to recombine. Due to the charges of the holes and electrons the conditions are ideal for diffusion of the holes towards the electron (i.e. from the right hand side of the junction to the left) and vice-versa. The material gains its p- or n-type characteristic due to its doping with donor and accepting elements that are held in fixed positions in the lattice (unless the semiconductor is heated and they can then diffuse). The electrons and holes from the donor and acceptor atoms are free to move. As the holes diffuse to the left side of the junction to combine with electrons, negative charges are left behind. Similarly, electron

moving from the left to the right will leave behind positive donor centres. An equilibrium condition is reached as shown in **Figure 9** in the region between the two dotted lines. This region can be termed the depletion region, (i.e. it is depleted of charge carriers). It is worth noting that the fixed charges builds up to a point where the electric field produced slows down the diffusion process. Away from the junction region, the material has no charge as the carriers still sit on the dopant centres. When the p and n type materials are brought together at thermal equilibrium, the Fermi levels on either side are forced to align, causing the valence and conduction bands to bend as shown **Figure 10**.

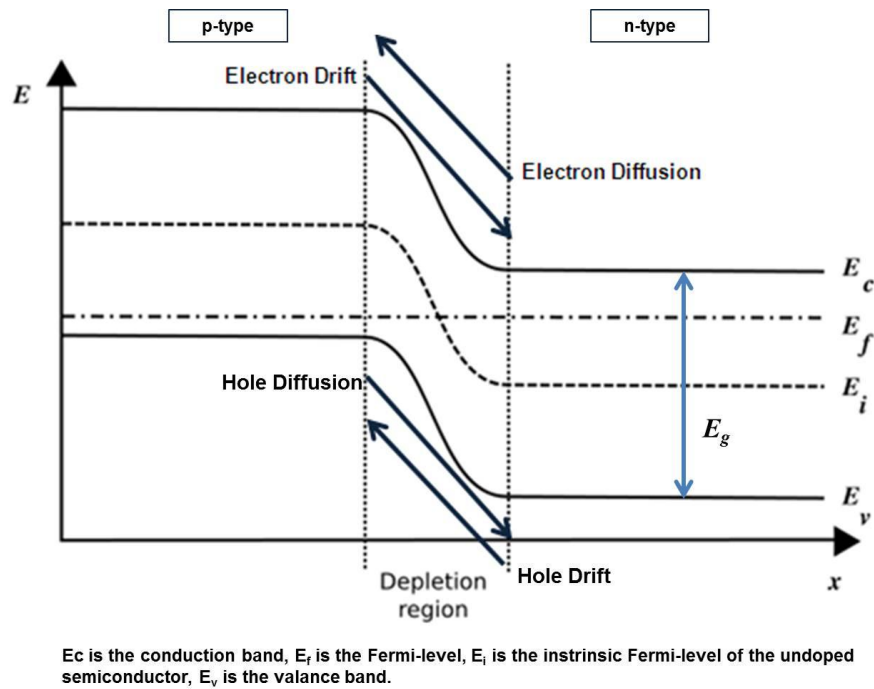


Figure 10 A p-n junction energy diagram. ^{11, 12}

The overriding factor is that the Fermi-level has to remain continuous at a junction. This then allows the movement of electrons and holes, which creates charge depletion regions and an altered band structure. In thermal equilibrium there is zero net current flow as the opposing drift and diffusion currents cancel each other out. Under non-thermal equilibrium conditions e.g. when a voltage is applied, one of the

current flow mechanisms dominates, resulting in a net-current flow in one direction. From looking at the diagram, the electrons diffusing from the n-type to the p-type have to overcome the potential barrier of the conduction band. A voltage (bias) can be applied to a junction by connecting the positive terminal of the voltage source to the n-side or p-side of the junction. The basic theory of current-voltage characteristics of p-n junctions was established by Shockley.^{16, 17} This theory was then extended by Sah, Noyce and Shockley.^{18, 19} **Figure 11** shows the p-n junction current and voltage, I-V characteristics.

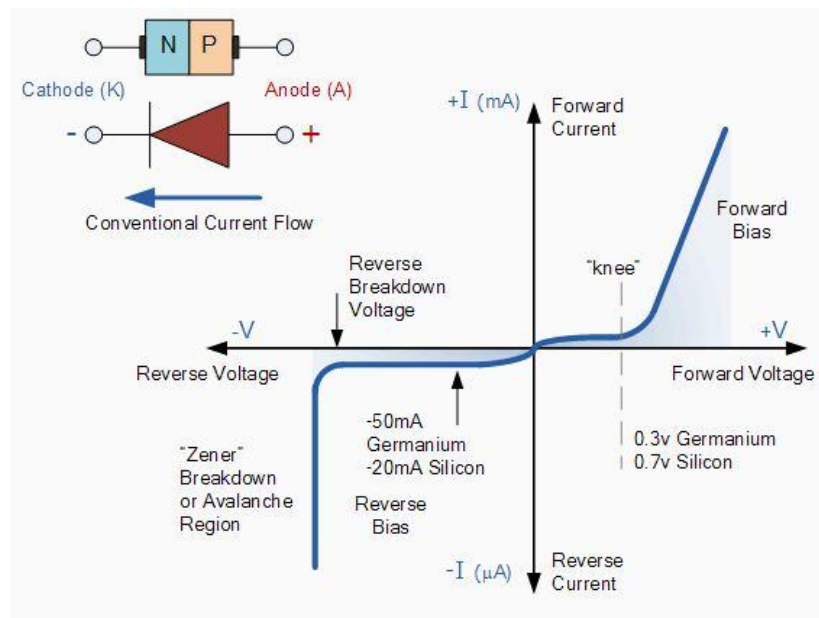


Figure 11 Current and voltage characteristics of a p-n junction.²⁰

From looking at **Figure 11** it is evident that current flows easily in one direction (forward bias) and little current flow in reverse bias. The current increases exponentially in the forward direction whilst for the reverse the current is low and constant until breakdown. For forward bias, the positive terminal is connected to the p-type material and the negative to the n-type. The holes in the p-type region and the electrons in the n-type region are pushed towards the junction. As the applied voltage increases, the depletion zone eventually becomes narrow enough that

electrons can cross the junction. The electrons penetrate only a short distance into the p-type material, as it is energetically favourable for them to recombine with holes. The electric current continues to flow as holes begin to move in the opposite direction.

For reverse bias, the negative terminal is contacted to the p-type material and the positive terminal is contacted to the n-type material. In the p-type material the holes move towards the terminal of the power supply and away from the junction. For the n-type material, the electrons are drawn towards the positive terminal. The width of the depletion zone increases. This results in a higher resistance to the movement of charge carriers, and thus the current generated is minimal, the p-n junction now behaves more like an insulator.

1.6.1 A p-n junction solar cell

Applications in which p-n junctions are incorporated into technology in the modern world include diodes, transistors, LEDs and photodetectors. The following text, together with **Figure 12** provides more detail on the mechanism and involvement of the p-n junction within a solar cell. As photons strike the semiconducting material, those with energy less than the band-gap are not absorbed by the cell, whilst those with energy in excess of the band gap, provide the additional energy required to promote an electron from the valence to the conduction band, thus electron hole pairs are generated on both sides of the junction. The n-type material is called the emitter, whilst the p-type the base. The generated electrons (from the base) and holes (from the emitter) then diffuse to the junction and are swept away by the electric field, thus producing electric current across the device. Negative charges flow out of the electrode on the n-type side, through a load (e.g. bulb). The electrons then flow into the p-type side, where they recombine with holes near the electrode. The light

energy originally absorbed by the electrons is used up while the electrons power the external circuit, thus, equilibrium is maintained.²¹ The incident light continually creates more electron-hole pairs and, more charge imbalance, the charge imbalance is relieved by the current which gives up energy in performing work.³ This is shown schematically in **Figure 12**.

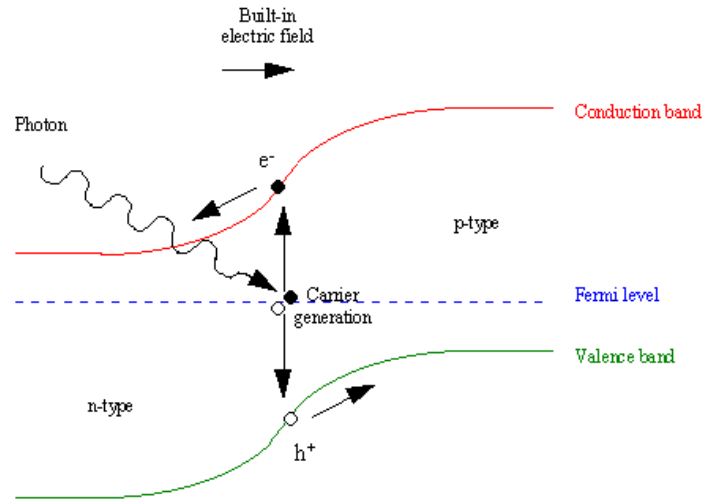


Figure 12 Carrier generation and current flow at the junction. ^{1, 11, 22}

Each semiconductor has its own band gap which means it can only convert certain parts of the solar spectrum. As all the generated electron-hole pairs have energy in excess of the band gap, immediately after their creation, the electron and hole decay to states near the edges of their respective bands. The excess energy is lost as heat and cannot be converted into useful power. This represents one of the fundamental loss mechanisms in a solar cell.

The generation and recombination of electron hole pairs control cell efficiency. The quantum efficiency (QE) or spectral response of a cell is given by:

Equation 18: $QE = QE(\lambda)$

Where: $QE(\lambda)$ is the ratio between the number of charge carriers the cell yields and the number of photon illuminating the cell for a given unit of time.

If $QE(\lambda)$ for a given solar cell is known then the maximum theoretical current density of the cell can be calculated for any given incident spectrum according to

$$\text{Equation 19: } J_{max} = q \int_{\lambda_0}^{\lambda_1} QE(\lambda)\Phi(\lambda)d\lambda$$

Where:

q =electron charge

λ =wavelength (where λ_0 and λ_1 are the limits of the wavelength range within which the cell shows photo-activity)

Φ =the flux of the spectrum illuminating the cell which in turn can be calculated by:

$$\text{Equation 20: } \Phi(\lambda) = \frac{P(\lambda)}{E(\lambda)} [\text{number of photons } m^{-2}s^{-1}nm]$$

Where:

$P(\lambda)$ is the spectral irradiance

$E(\lambda)$ is the photon energy given by $E=hc/\lambda$.

These equations allow an estimation of the upper limit of current generation in PV cells.²³ The efficiency (η) of a solar cell is defined as the power P_{max} supplied by the cell at the maximum power point under standard test conditions, divided by the power of the radiation incident upon it. Most frequent conditions for testing cell efficiency include an irradiance value of 100 mW/cm² with a standard reference spectrum, at a temperature of 25°C. The use of this standard is particularly convenient since the cell efficiency in per cent is then numerically equal to the power output from the cell in mW/cm². (Refer back to **Table 1**).

1.6.2 Target PV cell.

The theory and design of PV cells is too vast to include here. A brief summary for the constituents required for a functioning cell are summarised in the following text, with an indication for further reading given by the references. Although this thesis looks to material development, **Figure 13** highlights the two proposed structures for

comparison that could include the materials discussed. The nanostructured device on the right hand side has the advantage of an increased surface area (100mm² vs. approx. 1mm² for the same flat area), increasing the potential for light harvesting, and thus increased overall efficiency when compared to the more typical thin film device depicted on the left. The interface area of the p-n junction is increased resulting in increased charged separation at the surface.

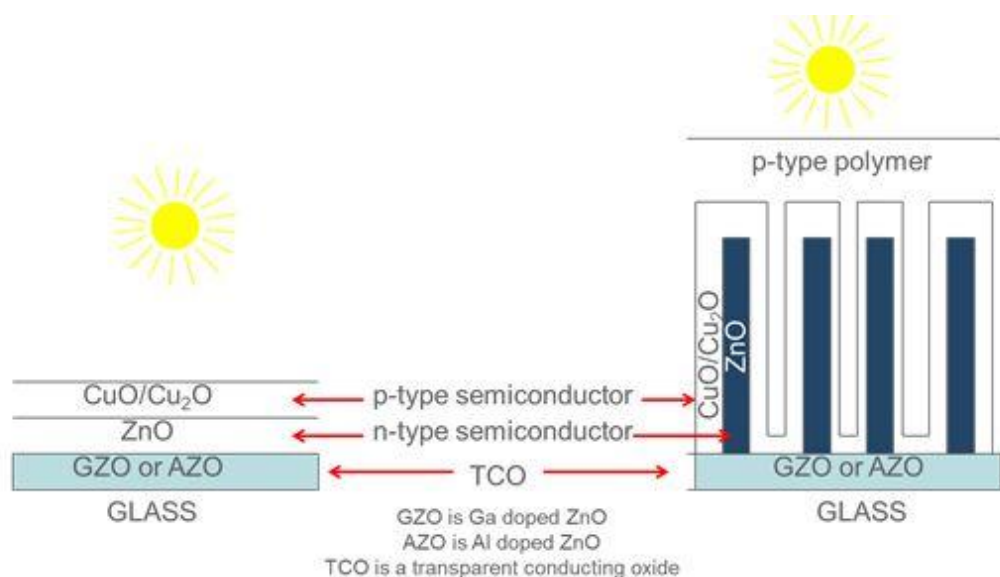


Figure 13 Schematic of PV cell.

Photovoltaics based upon zinc oxide and copper (II) oxide have been constructed before, but the process for manufacture has involved sputtering or electrochemical techniques which are unsuitable methods for large scale production of nanostructured devices due to them being line of sight techniques. MOCVD and ALD techniques, discussed in **section 1.9** are accepted by industry and can be seen as a low cost fabrication method with little waste of precursor. These techniques are the approach adopted for the target PV cell. Also, conventional PV technology is based upon high costing silicon or materials that contain a limited natural resource (e.g. indium) or are highly toxic (e.g. cadmium) in processing. Due to their potential use in large quantities, sustainable PV technologies need to be environmentally

friendly, manufactured from a metal that has a vast natural resources, are of low-cost to process and be able to absorb and wide range of the solar spectrum and be durable to solar radiation . Many metal oxide semiconductors are n-type in nature e.g. ZnO. Only a few p-type oxide semiconductors exist, and these include both CuO and Cu₂O. The aim of this thesis was to investigate these materials with a view for their incorporation into a nanostructured PV cell as structurally and electronically compatible layers enabling the absorption of a wide range of solar radiation. A wide range of band gap energies have been reported in literature for the n- and p-type semiconductors under investigation, these are summarised in **Table 2**.

ZnO	CuO	Cu ₂ O
3.4eV ²⁴⁻²⁶	1.2eV ²⁷	2.0 ^{25, 28}
3.37eV ²⁷	1.35eV, 1.44eV, 1.56eV ²⁹	2.1eV ³⁰
3.27eV ²⁸		

Table 2 Reported band gap energies for ZnO, CuO and Cu₂O.

Table 3 is a summary of the valence and conduction band offsets reported in literature.

System	Valence band offset (eV)	Conduction band offset (eV)	References
Cu ₂ O/ZnO	2.17	0.97	³¹
	1.3	0.1	²⁵
	2.4	0.8	³²
	2.82	1.81	³³
	2.3	0.9	²⁶
	2.27	1.0	³⁴
	2.2	1.0	²⁸
CuO/ZnO	1.72	0.28	³⁵
	1.72	0.28	³⁶

Table 3 Reported valence and conduction band offsets for Cu₂O/ZnO and CuO/ZnO systems. (Adapted from³¹)

The deposition of a p-n junction involving the zinc and copper oxide materials via ALD and CVD methods is lacking from literature, highlighting the novelty of the aim of the thesis. For reference, some of the techniques that have been successfully employed in the deposition of the ZnO/CuO/Cu₂O systems are discussed in **Table 4** to provide an insight into material properties. Generally, the efficiency is reported as less than 0.5% due to poor interface quality and interface defects,³⁷ although Mittiga *et al.* report a 2% efficiency for an ZnO/Cu₂O solar cell from sputtering and thermal methods.³⁸ The substrates and transparent conducting oxides will be discussed in **section 1.7 and 1.8**, followed by deposition techniques in **section 1.9**. The concept of nanowires (NWs) will be covered in **Chapter 2**.

Method of deposition	System described	Substrate	Results	Ref.
DC and RF Sputtering	n-ZnO (410nm) p-Cu ₂ O (650nm)	Glass	ZnO: E _g =3.27eV Carrier concentration = $5.4 \times 10^{18} \text{cm}^{-3}$ Mobility = $4.0 \text{cm}^2 \text{V}^{-1} \text{s}^{-1}$ Resistivity=0.29Ωcm Transmittance ~75-85% Cu ₂ O: E _g =2.00eV Carrier concentration = $3.1 \times 10^{16} \text{cm}^{-3}$ Mobility = $4.7 \text{cm}^2 \text{V}^{-1} \text{s}^{-1}$ Resistivity=58.3Ωcm Transmittance <30%	28
RF Magnetron sputtering of ZnO and electrodeposition of Cu ₂ O	n-ZnO (1μm) p- Cu ₂ O (4μm)	ITO	Maximum conversion efficiency of 0.46% achieved after annealing ZnO to remove dislocation and grain boundary effects. (ZnO formed larger particles, leading to increased electron mobility and higher conductance)	39
Sputtering	A:400nm ZnO NWs/ Cu ₂ O B:300nm ZnO film/400nm ZnO NWs/Cu ₂ O C:300nm a.ZnO film/400nm ZnO NW/ Cu ₂ O D:80nm ZnO film/400nm ZnO NWs/ Cu ₂ O E:300nm ZnO/ Cu ₂ O flat F:300nm ZnO/600nm ZnO NWs/ Cu ₂ O	ITO	A: V _{oc} 59.9mV, FF 24.6%, efficiency 0.083% B: V _{oc} 509.9mV, FF 40.9%, efficiency 0.423% C: V _{oc} 509.9mV, FF 41.3%, efficiency 0.461% D: V _{oc} 514.3mV, FF 41.5%, efficiency 0.564% E: V _{oc} 453.0mV, FF 26.7%, efficiency 0.253% F: V _{oc} 134.1mV, FF 28.3%, efficiency 0.014%	40
RF magnetron sputtering	n-ZnO NWs (l=2.1μm, dr=70-100nm) p- Cu ₂ O (1μm)	GZO	ZnO: Carrier concentration = $5.0 \times 10^{14} \text{cm}^{-3}$ Transmittance 42% Cu ₂ O: Carrier concentration = $6.36 \times 10^{14} \text{cm}^{-3}$ Overall Conversion energy 0.1%, V _{oc} 0.13V, FF 29	34
Sputtering of ZnO/MOCVD Cu ₂ O	n-ZnO (140nm) p- Cu ₂ O (280nm)	ITO	No efficiency recorded. Investigation into the lattice mismatch.	26
Electrochemical	n-ZnO NWs (l=2μm, d=80nm) p- Cu ₂ O	ITO	In this application the photocatalytic properties were investigated. ZnO could only absorb light in the UV region, once Cu ₂ O was deposited, absorption possible in the visible region.	41

Electrochemical deposition	n-ZnO NWs p- Cu ₂ O	FTO	Cu ₂ O /ZnO film: Conversion efficiency 0.02%, V _{oc} 0.19V, FF 26 Cu ₂ O film/ZnO NWs: Conversion efficiency 0.13%, V _{oc} 0.24V, FF 27 Cu ₂ O film/ZnO nanotubes (hollow): Conversion efficiency 0.11%, V _{oc} 0.21V, FF 023	42
Thermal oxidation of copper to CuO/Wet chemical deposition of ZnO	n-ZnO p-CuO NWs (l=1-20μm, d=50-220nm)	ITO	Overall power conversion energy 0.1%, V _{oc} 0.37 V, FF 37 Low power efficiency attributed to high sheet resistance of ITO, and low mobility in the ZnO layer caused by ZnO nanoparticles rather than a thin film.	36
Electrodeposition	CuO/ZnO ZnO/CuO	ITO	CuO/ZnO Conversion efficiency 0.001%, V _{oc} 0.0028V, FF 0.25 ZnO/CuO Conversion efficiency 0.000099%, V _{oc} 0.0082V, FF 0.28 Efficiency could be increased by increasing the crystallinity of CuO	43

Table 4 Cell efficiencies recorded for ZnO/Cu₂O and Zn/CuO based upon method of deposition (NWs=nanowires, V_{oc}=Open circuit voltage, E_g=band gap energy, FF=fill factor, ITO=Indium doped tin oxide, FTO=Fluorine doped tin oxide, GZO=Gallium doped tin oxide, a=annealed ZnO, MOCVD=Metal organic chemical vapour deposition)

1.7 Substrate

Referring back to **Figure 13**, the substrate used is glass as it is transparent and can allow the incident light to penetrate into the device. The research undertaken investigated a variety of substrates during deposition to help gain an understanding of growth mechanisms, composition and the impact of substrate on nucleation density. A brief description of each of the substrates used is given in the following text.

1.7.1 Glass

Glass has an extensive range of applications from architectural glazing and optics, to food containers. During manufacture, the properties of glass e.g. colour and thermal expansion can be tailored by adding alternative minerals. The large-scale glass manufacturing process for flat glass is termed the 'float glass' process and was introduced by Pilkington's Glass.⁴⁴ Glass is based on SiO_2 but often contains carefully controlled concentrations of other element oxides e.g. B, Ca, Mg, and Al, to control the desired mechanical properties. The surface is hydroxyl terminated (Si-OH bonds are formed from the reaction of the SiO_2 with moisture in the atmosphere) which makes it reactive towards further processing. Surface modification of glass via thin film coatings is a widely used industrial technique and has the advantage of altering surface chemical and physical properties while preserving the bulk. It often takes place 'off-line' in that it is a separate process that takes place after manufacture. CVD has been integrated into the glass industry to coat large areas of a large range of high purity thin films uniformly; this is relevant to the target device, as the TCO layer can be applied in this way.

1.7.2 Si(100) and Si(111)

Silicon substrates were employed as they are well defined in terms of crystal structure, optical property and surface smoothness. The supplied wafers were 100mm diameter from Compart Technology Ltd, Virgin Test Grade. Si(100) was predominantly used for the copper deposition, whilst both Si(111) and Si(100) were used for zinc oxide nanowire work. The face centred cubic crystal structure of silicon is shown in Figure 14 with the direction of the 111 and 100 planes highlighted.

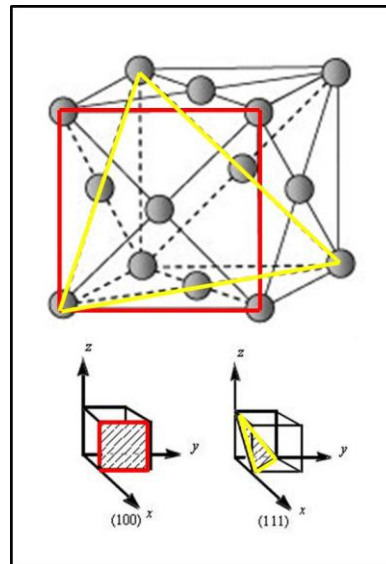


Figure 14 The crystal structure of silicon with (100) and (111) planes highlighted. ⁴⁵

Silicon is prone to surface oxidation when exposed to air. The substrates were used as supplied and a 20Å silicon dioxide layer was assumed. Ellipsometry was used for measuring film thickness. The silicon used was heavily n-doped and was therefore not suitable for electrical conductivity measurements. To accommodate this, soda lime glass microscope slides (75mm x 25mm) were also used as substrates. This also aided in the visual inspection of films to look for transparency, uniformity and if reflective metallic films were deposited. Films grown on glass provided thickness measurements based upon weight gain.

1.7.3 Titanium Nitride

Titanium nitride (TiN) is used as an adhesion layer and was used as a substrate to help study copper deposition. Copper metal formed part of this research due to the potential application of ALD copper as interconnect material in electronic devices. A more complete discussion can be found in **section 2.2.2.2**.

1.7.4 Plastic

A plastic substrate named Mellinex® 505 was used for the copper deposition work. This substrate has a thermal budget limited to 75°C, and was used to understand how suitable the low temperature copper deposition process was to flexible substrates, a current focus of the electronics industry.

1.8 Transparent Conducting Oxide

As glass is a non-conducting substrate, to enable an electrical contact (electrode) for the hypothesised PV cell, a transparent conducting oxide (TCO) is used. TCOs are used for many other applications including displays, circuitries and opto-electrical interfaces. A TCO is usually made from a semiconductor material which can absorb light at energies greater than the band gap energy, therefore semiconductors with band gaps greater than the highest energy visible light (approximately 3.0eV) will be transparent. TCOs enable light to pass through, with greater than 80% transmittance of incident light. TCO extracts photogenerated electrons and transfers them to external circuits. The conductivity can be tuned from insulating via semiconducting to conducting via doping and can have conductivities $>10^3$ S/cm for efficient carrier transport.⁴⁶

1.8.1 Indium Tin Oxide (ITO)

Indium oxide is a wide band gap semiconductor ($E_g=3.75\text{eV}$). Doping with tin (n-type) gives indium tin oxide (ITO), typically 90%_{wt} In_2O_3 , 10%_{wt} SnO_2 . ITO is the most widely used TCO as it has a high visible transmittance (>90%) and good resistivity.⁴⁷ The resistivity is related to the carrier concentration and mobility, which in turn is related to dopant levels and oxygen vacancies, crystallinity, film thickness and purity.⁴⁸⁻⁵¹ Introducing tin initially increases the conductivity by providing spare electrons, however at high dopant levels, scattering of charge carriers can occur reducing the charge carrier mobility and thus, overall conductivity. The highest conductivities are seen with 5-10at.% Sn. Precursors used for the deposition of ITO include tin tetrachloride and indium β -diketonate complexes. The deposition processes include, but are not limited to, electron beam evaporation,⁵²⁻⁵⁴ magnetron sputtering,^{55, 56} thermal evaporation and pulsed laser deposition.⁵⁷

1.8.2 Fluorine doped Tin Oxide (FTO)

The majority of research on zinc oxide nanowire based solar cells has used fluorine doped tin-oxide as the TCO material.⁵⁸⁻⁶⁰ However, the small difference in work function of ZnO (5.1-5.3eV)^{61, 62} and FTO (4.9eV)^{63, 64} does not provide sufficient driving force for the charge injection, leading to the need to look for an improved TCO for this application.

1.8.3 Aluminium doped Zinc Oxide (AZO)

Aluminium doped (n-type) zinc oxide thin films, AZO, contain about 2%_{wt} aluminium and can be produced by spray pyrolysis,^{65, 66} sol gel technology,⁶⁷⁻⁶⁹ sputtering,⁷⁰⁻⁷³ ALD⁷⁴ and CVD.^{75, 76} Nishino et report the deposition of AZO at 500°C via CVD using bis(2,4-pentanedionato) zinc and tris(2,4-

pentanedionato)aluminium. With the dopant level at approximately 0.8at.% Al, they reported an electrical resistivity of $4.9 \times 10^{-5} \Omega \cdot \text{m}$ at a 110°C , and 80+% transmittance (λ 400-820nm). AZO TCO has a work function of 3.7-4.6eV, which has the potential of increased charge extraction. Lee *et al.*⁷⁷ carried out a direct comparison of ZnO NW on both FTO and AZO TCO, with those grown on the AZO exhibiting an improved energy conversion. The AZO film had a higher sheet resistance ($12.2 \Omega/\square$) than the FTO ($10.0\Omega/\square$), therefore the increased efficiency can be ascribed to enhanced electron transport.

1.8.4 Gallium doped Zinc Oxide (GZO)

ALD GZO is shown to provide an effective TCO for CdTe-based solar cells. This material and method of growth has been investigated previously by Saito *et al.*⁷⁸ Diethylzinc (DEZn), water and triethylgallium (TEGa) were used as the Zn, O, and Ga precursors, respectively. To achieve the gallium-doping, the TEGa was simultaneously introduced with DEZn and the flow rates of the zinc and gallium precursors were altered by varying the bubbler temperature. Ga-doping was performed under Zn-rich growth conditions and electron concentrations of the order of 10^{20} cm^{-3} were reported. Work performed in the research group at University of Liverpool, also reported the growth of GZO by combining series of deposition cycles using the same precursors as Saito.^{79, 80} In contrast to the method used by Saito *et al.*, the approach from the team at Liverpool, controlled the doping via the cycle ratio of the DEZn:TEGa. The electrical sheet resistance of approximately 50nm thick GZO layers with varying gallium contents deposited at 250°C was measured. The sheet resistance was found to be a minimum at 4%–6% TEGa cycles (0.5–1 at. %) at approximately $5 \times 10^{20} \Omega/\square$. The maximum carrier concentration coincides with a carrier mobility of $7 \text{ cm}^2/\text{Vs}$. The optical properties of the GZO

films were assessed by UV–vis spectrophotometry and the transmissions of the films were approximately 80% in the visible spectrum. The ALD GZO was incorporated into a $\text{Cd}_{1-x}\text{Zn}_x\text{S}/\text{CdTe}$ device structure, grown using the atmospheric pressure metalorganic chemical vapour deposition (MOCVD) process described elsewhere.⁸¹ $\text{Cd}_{1-x}\text{Zn}_x\text{S}/\text{CdTe}$ photovoltaic cells deposited on GZO/glass substrates yielded a quantum efficiency of 10.8% which is comparable to cell grown on industry supplied TCO. Overall, GZO shows huge promise for use as a TCO in thin film CdTe PV devices. Due to the lower sheet resistance of GZO materials than AZO materials, the aim is to include GZO as the TCO for the PV cells depicted in **Figure 13**.

1.9 Film Deposition Techniques

Many of the major scientific and technological advances have been made possible due to substantial advances in the development and optimisation of thin film deposition techniques. There is a range of methodologies suited to film formation including physical vapour deposition (PVD), chemical vapour deposition (CVD) and atomic layer deposition (ALD).

1.9.1 Physical Vapour Deposition

The term physical vapour deposition (PVD) covers a wide variety of techniques in which a target material is evaporated under high vacuum and the resulting vapour deposited on a substrate surface. A high vacuum is used to eliminate trace element impurities, and often in-situ techniques such as Auger electron microscopy analysis can be used during deposition. The method of evaporation can be via electron beam, laser ablation and sputtering (magnetron and ion beam).⁸²⁻⁸⁴

Molecular beam epitaxy (MBE) is an epitaxial process whereby one or more thermally evaporated beams of atoms react with the surface of a crystalline substrate under ultra-high vacuum (10^{-8} Pa). This technique is useful for precision control of doping. A variation on this method uses metal-organic compounds and can be termed either metal-organic molecular beam epitaxy (MOMBE) or chemical beam epitaxy (CBE). Ion beam sputtering is a process in which a source of ions is accelerated towards the target to generate a flux, whilst magnetron sputtering uses a magnetic field to control the electrons. Sputtering techniques can be very quick (region of $1\mu\text{m}/\text{min}$) but the ion bombardment itself can cause damage to the layers. Although PVD techniques allow for a high degree of composition control, they are all ‘line of sight’ processes and are not well suited for conformal coatings onto high aspect ratio trench structures. As the reactive species is in vacuum there is little chance of collisions and the vapour tends to travel in a straight line, resulting in low deposition on trench walls. This is highlighted in **Figure 15**. As these structures are progressively being down sized, covering a structure becomes even more challenging.

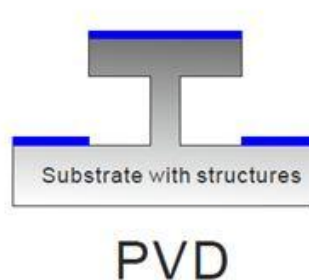


Figure 15 A schematic showing film formation from PVD (blue) on a structured substrate.

1.9.2 Chemical Vapour Deposition

The push for more efficient and reliable technology in thin film deposition led to the development of chemical vapour deposition (CVD). This process involves the

formation of a thin solid film on a substrate material by thermal decomposition of a chemical precursor which can occur both in the gas phase and on the substrate. One of the more commonly used CVD processes is metal-organic vapour phase epitaxy (MOVPE), which produces single crystal films on single crystal substrates from metal-organic precursors. CVD reactions are commonly assisted by using heat (thermal CVD), plasma (Plasma Enhanced CVD, PECVD) or higher frequency radiation (photo-assisted CVD). PECVD is a technique in which electrical energy is used to generate chemically active ions and radicals. These then participate in the heterogeneous reactions leading to deposition on the substrate. The advantage of plasma CVD is that deposition can occur at very low temperatures, enabling temperature sensitive substrates to be used. Other processes may involve the use of high vacuum, or may be at atmospheric pressure.

MOCVD is a specific CVD process that utilizes metal-organic (organometallic) precursors, and was pioneered by Manasevit in 1968.⁸⁵ An organometallic precursor is defined as a compound that contains a direct metal-carbon bond, however, due to the varied nature of the precursors used in MOCVD, there is an inclusion of precursors containing metal-oxygen, metal-nitrogen and metal-hydrogen bonds. Materials deposited by MOCVD include metals, oxides, nitrides and sulphides. The initial use of CVD included the blanket coverage of cutting tools to improve performance and prolong life. Now, MOCVD is widely used in the microelectronics industry. It forms part of the fabrication of semiconductor devices to deposit various films including, polycrystalline, amorphous and epitaxial silicon and high-K dielectrics. MOCVD is a technique which lends itself to end-use applications such as solar cells, glass coatings, and medical devices.

As the CVD process is carried out in higher pressures than the PVD techniques, the mean free path of precursor molecules is reduced, increasing the scattering in all directions leading to both surface and gaseous reactions. This now means that there is an enhancement in the conformality compared with PVD. This is highlighted in **Figure 16**.

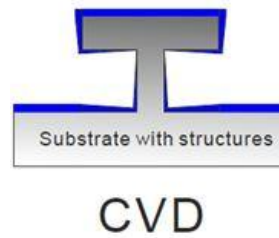


Figure 16 A schematic showing film formation from CVD (blue) on a structured substrate.

The schematic diagram in **Figure 17** helps to highlight the significant stages of MOCVD with the numbers being in reference to the text below.

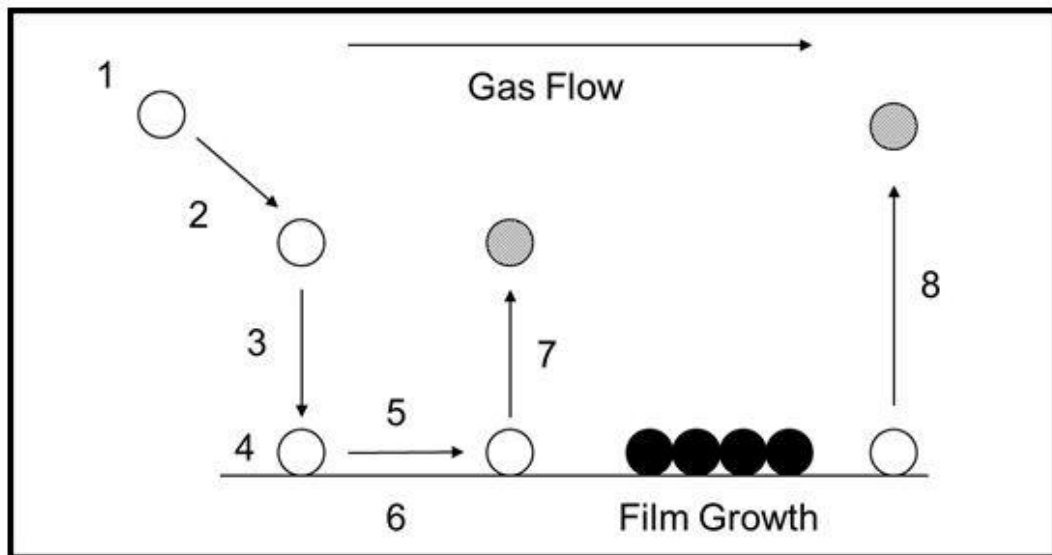


Figure 17 A representation of an MOCVD process.

Step 1: Vaporisation of the precursor and the transportation of these gas phase, usually in a carrier gas, to the deposition zone.

Step 2: Gas phase reactions of precursors in the reaction zone to produce reactive intermediates and gaseous by-products.

Step 3: Diffusion of this gas through a boundary layer. The boundary layer is a hot layer of gas adjacent to the substrate and describes the region where the gas phase reactions effect the layer formation.

Step 4: Absorption of the precursor onto the heated substrate.

Step 5: Thermal decomposition of the precursor in the presence of e.g. oxygen to from e.g. an oxide. The oxygen source could either be oxygen gas, or oxygen liberated from the molecule during its decomposition, an alcohol etc.

Step 6: Surface diffusion to growth sites, nucleation and surface chemical reactions leading to film formation.

Step 7: De-sorption of by-products

Step 8: Removal of decomposition fragments from the reaction zone.

1.9.2.1 Conventional MOCVD

Conventional MOCVD uses precursors housed in ‘bubblers’ (**Figure 18**) which are heated to a temperature at which the chemical can vaporise and be transported to the substrate, often termed a vapour draw method. A bubbling technique can be used for precursors with low volatility. The bubbler contains valves to allow an inert carrier gas (e.g. argon) to flow into the bubbler, through the dip-leg and pick up the material for transportation. The vapours are then carried out and along heated lines to the reaction chamber.



Figure 18 A stainless steel bubbler .

For this method, problems that can arise are often due to the trade-off between providing enough temperature to ensure the chemical is vaporised, whilst ensuring no thermal decomposition is occurring. Thermal aging of the precursor can often lead to inconsistent growth rates or transfer of decomposed species leading to a highly contaminated final film. When complex films are being grown using two or more sources, it is possible to control stoichiometry e.g. strontium barium titanate has been deposited as a dielectric for use in capacitors.⁸⁶

1.9.2.2 Liquid Injection MOCVD

Liquid injection metal organic chemical vapour deposition, (LI-MOCVD) was a technique developed to try to overcome some of the problems observed for conventional MOCVD.⁸⁷ In this process a liquid or solvated precursor can be directly injected at a precisely controlled rate into a heated evaporator. The vapours are then transported via carrier gas into the reactor chamber. This method enables the precursors to be held at room temperature, and further to this, LI-MOCVD can be a useful technique for low vapour pressure or temperature sensitive precursors or alternatively when there is a requirement for mass transport.

LI-MOCVD is well suited to multi component systems, as individual reservoirs and separate injectors can be utilised to enable metered precursor flow to allow correct stoichiometry and composition of thin films e.g. strontium titanate.⁸⁸

Potential drawbacks of LI-MOCVD for multi-component systems include the necessity for the precursors to be compatible and have a similar growth deposition temperature window. Also, it is of paramount importance that the compounds are stable in the organic solvent and no interactions occur. LI-MOCVD was utilised during this research using the Aixtron reactor and is discussed in **section 3.2.1.1**.

1.9.3 Atomic Layer Deposition

Atomic layer deposition (ALD) is a derivative of CVD, and was pioneered by Suntola *et al.*⁸⁹ originally described as Atomic Layer Epitaxy (ALE). It is a deposition process in which gaseous precursors are introduced sequentially to the substrate in a step-wise process. Current electronic devices that make use of this technique includes TFT displays and CMOS devices. It is a self-limiting process in which only surface reactions participate. The precursors and co-reactant are introduced alternatively, into the chamber, in a cyclic manner (e.g. Precursor → purge → co-reactant → purge), with the purge used to remove any residual precursor or decomposition products. Ideally the reaction should provide saturation of the substrate surface, ensuring that no further reaction can take place even if excess precursor is pulsed into the chamber (i.e. the growth rate is independent of the pulse length as shown in **Figure 19**).

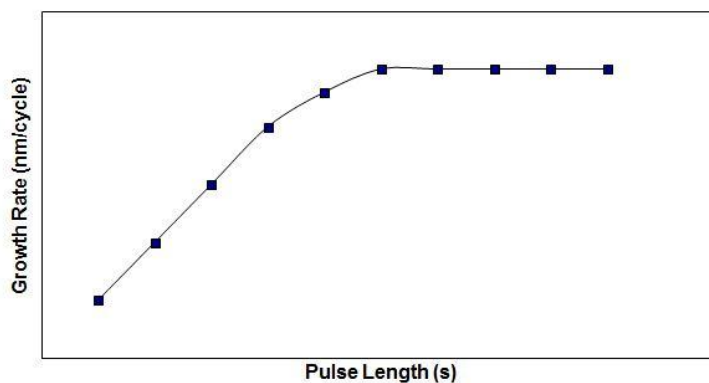


Figure 19 A growth curve for a saturative, self-limiting ALD process

This process provides a way of having monolayer growth. The thermal decomposition temperature of the precursor must not be reached during the process as this will result in contaminant incorporation within the film. For ALD reactions, typically lower temperatures, 100-400°C are needed. Due to the lower temperatures deposition rates can be slow and there is often a lower density in the films, this leads

to an increase in the potential of incorporating impurities. Another point of note is that the interface between the substrate and the film is not automatically smooth due to interfacial reactions.

An example of how ALD is used to deposit layers of hafnium oxide is described in

Figure 20:

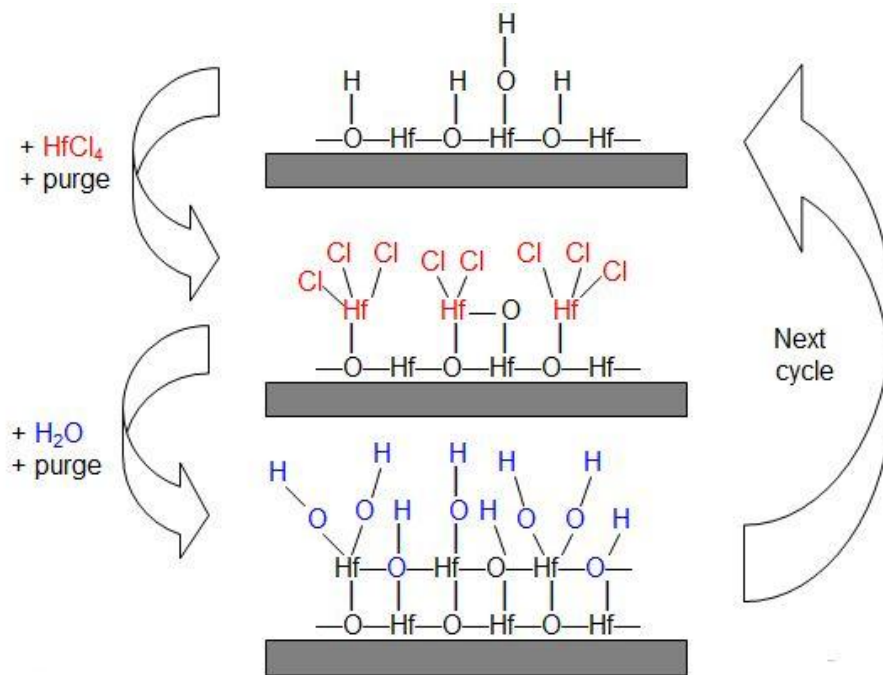


Figure 20 ALD of hafnium oxide.⁹⁰

Hafnium chloride, HfCl₄, is the hafnium precursor which is firstly transported, by a carrier gas, into the reaction chamber where it will react with a substrate and deposit a layer of one molecule thick on the substrate. Once all reactive sites are used up, a purge of gas is used to flush excess HfCl₄ from the system. Water is then added to react with HfCl₄ to form the hafnium oxide layer. The system is purged again with gas to remove the HCl by-product and the cycle is repeated. The next HfCl₄ pulse added to the system will then react with the hydrolysed surface and will deposit a layer of material that will self-limit at one monolayer. This process is simply

repeated until the film reaches the desired thickness, although long deposition times for thicker films can become impractical.

Figure 21 shows the typical growth curve observed in an ALD process.

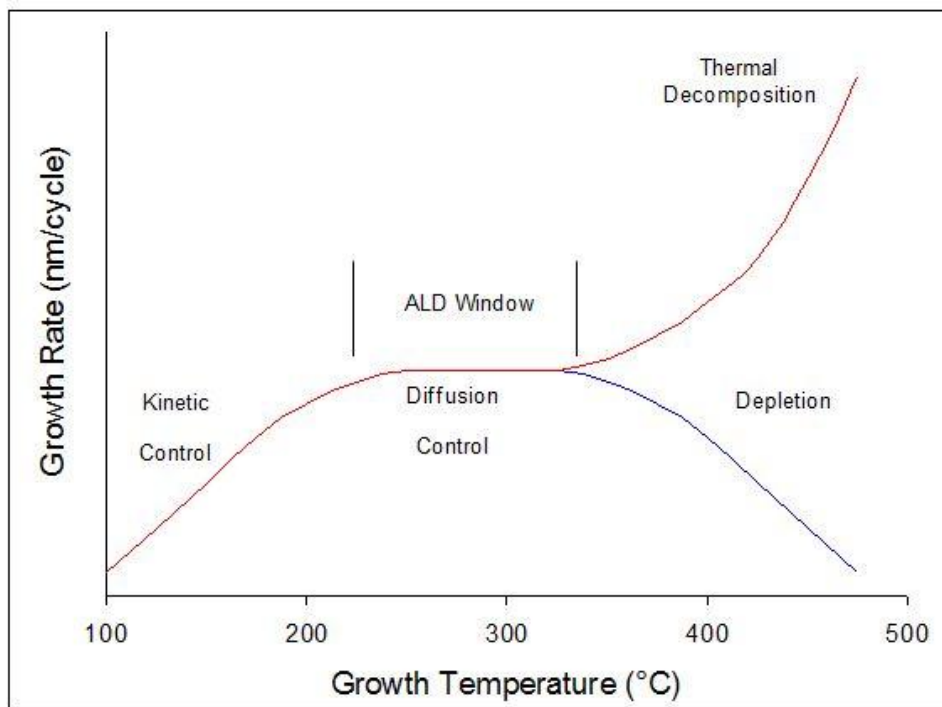


Figure 21 ALD growth curve.

Initially the growth rate is influenced by kinetics (i.e. controlled by the rate of the reaction of adsorbed species on the substrate surface) and is heavily dependent on the temperature of the substrate. In the diffusion controlled area, the growth rate is only weakly dependent on the temperature, but is controlled more by the boundary layer on the substrate surface. Finally, as the substrate temperature is increased, either the precursor reacts with the walls of the chamber before it reaches the substrate or desorption from the surface can become energetically favourable, with both effects reducing the rate. In addition, thermal decomposition of the precursor at higher temperatures results in an increased growth rate, often due to the incorporation of contaminants, e.g. carbon. When comparing ALD with MOCVD, the former ensures sophisticated structures can be produced, whilst with the latter

monolayer growth is difficult to obtain. Also in MOCVD, the temperature and molecular flux can vary at different points on the substrate wafer, leading to difficulties in controlling uniformity and thickness. ALD, however, overcomes these difficulties and offers unprecedented control at the monolayer level, there is complete substrate coverage at each step and overall, the ALD technique is less sensitive to flow rates than other methods. **Figure 22** shows a representation of the much improved conformal films that can be produced via ALD over CVD and PVD.

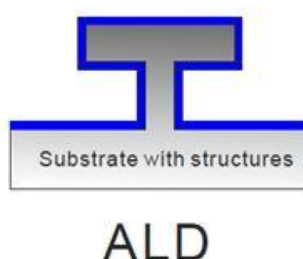


Figure 22 A schematic showing conformal film formation from ALD (blue).

For this study ALD was carried out using the OpAL reactor, see **section 3.2.1.2**.

1.10 Precursors

1.10.1 Precursor Properties

From the processes described above, it is clear that the precursors used in ALD and CVD must be carefully chosen. The ideal characteristics needed are listed below:

- Adequate volatility to ensure transport to the chamber is achievable, leading to acceptable growth rates at manageable temperatures.
- Have high thermal stability to ensure decomposition doesn't occur during volatilisation or transport.
- Decompose cleanly to ensure there are limited opportunities for contaminants to be incorporated into the final film.

- Give stable, non-toxic by-products which can be easily removed from the reaction chamber
- Have high chemical purity or be easily purified.
- Be readily and commercially available at low cost
- Be non-toxic, non-pyrophoric
- Long-shelf life (preferably not air and moisture sensitive)
- Good compatibility with co-precursors

It is difficult for all the above criteria to be fulfilled at once. As an example, many of the industrial CVD processes use simple precursors such as metal hydrides (e.g. SiH_4), metal alkyls (e.g. Me_3Al) and metal halides (e.g. SnCl_4). The latter usually requires a reducing agent and often liberates corrosive by products like HCl.

Factors which must be considered when choosing a precursor for a given process include:

- the type of ligand and the way in which it is bonded to the metal as this can help to determine the decomposition pathway of a material
- the film to be grown. If a nitride material is required, the precursor would not contain oxygen as this could potentially contaminate the layer.
- the temperature of the process to ensure the precursor is reactive yet does not decompose and generate impurities.
- the substrate to be grown on, potential temperature sensitive substrates, large area, high throughput, the requirement of a seed layer
- ease of chemical synthesis, purification and scale-up
- previous patents

Table 5 is included to highlight the vast range of chemical precursors used in ALD and/or CVD regimes. The materials deposited with them and the potential incorporation of these films into end applications in the electronics industry is summarised.

General Class of Material	Specific material	Applications	Typical Precursors
Dielectric Oxides	TiO ₂ , HfO ₂	High-K dielectrics in CMOS technology	Metal-β-diketonates e.g. [Hf(acac) ₄] (acac=acetylacetonate) + O ₂ or O ₃
Ferroelectric Oxides	SrTiO ₃ , BaTiO ₃	DRAMs, computer memories, infrared detectors, transducers, ceramic capacitors.	Metal-β-diketonates e.g. [Ba(thd) ₂], [Ti(O ⁱ Pr) ₂ (thd) ₂] (thd=2,2,6,6-tetramethylheptane-3,5-dione) + O ₂
Low-emissivity and conducting oxides	F-doped SnO ₂	Architectural coatings on flat glass for solar control and anti-reflections.	[SnCl ₄]/[NH ₄ F] + O ₂
Electrochromic	MoO ₃	Architectural coatings on flat glass	[Mo(CO) ₆] + O ₂
Self-cleaning coatings	TiO ₂	Architectural coatings on flat glass	[TiCl ₄]/[Ti(O ⁱ Pr) ₄] + O ₂
III-V compound Semiconductors	GaAs, AlGaAs GaP, GaN InGaN	Solar Cells, LEDs	Group III trialkyls e.g. [R ₃ M] M=Ga, Al, In R=CH ₃ and Group V tri-hydrides e.g. [PH ₃], [NH ₃] or organometallics e.g. [ButPH ₂]
II-IV compound semiconductors	ZnSe CdS/CdTe CdTe	Blue/green LEDs and lasers Solar cells Infrared detector, thermal-imaging	Group II dialkyls e.g. [R ₂ M] M=Zn, Cd, R=CH ₃ and Group VI dihydrides e.g. [H ₂ S] OR Group VI dialkyls e.g. [Et ₂ Se], [Et ₂ Te]
Metals	Al/Cu Pt,Pd,Ni Ru Ta	Interconnects in microelectronic devices Metal contacts microelectronic Diffusion barriers Capacitor and resistor	[AlH ₃ (NR ₃)] and Cu(II) β-diketonates/H ₂ [Pt(acac) ₂], [Ni(MeCp) ₂] [Ru ₃ (CO) ₁₂], [RuCp ₂] [TaCl ₅]
Metal Nitrides	AlN/Si ₃ N ₄ TiN, ZrN,HfN TaN, NbN	Packaging material in devices Passivation, wear resistant, transparent optical, diffusion barriers, gate electrodes. Diffusion barriers for Cu	[AlMe ₃ /NH ₃] and [SiH ₄]/[NH ₃] [TiCl ₄]/[NH ₃] and [M(NR ₂) ₄]/[NH ₃] [TaCl ₅]/[NH ₃]
Metal carbides	TiC ZrC HfC	Hard coating for tools Coating for nuclear fuel particles Oxygen resistant coating for composites	[Cp ₂ TiCl ₂]/[H ₂] [ZrCl ₄] [HfCl ₄]/[CH ₄]

Table 5 A selection of typical precursors used for various electronic applications .⁹¹

In any chemical process, the purity of the reactants is most important. For thin film deposition this is also the case. Impurities in concentrations of parts per billion (ppb) can have a negative effect on the end use of the electronic device e.g. trace chloride incorporated into a thin film introduces another charge carrier which would hinder current flow in a final device. Sometimes, unintentional doping can occur due to the way in which a precursor is manufactured. The precursor can be characterised and purity checked by Nuclear Magnetic Resonance (NMR), Inductively Coupled Plasma Mass Spectroscopy (ICPms) and Inductively Coupled Plasma Optical Emission Spectroscopy (ICPoes), with these techniques discussed in **section 3.1**.

Within the thin film deposition process, carbon and oxygen contaminants are a major issue. In the final layer, the carbon and oxygen can become incorporated either from the decomposition of the organic ligand or from leaks in the system offering a point of ingress for oxygen. Methods for thin film thickness analysis includes ellipsometry. X-ray diffraction (XRD), Scanning Electron Microscopy (SEM) and Tunnelling Electron Microscopy (TEM) are techniques to look at material crystallinity, composition and film morphology. Combinations of these experimental techniques have been used for this research. Details for these techniques are provided in **section 3.3**.

1.10.2 Precursor Volatility

To ascertain if compounds have suitable volatility, thermal stability and high purity, thermogravimetric analysis (TGA) can be used. It helps provide insight into the temperature required to volatilise the precursor. Due to the air/moisture sensitivity of the precursors, this technique is often carried out in a nitrogen glovebox. Further experimental details are given in **section 3.1.3**. TGA is a measure of weight loss as a

function of increasing temperature. **Figure 23** below is a generic TGA highlighting the key features.

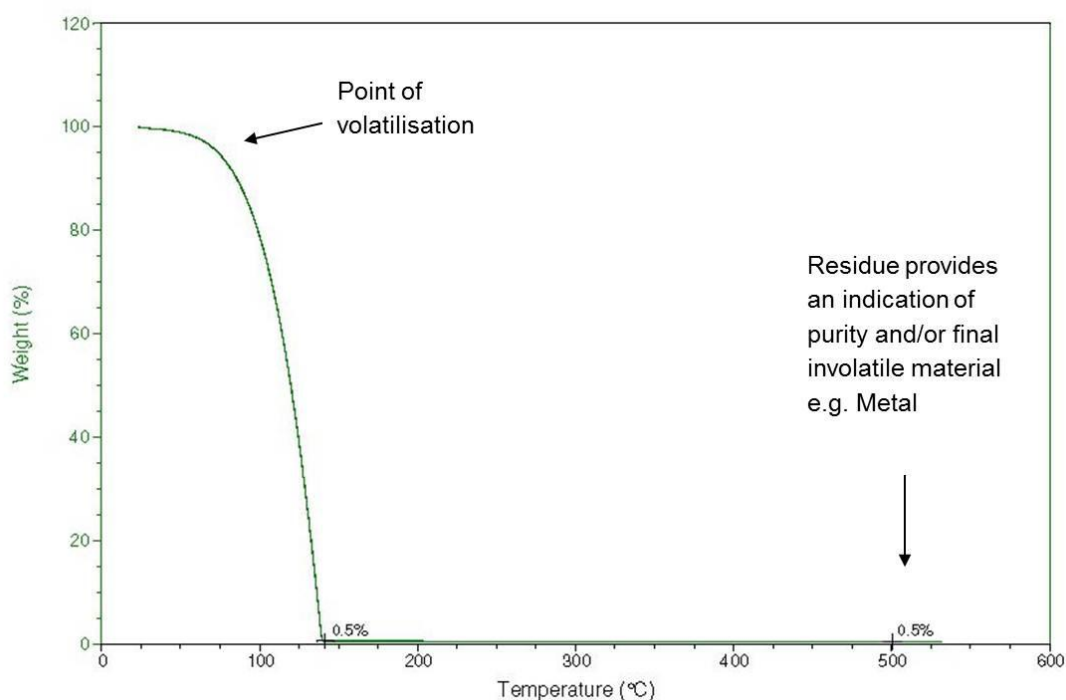


Figure 23 A generic TGA highlighting the key features used to understand thermal stability and volatility of precursors.

An ideal precursor should have a rapid mass drop over a small temperature range correlating to volatilization of the precursor, ideally at a low temperature. For the TGA shown here, this suggests that at around 75°C the precursor vaporises. If this sample was thermally unstable there would be more thermal events within the TGA. Looking at the residue in this sample, it is extremely low which suggests the precursor was probably pure, has very good volatility and does not decompose into a high molecular weight fragment. The percentage loss can provide an insight into the final species e.g. the percentage mass of a metal compared to the initial starting compound. A high residue could indicate thermal decomposition.

The vapour pressure of a precursor can also be determined, though reproducibility of results can be a problem. The vapour pressure of a compound (e.g. naphthalene) is

measured at various temperatures to obtain a plot shown in **Figure 24**, the experimental details are given in **section 3.1.4**.

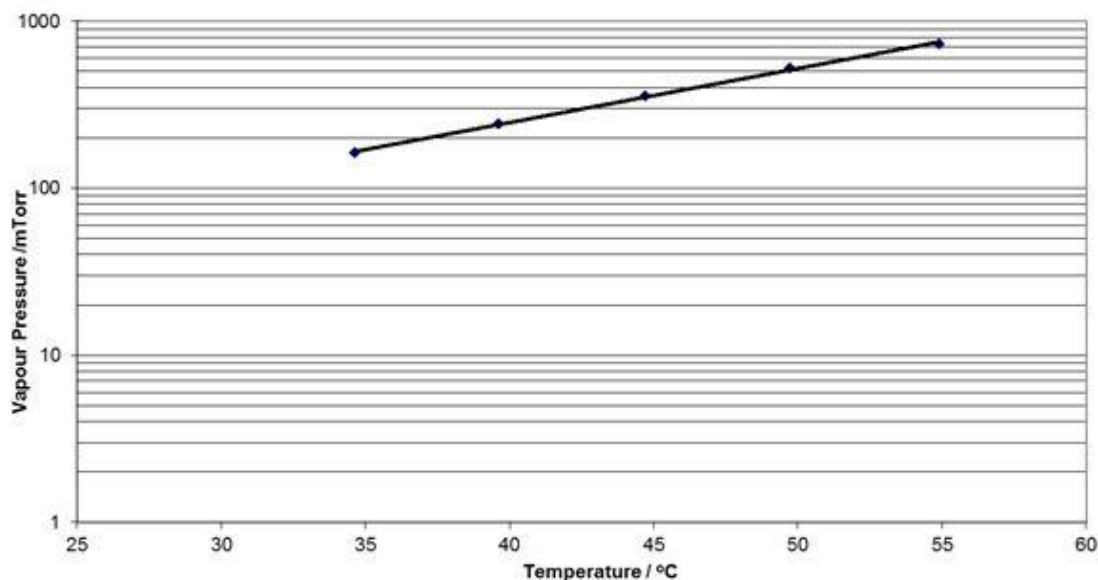


Figure 24 Vapour pressure plot for naphthalene.

Through manipulation of the graph, the calculation of vapour pressure for naphthalene at any specific temperature can be obtained from:

$$\text{Equation 21:} \quad \text{Log}_{10}P(\text{mTorr}) = -\frac{3272.7}{T(\text{K})} + 12.847$$

The vapour pressure of the material provides an insight in the bubbler temperatures needed to allow transport of the precursors. High thermal stability is required for CVD precursors, to ensure the molecules don't decompose during evaporation or transport, for ALD, as it's a self-limiting process, thermal stability is a requirement to avoid unnecessary impurities.⁹²

1.11 Summary

A literature review in **Chapter 2** will introduce copper and zinc chemistry and film deposition of zinc oxide, copper, and copper oxide. The remainder of the thesis is organised as follows; **Chapter 3** discusses the experimental methods used for both chemical and thin film characterisation. Moving on to **Chapter 4** and **5**, details of the results obtained from the synthesis and characterisation of novel precursors, in addition to the deposition methods employed and film characterisation are discussed. MOCVD was the deposition method of choice for the growth of n-type Zinc Oxide nanowires, whilst ALD of p-type Copper Oxide was trialled with a view to try to conformally coat the nanowires. A final discussion on film compositional analysis as well as a study of the morphology and electronic properties is included. **Chapter 6** draws conclusions from the study and indicates direction for future work.

Chapter 2 Literature Review

2.1 Zinc

Zinc is bluish-white to silvery grey metal and is the 24th most abundant element in the Earth's crust at a level of 75ppm (0.0075%). It is found in minable quantities in Australia, Asia and the United States, with the largest reserves in Iran. Zinc is usually found with other base metals such as copper and lead in ores, with the most commonly mined zinc ore being that of spharelite (also known as zinc sulphide or zinc blende), where zinc accounts for 60% of the concentrate. Over 350 million tonnes of zinc have been extracted throughout history, with over 100 million tonnes still in use today.^{93, 94} Some of the varied uses of zinc are highlighted in **Figure 25** below.

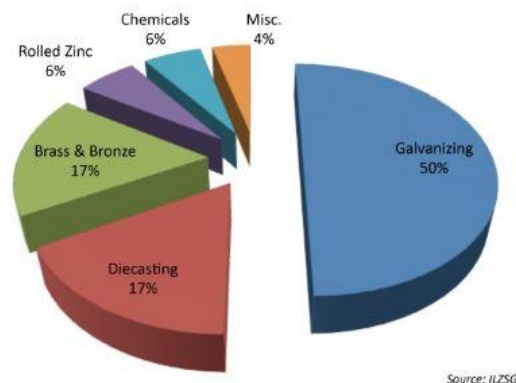


Figure 25 Uses of zinc.⁹³

Zinc is an essential mineral and is important to many aspects of human health. It is also used as an anti-corrosive agent and can be used as an anode. Another application of zinc is in the process of galvanization where zinc is combined with other metals to form iron or steel to coat other metals, this accounts for 50% of the world's zinc usage. It can be alloyed with copper to create brass and with nickel silver to create soft aluminium solder and commercial bronze. Zinc is used in conjunction with copper, magnesium and aluminium in die casting and spin casting

methods which are used in the automotive, electrical, and hardware industries. Zinc has many applications in the chemical industry. In synthetic chemistry, zinc-based compounds, when combined with transition metal reagents such as nickel or palladium, are used for cross-coupling reactions, copper mediated substitution and addition reactions, and catalytic asymmetric addition to aldehydes.⁹⁵

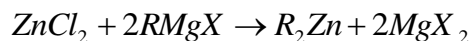
2.1.1 Zinc Chemistry

Zinc is found in group 12 in the periodic table and has an electronic configuration of $[\text{Ar}] 3d^{10}, 4s^2$. The maximum oxidation state for zinc is (II); this can be reasoned by analysing the ionization potentials. The first and second potentials, (corresponding to the 4s electrons) are 9.39eV and 17.89eV respectively, whilst the third ionisation potential, (corresponding to the removal one of the d-electrons from the filled shell) is 40.0eV. As the d-level is full, the lack of participation of the d-electrons with bonding prevents complexes with ligands including carbon monoxide, as there are no electrons on the metal available for back donation, but complexes with ligands such as NH_3 , H_2O and halide ions are readily formed.

2.1.1.1 Dialkylzinc Chemistry

Organozinc chemistry originated in the synthesis of dimethyl- and diethyl- zinc by Frankland in 1849, which were the first organometallic compounds having a metal-carbon σ -bond.⁹⁶ The discovery was accidental as Frankland was interested in the isolation of the ethyl ‘radical’ by the action of a metal on methyl/ethyl iodide and hydrolysis experiments of the distilled material helped to identify the compounds.⁹⁷ There have been many subsequent attempts to identify and understand the structure and bonding of these compounds.⁹⁸⁻¹⁰¹ The research within this body of work has led to the first crystal structure determination of both diethyl and dimethyl zinc¹⁰² and is discussed in **Chapter 4**.

The route most commonly used to synthesise dialkylzinc compounds is the reaction between anhydrous zinc chloride solvated in ether, with Grignard or lithium reagents.

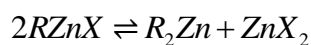
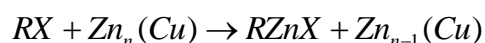


Where R=Me, Et etc. and X=Cl, Br, F

After the solvent is removed under vacuum, the dialkyls can be distilled.¹⁰³ The potential drawback of this reaction for use of the product within the electronics industry is halide trace impurities (e.g. RZnX, RX) which can act as n-type dopants during the growth of II-IV alloys. If, however, the dialkylzinc compound is to be used as a p-type dopant during the growth of III-V layers the potential problem could be the incorporation of oxygen based contaminants arising from solvents used during synthesis.

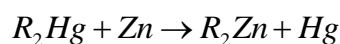
There are two further ways in which organozincs can be formed:

1. by the direct reaction of activated zinc metal (usually by zinc-copper or zinc-silver couple) with the required alkyl bromide or iodide, an equilibrium is established in which the diorganozinc is formed:



Where R=Me, Et etc. and X=Cl, Br, F

2. or a method rarely used now, due to the high toxicity of mercury, is a transmetalisation reaction with zinc metal and the bisalkyl mercury compounds.



Where R=Me, Et etc.

Dialkylzinc compounds are generally colourless liquids or volatile white solids and very air and moisture sensitive. For both the dimethyl- and diethylzinc, they are pyrophoric. This pyrophoricity is a consequence of the kinetic instability of the compounds towards hydrolysis and atmospheric oxygen. For ZnR_2 as the R group increases in size, so too does the stability of the complex.

2.1.2 Zinc Adduct Chemistry

The zinc alkyls are soluble in organic (non-protic) solvents, and since these compounds are electron deficient and unable to form alkyl bridges, it is inevitable that they readily form acceptor-donor complexes with suitable electron rich ligands. With polar solvents, adducts are formed. Original work on dimethylzinc adducts was carried out in the 1950/60s. Within the scope of the research presented, adducts formed with O, N and S containing ligands are discussed within this section. Experimental results for the adducts synthesised, characterised and used for deposition trials are discussed in **Chapter 4**. Adducted compounds are generally less volatile (removing the need to cool bubblers) and more stable (thermodynamically and kinetically) than the parent alkyl making them easier to handle. **Figure 26** helps to show the possible bonding available with a zinc metal centre when donor molecules are introduced.

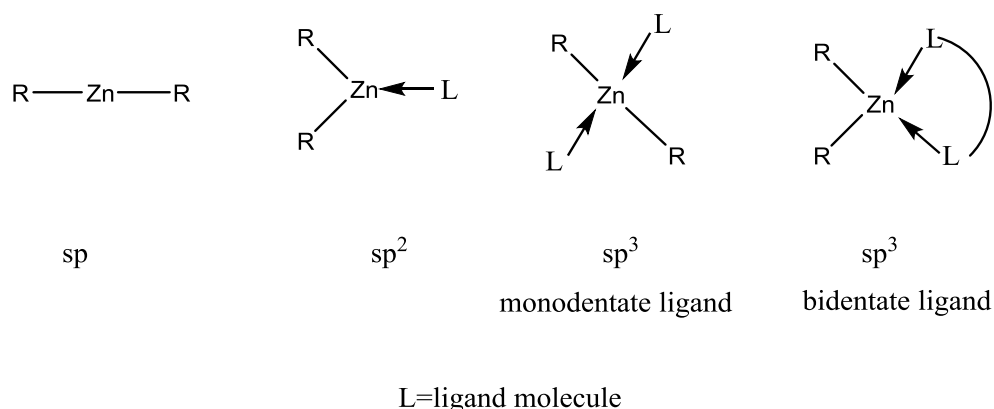


Figure 26 Possible bonding modes possible for a zinc centre. ¹⁰⁴

Throughout this study the adducted compounds will carry the notation DMZn.L where L is the ligand used.

2.1.2.1 Oxygen Donor Adducts

Oxygen donor complexes formed with dialkyl zinc increase in stability from simple ethers < cyclic ethers < chelating ethers. The Zn atom bonds with the oxygen on the donor ligand. An example of a complex with a simple ether is $\text{Me}_2\text{Zn} \cdot \text{O}(\text{CH}_3)_2$ formed with dimethyl ether, $(\text{CH}_3\text{OCH}_3)$. This adducted species has a boiling point of 47°C , just 3°C higher than that of dimethyl zinc. With simple ethers, the purification distillation process can cause partial separation even at atmospheric pressure. Cyclic ethers e.g. tetrahydrofuran, THF, $(\text{O}(\text{CH}_2)_4)$ and 1,4-dioxane $(\text{O}(\text{C}_2\text{H}_4)_2\text{O})$ are more stable due to the increased steric bulk. These compounds are miscible in water as the oxygen atom is more available for hydrogen bonding when compared to aliphatic ethers. The DMZn.L adducted species using both THF and 1,4-dioxane cyclic ligands, were target molecules and are discussed in-depth in **Chapter 4**. Chelating ethers are most stable and often incorporate multi-dentate ligands. Previously, the DMZn.L where L=1,2-dimethoxyethane was reported as a non-chelating compound¹⁰⁵, this study concludes that this complex is monomeric featuring a chelating 1,2-dimethoxyethane ligand.¹⁰⁶

2.1.2.2 Nitrogen Donor Adducts

Research on reactions between zinc alkyls and amines has been extensive. **Table 6** has been compiled from the literature and includes some of the DMZn.L compounds (where L=a nitrogen containing ligand) reported. The ligands are indicated along with melting point and boiling points of the final compounds with DMZn included for reference.

Compound	Ligand	Zn: Ratio	Melting Point (°C)	Boiling Pont (°C)	Vapour pressure @ 20°C (T)	Reference
DMZn	-	-	29.2	46	459.41	¹⁰⁷
DMZn.NEt ₃	Triethylamine	1:1			35.06	^{107, 108}
DMZn.(NEt ₃) ₂	Triethylamine	2:1			67.00	¹⁰⁷
DMZn.NMe ₃ *	Trimethylamine	1:1		84		¹⁰⁹
DMZn.(Me ₂ NCH ₂) ₂	Dimethylmethylamine (TMMD)	1:2	57-58		45.12	^{107, 110}
DMZn.(Et ₂ NCH ₂) ₂	Diethylmethylamine	1:2	66			¹⁰⁹
DMZn.(CH ₃) ₂ NCH ₂ CH ₂ N(CH ₃) ₂	Tetramethylmethylenediamine (TMEN)				11.53	¹⁰⁷
DMZn.(CH ₂ NMe ₃) ₂	1,3,5-Trimethylhexahydro-1,3,5-triazine (TMTZ)	1:2	37		36.63	^{107, 108}
DMZn(CH ₃ CH ₂ NMe ₃) ₂	1,3,5-Triethylhexahydro-1,3,5-triazine	1:2				¹⁰⁸

Table 6 Nitrogen based adducted dimethylzinc compounds (*Note: 1:2 complexes are dissociated into the 1:1 complex and free amine in benzene solution).

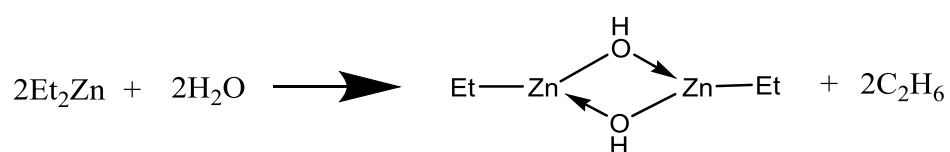
Nitrogen donor adducts have been extensively used for deposition studies of zinc oxide, zinc sulphide and zinc selenide thin films. Deposition using this type of complex is discussed further in **section 2.1.3**.

2.1.2.3 Sulphur Donor Adducts

Zinc forms relatively unstable complexes with sulphides due to its A-type acceptor character, forming complexes more readily with oxygen and nitrogen than the heavier donors with the need for d-orbital involvement. If zinc is bound to electron-attracting groups, then its acceptor character is enhanced. Literature suggests that for thin film deposition involving zinc, co-reagents are often used containing the sulphur/selenium atom with un-adducted dialkylzinc for zinc sulphide or zinc selenide film growth.

2.1.2.4 Alkylzinc Alkoxides

The zinc alkyls readily react with substances containing acidic hydrogens, and one or both organic groups are displaced according to the nature of the acid and the reaction conditions. When diethylzinc is reacted with water at 0°C, only one ethyl group is displaced and a dimer is formed:



Crystalline products, RZnOR' from zinc alkyls and alcohols have been studied before, with MeZnOMe first described by Butlerow in 1864.¹¹¹ Unless bulky groups are attached to the oxygen atom, the compounds formed from the dialkyls are all tetramers in solution e.g. (MeZnOMe)₄, (MeZnO^tBu)₄ and (EtZnOⁱPr)₄ which indicates the possibility of cubic or near-cubic structures in which the zinc and oxygen atoms are four co-ordinate.¹¹⁰ The highly symmetrical crystal structure of

the methylzincmethoxide tetramer has been determined by x-ray diffraction¹¹² and further studies have looked to the oxidation of the dimethylzincs dependence on the structure formed due to the presence of water and oxygen.¹¹³ This complex will be revisited with further reference in **Chapter 4**.

2.1.3 Application of Dialkylzinc and Dialkylzinc Adducts

Within the electronics industry, dialkylzinc and dialkylzinc adducts have been successfully used for the deposition of ZnO, ZnSe and ZnS. This work investigates the use of adducts for the deposition of zinc oxide. This material has many potential applications in photonic and electronic devices including solar cells, gas sensors, LEDs and UV laser diodes. The methods employed for the deposition of zinc oxide, as well as the properties of the material are discussed more completely in **section 2.1.4** and **2.1.5**. In the work presented here, it is hoped that the growth and analysis, when coupled with the crystal structures, go some way to add merit to the use of adducted zinc species in the deposition of zinc oxide. An important advantage of using adducted zinc species for the deposition of zinc oxide is the reduction in the homogenous pre-reaction. When the parent alkyl is used with oxygen/oxygen based co-reagent, an instantaneous reaction can occur which can often lead to particulates and oxide contamination prior to the precursors reaching the substrate. The benefits of reduced reactivity by using adducted zinc compounds can help to negate this and the associated handling and volatility issues. This will be discussed in more detail in **section 2.1.5.3**.

2.1.4 Zinc Oxide: Basic Properties and Applications

Zinc oxide has been widely studied since 1935¹¹⁴ and is a II-VI wide band gap (3.4eV) semiconductor with many promising properties highlighted in **Table 7**. The

following sections aim to provide an understanding of the properties that make ZnO suitable for the applications given.

ZnO Property	Potential Application
Polycrystalline form	Sunscreens, catalysts, lubricants, varistors and transparent conducting electrodes.
Band-gap energy of 3.37eV	Transparent in visible light and operates in the UV to blue wavelengths.
Exciton binding energy is ~60meV (c.f GaN~25meV)	Higher exciton binding energy enhances the luminescence efficiency of light emission.
Room temperature Hall mobility in single crystal ZnO is $\sim 200\text{cm}^2\text{V}^{-1}\text{s}^{-1}$	High electron mobility, good semiconductor.
Can form nanostructures	High surface area to volume ratio makes them ideal as gas sensors or PV devices.
Doping with a transition metal e.g. Mn shows ferromagnetism	Spintronic devices.
Doping can lead to tuning of the band gap	Match the energy of light to promote the valence electrons.

Table 7 The beneficial properties of Zn.

2.1.4.1 Crystal Structure

The crystal structures shared by ZnO are wurtzite, cubic zinc blende¹¹⁵⁻¹¹⁷ and rocksalt (at high pressure)¹¹⁸ and are shown in **Figure 27**.

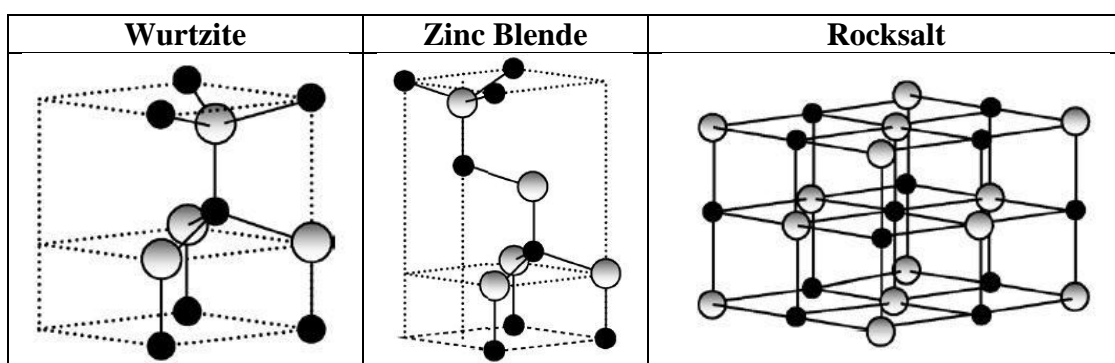


Figure 27 Ball and stick representation of ZnO (grey spheres=Zn, black spheres=O)¹¹⁹

At ambient temperatures and pressures, the hexagonal structure of wurtzite is favoured which consists of two hexagonal close packing (hcp) sub-lattices of Zn^{2+}

and O^{2-} . Each Zn ion is surrounded by a tetrahedron of O ions and vice versa. The tetrahedral co-ordination leads to polar symmetry along the hexagonal axis. This polarity is responsible for the piezoelectric properties, and is a key factor in crystal growth and defect generation in ZnO.¹²⁰ The tetrahedral co-ordination is an indicator of sp^3 covalent bonding, however, the Zn-O bond possesses a very strong ionic character, and thus, ZnO lies on the border of being classed as ionic or covalent.¹²¹ The lattice parameters of the hexagonal unit cell are $a=3.2495\text{\AA}$ and $c=5.2069\text{\AA}$ with a density of 5.605gcm^{-3} .¹²² At high pressures in the region of 10GPa there is a reduction of the lattice dimensions, causing the Coulomb interaction to favour the ionic over the covalent structure and the rocksalt structure is formed, but is difficult to stabilize.¹¹⁸ The zinc-blende structure is only stabilized by growth on cubic substrates such as GaAs, SiO_2 , and Si indicating the need for lattice matching to overcome the tendency to form the wurtzitic phase. A more comprehensive discussion of the crystal structures, with supporting references, is given by Özgür *et al.* in a review article entitled ‘A comprehensive review of ZnO materials and devices’.¹²³

2.1.4.2 Band Structure

Understanding the band structure of a semiconductor is essential for determining its potential use and incorporation into a device. Numerous theoretical and experimental studies have been employed to try to establish the band structure of the electronic states of wurtzitic ZnO. Absorption or emission techniques using X-rays or UV have been used to measure the energy difference by inducing transitions between electronic levels. Photoelectron spectroscopy is based upon the photoelectric effect, whereby the peaks in the emission spectra correspond to electron emission from a core level without inelastic scattering. Angle-resolved

photoelectron spectroscopy is a further advancement which enables experimental bulk and surface electronic band-structure determination under the assumptions of conservation of momentum.¹²⁴ The band structure of ZnO has been discussed within the literature from 1960s¹²⁵ and work continues to be published to the present day.¹²⁶ The most commonly referred to band structure is that reported by Vogel *et al.*¹²⁷ II-VI semiconductors are very demanding because of the need to take the d-electrons into account. Local-density approximations of bulk¹²⁸⁻¹³⁰ and surface properties¹³¹ had previously been calculated based upon d electrons being treated as core electrons. This led to underestimated lattice constants by as much as 13% for wurtzitic ZnO. If the d electrons are taken into account the band gap can be underestimated, and the occupied d bands reside roughly 3eV too high in energy compared to experimental values. Vogel *et al.* used an approach first discussed by Perdew¹³², whereby self-interaction corrections apply. The local density approximations for the band structure of bulk ZnO are shown in **Figure 28** which is taken from the original publication.

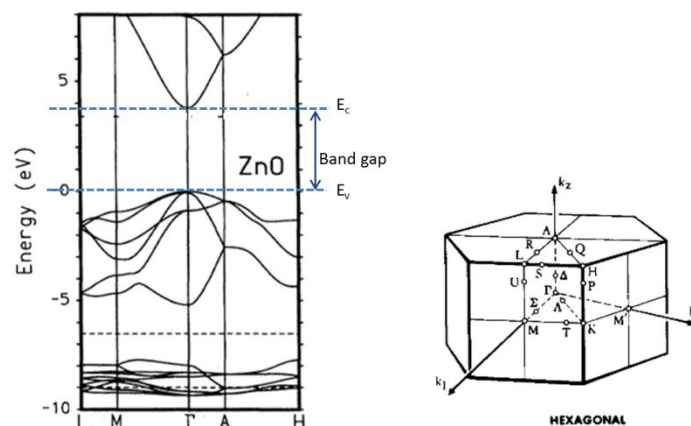


Figure 28 Local density approximation of the band structure of bulk ZnO.¹²⁷

To be able to interpret **Figure 28**, further understanding is needed. A more complete view of the band structure, than that discussed in **Chapter 1**, takes into account the

periodic nature of a crystal lattice. Brillouin zones are an important characteristic of crystal structures. A Bragg plane for two points in a lattice is the plane which is perpendicular to the line between the two points and passes through the bisector of that line. The first Brillouin zone for a point in a lattice is the set of points that are closer to the point than the Bragg plane of any point. In other words one can reach any of the points in the first Brillouin zone of a lattice point without crossing the Bragg plane of any other point in the lattice. The importance of the Brillouin zone for band structure stems from the Bloch wave (the wave function of an electron placed in a periodic potential) solutions of the Schrödinger equation. The wave vector, k , takes on values within the Brillouin zone corresponding to the crystal lattice, and particular directions. Points within the Brillouin zone are assigned for the hexagonal wurtzitic ZnO as shown on the right hand side in **Figure 28**. The available energies for the electron depend upon the wave vector. In the left hand side of the figure, the topmost energy of the valence band is labeled E_v and the bottom energy in the conduction band is labeled E_c . Note that for ZnO E_c and E_v are at Γ , reinforcing that ZnO is a direct band-gap semiconductor (no change in momentum is required). The bottom ten bands around -9eV correspond to the Zn 3d levels. The next bands from -5eV to 0eV corresponds to the O 2p bonding states. The first two conduction bands shown at 4eV and higher correspond to the empty Zn 3s levels. The band structure of ZnO is highly relevant to the thesis aim discussed previously in **section 1.6.2**.

2.1.4.3 Electrical Properties

As ZnO is a direct wide band gap semiconductor it has advantages including:

- higher breakdown voltages
- the ability to sustain large electric fields

- high-temperature/high power operation

ZnO has been extensively studied, and due to this there is a large variance in the quality of samples, and in turn, electrical properties reported. Looking to electron mobility values at room temperature, the values include 120, 137 and 145 cm²V⁻¹s⁻¹.^{133,134,135} Kaidashev *et al.*¹³⁶ report the best reproducible electron motilities from 115 to 155 cm²/V at 300K for a carrier concentration range of 2x10¹⁶ to 5x10¹⁶ cm⁻³ for a 1-2 μm ZnO thin film. It is worth reinforcing here, that often undoped wurtzitic ZnO can become an n-type semiconductor due to defects such as Zn on O, Zn interstitial and O vacancies.¹³⁷⁻¹³⁹

2.1.4.4 Thermal Properties

2.1.4.4.1 Thermal Expansion Co-efficient

The thermal expansion co-efficient of a material describes the lattice expansion as a function of temperature. This property is dependent on stoichiometry, defects and free carrier concentration.¹²³ For zinc oxide these co-efficients are given as $\alpha_a=4.31 \times 10^{-6} \text{K}^{-1}$ (normal to the c-axis) and $\alpha_c=2.49 \times 10^{-6} \text{K}^{-1}$ (parallel to the c-axis) at 300K.¹⁴⁰ For possible future applications of the wide-gap material ZnO in high temperature electronics, the thermal expansion coefficients at elevated temperatures are of relevance. Ibach¹⁴¹ presented data up to T =800 K that there is an increase in the thermal expansion coefficient with temperature, with saturation near to 800K, yielding the high-temperature values $\alpha_a=4.98 \times 10^{-6} \text{K}^{-1}$ and $\alpha_c=8.30 \times 10^{-6} \text{K}^{-1}$ i.e. an enhancement factor of about 1.7 with respect to the 300K values.¹⁴²

2.1.4.4.2 Thermal Conductivity

The bulk thermal conductivity of ZnO, denoted κ (Wcm⁻¹K⁻¹) has yet to be confirmed, with reported literature values ranging from 0.6 to 1.2 Wcm⁻¹K⁻¹.^{123, 143}

This kinetic property is important when considering high power/temperature devices. It is influenced by the vibrational, rotational and electronic degrees of freedom and is ultimately limited by phonon-phonon scattering in a crystal.¹⁴⁴ ZnO contains a large number of defects which reduces the thermal conductivity. A more comprehensive discussion is given in the following review article by Özgür *et al.*¹²³

2.1.5 Zinc Oxide Thin Film Growth

Growth techniques to fabricate ZnO range from low cost wet chemical growth at almost room temperature, to high purity deposition at temperatures above 1000°C.

Previously ZnO has been deposited by many different methods including:

- vapour liquid solid epitaxial growth (VLSE)
- pulsed laser deposition (PLD)
- magnetron sputtering
- molecular-beam epitaxy
- hydrothermal (low temperature-solution process)
- electrochemical

High temperature gas-phase processes often generates high quality ZnO but the commercial potential is restricted due to cost implications of achieving this high temperature, and the previous/subsequent thermal budget in the device structure. In contrast, the low temperature solution routes are of lower cost, and suitable for large scale production. In most cases, there is a strong tendency of c-axis orientated growth, leading to higher growth rate in this direction over other crystal directions. This often leads to columnar growth even at low temperatures. This phenomenon can result in the formation of nanowires, (a 3D structure with diameter of the order of a nanometer (10^{-9} m)) and is discussed further in **section 2.1.6**. The data reported in the literature for ZnO deposition is too extensive to cover here. To remain focused

on the relevant prior work in the areas discussed within context for this research, this literature review will focus on MOCVD of ZnO thin films and nanowires grown only from simple zinc alkyls, alkylzinc alkoxides and adducted zinc alkyls. MOCVD was the method of choice for the research presented due to its advantages highlighted previously in **Chapter 1**.

2.1.5.1 ZnO Deposition using Dialkylzinc

Traditional methods for ZnO growth by MOCVD has involved the pyrolysis of dimethylzinc¹⁴⁵ or diethyl zinc¹⁴⁶⁻¹⁴⁸ in the presence of oxygen and/or water. For MOCVD surface reactions at the substrate should occur, but not in the gas phase. The alkyl zincs are highly oxygen sensitive and often pre-reaction in the gas phase can form oxide particulates upstream of the substrate. MOCVD methods have looked to reactor pressure to try to control the reaction, with the range spanning 5-250 torr,¹⁴⁹⁻¹⁵¹ with superior crystal quality observed for ZnO grown at 6 Torr as opposed to <1Torr.¹⁵² The effect of altering the oxygen partial pressure during deposition on structure, optical and electrical properties has also been studied.^{153, 154}

Another approach to try to overcome pre-reaction, was to look towards less reactive oxidants. These include CO₂¹⁵⁵, N₂O¹⁵⁵⁻¹⁵⁷ and NO₂¹⁵⁷⁻¹⁶⁰ or alternatively alcohols such as methanol, ethanol, isopropanol^{161, 162} or tertiary-butanol.¹⁶³

Ogata *et al.* highlighted the potential use of nitrous oxide to grow highly crystalline ZnO films with good optical properties.¹⁶² Kirchner *et al.* have carried out a comparison of using alternative precursors for oxygen using DEZn with isopropanol and tertiary butanol co-reagents on a sapphire substrate.¹⁶⁴ There was a large discrepancy in the growth rate with temperature dependence between the two oxygen sources. Tertiary-butanol had a constant growth rate (2.1µm/hr) for the temperature range 380-510°C. When isopropanol was used the maximum growth

rate was achieved at 380°C and at higher temperature fell rapidly. Film analysis showed superior quality in the tertiary butanol grown samples. It has been proposed that reaction of the alcohols with the dialkylzincs leads to alcohol adducts or zinc alkoxides as the gas-phase intermediates. This theory is further supported by the growth of ZnO by single-source zinc precursors e.g. [MeZn(OⁱPr)] and [MeZn(O^tBu)] without the need for an additional oxygen source.¹⁶⁵ A decomposition pathway, reported by Auld, proposed the the removal of a β-hydrogen results in the elimination of methane and an alkene.¹⁶⁵

ZnO has been successfully grown on numerous types of substrates including, but not limited to, silicon,¹⁶⁶ glass,¹⁶⁷ gallium arsenide,¹⁶⁸ diamond¹⁶⁹ and sapphire.¹⁷⁰ The study presented in **Chapter 4** uses silicon and glass substrates.

2.1.5.2 ZnO Deposition using Dialkylzinc Adducts

Using adducted zinc species for ZnO deposition has the advantage of a reduction in the homogenous reaction before the precursors reach the substrate. Although reaction design can help to limit the pre-reaction, making alterations to the Zn species to make them less reactive towards oxygen, has resulted in a large number of adducts being examined as potential precursors. Adducts of zinc with 1,4-dioxane,¹⁷¹⁻¹⁷³ thioxane,¹⁷³ triethylamine,¹⁷⁴⁻¹⁷⁹ or triazine¹⁷⁴ have been used as precursor for MOCVD and can be successfully use to inhibit the pre-reaction for chalcogenide and metal alkyls. Dimethylzinc.complex triethyl amine synthesis was reported by Thiele in the 1960s, and has been used to study the p-type doping of III-V materials with zinc^{180, 181} and also useful for the deposition of chalcogenides.¹⁸² Despite using such compounds during MOCVD, little is known about the gas species present during the reaction. Infrared studies have been performed in the past which show the adducts of dimethylzinc to be fully dissociated in the gas phase.¹⁸³

2.1.5.3 Use of Adducts for the Prevention of Pre-reaction.

There are a number of ways in which adducts could be operating in controlling unwanted reactions:

- decreased reactivity of the adducted species compared to the parent alkyl ensure surface catalysed reactions in the cool zone of the reactor are less likely.
- using high purity reagents leads to less unwanted side reactions. The improved purity of the alkyls due to subsequent reactions/purifications may prove important.
- the pure alkyls are extremely volatile. With an adducted species, mass flow can be more controlled. As the homogenous reactions are likely to proceed at rates proportional to the partial pressure of the alkyls, a lower partial pressure for the adducted species leads to a lower rate of homogenous reaction.
- The Lewis bases from which the adducts are formed may play a role in trapping intermediates generated during the decomposition of alkyls.

It is important to note that the adducts do not need to stop the formation of precipitates from the vapour phase, but only to inhibit their formation so that they can pass through the hot zone of the reactor.

2.1.6 Zinc Oxide Nanowire Growth

Since the surface properties of ZnO are very different for the different crystal forms, chemical reactivity and growth rate vary drastically as a function of surface orientations. In combination with a large surface diffusion of Zn, this often leads to the formation of ZnO crystallites on the micro- or nano-scale. Under some

circumstances ZnO columns can be formed with very large aspect ratios. Recent interest in ZnO nanostructures, stems from their potential applications in gas-sensors,¹⁸⁴ UV laser diodes,¹⁸⁵ light-emitting diodes¹⁸⁶ and as an electron transport material in excitonic solar cells.¹⁸⁷ One exciting commercial application is the use of nanowires in solar cells. With an increased surface area when compared to a thin film, there is greater light harvesting capability. There is an increase in electron mobility and a reduction in electron recombination rate with the p-type polymer (**Figure 13**). The nanowire helps to establish an interface that dissociates the photogenerated excitons into electrons and holes. Due to its band structure, the nanowire provides a direct conduit for electrons to be transported to the device electrode where it can contribute to current conduction.¹⁸⁸ With further development and the introduction of dopants to the system, there is a chance to tune the morphology of the nanowire as well as its light harvesting properties respectively. Power conversion efficiencies of upto 2% have been reported for hybrid ZnO NW/polymer solar cells.^{189, 190} A review article by Zhang *et al.*¹⁹¹ provides a comprehensive overview of the synthesis, characterisation and applications of nanowires. Vapour phase, solution phase and hydrothermal methods are all included for discussion within the paper. MOCVD was the method of choice for ZnO nanowire formation in this body of work, due to the advantages over other deposition techniques.

2.1.6.1 ZnO nanowires using dialkylzinc precursors

Park *et al.* have shown that ZnO nanowires have been fabricated from dialkyl zinc and oxygen as precursors.¹⁹² As a consequence, the reactor pressure was kept low to prevent the gas phase reactions. After growing a ZnO buffer layer at temperature

below 400°C on Al₂O₃ substrate, nanowires were grown in the temperature range was between 400-500°C. **Figure 29** shows the SEM images of the nanowires grown.

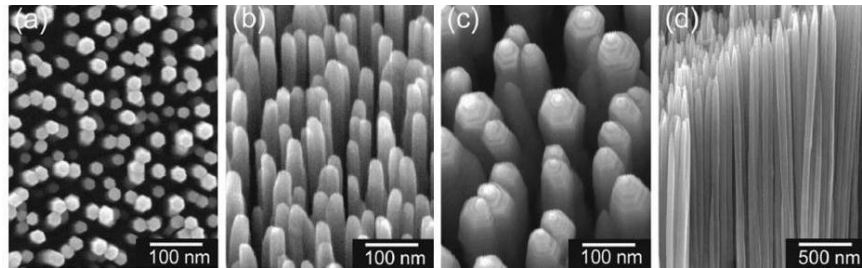


Figure 29 SEM images of ZnO nanowires from dialkylzinc and oxygen recorded by Park *et al.*¹⁹² showing a) plan view b) tilted images(diameter 25nm) c and d) tilted and cross-sectional view of nanowires with 70nm.

Lui *et al.*¹⁹³ also report ZnO nanowire growth using the same precursors. The substrates used, c-plane sapphire, platinum on SiO₂/Si and Si(100), were held at a temperature of 700°C. An initial plasma step was performed to provide a nucleation layer of ZnO. Sapphire and platinum surfaces gave well aligned nanowires, whilst those on Si were randomly orientated. The dimensions of the wires were reported to be between 20-75nm in diameter and 2µm in length.

DEZn and oxygen have also been used to deposit ZnO nanowires on αAl₂O₃(0001) substrates with different ZnO buffer layers via MOCVD both in-situ and ex-situ;¹⁹⁴

- In-situ
 - ZnO buffer layer deposited on Al₂O₃ substrate and subsequently ZnO nanorods grown on the buffer layer by MOCVD with substrate temperatures of 350-650°C.
- Ex-situ
 - ZnO buffer layer sputtered onto Al₂O₃ substrate held at 600°C. The ZnO buffer layer/Al₂O₃ transferred to MOCVD chamber in air. The ZnO nanorods were then grown on ZnO buffer layer by MOCVD.

The growth rate for both processes was approximately 20nm/min, with nanowire length between 70-100nm depending on substrate temp. No distinguishable difference in nanowire quality for the processes was observed. Within this study they suggested that lattice mismatch was enough to seed island growth.

2.1.6.2 ZnO nanowires using methylzinc alkoxide complexes

In section 2.1.2 the chemistry of the co-ordination complexes of zinc was discussed.

Table 8 highlights the use of two such zinc compounds, with the first [MeZn(OⁱPr)] by J.Auld *et al.*¹⁶⁵ and the second, [MeZn(O^tBu)] by Kaufmann.¹⁹⁵

Precursor	[MeZn(O ⁱ Pr)]	[MeZn(O ^t Bu)]
Substrate	Soda Lime Glass	Soda Lime Glass
Precursor Temp (°C)	70	80
Growth rate	0.2 to 1.1µmh ⁻¹	3.7 to 4.4µmh ⁻¹
Temperature range	250 to 350°C	250 to 400°C
Cell pressure	15Torr	
Carrier Gas	N ₂	N/A
Comments	At 250°C nanowires ~0.1µm in diameter. 300°C smooth film. 350°C disordered	At 250°C irregular surface. 300°C nanowires ~0.1µm in diameter. 350°C larger, bulbous columns 1.0µm

Table 8 Summary of the conditions used for the deposition of ZnO NWs.

Both have shown the successful growth of nanowires at temperatures below 500°C on soda lime glass and SEM images are shown in **Figure 30**. Image **a**) shows the nanowires deposited at 250°C with [MeZn(OⁱPr)], whilst image **b**) are the nanowires deposited using [MeZn(O^tBu)] at 300°C.

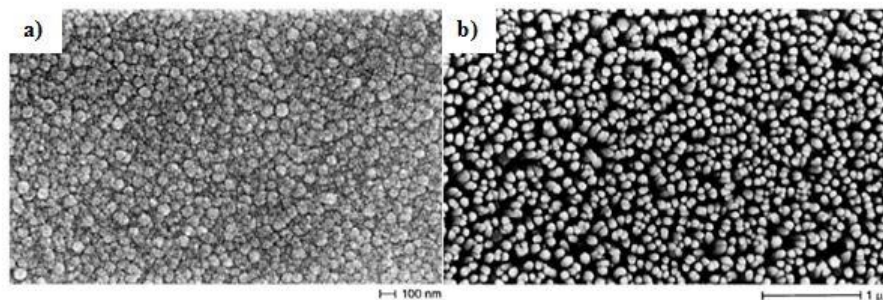


Figure 30 SEM images of ZnO nanowires grown using [MeZn(OⁱPr)] and [MeZn(O^tBu)]

2.1.6.3 ZnO Nanowires using Dialkylzinc-adduct Precursors

Within the research group at the University of Liverpool, Black *et al.*¹⁹⁶ have previously proven that ZnO NW can be grown in an ordered fashion using LI-MOCVD with dialkylzinc adducts. The original aim of Black's work was to investigate compliant substrates for materials on silicon. This involved the deposition of ZnO thin films. Compounds of [Me₂Zn(L)] (L= oxygen donor e.g. THF, THP, Furan) dissolved in octane (0.1M) were used for depositions between 350-550°C. By chance, at 500°C nanowire morphology was observed, whilst at other temperatures continuous polycrystalline films were deposited. Analysis of the nanowires by XRD showed the (0002) of the wurtzitic phase. This was the first reported use of such precursors for ZnO nanowire growth. Subsequently, there was a push to try to understand the mechanism of growth and see if nanowire formation could be controlled by various factors including, but not limited to, the effect of the ligand used, the oxygen/zinc ratio, and the substrate.

Experimental results in **Chapter 4** report the deposition of ZnO nanowires with various [Me₂Zn(L)] without the requirement of a seed layer, via LI-MOCVD. With reference to **Figure 13**, the next section introduces copper and copper oxide. Copper oxide was the chosen p-type material to be used with the n-type zinc oxide in the PV cell design.

2.2 Copper

Copper is an extremely ductile metal and is distinctively red in colour. It is an excellent electrical conductor, with high thermal conductivity and is also corrosion resistant and antibacterial. Copper can be naturally occurring but today is obtained from minerals such as azurite (copper carbonate ($\text{Cu}_2(\text{OH})_2\text{CO}_3$)); chalcocite (copper sulfide (Cu_2S)); chalcopyrite (copper iron sulfide (CuFeS_2)); and cuprite (copper oxide (Cu_2O)). Copper is mined in more than 50 nations, with over 50% of the world's copper coming from the leading producers Chile and the United States.¹⁹⁷

2.2.1 Copper Chemistry

Copper is found in group 11 in the periodic table. It is a transition metal with an electronic configuration of $[\text{Ar}] 3d^{10}, 4s^1$. Copper metal is therefore paramagnetic due to the unpaired electron in the 4s orbital. The two most common ions formed by copper are the +1 (cuprous) and +2 (cupric).¹⁹⁸ The cuprous ion is the less stable of the two oxidation states and has the electron configuration of $4s^0 3d^{10}$ and it is therefore diamagnetic. The cuprous ion has a high charge to size ratio which causes the 3d orbitals to be relatively contracted which results in poor overlap with ligand orbitals resulting in poor back donation. The empty 4s orbital is relatively less contracted and is available for bonding, thus, copper (I) forms strong bonds with good σ donor ligands. Therefore, due to the potential for oxidation, any work done with copper (I) compounds must be carried out in an inert atmosphere. Removal of a second electron from copper results in the $4s^0 3d^9$ configuration; therefore the cupric ion is paramagnetic. The cupric ion tends to exhibit square planar or distorted octahedral geometries.

2.2.2 Application of Copper Precursors

For the purposes of this study, copper precursors can be used for the deposition of both copper metal and copper (I/II) oxide. The next section includes a discussion on the properties of these materials as well as their application within the microelectronics industry.

2.2.2.1 Crystal Structure

The crystal structure of copper metal is a face centered cubic (fcc) structure. A copper atom is found at each corner and in the center of each face of a cube as depicted in **Figure 31**.

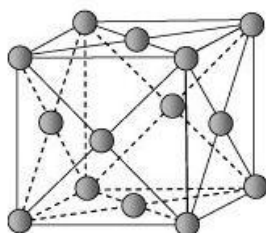


Figure 31 Face centred cubic structure of copper metal.

The number of atoms in the unit cell is four with the atomic packing factor (the volume of atoms belonging to the unit cell divided by the volume of the unit cell) of 0.74, this is the most densely packed structure that can be obtained. In the fcc structure the Cu atom has 12 nearest atom neighbours and a stacking sequence of *ABCABC*.¹⁹⁹

2.2.2.2 Application for Copper Metal

Copper has the highest electrical conductivity of any metal at 5.96×10^7 S/m at 20°C. It also has a high thermal conductivity of $401 \text{ W m}^{-1} \text{ K}^{-1}$ at 27°C and a resistivity of $1.678 \mu\Omega \text{ cm}$ at 20°C.^{91, 200} These properties make copper an attractive material for use as interconnects in integrated circuits. The integrated circuit (IC) forms part of many electronic devices and is constructed from transistors (semiconducting materials used to amplify and switch electronic signals), resistors (resists the flow of

electric current) and capacitors (storage electric charge). These semiconducting components are all joined together by 'wires' in IC. Historically aluminium has been the material of choice for these wires which are deposited on onto the surface of the processed silicon wafer and are known as interconnects. Aluminium has sufficient conductivity, can be prepared in high purity and adheres strongly to silicon dioxide.²⁰¹ As IC have continued to get more complex and smaller, the space available for the interconnects has decreased. This has resulted in thinner interconnects handling larger currents. This exposed aluminium's susceptibility to electromigration. Electromigration is the movement of individual atoms, in this case aluminium, through an interconnect in the direction of current flow. This diffusion can result in thinning and even complete fracture which creates voids and ultimately breaks the interconnects. This problem focused research groups to look to more highly conductive materials which suffer less from electromigration.^{202, 203} The obvious choices were silver, gold and copper. Copper was more intensely studied as it is relatively cheaper. Copper wires have many advantages over aluminium. Copper can conduct electricity with 40% less resistance than aluminium, this translates to as a much as a 15% increase in the speed of a microprocessor. Other advantages are listed below:

- Copper is less vulnerable to electromigration than aluminium.
- Depositing copper has a potential cost saving of 30% for the wiring or 10-15% for the whole silicon wafer.
- The width of copper wire can be squeezed down to the 0.2micron range. This enables further miniaturisation of electronic devices as 150-200 million transistors would be able to fit on one chip.

There are some disadvantages to using copper, it has an increased rate of diffusion into silicon which can result in device malfunction.²⁰¹ Also, copper does not adhere to silicon as well as aluminium. These problems can be overcome with additional processing steps to form a layer between the copper and silicon to act as a barrier layer and also to increase adhesion.

For the current technology aluminium is deposited over the entire wafer and then patterned by a process known as reactive ion etching (RIE), unwanted metal is then etched away. Trials to pattern copper by this RIE method failed. This led to the need for a new process to deposit high purity copper.²⁰⁴ Various forms of physical vapour deposition (PVD) including sputtering, CVD and electroless plating were trialled.²⁰⁵ Covering trench walls was difficult with PVD whilst CVD grew conformal films which leaves a seam in the middle of the trench.²⁰⁶ The Damascene Process, shown schematically in **Figure 32**, was first developed by IBM engineers, and provided a solution which led to the mass production of copper wired IC in 1998.

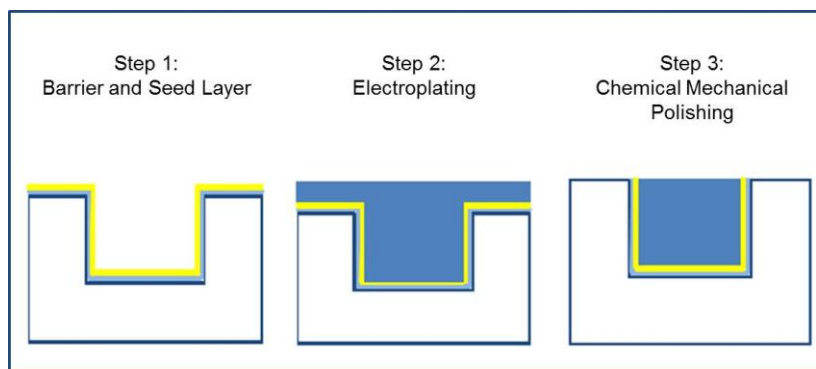


Figure 32 A schematic of the Damascene process.²⁰⁴

This process has three main steps:

Step 1: Growth of a smooth, continuous, conformal barrier layer onto the dielectric material via ionized PVD, followed by a copper seed layer grown via ionized PVD or CVD.

Step 2: The pattern is then filled using electroplating (electrolysis of copper ions from solution onto the seed layer).

Step 3: Chemical mechanical polishing (CMP) is used to remove excess copper and to planerise the wafer.

Although this method provided some way of incorporating copper interconnects, the continued drive for reduction in size and increase in speed of IC, led to multilevel ICs. The interconnects are then subsequently joined by vias (small opening in an insulating oxide layer that allows a conductive connection between different layers). As the height of the via increases, the width remains the same leading to an increase in aspect ratio. As PVD is a line of sight technique, these high aspect ratio structures have poor step coverage. Copper deposited by this method has the potential to build up at the entrance to the via blocking any deposition at the base. Ideally, ALD would be the technique of choice to overcome the issue of the difficulty in depositing conformal layers with high aspect ratios. This research looks to the development of an ALD process for the deposition of copper metal using different precursors with a series of potential co-reagents. The experimental work and results are discussed in **Chapter 5**.

2.2.3 Basic Properties of Copper Oxides

2.2.3.1 Crystal Structure

The crystal structure of both forms of copper oxide are shown in **Figure 33**. The unit cell of cuprous oxide, Cu_2O , contains 4 copper atoms and 2 oxygen atoms, with a lattice constant of 4.2696\AA .²⁰⁷ The unit cell is a body centered cubic lattice of oxygen ions, in which each oxygen ion occupies the center of a tetrahedron formed by copper ions, whilst the copper atoms arrange in a face centered cubic sublattice. The molar mass of Cu_2O is 143.09g/mol and it's melting and boiling points are

1235°C and 1800°C respectively. This form of copper oxide adopts a red colouration.

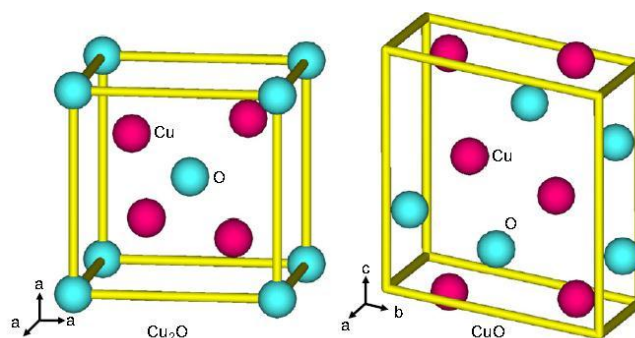


Figure 33 Crystal structure of CuO and Cu₂O.²⁰⁸

Copper(II) oxide is black in colour and belongs to the monoclinic crystal system, with lattice parameters $a=3.4226\text{\AA}$, $b=4.6837\text{\AA}$ and $c=5.1288\text{\AA}$. The copper atom is coordinated by 4 oxygen atoms in an approximately square planar configuration.

2.2.3.2 Application for Copper Oxides

Copper oxides can be used for catalysis,²⁰⁹ gas sensors²¹⁰ and superconductors²¹¹ and are of recent research interest because of their potential applications in photovoltaic devices. Both of the copper oxides are p-type semiconductors. Films of CuO and Cu₂O have been extensively studied due to suitable band gap energies (discussed earlier in **section 1.6.2**) Both materials also have high optical absorption to allow for light harvesting.²¹² The properties of the copper oxide films grown are very much dependent on the growth methods used, and within this chapter, it is hoped an insight into previous research is given.

2.2.4 Copper Metal Deposition: Precursors and Growth

2.2.4.1 Chemical Vapour Deposition

For the deposition of copper metal, many precursors have been trialled. They can be separated into two main groups due to their deposition pathways. In general Copper (II) precursors require a reducing agent, whilst copper (I) precursors can undergo disproportionation reactions to deposit metallic copper. Hydrogen gas is the most commonly used reducing agent²¹³ and with advances in plasma technology, the activation energy can be reached more easily with the generation of hydrogen radicals. This advancement has enabled copper films to be deposited at lower temperatures.^{214, 215}

2.2.4.1.1 Deposition from Copper (I) Precursors

Disproportionation involves one metal serving as both an electron donor and acceptor. Monovalent copper is one of the more common metal/oxidation state combinations that can exhibit disproportionation. Precursors including Cu(I) cyclopentadienyl and t-butoxide and their derivatives have been used previously, however, the most widely used Cu(I) precursors are adducts of Cu(hfac) with a general formula Cu(hfac)(L) where L= alkene, alkyne, diene or phosphine.^{216, 217} The most thoroughly studied Cu(I) precursor is the extremely air sensitive, 2Cu(hfac)(vtms) (Where hfac = hexafluoroacetylacetone and vtms= vinyltrimethylsilane, Cuproselect® Air Products), with its planar structure shown in **Figure 34.**

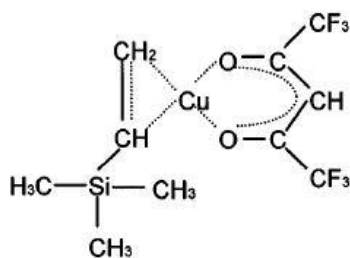
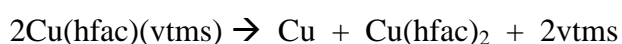


Figure 34 Cu(hfac)(vtms).

For this compound the CVD processes follows disproportionation:



CVD was reported in 1991, with precursor temperatures between 25-40°C and deposition temperatures between 100-250°C. He, N₂, Ar or a mixture with H₂ were used as the carrier gas.^{218, 219} Jakob and co-workers²²⁰ presented a paper in 2008 in which copper (I) carboxylates of the type [(ⁿBu₃P)_mCuO₂CR] (where m=1,2,3 and R=Me, CF₃, Ph, CH=CHPh, (CH₂OCH₂)₃) are analysed for synthesis, properties and their use as CVD precursors. Based upon the thermal properties recorded by TGA and DSC (differential scanning calorimetry), the complex [(ⁿBu₃P)₂CuO₂CCF₃] was trialled. The precursor was held at 120°C, and, in the absence of co-reagent, at 480°C, on a TiN-coated oxidised silicon substrate, copper was deposited. The SEM image in **Figure 35** shows the film morphology was not completely continuous and consisted of loose clusters of copper particles which coalesce.

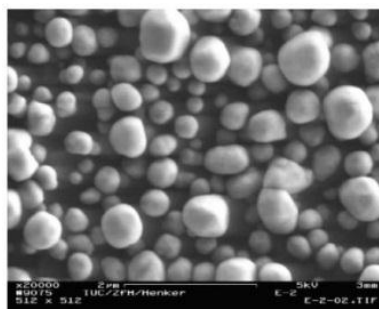


Figure 35 SEM image of a copper film obtained from [(ⁿBu₃P)₂CuO₂CCF₃] on a TiN-coated oxidized silicon substrate 480 °C.²²⁰

Copper grains of about 200nm size are apparent as the nucleation layer, with a layer of large irregular copper grains of approximately 780nm above the nucleation layer. Phosphite copper (I) trifluoroacetates were the subject of a follow-up paper. $[(\text{CH}_3\text{O})_3\text{P}]_3\text{CuO}_2\text{CCF}_3$ was held at 65°C and deposition experiments were carried out at 380°C again on TiN-coated oxidised silicon.²²¹ Again without co-reagent, copper particles were deposited in a non-uniform, non-continuous film. A nucleation layer of grains approximately 200nm and larger particulates closer to 1200nm were observed. This complex was more suited than the earlier proposed precursor due to the lower transportation temperature needed. Induction periods are often observed during the CVD of metals on non-metallic substrates due to the higher activation energies required for nucleation. On non-metallic substrates, large grain microstructures are formed and often lead to rough films, because the probability would be greater for the precursor to desorb or diffuse to an existing nucleus rather than form a new nucleus.⁹¹ The chemical reactions involved in the transformation of a molecular precursor into a metal film will depend on the surface. CVD using Cu(hfac)(vtms) has been conducted on metals, semiconductors, nitrides and oxides with an excellent overview provided in the RSC publication, Chemical Vapour Deposition.⁹¹ Copper nucleation has been the challenge in obtaining high quality films, with this concept becoming more important in **Chapter 5**.

2.2.4.1.2 Deposition using Copper (II) Precursors

2.2.4.1.2.1 β -diketonates

The most common Copper (II) β -diketonate compounds are based on the structure shown in **Figure 36**:

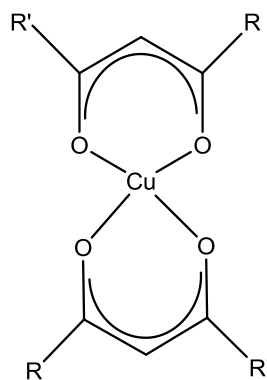


Figure 36 Basic Cu(II) β -diketonate CVD precursor.

Where:

Compound	R	R'
Cu(acac) ₂	CH ₃	CH ₃
Cu(hfac) ₂	CF ₃	CF ₃
Cu(tfac) ₂	CH ₃	CF ₃
Cu(thmd) ₂	C(CH ₃) ₃	C(CH ₃) ₃
Cu(ppm) ₂	C(CH ₃) ₃	CF ₂ CF ₃
Cu(fod) ₂	C(CH ₃) ₃	CF ₂ CF ₂ CF ₃
Cu(tdf) ₂	CF ₂ CF ₂ CF ₃	CF ₂ CF ₂ CF ₃

Table 9 Copper (II) β -diketonate CVD Precursors.

Cu(hfac)₂ is the most widely researched β -diketonate for copper metal deposition and was reported in 1965, in the first use of copper CVD.²²² Anhydrous Cu(hfac)₂ exists as blue-violet crystals with a melting point of 95-98°C.^{223, 224} This is a monomeric square planar compound and the crystal structure shown in **Figure 37**.

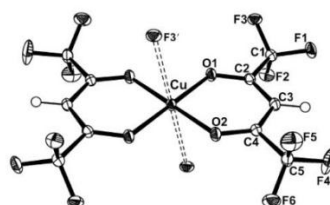
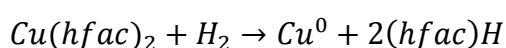


Figure 37 Cu(hfac)₂.²²⁴

This copper (II) precursor has been used for deposition temperatures ranging from 250-400°C.^{216, 217} The lowest-resistivity films (e.g. ca. 20μΩcm) were obtained when H₂ was used as a co-reagent.^{213, 225, 226} The fluorinated complex is chosen over the acac derivative as the fluorine molecules increase the volatility of the compounds. The negatively charged atoms help to increase the repulsive Van der Waals forces between the precursor molecules. The suggested reaction pathway of this molecule with a H₂ carrier gas (reducing agent) is given below:



More generally, the mechanism for copper(II) β-diketonate precursors is shown schematically in **Figure 38**. It is a process of Cu(II) reduction followed by ligand dissociation.²²⁷

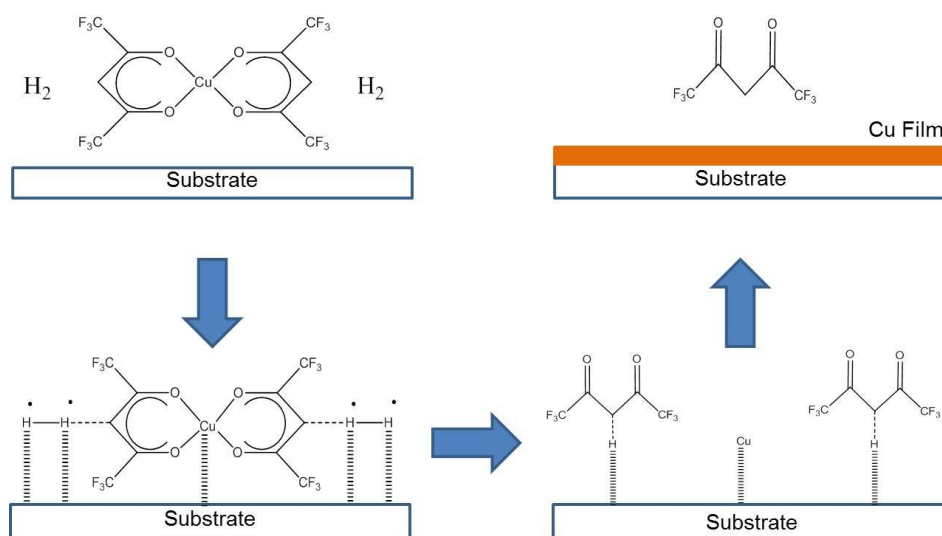


Figure 38 Proposed mechanism for copper deposition by CVD for Copper (II) β-diketonate precursors.

Reaction kinetics and mechanism is discussed more completely in the following articles.^{213, 225, 228, 229} Without the reducing agent, higher substrate temperatures are needed to decompose the precursor, however this can lead to increased impurities within the film.²³⁰ One of the drawbacks of this compound are the fluorine atoms, as

when incorporated into films can lead to electronic malfunctions. The addition of water or alcohols during deposition helped to increase growth rate and film morphologies by enhancing Cu nucleation, however, the H₂ was still required to ensure copper oxides didn't form.²³¹ There have been other methods trialled with this precursor including SiO₂ substrates modified with self assembled monolayers^{232, 233} and depositions in supercritical CO₂ environments.^{234, 235}

Table 10 is included to highlight some of the conditions successfully employed with various β-diketonate complexes to form copper films.

Precursor(*)	Evaporation Temp. (°C)	Deposition Temp. (°C)	Carrier Gas
Cu(acac) ₂	180-200	225-250	H ₂ /Ar
Cu(hfac) ₂	120	340-390	H ₂ /Ar
Cu(tfac) ₂	135-160	250-300	H ₂
Cu(thmd) ₂	100	400	None
Cu(ppm) ₂	100	400	None

Table 10 Evaporation and deposition temperature for selected Cu(II) β-diketonate precursors.^{216, 217, 236}

*Refer to **Table 9** for precursor composition.

2.2.4.1.3 Other copper(II) Precursors

To overcome the possible incorporation of fluorine contaminants, further work into substituting the fluorine containing ligands for ester groups was carried out.²³⁷

Figure 39 shows the basic structure of Cu(II) bis(β-diketoesterates) whilst **Table 11** highlights the precursors reported in literature.

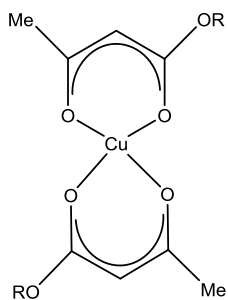


Figure 39 Ester functionalised Cu(II) bis(β -diketoesterates) precursor.

Compound	R
Cu(mtac) ₂	CH ₃
Cu(etac) ₂	CH ₂ CH ₃
Cu(tbac) ₂	C(CH ₃) ₃
Cu(beac) ₂	CH ₂ Ph
Cu(meta) ₂	CH ₂ CH ₂ OCH ₃

Table 11 Ester functionalised Cu(II) β -diketonate precursors.

The ester functionalised Copper (II) precursors have been shown to successfully deposit copper metal. Plasma enhanced CVD has been used with the Cu(etac)₂ precursor and a conducted copper film has been grown at 240°C²³⁸. Cu(meta)₂ has shown deposition at temperatures as low as 160°C.²³⁷ Adducts of the Cu(II) complexes with neutral bidentate ligands (e.g. diamines and amino alcohols) have been studied due to the unsaturated copper centre. In these complexes copper can be five (in dimers) or six (in monomers) coordinate.²³⁹⁻²⁴¹ Examples include Cu(hfac)₂(H₂NCH₂CH₂OH)²³⁹ and Cu(hfac)₂.TMEDA (TMEDA=N,N,N',N'-tetramethylethylenediamine). Most of the precursors and their use in Cu CVD have been reviewed.^{216, 217, 236} One of the most commonly reported is Cu(hfac).COD (COD=cyclo-octadiene). This is one of the compounds used within this body of work and is discussed later in **Chapter 5**. One final comment should be made on the

recent interest seen in the development of amino-alkoxides²⁴²⁻²⁴⁷, although incorporation of impurities and high resistivities leave room for development.

2.2.4.2 Atomic Layer Deposition

2.2.4.2.1 Deposition from Copper (I) Precursors

Juppó et al. trialed copper ALD using copper chloride followed by a reduction with zinc to give Cu(0).²¹⁵ For this method high temperatures of 400°C, together with films contaminated with zinc, highlighted its inadequacies for the microelectronics industry. The use of copper chloride, with hydrogen gas as the reducing agent, removed the zinc contaminate, but still, high temperatures of 300-400°C were required due to the low volatility of CuCl.²⁴⁸ For both experiments, rough films were afforded. A copper (I) β -diketonate compound, namely [ⁿBu₃P]₂Cu(acac)] has been investigated by Mueller *et al.*²⁴⁹ With a co-reagent of a mixture of water vapour and oxygen, and temperatures between 100 and 130°C, this study looked to the reduction of copper oxide films to copper metal. This was to look at the suitability for forming copper seedlayers on ruthenium. Again, the complexity of the process would make it unsuitable for large scale production.

Cu(I) amidinates, have been investigated.^{70, 250, 251} Dimeric [Cu(RNC)(CH₃)NR]₂, (where R=isopropyl), with a hydrogen co-reagent showed no deposition below 180°C. At 250°C crystallites were formed and the lack of a uniform thin film hindered further work with this precursor. Cu(I) N,N-di-sec-butylacetamidinate (**Figure 40**) was found to be the most suitable amidinate complex for Cu ALD.²⁵² It has a melting point of 77°C and reactive towards a H₂ reducing agent.

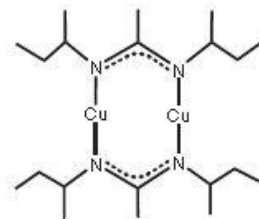


Figure 40 Structure of Cu(I) N,N'-di-sec-butylacetamidinate. ⁹¹

Continuous and conductive Cu films were deposited conformally in high aspect ratio structures (aspect ratio 35-40), at temperatures between 150-190°C on metals, oxides and nitrides. Gordon *et al.* subsequently investigated the growth mechanism using this precursor. ²⁵³ It was found that the molecule adheres to the Si-OH terminated surface through a Si-O-Cu bond, displacing one of the ligands. The subsequent hydrogen pulse removes surface ligands. The copper atoms on the surface are then free to agglomerate, exposing more Si-OH sites for further copper growth.

2.2.4.2.2 Deposition from Copper (II) Precursors

Copper (II) β -diketonate compounds have been investigated. Cu(thmd)₂ with hydrogen gas shows an ideal ALD self-limiting growth temperature window between 190-260°C and copper films with the lowest resistivity of 8.1 $\mu\Omega\text{cm}$ being produced. ²⁵⁴ Further work by Mane *et al.* using the same precursor and co-reagent, but at an increased temperature of 350°C measured a resistivity approaching that in bulk copper. ²⁵⁵ Ritala *et al.* have successfully used Cu(acac)₂ in a radical-enhanced-ALD process. ²⁵⁶ A plasma was used to generate reactive hydrogen radicals, which helped to drive down the required deposition temperatures to 140°C. Although the resistivity of the copper film was measured at 15 $\mu\Omega\text{cm}$, this process may prove unsuitable for the electronics industry as the added energy from the plasma may lead to damage to the substrate. ²⁵⁰ Cu(thd)₂ with a hydrogen reducing agent at 350°C on

SiO₂/Si resulted in the deposition of Cu predominately in the Cu(111) phase.²⁵⁵ As the number of cycles was increased, **Figure 41** is the SEM which indicates that the coalescing of islands also increased.

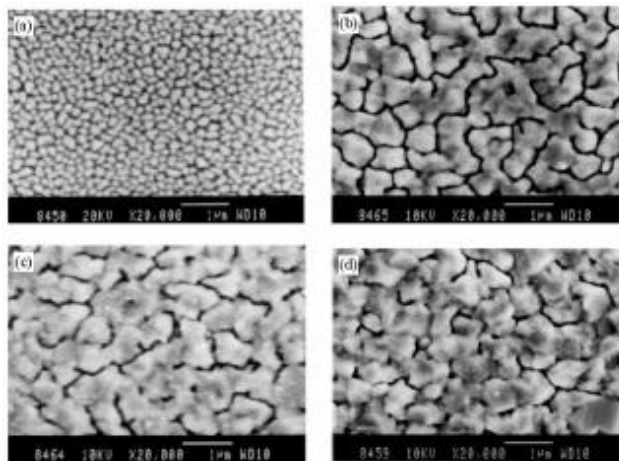


Figure 41 SEM micrographs of Cu films grown on SiO₂/Si(100) substrate with varying ALD cycles (a) 300 (b) 450 (c) 720 and (d) 1000 ALD cycles. Deposition temperature 350°C.²⁵⁵

The most encouraging results from a β -diketonate complex involved the use of Cu(hfac)₂. In a two step process, Cu(hfac)₂ and H₂O were introduced in the first step and isopropanol or formaldehyde solution was introduced in the second step.^{257, 258} At 300°C a resistivity of 1.78 $\mu\Omega$ cm was reported. Cu(hfac)₂ has also been used for Cu ALD on several substrates with hydrogen as the reducing agent. The reported growth rate was extremely low at 0.018nmcycle⁻¹.²⁵⁶ Decomposition of the β -diketonate complexes can incorporate oxygen and carbon impurities, which can degrade the film quality. All the Cu β -diketonates have low reactivity with hydrogen due to their strong Cu-O bonds leading to high deposition temperatures. The lack of reducing agents compatible with existing copper precursors, has been the limiting factor in securing an ALD process for copper deposition from Cu(II) β -diketonate compounds. In a quest to overcome this problem, more complex schemes have been

investigated. Sung *et al.* reported a multi-reagent ALD process which is summarised in **Figure 42**.²⁵⁹

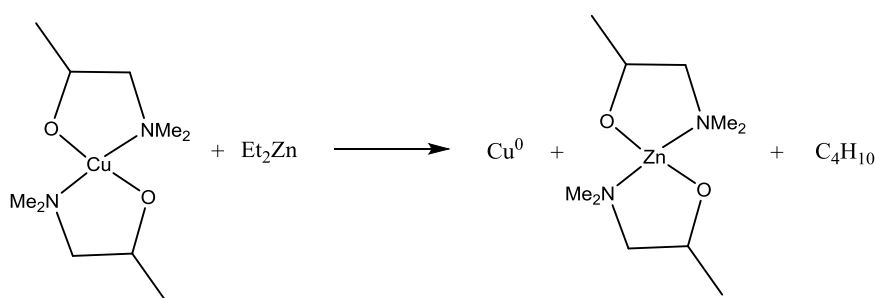


Figure 42 Reaction between [Cu(dmap)₂] and Et₂Zn.

At temperatures between 100-120°C uniform, highly conformal films of copper were deposited. However, below 100°C, condensation on the substrate occurred leading to films contaminated with zinc, carbon and oxygen, whilst above 120°C thermal decomposition of the precursor occurred. Work by Kinsley *et al.* looked at the precursor sequence using Cu[OCHMeCH₂NMe₂]₂, formic acid and hydrazine.²⁶⁰ Cu[OCHMeCH₂NMe₂]₂ is unreactive towards hydrazine but is transformed to copper (II) formate which is then reduced to copper metal by the hydrazine pulses. A deposition temperature of 120°C gave a self-limiting ALD process. XPS showed on surface impurities of oxygen and carbon, whilst XRD showed Cu films with (111), (200) and (220) planes. Measured resistivities were from 9.6-16.4 μΩcm for the temperature range 100-140°C, which can be compared to the bulk resistivity of 1.72 μΩcm.

A further comment should be made on a screening experiment conducted by Emslie *et al.*²⁶¹ They used an extensive range of Cu precursors of the type [CuL₂] (L= acac, hfac, N-isopropyl-β-ketiminate, N,N-dimethyl-β-diketiminate, 2-pyrrolylaldehyde, N-isopropyl-2pyrrolylaldiminate, N-ethyl-2-pyrrolylaldiminate and N-isopropyl-2-salicylaldiminate) dissolved in toluene and assessed the impact of adding 5 equivalents of triethylboron, trimethylaluminium and diethylzinc. These mixtures

were then subjected to temperatures of 25, 50, 75, 100 and 120°C for 24 hours. A copper precipitate was found for each solution. When this was repeated in the presence of substrates, copper films with varying amounts of carbon, oxygen, boron, zinc and aluminium were afforded. Films produced with diethylzinc at 120-150°C showed most promise, but the high contamination gave a resistivity of 89 $\mu\Omega\text{cm}$.

2.2.5 Copper Deposition for this research

From the earlier sections, it is apparent that copper metal deposition via ALD has still not been successfully achieved for industry requirements. A controllable low temperature process producing conformal, uniform, dense conductive copper films is required. SAFC Hitech formed a collaboration with the University of Bath which looked to develop complexes of the type [CpM(L)]. This has remained a less studied area of copper chemistry. For a comprehensive background of the chemistry and precursors chosen please refer to Willcocks' thesis.²⁰²

ALD precursors have historically incorporated the Cp ligand, with many metallocene-type complexes giving high volatility and thermal stability. This inherent stability is due the fact that the Cp ligands occupies 3 potential coordination sites and can bind to a metal centre through multiple molecular orbitals. It is also generally inert to electrophilic and nucleophilic attack. Cu(I) has a full d shell, so any ligand interactions are with the empty 4s and 4p orbital. Cu(II) complexes are less stable, it has 9 d-electrons in its outer shell which can be easily reduced. This can occur via two routes:

- A one-electron process with the formation of Cu(I)-R species and a radical species
- A two-electron reductive elimination process with the formation of Cu(0) and a R-R species.

The instability from the Cu(II) complexes, means that they were discounted as possible ALD sources, by the collaborators at the University of Bath. For Cu(I) the Cp adopts an η^5 bonding mode. In the notation, $[\text{CpM(L)}]$, L can be used to represent a σ -donating ligand. Isocyanides, -RNC ligands are known to form stable organometallic complexes. The resonance form for the RNC group is between a double and a triple bond. The lone pair of electrons available for metal coordination resides in the non-bonding orbital of the carbon atom. For this body of work, a Cu(II) β -diketonate $[\text{Cu}(\text{hfac})(\text{COD})]$ and a Cu(I) complex namely $\text{CpCu}(\text{}^t\text{BuNC})$ are compared. The co-reagents trialled were tertiary butylhydrazine and hydrogen plasma. A discussion is provided on chemical synthesis and characterisation, as well as subsequent film growth. ALD and CVD methods were trialled on multiple substrates.

2.2.6 Copper Oxide Deposition: Precursors and Growth

Although much work has been devoted to the growth of metallic copper thin films by ALD and CVD, very little attention has focused on the growth of copper oxides, adding further weight to the need to develop a copper precursor suitable for the conformal deposition of p-type Cu_2O material for structured PV devices.

2.2.6.1 Chemical Vapour Deposition

To achieve the aim of finding a copper precursor suitable for the ALD of copper oxides, a study of the prior literature for the deposition of copper oxides has been carried out and is detailed in the following section.

2.2.6.1.1 Copper (I) Precursors

2.2.6.1.1.1 Copper (I) oxide: Cu₂O

Development for copper oxide precursors has been ongoing. In 1993, Cu(I) complexes with trimethyl phosphite, P(OMe)₃, and aliphatic perfluorinated carboxylates (RCOO) of the type [Cu₂(P(OMe)₃)₂(μ-RCOO)₂] where R=CF₃, C₂F₅, C₃F₇, C₆F₁₃, C₇F₁₅, C₈F₁₇, C₉F₁₉ have been prepared.²⁶² Although no growth data has been presented, [Cu₂(P(OMe)₃)₂(μ-C₆F₁₃COO)₂] was suggested as the most suitable based upon thermal analysis. A complex like this is less likely to be used in the electronics industry due to manufacturing time and costs. The inclusion of P and F atoms also has the potential for film contamination.

The tetrameric alkoxide precursor, copper (I) tertiary butoxide, (Cu(O^tBu)₄), has been reported by Jefferies *et al.*²⁶³ It has a vapour pressure which is much lower than that of the copper β-diketonates as it sublimates at 110°C at 10⁻⁴ Torr. At 237°C on borosilicate glass, a film analysed by XRD as Cu₂O was deposited simply by passing the precursor over the heated substrate without co-reactant. Unfortunately, on SEM analysis, the deposited material was a mass of whiskers 0.5-0.75 μm thick and up to 35 μm long. The whiskers were not well adhered to the substrate. This poor film coverage and the low volatility of the precursor make it an unlikely source for use in industry. Interestingly, at higher temperatures, closer to 400°C, Cu metal can be deposited from this precursor, although, this too has poor film coverage, with copper island formation.

2.2.6.1.1.2 Copper (II) oxide: CuO

Copper chloride with an alternate supply of O₂/H₂O as the oxidant has been successfully used to deposit copper (II) oxide²⁶⁴ on a MgO (100) substrate at 410°C. The XRD pattern shows the expected diffractions for CuO(111) and CuO(222).

2.2.6.1.1.3 Mixed Copper Oxides

Two copper (I) precursors have been reported that can form both CuO and Cu₂O depending upon growth conditions. The first is Cu(hfa)₂.TMEDA (hfa=1,1,1,5,5,5-hexafluoro-2,4-pentanedionate, TMEDA=N,N,N',N'-tetramethylethylenediamine) which is held at a temperature of 70°C. Barreca has presented three papers on this precursor and its potential use for nanosystems for innovative gas sensors.²⁶⁵⁻²⁶⁷ The results of the findings are highlighted in the table below:

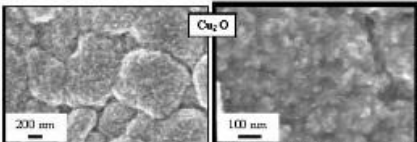
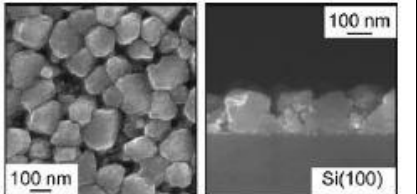
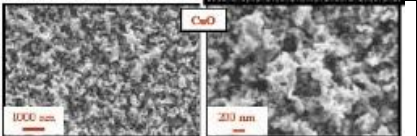
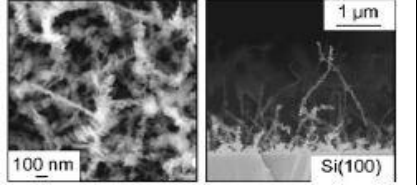
Co-reactant	Substrate	Substrate Temp. (°C)	Phase via XRD and characteristics of the films deposited	SEM image
O ₂ /H ₂ O	Alumina	350	Cu ₂ O Estimated film thickness 125nm	
	Si(100)	350	Cu ₂ O	
O ₂	Alumina	550	CuO Estimated film thickness 390nm	
	Si(100)	550	CuO	

Table 12 Controlling the copper oxide phase using either oxygen or a mixture of oxygen/water with Cu(hfa)₂.TMEDA.

From looking at the SEM images in the table, on alumina, at 350°C globular aggregates appear to uniformly cover the underlying alumina substrate. At 550°C the film morphology is markedly different and appears less densely coated with much smaller structures. On silicon substrates, the film morphology again varies drastically with temperature. The lower temperature sample again shows globular

growth but has an increased number of voids when compared to the alumina sample. At the higher temperature a much more open structure of nanowires is observed, and this is attributed to a higher surface mobility. The side branches are formed due to lattice stresses. Once again, the poor coverage of the substrates would limit its use in industry.

The second precursor is copper (I) iodide. Hong²⁶⁸ and later Ottosson²⁶⁹ detail experimental work with O₂ and O₂/N₂O oxidants respectively. Hong studied the effects of reactant concentration, reaction temperatures, reactor diameter and total reactor pressure on the growth rate. He reported the film growth observed on the walls of the reactor when deposition temperatures of 600, 700, 800°C were used. Interestingly, the species of copper oxide formed changed as the distance from the precursor inlet increased. At the inlet, a dense Cu₂O (111) film was formed, whilst downstream, a porous Cu₂O and CuO film was detected by SEM/XRD. Ottosson carried out similar work to investigate the parameters that control the phase stability based on earlier publications. CuI was heated to 500°C was reacted with O₂ or N₂O or a mixture of Ar + O₂(N₂O). The impact of altering the oxygen partial pressure is summarised in **Table 13**.

Oxygen pressure (T)	Oxygen flow (sccm)	Phase via XRD and characteristics of the films deposited
0.2	3	Cu ₂ O. Growth rate:3-13Åmin ⁻¹ . Small change in deposition temp. led to large change in growth rate.
0.5	7.5	Growth rate:13-130Åmin ⁻¹ . Maximum deposition rate approx.. 30cm from inlet. Before maximum, Cu ₂ O Observed, at maximum both Cu ₂ O and CuO and after maximum just CuO.
1.0	15	As above, but maximum more distinct with a growth rate of 180Åmin ⁻¹ . After maximum growth rate dropped to zero as CuI was depleted.

Table 13 Impact of altering oxygen partial pressure for a copper oxide film grown on single crystalline sapphire with rough reverse side upwards to enhance nucleation.

Ottosson also looked at the impact of iodine in the reaction chamber. Iodine is generated as a by-product, and it was found that the kinetics changed due to an increased iodine concentration. By repeating the above experiments but with dosing in iodine, no maximum was observed, and CuO instead of Cu₂O was the phase deposited. By using N₂O as the oxygen source, Cu₂O could be exclusively deposited at temperatures higher than 600°C.

2.2.6.1.2 Copper (II) Precursors

2.2.6.1.2.1 Copper (I) Oxide:Cu₂O

The use of copper (II) precursors for copper (I) oxide deposition is limited in the literature. Cu(dpm)₂ with oxygen has been used to successfully deposit Cu₂O on MgO substrates. The lattice mis-match between cubic Cu₂O (a=0.427nm) and MgO

($a=0.422\text{nm}$) is small, therefore MgO should be suited for the growth of high quality Cu₂O thin films. The crystallinity of the films grown increased with increasing deposition temperature, with the temperature range from 675-800°C investigated. At 790°C a growth rate of 0.25Å/s was achieved and a film morphology of islands ranging between 300-500nm in diameter. At a lower temperature of 690°C the islands are 500nm in size and in contact with one another except where micropores are present.

2.2.6.1.2.2 Copper (II) Oxide:CuO

Solvated Cu(thd)₂ has been used as a single-source CVD precursor. Klippe *et al.* documented a process by which the precursor solution is kept outside of the vacuum system in a reservoir.²⁷⁰ It is then dosed into the reactor via a mass flow controller and exposed to temperatures of 60°C to flash evaporate the solvent. Over the deposition temperature of 225-700°C CuO layers were deposited. Another β-diketonate precursor, Cu(hfac)₂, was very recently reported by Koh.²⁷¹ A variant on a CVD process, a high pressure micro-plasma jet system was used. The aim of this study was to analyse CuO nanostructures. With a N₂ co-reagent, vertically aligned monocrystalline CuO nanowires were grown on silicon with a growth rate of ~120nm/min. Conversely, when oxygen gas was used, there was a drastic change in film morphology, to larger diameter wires, with spiral like formations suggesting screw dislocation growth.

2.2.6.1.2.3 Mixed Copper Oxides

Copper β-diketonates have been used most widely in the deposition of copper oxide, although the resulting films are often mixed phase oxides. Cu(acac)₂ held at 175°C and used with oxygen was used to deposit onto MgO (good lattice match) an Al₂O₃ (cheap, transparent and standard) substrates.²⁷² They report no film growth below

350°C, and no significant effect on layer growth in the temperature range 350-500°C. On sapphire substrates, by controlling the oxygen flow they could choose the copper oxide formed; low oxygen flows (20sccm) gave Cu₂O, whilst at high flows (150sccm) CuO was deposited. MgO substrates showed that the Cu₂O was the dominant phase. Morphology of the film was dependent on the substrates. All films grown were polycrystalline and ranged in thickness from 60-90nm (25±5nm/hour). The layers on sapphire were unordered nanocrystalline structures, whilst on the MgO larger grains with diameters ranging 0.5-1.0µm were formed. The same precursor was used previously by Holzschuh.²⁷³ In a high temperature, plasma enhanced process, by control of the bias of the plasma and the substrate temperature, using the same precursor, carrier gas, power density and pressure it was possible to deposit either mixed CuO and Cu₂O, solely Cu₂O, Cu or CuO films by varying the substrate temperature to 300°C, 400°C, 500°C, 500°C with a large negative bias respectively. Controlling the bias helped to prevent oxygen deficiencies in thin films even at high deposition temperatures. Valtierra *et al.*²⁷⁴ also report the CVD of this precursor, via an atmospheric method. This group used fiberglass as the substrate, and the influence of the substrate temperature was again analysed and is summarized in the **Table 14**:

Deposition Temperature (°C)	Phase via XRD and characteristics of the films deposited
320	Light brown film, Cu ₂ O, crystallites of 83Å
325	Dark brown film, 6CuO.Cu ₂ O, crystallites of 70 Å
340	Grey film, CuO, crystallites of 79Å

Table 14 Cu(acac)₂ used for copper oxide deposition on fibreglass at various substrate temperatures.

Interestingly, the group report the deposition of $6\text{CuO}\cdot\text{Cu}_2\text{O}$ from $330\text{-}340^\circ\text{C}$ and for this phase both SEM and AFM show uniform complete coverage of the fiber glass with smooth and regular crystallites.

Maruyama investigated another β -diketonate precursor namely, $\text{Cu}(\text{thd})_2$ which was held at 220°C .²⁷⁵ Oxygen gas was used as the oxidant in an atmospheric pressure CVD process. Borosilicate glass was used as the substrate and deposition trialled at 300 and 500°C . Similarly to the methods already described, the formation of Cu_2O or CuO was obtained by adjusting the oxygen partial pressure. At higher partial pressures, monoclinic CuO formed, whilst at lower pressures, cubic Cu_2O was predominant. Interestingly the surface morphology for CuO alters with reaction temperature. Whilst at 300°C the films exhibits a coarse three-dimensional network structure, the film deposited at 500°C shows a much more 3D-like stack of angular lumps.

A final copper source worth mentioning is aqueous cupric nitrate, $\text{Cu}(\text{NO}_3)_2$.²⁷⁶ A flame assisted CVD process for a substrate temperature range of 100 and 400°C enabled the deposition of copper oxide thin films. Again the film morphology is dependent upon the substrate temperatures. At 200°C island growth with particle diameters $102\text{-}173\text{nm}$ was observed. At 300°C the islands appeared to coalesce and form a continuous film, which, by 400°C , has returned back to an island formation, note though, this time with an increased particle size ($229\text{-}323\text{nm}$) but with a large separation. The authors attribute this to mostly Cu_2O at low temperatures and CuO at higher temperatures which was confirmed by XRD. Mixed phase CuO copper was detected at 200°C , mixed $\text{CuO}/\text{Cu}_2\text{O}$ at 300°C and by 400°C , only CuO reflections were observed.

2.2.6.2 Atomic Layer Deposition

For the development of materials for the nanostructure PV cell, ALD is the deposition method of choice to coat 3D ZnO NW to maximise the surface area of the pn junction and thus maximise efficiency. ALD methods are rarely reported in previous research.

2.2.6.2.1 Copper (I) Precursors

Waechtler and co-workers investigated the ALD of the liquid precursor bis(tri-n-butylphosphane)-copper(I)acetylacetonate **Figure 43**.²⁷⁷

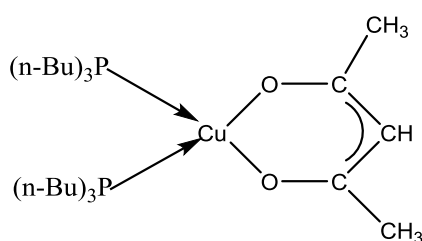


Figure 43 Structure of $[(n\text{Bu}_3\text{P})_2\text{Cu}(\text{acac})]$.

Previously, this source was used to deposit Cu via thermal disproportionating in CVD at 220°C .²⁷⁸ Waechtler reports that with wet oxygen as a co-reagent, and ALD process at temperatures of $<160^\circ\text{C}$, yielded Cu_2O on Ta, TaN, Ru and SiO_2 substrates. Ru has the lowest temperature window with ALD at 100°C . TaN and SiO_2 showed a continuous film between $110\text{-}125^\circ\text{C}$, whilst on the Ta substrate isolated clusters and some continuous films were obtained at 135°C . This non-uniform growth was attributed to precursor decomposition. In addition to this work, Mueller²⁴⁹ used this ALD process to study the reduction of copper oxide films to copper metal. With the help of formic acid, at temperatures less than 130°C , on Ru substrates successful reduction to copper metal was achieved. Due to the catalytic effect of Ru, films were then grown which incorporated a Ru precursor (1 mol %),

$[(\text{I})^5\text{-C}_5\text{H}_4\text{SiMe}_3)(\text{I})^5\text{-C}_7\text{H}_{11})\text{Ru}]$, and used formic acid, to grow copper on a range of substrates including TaN, Ni and Co.

Recent work by Muñoz-Rojas *et al.* reports the use of (trimethylvinylsilyl)hexafluoroacetylacetonato copper(I), Cu(I)(hfac)(TMVS) , (CupraselectTM Air Products and Chemicals Inc.) held at 65°C, with water as the oxidizer.²⁷⁹ The substrates used were borosilicate glass at temperatures between 150 and 350°C and also plastic substrates (PEN films from Dupont) at 150 and 200°C. The achieved growth rate was $\sim 1\text{nm}\cdot\text{min}^{-1}$. Cu_2O films were grown on both substrates using atmospheric ALD in the temperature range of 150-225°C. The application of copper (I) precursors in the deposition of CuO appeared lacking from a literature survey.

2.2.6.2.2 Copper (II) Precursors

Copper (II) precursors are reported in literature for the deposition of CuO only, not Cu_2O . Alnes *et al.* have reported the use of $\text{Cu}(\text{acac})_2$ with ozone for the deposition of copper (II) oxide.²⁸⁰ They report an ALD window of 150-230°C with a growth rate of $\sim 0.04\text{nm}/\text{cycle}$, however the uniformity and surface roughness was much better at lower temperatures.

2.2.7 Copper Oxide Deposition for this research

The copper precursors $\text{Cu}(\text{hfac})(\text{COD})$ and $\text{CpCu}(\text{tBuNC})$ were used to try to deposit copper oxide layers. Water, ozone and oxygen plasma were studied as co-reagents. **Chapter 5** presents the results from the experimental work.

2.2.8 Copper Oxide Nanowires

Although not directly relevant to the research here, like zinc oxide, nanostructures of copper oxide can be deposited. Cuprous oxide (Cu_2O) and cupric oxide (CuO)

nanowires have become more important in the study of energy conversion and optoelectronic devices. Although the properties of these materials are well suited to the end applications, large-bulk synthesis routes have yet to be established. A recent review by Filipič and Cvelbar provides an extensive overview into copper oxide nanowires and the growth methods employed.²⁸¹ The NWs can be produced using different approaches e.g. wet chemical, electrochemical, hydrothermal and thermal oxidation methods, and as such the NWs can have different lengths, diameters, morphologies or even chemical composition. Copper oxide NWs can be Cu₂O or CuO, they can be single-crystalline, or polycrystalline or even a mixture of a crystalline material with an amorphous sheath²⁸². For NWs to be incorporated into commercial devices, they must be produced quickly, controllably and in large quantities. The advantages of NWs have been highlighted previously in **Chapter 1**. The large surface area can lead to a higher absorption of photons in PV devices which results in greater efficiency. Similarly, for sensors, the increased surface area means a higher probability of species absorption which leads to a better response. Cu₂O nanowires have been reported to have a slightly higher band gap of 2.69eV when compared to bulk thin film Cu₂O at 2.2eV. This can be understood on the basis of quantum size effect which arises due to a very small size of nanostructures in one dimension.²¹² Copper oxides NW were not investigated as part of this study, however, the possibility opens up the potential of inverting the system highlighted previously in **Figure 13** i.e. copper oxide nanowires conformally coated with a n-type ZnO layer.

Chapter 3 Experimental Methods

3.1 Chemical Characterisation

3.1.1 ¹H Nuclear Magnetic Resonance (NMR)

NMR is a phenomenon that occurs when the nuclei in an atom are held in a static magnetic field and exposed to a second oscillating field. Only nuclei with spin are affected by the magnetic field. Protons, electrons and neutrons all have the spin property, which comes in multiples of $\frac{1}{2}$ and can be either plus or minus. For NMR we look only to the nuclei of the atom, so in the case of ¹H NMR, hydrogen (¹H) has one proton resulting in a net spin of $\frac{1}{2}$. In NMR it is the unpaired spin that is important. When placed in a magnetic field of strength B, a particle with a net spin can absorb a photon, of frequency ν . The frequency ν depends on the gyromagnetic ratio (ratio of the magnetic dipole moment to the angular momentum), γ of the particle,

Equation 22:
$$\nu = \gamma B$$

Nucleons fill orbitals like electrons, and as nucleons possess spin, they pair up as the orbitals are filled and if there are two spins of opposite sign, they can cancel each other out. When the nuclei are exposed to the external magnetic field, it can be thought of as a magnet, the spin vector aligns with the magnetic field. The low energy state is when the poles are aligned N-S-N-S and the high energy state is N-N-S-S. A transition between the two energy states can occur on absorption of a photon. The energy of the absorbed photon must exactly match that of the energy difference in the two states.

The energy, E , of a photon is related to its frequency, ν , by Planck's constant ($h = 6.626 \times 10^{-34} \text{ m}^2 \text{ kg / s}$).

Equation 23:
$$E = h \nu$$

In NMR, ν is referred to as the resonance frequency. Using equation 22 and 23 the energy of the photon needed to cause a transition between the two spin states is:

Equation 24:
$$E = h \gamma B$$

In NMR the frequency is often in the range of 60-800MHz for H nuclei. In this body of work a Varian 400MHz NMR was used to study ^1H NMR. The NMR chemical shift allows us to distinguish magnetically un-equivalent nuclei in a molecule. Hydrogen atoms in the molecule feel different magnetic fields depending upon their location and the neighbour they are directly attached to. The nuclei of a molecule will always feel the effect of the outer electrons, and thus, the field felt by the nucleus isn't equal to the applied external magnetic field. The difference between the external magnetic field and the field felt by the nucleus is very small and measured in ppm (parts per million). This small difference is termed shielding. Shielding is a barrier made of inner-shell electrons and it decreases the pull of the nucleus on the outer electrons. Shielded protons are normally found upfield, towards 0ppm, in NMR spectra. Conversely, deshielded protons are found downfield, towards 10ppm. This is when the chemical shift of a nucleus has been increased due to removal of electron density (due to electronegative atoms), magnetic induction, or other effects. Also, anisotropy, due to magnetic fields generated by p bonds, can impact deshielding. **Figure 44** presents an overview for the chemical shifts observed for protons.

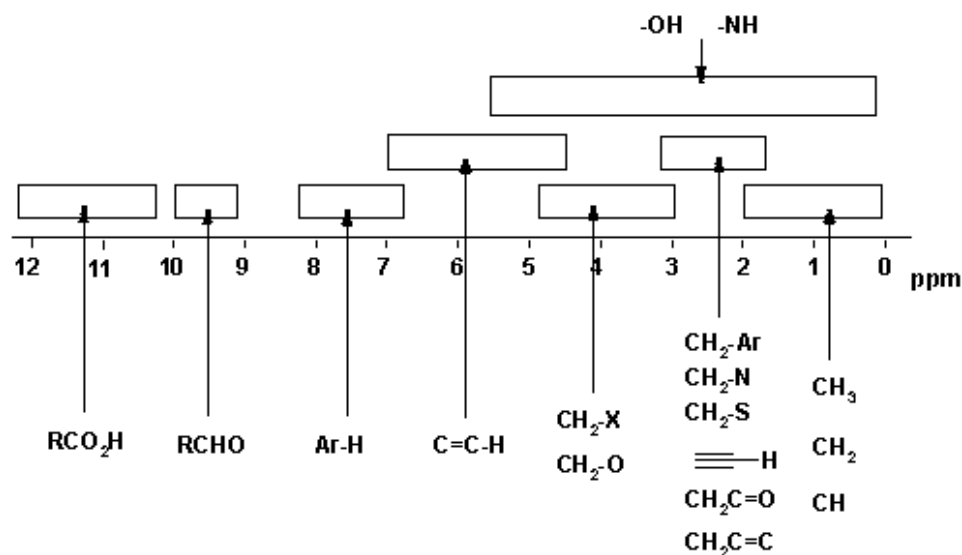


Figure 44 Overview of expected proton chemical shifts. Note that the figure shows the typical chemical shifts for protons being influenced by a single group²⁸³.

When a ^1H NMR is completed for a compound, a standard reference is used to help assign peaks. In the case here, deuterated benzene, (C_6D_6) is used as a reference. The sample is dissolved in deuterated benzene which has a ‘heavy’ hydrogen, with the nucleus containing one proton and one neutron. A characteristic peak at 7.15ppm appears in the NMR to which, then all other protons can be referenced. In NMR spectra the area of a peak, i.e. its integral, is proportional to the number of Hs that the peak represents. NMR spectra usually have peaks that appear as groups of peaks due to coupling with neighbouring protons. Coupling arises because the magnetic field of vicinal (adjacent) protons influences the field that the proton experiences. The coupling rules are:

- The proximity of "n" equivalent H on neighbouring carbon atoms causes the signals to be split into "n+1" lines. This is known as the multiplicity or splitting or coupling pattern of each signal.
- Equivalent protons (or those with the same chemical shift) do not couple to each other.

If the neighbours are not all equivalent, more complex patterns arise. The coupling constant, J (usually in frequency units, Hz) is a measure of the interaction between a pair of protons. In a vicinal system of the general type, $H_a-C-C-H_b$ then the coupling of H_a with H_b , J_{ab} , must be equal to the coupling of H_b with H_a , J_{ba} , therefore $J_{ab} = J_{ba}$. The implications are that the spacing between the lines in the coupling patterns are the same. The relative intensities of the lines in a coupling pattern are given by a binomial expansion or more conveniently by Pascal's triangle. To derive Pascal's triangle, starting with the number 1 at the top of the triangle, each lower row is generated by adding the two numbers above and to either side in the row above together, this is shown in **Figure 45**.

n	$(n+1)$	multiplicity	relative intensities	multiplet name
0	1		1	singlet
1	2		1:1	doublet
2	3		1:2:1	triplet
3	4		1:3:3:1	quartet
4	5		1:4:6:4:1	quintet
5	6		1:5:10:10:5:1	sextet
6	7		1:6:15:20:15:6:1	septet
7	8		1:7:21:35:35:21:7:1	octet

Figure 45 Coupling patterns with relative intensities for 1H NMR for n proton neighbours.²⁸⁴

So for H-NMR a proton with zero neighbours, $n = 0$, appears as a single line, a proton with one neighbour, $n = 1$ has two lines of equal intensity, a proton with two neighbours, $n = 2$, has three lines of intensities 1 : 2 : 1, etc. In reality, coupling patterns are often more complex than the simple $n+1$ rule since the neighbouring protons are often not equivalent to each other (*i.e.* there are different types of neighbours) and therefore couple differently. In these cases, the " $n+1$ " rule has to be refined so that each type of neighbour causes $n+1$ lines. For example for a proton with two types of neighbour, number of lines,

$L=(n_1+1)(n_2+1)$. However, in many cases the lines overlap with each other and the result is further distortion from the "ideal" pattern. Coupling patterns involving aromatic or alkene protons are often complex.

3.1.2 Inductively Coupled Plasma (ICP)

ICP is a method of detecting trace impurities within chemical samples. A plasma is a highly energized 'cloud' of gaseous ions and their electrons. An ICP can be generated by coupling the energy of a radio frequency generator into a suitable gas, usually argon. This coupling is achieved by generating a magnetic field by passing a high frequency electric current through a cooled coil. This inductor generates a rapidly oscillating magnetic field orientated in the vertical plane of the coil. The plasma is initiated by seeding the argon gas with electrons via such means as a spark. The electrons are then accelerated in the magnetic field, rapidly reaching the ionization energy. This process combined with collision of argon atoms make the plasma self-sustaining. As the electrons and ions are under the influence of the magnetic field, the flow is directed. The high temperature of the plasma (upto 10,000K) ensures complete atomization, ensuring elemental analysis can be determined. There are two types of ICP analysis that were used within this body of work: ICP-Mass Spectrometry (*ICP-MS*) is based on the production, sampling and mass filtering of positive ions. This is shown schematically in **Figure 46**.

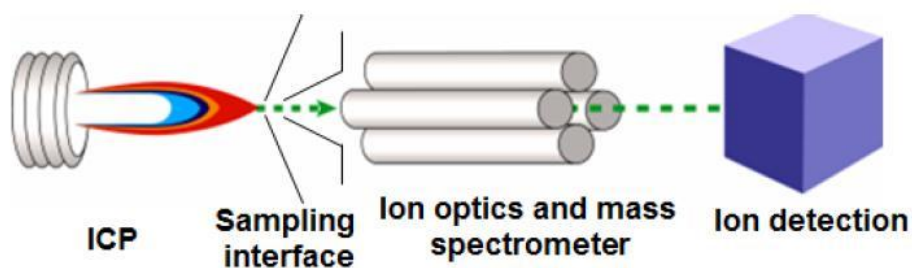


Figure 46 Schematic for ICP-MS. ²⁸⁵

The chemical to be analysed is diluted in water. Calibration standard solutions for the potential impurities are also made in water to enable a comparison to be drawn. The sample is introduced into the plasma as a fine aerosol. Resultant spectrum of transmitted masses reflects the isotope pattern of each element and the signal intensity is proportional to concentration. ICP-Optical Emission Spectrometry (*ICP-OES*) is where the atomised sample is passed through a spectrometer and a detection system. This is shown as a process flow in **Figure 47**.

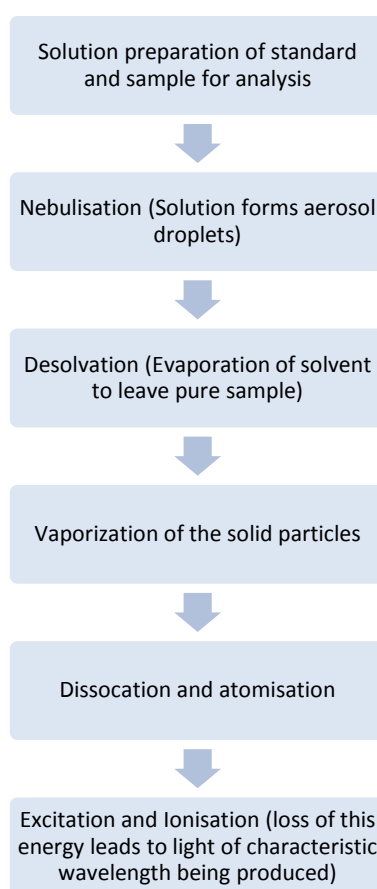


Figure 47 A flow chart defining ICP-OES analysis. ²⁸⁵

The MS technique is much more sensitive than OES with a detection limit range of 0.1ppb (parts per billion) to 1 ppm (parts per million) for most metallic elements. For OES the detection limit ranges from 10ppb (for elements such as Si, Mg, Cd, Y, Mn) to 0.5ppm (for Al, Sn, S, Te, Se). Advantages of the OES method include the fact that samples can be run in organic solvents and non-metals can be

detected. The analysis time is generally shorter as there is less sample preparation required. It is also much easier to clean the equipment from heavily contaminated samples. The equipment used was a Varian 725ES Radial View, ICP-OES and a Thermo X series quadrupole ICP-MS.

3.1.3 Thermogravimetric Analysis: TGA

The method for TGA has been discussed previously in **section 1.10.2**. During this scope of work, a TA Instruments Q500 machine with the evolved gas analysis furnace was used, note however, no mass spectrometer or infra-red analyser was used. The standard run conditions are listed below:

- Heat Rate: 10°C / min
- Temp Range: 25 – 550°C (actual sample finish temperature is around 530°C)
- Nitrogen gas flow over sample: 90ml / min
- O₂ Levels in box nitrogen: < 10 ppm
- Pans: Aluminium
- Typical Sample Size: 10 – 50mg

3.1.4 Vapour pressure

The vapour pressure technique has previously been discussed in **section 1.10.2**.

Figure 48 is a photograph the system built in-house with the assistance of MKS instruments.



Figure 48 The vapour pressure system at SAFC Hitech.

All details are provided from an SAFC Hitech publication.²⁸⁶ The key sections of the system are located inside an oven to ensure uniform heating of all parts is achieved to prevent condensation issues. The sample chamber is attached to a vacuum manifold equipped with a BaratronTM pressure measurement gauge and a second BaratronTM is located outside the oven along with the computer connections etc. The construction material is stainless steel with high integrity joints throughout. The sample for study is placed in the test chamber and vacuum applied to remove inert atmosphere process gas. It should be noted that out gassing from the sample is of critical importance when investigating vapour pressure measurement, especially in the less than 1Torr range. The trial temperature is established and pressure readings taken over several minutes to establish an accurate, stable value. Once three steady readings have been recorded the temperature is raised and allowed to equilibrate before repeating the process to get a second point. The temperature is raised again to get a third and so on until a maximum temperature is reached.

3.1.5 Crystal Structures

Crystal structure data was collected by Dr. Steiner and Dr. Basca at the University of Liverpool using a Bruker D8 diffractometer with an APEX CCD detector, and 1.5 kW graphite monochromatic Mo radiation. Specific details for each structure are given within the experimental section of each results chapter.

3.2 Thin Film Deposition

3.2.1 Reactors

3.2.1.1 LI-MOCVD

Figure 49 below shows the modified Aixtron 200 FE Liquid Injection MOCVD²⁸⁷ reactor used for both the zinc oxide and the copper/copper oxide deposition work from the DMZn.L and Cu(hfac)COD precursors respectively.

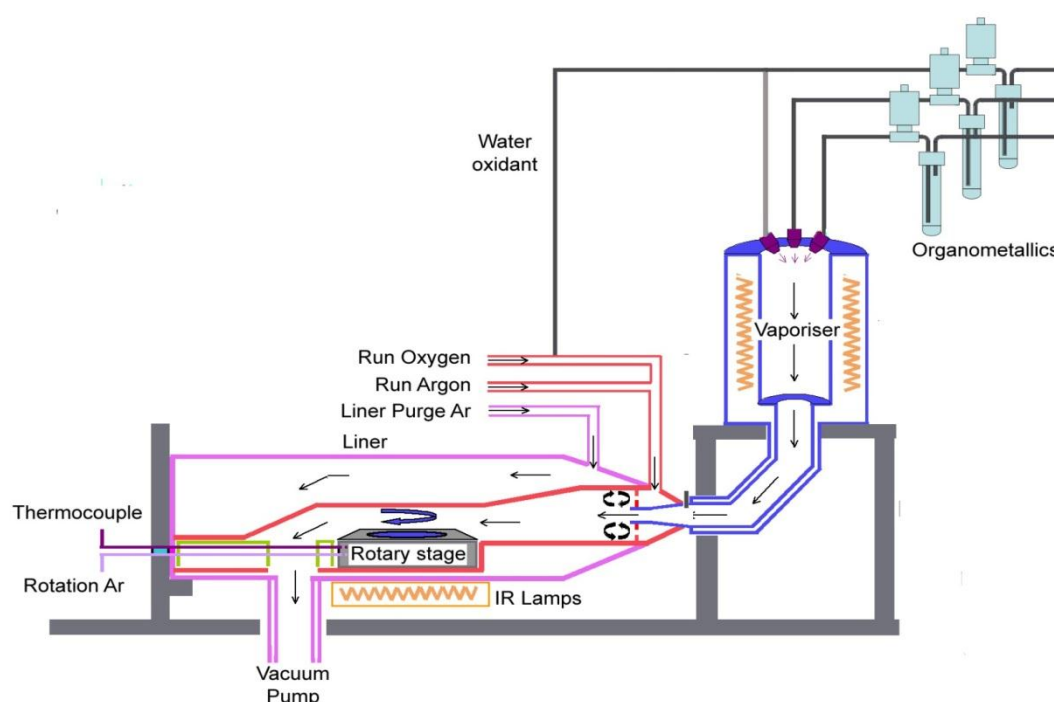


Figure 49 Aixtron reactor used for LI-CVD.

The organometallic/solvent precursor is charged into a glass bottle (shown on the right hand side of the diagram). These bottles are at room temperature enabling thermally sensitive materials to be used. The bottles can be exposed to both vacuum and argon, ensuring the lifetime of the precursor is maximized. A continual purge of argon is used so no pressure difference is observed on closing/opening valves. The precursor is injected into the quartz horizontal CVD reactor via a Jiplec Triject ® system. The injectors are based upon car fuel injectors and are solenoid valves

which can be controlled to meter and spray precursor into the vaporiser (maximum temperature 250°C) in a controlled manner. Each injector tip is supplied with a stream of heated argon carrier gas to assist with vaporization. Cooling is incorporated to ensure the injector is kept at a temperature of 50°C (for the experimental work here), to help prevent solvent boil-off and thus the injector blocking. This temperature also ensures condensation is prevented which could result in precursor droplets rather than spray leading to uncontrollable growth.

Moving through the reactor to look at the deposition zone is the graphite stage which can house a 2 inch diameter wafer. The stage can be rotated using argon gas, with the aim being to try to increase uniformity of growth across the wafer. The stage is heated by infra-red lamps, with control over the temperature range (100-525°C). This is held within a quartz liner within a vacuum vessel. This is to help with ease of maintenance. Gases and by-products can pass through a water filled filter to help condense material before it reaches the vacuum pump. The reactor pressure is controlled by a butterfly valve on the pump. All gas flows within the reactor are controlled by mass flow controllers (MFCs). For deposition work involving ZnO NW's and some copper/copper oxide the Aixtron reactor was used. Experimental details and reactor parameters are given in the results chapter within each section.

3.2.1.2 ALD/CVD

An Oxford Instruments OpAL reactor, **Figure 50**, was used for the copper and copper oxide deposition.

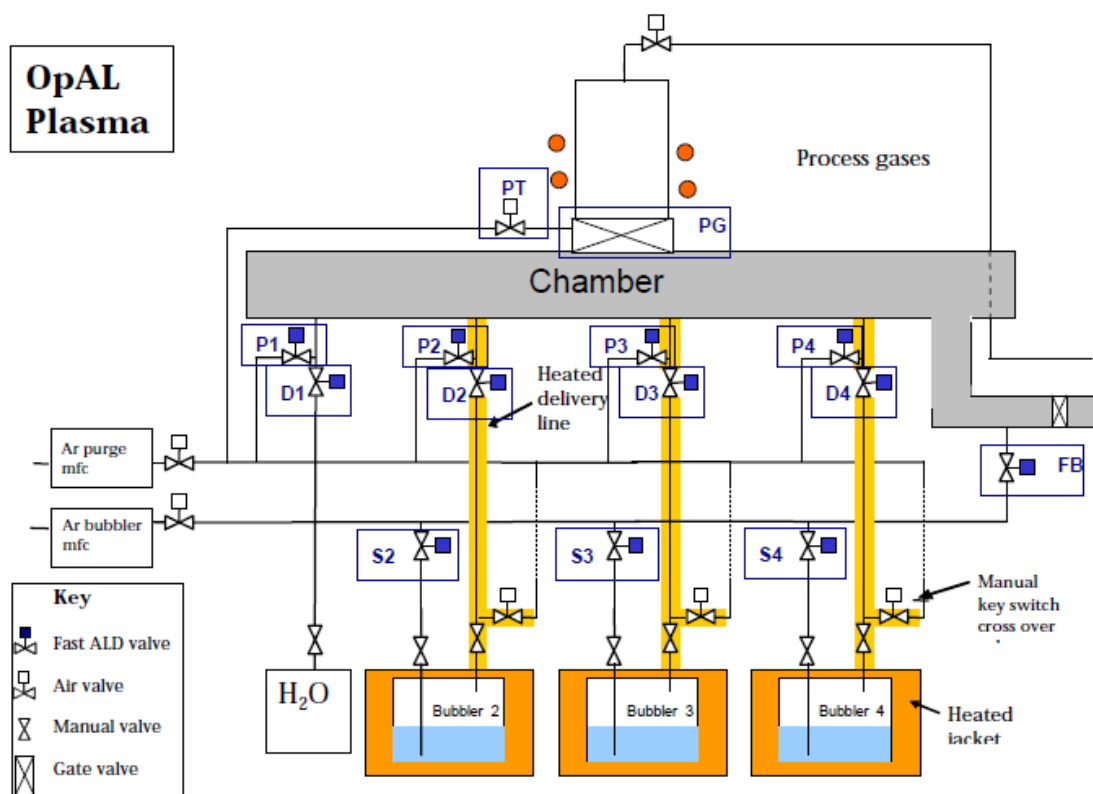


Figure 50 OpAL ALD Reactor.²⁸⁸

This reactor can house four precursors simultaneously. Each has its own heater jacket complete with trace heating on inlet pipes to the reactor chamber. The temperature can reach 200°C. Each source can also be bubbled using argon or nitrogen carrier gas. The chamber can hold substrates up to a diameter of 200mm and, due to the inner clearance, 3D substrates can be coated. The wafer stage temperature can be controlled in the range 25-400°C. The reactor runs at a base pressure of 10^{-3} Torr. There is a pot available to use water as the co-reagent. The system at Liverpool has a remote plasma unit, shown in **Figure 51**.

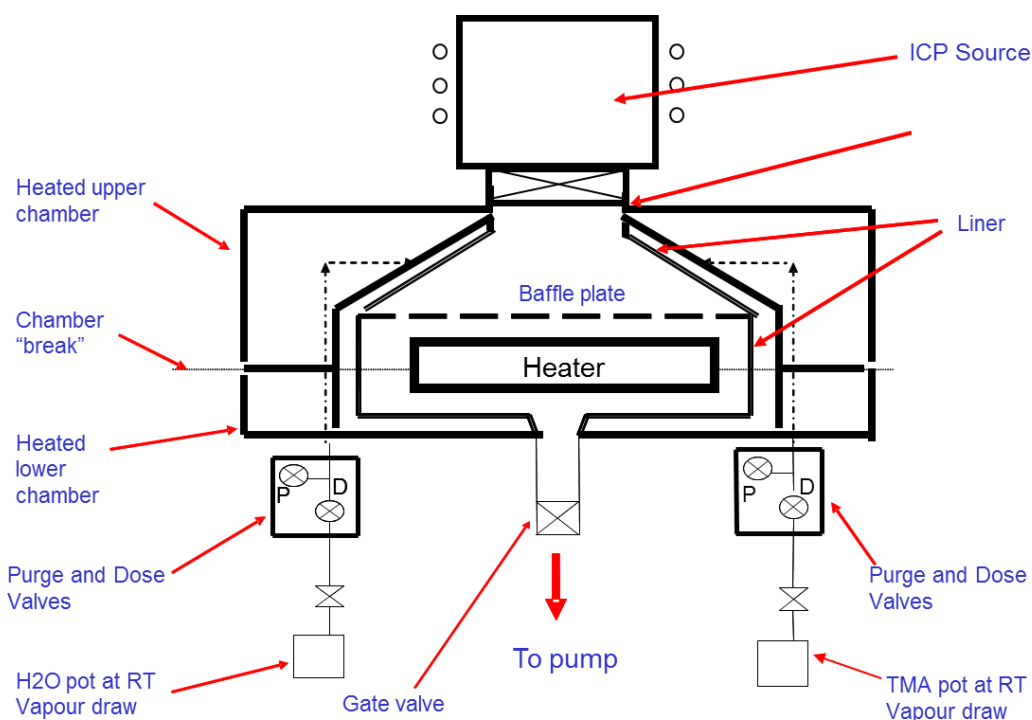


Figure 51 Plasma unit of OpAL ALD reactor. ²⁸⁸

The plasma helps to generate radicals and ions which are more reactive than conventional co-reagents. This can help to drive down the processing temperature for ALD and often increase growth rates. Often, plasma can also help to generate higher quality films with fewer impurities. The literature review in **Chapter 2** shows how hydrogen and nitrogen plasma has been successfully employed in the deposition of metal films. The plasma can also be used to clean the chamber and to prepare the substrate surface. As this is a remote plasma system, the film quality is further improved as there is a lower risk of plasma damage, a higher control of the plasma leading to an increased plasma density with an increased number of radical species. For the work presented, the OpAL reactor was employed in copper/copper oxide deposition using water, tertiary butyl hydrazine and oxygen, and hydrogen plasma. Again, each chapter contains information on experimental details and reactor parameters.

3.3 Thin Film Characterisation

3.3.1 X-ray Diffraction (XRD)

X-ray diffraction has been used to study the films grown to help to identify the crystal structures. **Figure 52** shows how two incident parallel rays of light are diffracted by two adjacent layers of atoms separated by a distance d (termed d -spacing). When the rays are in-phase on leaving the film, a higher amplitude wave results and conversely, when they are out of phase the wave has a much lower amplitude.

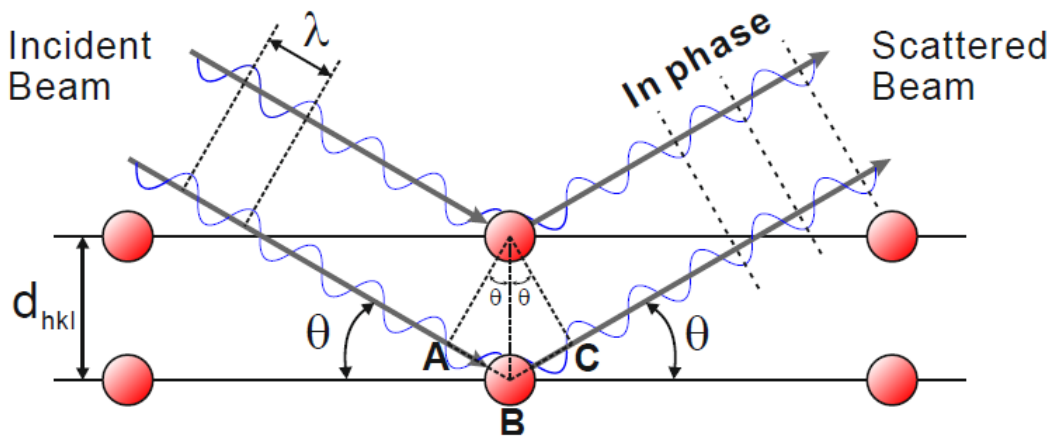


Figure 52 X-Ray diffraction. ²⁸⁹

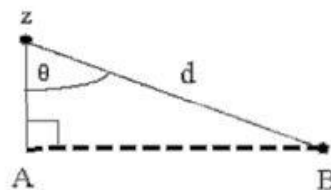
For the two exit waves to constructively interfere:

Equation 25: $n\lambda = AB + BC$

But knowing $AB = BC$

Equation 26: $n\lambda = 2AB$

Also as



Equation 27: $\sin\theta = \frac{AB}{d}$

Rearranging gives:

Equation 28: $AB = d\sin\theta$

Therefore, using equations 23 and 25 Bragg's Law is formulated.

Equation 29: $n\lambda = 2d\sin\theta$

Where: n=integer

λ =radiation wavelength

d=atomic spacing (Å)

θ =diffraction angle (°)

To carry out this technique, the wavelength of the radiation used must be smaller than the d-spacing. Metal sources are used to generate X-rays of different wavelengths. By detecting and plotting the intensity and angle of the exit rays, it is possible to determine if a material is regularly ordered i.e. crystalline, calculate d-spacing and by comparing the results with a standard database, determine structure and phase. Recording emitted X-ray intensity as a function of angle yields diffraction peaks which correspond to lattice planes. Miller indices can be used to identify these planes. A Miller index is defined as the reciprocal of the fractional intercepts which the plane makes with the crystallographic axes. It is more easily described using an example. **Figure 53** highlights a unit cell complete with axis and axial length identified.

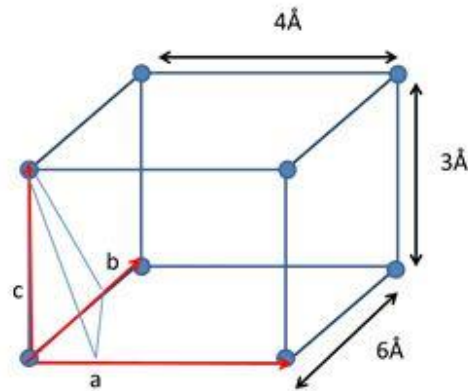


Figure 53 Miller Indices.

To determine the Miller indices for the plane identified in the figure:

Axis	a	b	c
Axial length	4Å	6Å	3Å
Intercept length	1Å	3Å	3Å
Fractional intercepts	1/4	3/6=1/2	3/3=1
Miller indices	4	2	1

A plane parallel to an axis has an intercept at infinity and the Miller index is zero. Also, if the plane intercepts the axis at a negative value, the Miller index can have a bar above the number to indicate this. In this thesis, the XRD diffraction patterns will be annotated with the Miller index values. XRD measurements throughout were made on a Rigaku Miniflex diffractometer using water cooled Cu target $K\alpha$ radiation ($\lambda=1.5405\text{\AA}$, 40kV, 50mA). Scans between 5° and 150° 2θ are possible at speeds down to a minimum of $0.01^\circ/\text{minute}$ in continuous mode. The angle measured experimentally between incident and diffracted beam is 2θ rather than θ due to the geometry of the diffractor assembly. The diffractometer has a detector set on a goniometer arm and the specimen stage and detector arm move together to form the angles scanned. The technique results in no damage to the specimens but is limited to 15mm^2 .

3.3.2 Raman

Raman spectroscopy is a non-destructive technique which can provide information on the physical structure and phase of a material as a result of the inelastic scattering of light. When a photon of visible light that is too low in energy to excite an electronic transition interacts with a molecule, it can be scattered and therefore retains its incident energy. Rayleigh scattering arises from transitions that start and finish from the same vibrational energy level. Stokes Raman scattering arrives from transitions which start at the ground state vibrational energy level and finish as higher vibrational energy level, the photon has lost energy to the molecule. Anti-Stokes Raman scattering involve a transition from a higher to a lower vibrational energy level, the photon has gained energy. Since molecular energy levels are quantised this produces discrete lines from which we can gain information on the molecule itself. This is shown schematically in **Figure 54**.

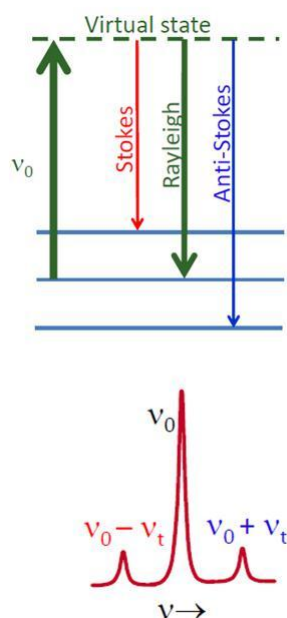


Figure 54 Raman scattering modes. ²⁹⁰

The Raman shift depends on the energy spacing of the molecules' modes. However not all modes are "Raman active" i.e. not all appear in Raman spectra. For a mode to be Raman active it must involve a change in the polarisability, α of the molecule. This can be caused by vibrational, rotational and electronic modes. Theory can regard the scattering molecule as a collection of atoms undergoing simple harmonic vibrations and takes no account of quantisation of the vibrational energy. If the molecule is placed in an electric field, its electrons are displaced relative to its nuclei and therefore it develops an electric dipole moment. The induced dipole moment μ_i is proportional to the field strength ε :

Equation 30:
$$\mu_i = \alpha\varepsilon$$

A fluctuating electric field produces a fluctuating dipole moment of the same frequency. The electromagnetic radiation is responsible for the generation of the electric field and this can be expressed as:

Equation 31:
$$\varepsilon = \varepsilon^0 \cos 2\pi t v_0$$

Where: ε^0 is the equilibrium field strength

v_0 is the angular frequency of the radiation.

In this study, Raman experiments were conducted by Dr Peter King using a Renishaw Compact System 100. The apparatus consists of an optical microscope and several laser sources, from which the beam is focused through a series of optics. The laser focuses on a specimen surface at the same point the visible light comes into focus. A choice of lasers are available, with a 325nm HeCd ultra-violet (UV) and an Argon ion (Ar+) laser at 514.53nm most useful for thin-film analysis. The spectrometer sweeps a wavenumber range with the time spent and number of acquisitions per wavenumber band set before operation. Experimental parameters are given within the experimental details section of each chapter.

3.3.3 Scanning Electron Microscopy (SEM)

The scanning electron microscope (SEM) uses a focused beam of high-energy electrons to generate a variety of signals at the surface of solid specimens. The signals that derive from electron-sample interactions reveal information about the sample including external morphology, chemical composition, and crystalline structure and orientation of materials making up the sample.

A beam of electrons is produced at the top of the microscope by an electron gun. The electron beam follows a vertical path through the microscope, which is held within a vacuum. The beam travels through electromagnetic fields and lenses, which focus the beam down toward the sample. Accelerated electrons in an SEM carry significant amounts of kinetic energy and this energy is dissipated as a variety of signals produced by electron-sample interactions when the incident electrons are decelerated in the solid sample. These signals include secondary electrons (that produce SEM images), backscattered electrons, (used to determine crystal structures and orientations), and photons (characteristic X-rays that are used for elemental analysis). Secondary electrons and backscattered electrons are commonly used for imaging samples: secondary electrons are most valuable for showing morphology and topography on samples and backscattered electrons are most valuable for illustrating contrasts in composition.

For this research, SEM imaging was employed to reveal surface morphology and was conducted by Dr. Simon Romani, Dr Kerry Abrams, Dr Tobias Heil or Dr Karl Dawson. For the copper metal and oxide analysis a Jeol 7001F SEM and a FEI Helios 600i FIB SEM was used. For the zinc oxide analysis imaging was conducted by both Dr Matt Werner and myself with a field emission Hitachi S-2460N SEM, at an acceleration voltage of 20 kV. For the later SEM, wafer sections were divided

and mounted with conductive tape onto the goniometer stage of the microscope, enabling the samples to be examined in all directions.

3.3.4 Energy Dispersive X-ray (EDX)

Elemental analysis is possible due to the unique characteristic X-ray emissions that occur from the inelastic interaction of the electron beam in an SEM with individual atoms. This phenomenon arises when a high-energy beam electron penetrates and interacts with the inner shell electrons of the atom. During this interaction, if sufficient energy is transferred to one of the core electrons, the electron is ejected and the atom is left in an excited state. In order to return to its ground state, the hole is filled by one of the outer shell electrons and to ensure the energy is conserved, an x-ray is emitted. The energy of this emission is characteristic of the difference in energy of the two electron shells involved and thus is unique to the atom or element. In thin film analysis, the peaks for all elements present, including the substrate, will be observed. EDX does have limitations. It is more sensitive to higher atomic number elements than lower atomic number elements e.g. carbon and oxygen.

3.3.5 Transmission Electron Microscopy (TEM)

TEM was used to gain information on film morphology and crystalline phase, as well as film thickness. This technique uses transmitted electrons which pass through the sample, limiting specimen thicknesses to a few hundreds of nanometres. For TEM analysis of this work, TEM grids were placed in the reactor during depositions. Although this does not fully replicate the film deposited on the various substrates, it negates the need for time intensive sample preparation. TEM beam energy is much higher (50-300keV) than SEM since the incident electrons require higher energy to pass through the sample. Elastic scattering of electrons in crystalline materials give rise to characteristic diffraction patterns, whilst both elastic

and inelastic effects are used to generate TEM images in either bright or dark field. When an image is formed using the central spot from the direct beam, a bright field image is seen. Low atomic number elements scatter electrons through a smaller angle, so these appear light in an image; whereas, higher atomic number elements scatter electrons at higher angles and so appear darker. By contrast, when some or all of the scattered electrons are used we generate a dark field image. This examines higher angles of electron scattering, where low atomic number elements appear dark, and higher atomic number elements appear light. To choose which electrons form the image, an aperture is inserted thus blocking out most of the diffraction pattern except that which is visible through the aperture, this is often dependent upon sample composition.

For this research, TEM imaging was conducted by Dr. Simon Romani, Dr Kerry Abrams, Dr Tobias Heil or Dr Karl Dawson. The TEM used was a Jeol 2100F TEM.

3.3.6 Energy Electron Loss Spectroscopy (EELs)

EELs measures any changes in energy when electrons pass through a sample. Elastic scattering occurs when the electron interacts with atomic nuclei. As the nucleus is highly charged, the electric field felt by the electron is large, resulting in high angles of scattering. Inelastic scattering occurs when the incident electrons interact with the atomic electrons in the sample. Sometimes, this can promote an inner shell electron to a higher empty orbital, which, at some time will decay back down to its ground state and emit the excess energy as e.g. an xray or to another atomic electron (Auger electron). If the incident electron collides with an outer shell electron, there may be enough energy to emit the outer electron, resulting in the release of a secondary electron.

The secondary processes of electron and photon emission from a specimen can be studied in detail by appropriate spectroscopies. In EELs the primary process of electron excitation, which results in the fast electron losing a characteristic amount of energy is studied. The transmitted electron beam is directed into a high-resolution electron spectrometer that separates the electrons according to their kinetic energy and produces an electron energy-loss spectrum showing the number of electrons (scattered intensity) as a function of their decrease in kinetic energy. An EELs spectra often has a 'zero loss' peak in which the electrons pass straight through the sample with no change in energy. Inner shell excitations are observed as sharp edges, with the sharp rise occurring at the ionization threshold. This is where the energy-loss is approximately the binding energy of the corresponding atomic shell. Since inner-shell binding energies depend on the atomic number of the scattering atom, the ionization edges present in an energy-loss spectrum reveal which elements are present within the specimen. If the energy-loss spectrum is recorded from a thin sample, each spectral feature corresponds to a different excitation process. In thicker samples, there is a substantial probability that a transmitted electron will be inelastically scattered more than once, giving a total energy loss equal to the sum of the individual losses.

For the work presented within this thesis, EELs spectra were recorded by Dr Tobias Heil on copper samples of less than 80nm. The IMFP of copper for the used electron energy of 200kV is 96nm.²⁹¹

3.3.7 Auger Electron Spectroscopy (AES)

Auger Electron Spectroscopy (AES) is an analytical technique that uses a primary electron beam to probe the surface of a solid material. The basic Auger process starts with removal of an inner shell atomic electron to form a vacancy. Several processes

are capable of producing the vacancy, but bombardment with an electron beam is the most common. The inner shell vacancy is filled by a second atomic electron from a higher shell. Energy must be simultaneously released. A third electron, the Auger electron, escapes carrying the excess energy in a radiationless process. The process of an excited ion decaying into a doubly charged ion by ejection of an electron is called the Auger process. As described, the Auger process requires three electrons, thus we cannot detect H or He but can detect all other elements from Li and up. Secondary electrons that are emitted as a result of the Auger process are analysed and their kinetic energy is determined. The identity and quantity of the elements are determined from the kinetic energy and intensity of the Auger peaks. The nature of the Auger surface analysis process is such that Auger electrons can only escape from the outer 5-50 Å of a solid surface at their characteristic energy. This effect makes AES an extremely surface sensitive technique. A finely focused electron beam can be scanned to create secondary electron and Auger images, or the beam can be positioned to perform microanalysis of specific sample features.

AES was carried out as part of the previous work by Black¹⁹⁶. AES data were excited using the 325nm wavelength from a He-Cd laser. The atomic compositions quoted in **Chapter 4** are from the subsurface of the nanowire structures, and were obtained by combining AES with sequential argon ion bombardment until comparable compositions were obtained for consecutive data points. Compositions were based on a ZnO powder reference.

3.3.8 Photoluminescence (PL) Spectroscopy

Photoluminescence (PL) spectroscopy is a contactless, nondestructive method to probe the electronic structure of materials. Photoluminescence occurs when an external source of energy, in the form of electromagnetic radiation, is absorbed by

an atom. If a light particle (photon) has an energy greater than the band gap energy, then it can be absorbed and thereby raise an electron from the valence band up to the conduction band across the forbidden energy gap. In this process of photoexcitation, the electron generally has excess energy which it loses before coming to rest at the lowest energy in the conduction band. At this point the electron eventually falls back down to the valence band. As it falls down, the energy it loses is converted back into a luminescent photon which is emitted from the material. Thus the energy of the emitted photon is a direct measure of the band gap energy. The PL spectrum often reveals spectral peaks associated with impurities contained within the host material. The high sensitivity of this technique provides the potential to identify extremely low concentrations of intentional and unintentional impurities that can strongly affect material quality and device performance. The quantity of PL emitted from a material is directly related to the relative amount of radiative and nonradiative recombination rates. Non-radiative rates are typically associated with impurities and thus, this technique can qualitatively monitor changes in material quality as a function of growth and processing conditions. A PL spectrum was collected as part of the work of Kate Black on ZnO NWs. PL data were acquired using a Jobin-Yvon LabRam HR consisting of a confocal microscope coupled to a single grating spectrometer equipped with a notch filter and a CCD camera detector. All of the spectra were recorded in a backscattering geometry.

3.3.9 Ellipsometry

Ellipsometry measures a change in polarization as light reflects or transmits from a material structure. The polarization change is represented as an amplitude ratio, Ψ , and the phase difference, Δ . The measured response depends on optical properties and thickness of individual materials. Thus, ellipsometry is primarily used to

determine film thickness, and thus, quantifying growth rates as well as optical constants. A schematic of a nulling ellipsometer is shown in **Figure 55** .

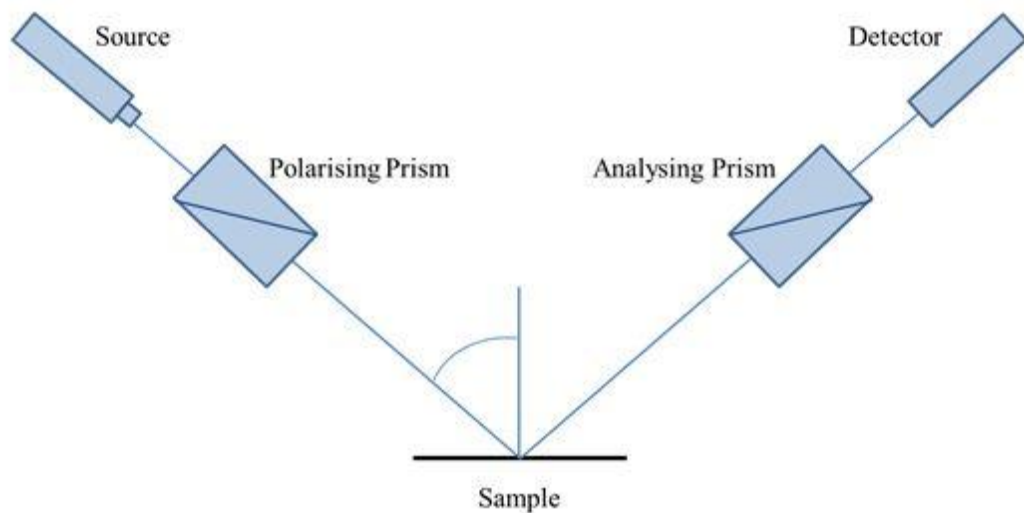


Figure 55 A simplified schematic representation of an ellipsometer.²⁹²

When undertaking measurements, the results are interpreted on the basis of model calculations. The equipment alters the polariser and analyser to find parameters for which a null result is gained, i.e. when light is extinguished at the detector. A Rudolph Auto EL-IV null ellipsometer was used to determine film thickness. A source of light with wavelength of 632.8nm was typically used for this work. The ellipsometer was calibrated daily using a standard silicon oxide sample of known thickness and refractive index. For samples, a thickness measurement was recorded both before and after deposition. For depositions involving zinc and copper oxide, ellipsometry was an extremely useful, non-destructive technique. For metallic films, as the film thickness increases so too does the opacity. If the ellipsometer incident light does not reach the lower interface, having more material does not change the measured quantity. This led to the need to use weight gain measurements to determine film thickness for some deposited samples.

3.3.10 Film thickness from weight gain measurements

The average film thickness can be determined by measuring the weight gain of a wafer during coating and inputting this into equation 32

Equation 32:
$$t_a = \frac{10^7 W_w}{\rho A_w}$$

Where: t_a is the average film thickness (nm)

W_w is the weight gain of the deposited sample (g)

A_w is the area of the substrate (cm²)

ρ is the film density (taken from literature) (g/cm⁻³).

Potential errors for this technique arise from

- weighing-error of the weigh scale is ± 0.001 g.
- area-due to the range of substrates used for this work, the area and shape of such substrates varied dramatically.
- film composition and density-deposited samples may vary from those reported in the literature due to reactor conditions and parameters. These sources of variation are not always possible to quantify accurately.

Within the experimental sections, the method chosen for film thickness analysis will be justified and described, and the possible errors accounted for.

3.3.11 Four point probe

A four point probe is a simple apparatus for measuring the resistivity of semiconductor samples. By passing a current through two outer probes and measuring the voltage through the inner probes, the substrate resistivity can be determined. Electrical resistivity measurements were made with a four-point probe system comprising a Lucas Signatone Corp SP4 Four Point Probe Head and a Keithley Series 2400 SourcemeterVR.

Chapter 4 Zinc Results and Discussion

4.1 Overview

The overall thesis aim, given in **section 1.6**, can be further cascaded for zinc precursor development and subsequent zinc oxide deposition studies. The objectives included:

- the development of a commercially viable precursor for the MOCVD of ZnO nanostructures with full characterisation
- to gain an understanding of the reaction mechanism in the MOCVD process and how the deposition mechanism is altered by e.g. temperature, pressure, precursor, and co-reactant
- full analysis of the deposited ZnO

The research carried out on dialkylzinc and dialkylzinc adducts and the use of them within MOCVD has proven vital to the developments within its field. The following references are the peer reviewed papers published during the time-span of this work.^{102, 106, 293, 294} This chapter details work from these publications carried out by K. Black and S. Ashraf, along with my personal input of precursor development and characterisation and some deposition studies. From precursor synthesis and characterisation, to zinc oxide deposition and final film analysis, all data is included here for to help draw comparisons and conclusions.

4.2 Dialkylzinc Precursor Characterisation

4.2.1 Dialkylzinc Crystal Structures

Although R_2Zn ($R=Me, Et$) compounds have been used extensively in both chemical synthesis and thin film deposition, the solid-state structure of these species have remained elusive. Within the scope of the work undertaken for this body of research,

the need to obtain the crystal structures of the parent alkyls was revisited. Crystal structures were carried out by Dr John Bacsá, Dr Aggí Steiner, Felix Hanke, with computational analysis completed by Dr George Darling all at the University of Liverpool. It was found that Me_2Zn undergoes a phase transition giving rise to a high and low-temperature phase, named $\alpha\text{-Me}_2\text{Zn}$ and $\beta\text{-Me}_2\text{Zn}$ respectively. Both forms of Me_2Zn and Et_2Zn contain linear diorganozinc molecules, which interact via weak interactions with small covalent contributions, these are discussed in the following text.

4.2.1.1 Diethylzinc

Large single crystals of Et_2Zn were formed when a capillary containing the compound was gradually cooled to 100K in the cold stream on the X-ray Diffraction equipment. From looking at **Figure 56**, a tetragonal body-centred unit cell is observed with space group symmetry $I4_1md$. Looking to the centre ball-and-stick model, note how the zinc atom and the four carbon atoms are co-planar and display C_{2v} symmetry. The C-Zn-C bond angle deviates slightly from the ideal 180° at $176.2(4)^\circ$. Also, note how the ethyl groups are in a mutually cis-position (bond angle $115.9(4)^\circ$). The Zn-C bond measures $1.943(5)\text{Å}$, marginally longer than in Me_2Zn (see **section 4.2.1.2 and 4.2.1.3**).

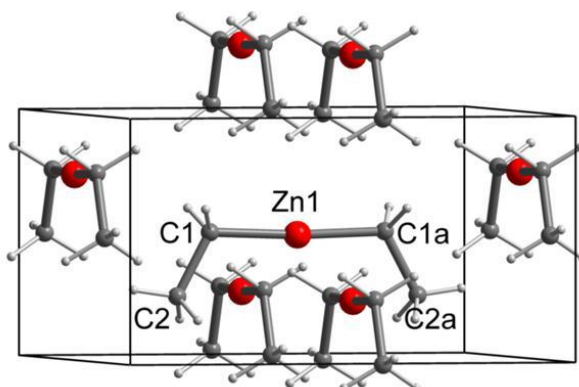


Figure 56 X-ray crystal structure of Et_2Zn .

Looking at the packing of the molecule, **Figure 57**, all the ethyl groups face in one direction along z , and each molecule has eight neighbours to which is aligned orthogonally. The Zn atom has neighbouring groups consisting of two CH_2 and two CH_3 groups in its intermolecular environment.

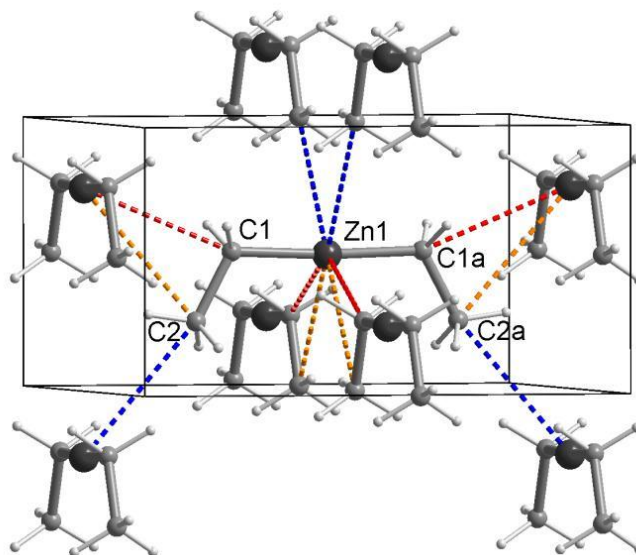


Figure 57 Packing diagram of Et_2Zn . Shortest intermolecular Zn-C distances: 3.254(6) Å (red), 3.482(6) Å (orange), 3.504(6) Å (blue).

A computational study, using density functional theory, was carried out on this structure¹⁰² which shows the crystals are held together by weak interactions of Van der Waals forces.

4.2.1.2 α -Dimethylzinc

The crystal structure of the high-temperature phase of dimethylzinc (α -Me₂Zn) was achieved by gradually cooling a sample to 200K to produce a single crystal. **Figure 58**, shows the tetragonal unit cell observed.

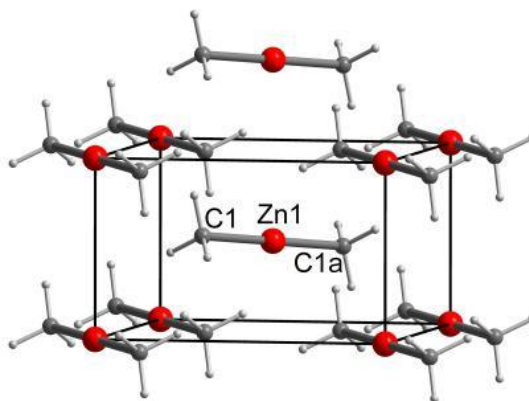


Figure 58 X-ray crystal structure of α -Me₂Zn.

A good agreement with the gas phase structure^{98, 100, 101} was observed when refinement was used. From looking at the central structure within **Figure 58**, the two methyl groups adopt a staggered conformation. The C-Zn-C is perfectly linear at 180°, with a bond length of 1.926(6)Å. **Figure 59** shows that each zinc atom is surrounded by four methyl groups of neighbouring molecules with two shorter and two longer methyl-Zn distances (3.490(7) and 3.709(7)Å) respectively.

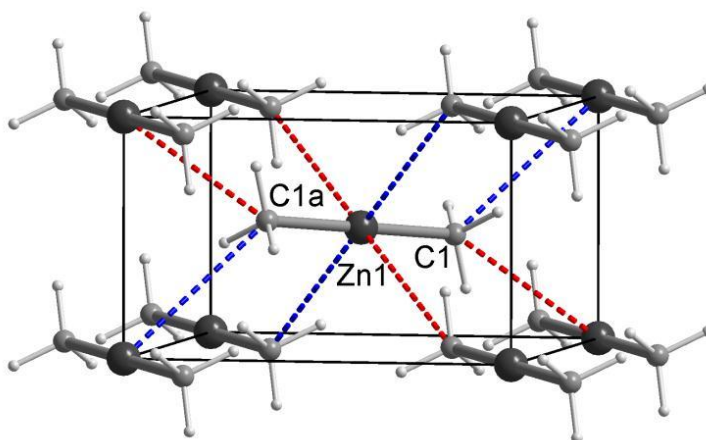


Figure 59 Interactions between α -Me₂Zn molecules. Shortest intermolecular Zn...C distances: 3.491(7) Å (red), 3.708(7) Å (blue)

The molecules stack along the c-axis and can adopt two tilt-orientations as shown in **Figure 60**, constructed with the help of computation.

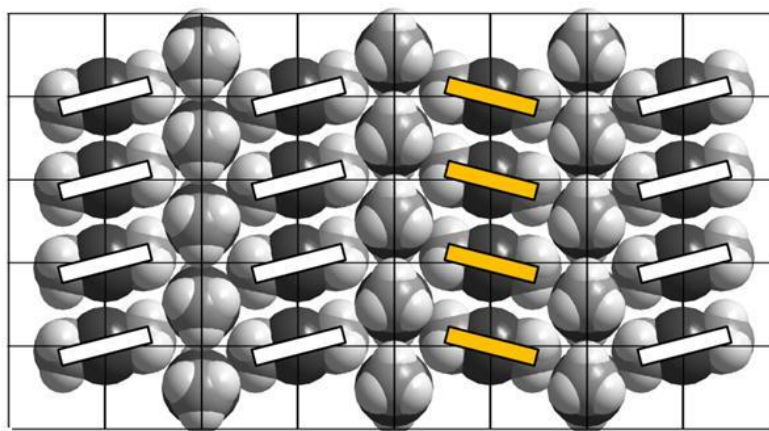


Figure 60 Disorder of stacks in α -Me₂Zn.

Crystal packing diagrams of α -Me₂Zn are shown in **Figure 61**.

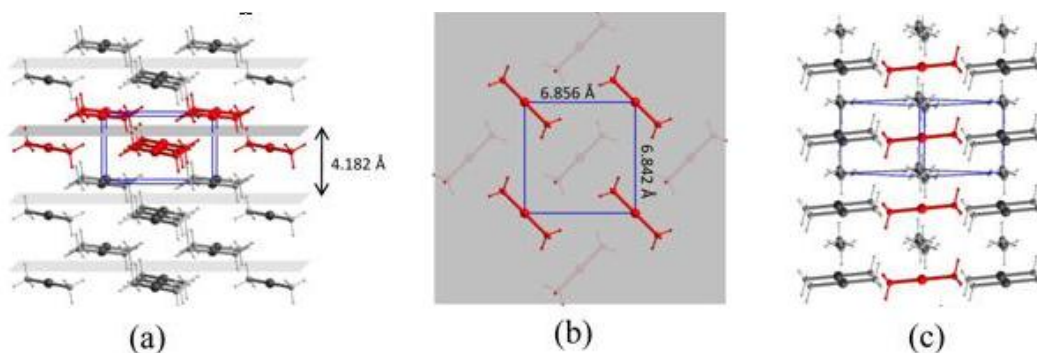


Figure 61 Crystal packing diagrams of α -Me₂Zn (a) view along the a-axis, (b) view onto the ab plane, (c) view along [110].

In (a) and (b) the mean planes through the layers of molecules are shown in grey and one layer is highlighted in red, (c) highlights the stacking of molecules along *c*; such stacks are shown in red. The structure of α -Me₂Zn features molecules of two orientations that are perpendicular to each other, but these are arranged in alternate layers.

4.2.1.3 β -Dimethyl Zinc

Single crystals of the low temperature form were obtained at 150K. The resultant structure is shown in **Figure 62**.

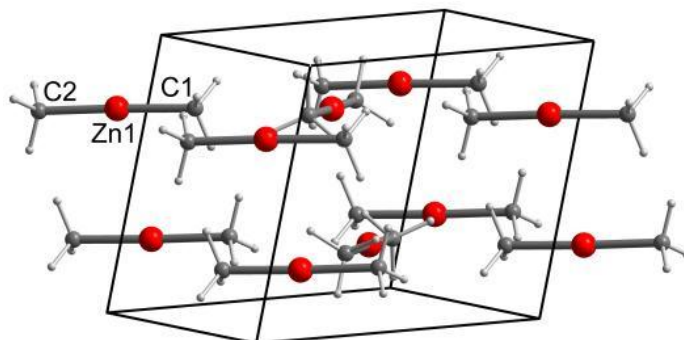


Figure 62 X-ray crystal structure of β -Me₂Zn.

The β -phase exhibits a monoclinic unit cell of space group symmetry $P2_1/n$ containing four molecules. The molecule deviates slightly from linear with a bond angle of $178.2(6)^\circ$ and with Zn-C bond lengths of $1.911(14)\text{\AA}$ (Zn1-C1) and $1.920(13)\text{\AA}$ (Zn1-C2).

From **Figure 63**, each zinc atom forms two interactions with methyl groups of neighbouring molecules showing intermolecular distances of Zn1-C1 at $3.327(14)\text{\AA}$ (red), Zn-Zn at $3.424(14)\text{\AA}$ (orange), Zn1-C2 at $3.455(15)\text{\AA}$ (blue).

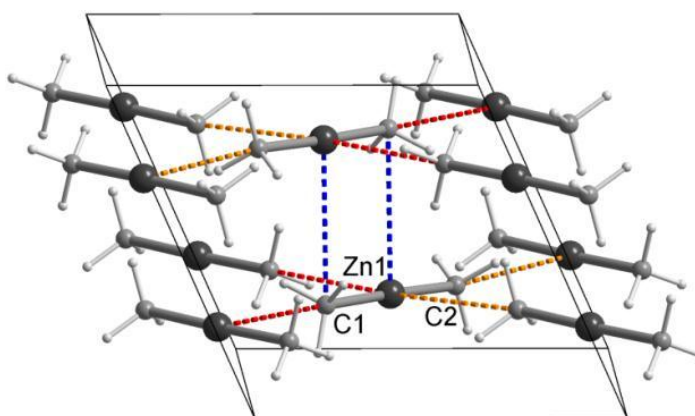


Figure 63 Interactions between β -Me₂Zn molecules.

For this phase, the layers are stacked upon one another such that the Me_2Zn molecules of adjacent layers align in parallel, this can be seen in **Figure 64**.

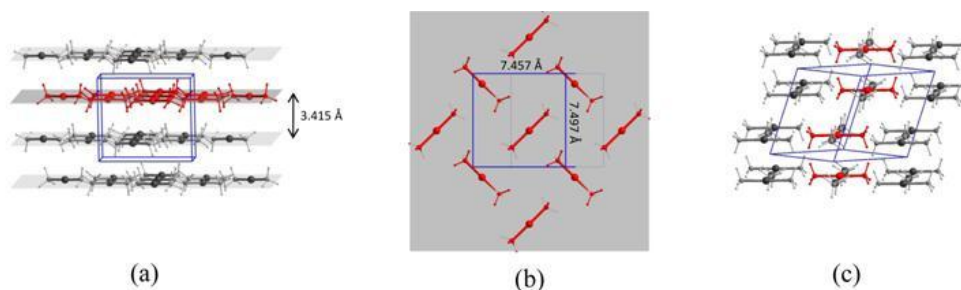


Figure 64 Crystal packing diagrams of $\beta\text{-Me}_2\text{Zn}$ (a) view along the a -axis, (b) view onto the ab plane, (c) view along $[110]$.

$\beta\text{-Me}_2\text{Zn}$ forms compact layers parallel to the ab -plane, which are more or less planar. These layers contain molecules aligned in two different orientations perpendicular to each other forming T-shaped interactions which yield a square grid type of layer arrangement. While $\beta\text{-Me}_2\text{Zn}$ forms more compact layers in the form of a planar square grid in the ab -plane, these layers are stacked in lower symmetric fashion along the c -direction, in contrast to $\alpha\text{-Me}_2\text{Zn}$.

Table 15 helps to summarise some important parameters gained from the crystal structures of the dialkyl zincs.

Compound	Et ₂ Zn	α-Me ₂ Zn	β-Me ₂ Zn
Chemical formula	C ₄ H ₁₀ Zn	C ₂ H ₆ Zn	C ₂ H ₆ Zn
Formula weight	123.49	95.44	95.44
Temperature (K)	100	200	150
Crystal system	Tetragonal	Tetragonal	Monoclinic
Space group	<i>I4₁md</i>	<i>P2₁/n</i>	<i>P2₁/n</i>
<i>a</i> (Å)	9.893(7)	6.849(4)	7.457(13)
<i>b</i> (Å)	-	6.842(5)	7.497(14)
<i>c</i> (Å)	5.300(4)	4.182(3)	7.484(13)
<i>β</i> (°)	-	89.970(11)°	114.12(3)
<i>V</i> (Å ³)	518.8(6)	196.2(2)	381.9(12)
<i>Z</i>	4	2	4
<i>ρ</i> (calc)/gcm ⁻¹	1.581	1.616	1.660
<i>R</i> 1 (<i>F</i> > 4σ(<i>F</i>))	0.0320	0.0197	0.0566

Table 15 Key parameters for the crystal structures of diethyl and dimethyl zinc.

4.3 Dialkylzinc Adduct Precursor Synthesis

The instantaneous reaction of dimethylzinc with oxygen can be problematic during MOCVD, the reaction can occur before the precursor reaches the reaction zone, which can lead to particulates forming, injectors blocking and uncontrollable composition and film thickness. To try to combat these problems, and knowing that nitrogen donor ligands had been extensively and successfully used by Jones and co-workers (**Chapter 2**), the research presented here involves the use of oxygen donor adducts. In the MOCVD process the aim was to understand if the ligand did play a part in the deposition mechanism, and if so, was it a beneficial advantage. Pre-reaction needed to be prevented, whilst volatility was needed. Both mono and bidentate ligands were trialled and are shown in **Table 16**, The aim was to understand the Zn-O bonding, and the steric implications of aliphatic (e.g. DMOE) versus cyclic monodentate (e.g. THF) versus cyclic bidentate (e.g. 1,4-dioxane) ligands.

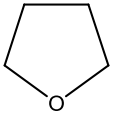
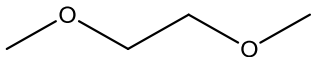
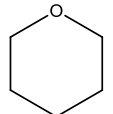
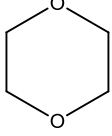
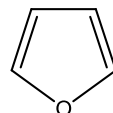
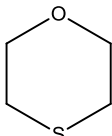
Monodentate	Bidentate
Tetrahydrofuran (THF) 	1,2-dimethoxyethane (DMOE) 
Tetrahydropyran (THP) 	1,4-dioxane 
Furan 	1,4 thioxane 

Table 16 Ligands used for DMZn.L adduct synthesis

4.4 Dialkylzinc Adduct Precursor Characterisation

The dimethyl zinc adducts were synthesised according to the experimental details given in **section 4.8.1**. ^1H NMR was used as a tool to help confirm if the ligand added co-ordinated to the zinc centre. For this study, TMS was used as the reference due to the potential overlap of $\text{C}_6\text{D}_6/\text{THF}$ peaks at $\sim 7\text{ppm}$. The blue spectra in **Figure 65** shows the ^1H NMR recorded when the DMZn.THF was dissolved in TMS solvent. Alternatively, the red spectra shows the peaks obtained when THF was sealed in a capillary tube and placed within an NMR tube containing DMZn and TMS.

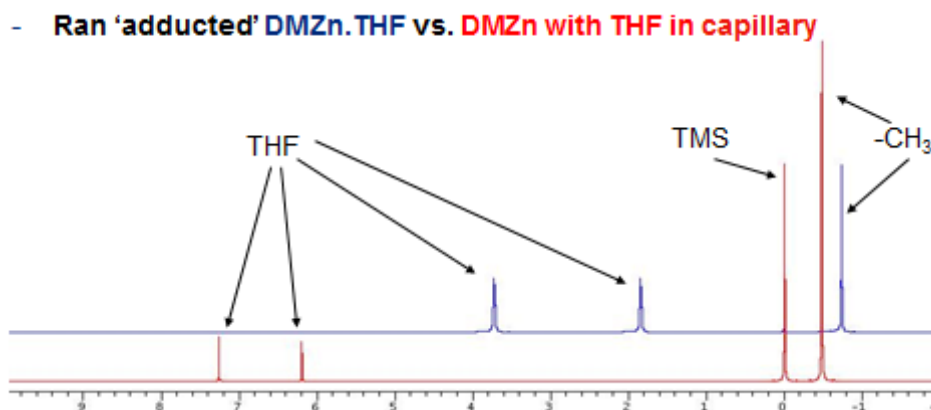


Figure 65 ^1H NMR spectra of DMZn.THF to analyse ligand co-ordination in the case of DMZn.THF.

For the DMZn.THF sample, the THF peaks occur at around 1.8ppm and 3.7ppm. This is markedly different to that of the THF held in a capillary tube. The THF maintains its expected position (aromatic compound with an oxygen atom) at 6.2 (OCH₂) and 7.2ppm.(CH₂CH₂). This is indicative that co-ordination is taking place. When the ligand is placed in proximity to the DMZn, there is a shift in the THF peak to a more upfield position due to the increased electron density provided by the zinc centre. The NMR also helps to show that it's a high purity compound as additional peaks are absent.

4.4.1 Dimethylzinc Adduct Crystal Structures

Although diemthylzinc adduct complexes have previously been reported, structural data was absent from the literature. The crystal structures of the dimethylzinc adducts are now reported and these represent the first structurally characterised dialkylzinc-ether complexes.

4.4.1.1 Dimethylzinc.tetrahydropyran

On trying to obtain a crystal structure for the monodentate tetrahydropyran ligand, the oxidation product^{112, 113} **Figure 66** was obtained.

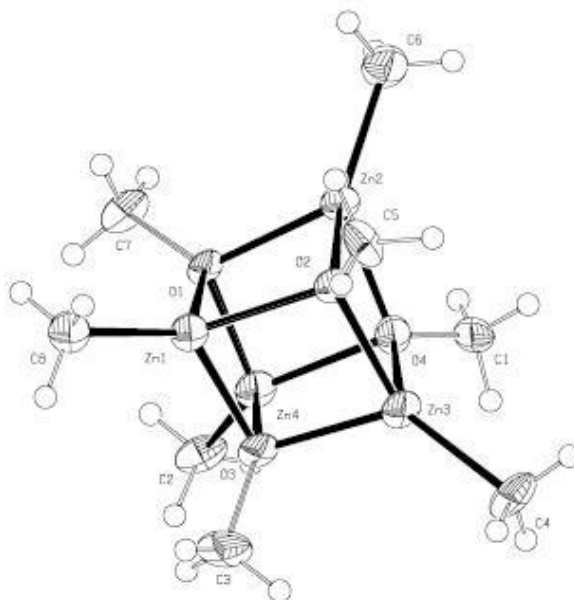


Figure 66 The oxidation product: $(\text{MeZnOMe})_4$.¹¹² Zn-C, 1.94; O-C, 1.46; Zn-O, 2.07Å. Average angles 96° at oxygen and 84° at zinc

Ideally zinc would prefer to be four co-ordinate, when the monodentate ligands (THP, THF and Furan) are employed, the zinc is only three co-ordinate which makes oxygen insertion much more easy. The oxygen can come from trace moisture or oxygen during preparation of the samples. Jana *et al.* have reported the oxygenation of dialkyl zinc and the dependence of the product formed on the presence of water¹¹³ is taken from the paper and summarizes the findings that in the presence of both water and oxygen, a single cubane structure is observed, whilst with just oxygen, a bis-heterocubane structure is formed. This suggests that the oxygenation product formed on synthesis of DMZn.L where $\text{L}=\text{THP}$ must have contained some trace moisture either from the solvent used or the capillary tube preparation.

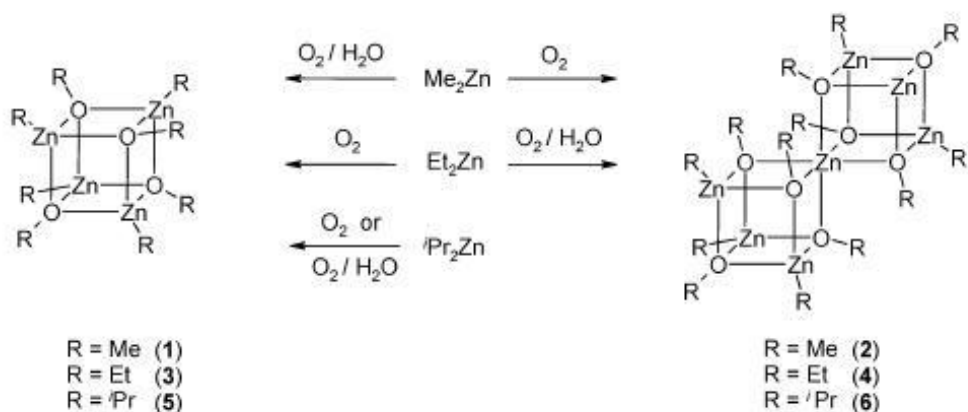


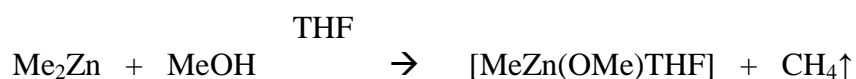
Figure 67 Dependence of the oxidation product formed in the presence of water and/or oxygen, summary of the findings by Jana *et al.*¹¹³

Following on from this discovery and knowing that MeZn-alkoxide structures have been used before as single-source precursors, further experimental work looked to investigate the synthesis of MeZnOMe. The drive was to analyse if it was possible that structure could accommodate an adducted ligand, how strong the co-ordination is and also if tetramer formation could be prevented. This is discussed in the next section.

4.4.1.1.1 Synthesis of MeZnOMe

The aim was to try to synthesise [MeZn(OMe)(THF)] and correlate this with a crystal structure to gain some understanding of how strongly the THF co-ordinated.

The reaction scheme below was carried out at both room temperature and at -30°C:



Extra precaution was taken to ensure the possibility of moisture incorporation was minimised. For both the -30°C and the room temperature reaction the ¹H NMR data was the same as that reported for bis heterocubane, [(MeZn)₆Zn(OMe)₈] structure¹¹³ with an unequal doublet for the MeO peak which correlates with literature.²⁹⁵ In this

instance, the methanol is introducing the oxygen, and no trace moisture was present. On pumping the sample at room temperature and further ^1H NMR analysis, the THF peak had decreased significantly, suggesting that the THF is not adducted. This is confirmed by the simplicity of the NMR with no differing Me/OMe environments found. **Figure 68** is a photograph of the white solid product that was yielded.



Figure 68 $[(\text{MeZn})_6\text{Zn}(\text{OMe})_8]$.

Solubility studies of this compound were trialled in hexane, octane and toluene. Toluene showed the most promise but all three solvents provided some decomposition observed as discolouration of the white powder/clear solution to a sand/brown coloured gel in a clear solution. In conclusion this proved that $[\text{MeZn}(\text{OMe})(\text{THF})]$ cannot be isolated in crystal form. $[(\text{MeZn})_6\text{Zn}(\text{OMe})_8]$ is the thermodynamically more favoured product and is likely that this structure is formed due to catalytic amounts of oxygen. $[(\text{MeZn})_6\text{Zn}(\text{OMe})_8]$ is difficult to dissolve which rendered is unsuitable for LI-MOCVD studies.

4.4.1.2 Dimethylzinc.dimethoxyethane

The molecular structure of $[\text{DMZn.DMOE}]$ is shown in **Figure 69** This compound crystallises in the orthorhombic space group $Pbcn$, exists as a monomeric complex featuring a chelating 1,2-dimethoxyethane ligand.

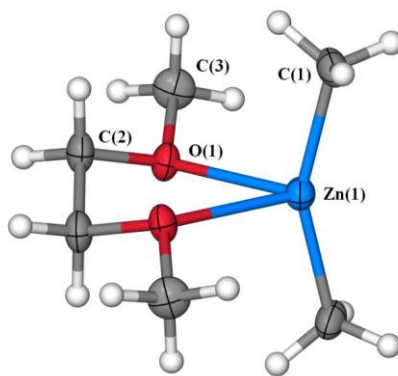


Figure 69 Crystal structure of [DMZn.DMOE].

The complex is situated on the crystallographic two-fold axis and displays C_2 symmetry. The zinc centre can be described as highly distorted tetrahedral, showing exceedingly wide [Me-Zn-Me] angles of $154.5(2)^\circ$. The [Me-Zn-Me] angle is also a convenient measure for assessing the strength of Me_2Zn -adducts. The smallest [Me-Zn-Me] angle of 121° is found in an $[\text{Me}_2\text{Zn}]$ adduct of the amide anion 2,2,6,6-tetramethylpiperidide²⁹⁶ while adducts of neutral amines display wider angles ranging from 125 to 145° ,²⁹⁷⁻³⁰⁰ thus the wider [Me-Zn-Me] angles found in [DMZn.DMOE] suggests that dimethylzinc forms rather weak interactions with the 1,2-dimethoxyethane ligands. The Zn-O bonds in [DMZn.DMOE] ($2.328(3) \text{ \AA}$) are fairly long compared with those of ether adducts of Zn(II) compounds that display greater ionic character. For example, $[\text{Br}_2\text{Zn}(\eta_2\text{-}1,4\text{-dioxane})]$ which forms a coordination polymer similar to that of [DMZn.DMOE] displays considerably shorter Zn-O bonds measuring 2.04 \AA .³⁰¹ Also the 1,2-dimethoxyethane adduct of diphenylzinc has somewhat shorter Zn-O bonds (2.26 and 2.29 \AA) and a tighter C-Zn-C angle (146.6°). The large [Me-Zn-Me] angle and the long Zn-ligands bonds reflect the low Lewis-acidity of the zinc atom and the relatively large covalent contribution to the [Zn-C] bonds in $[\text{Me}_2\text{Zn}]$.^{100, 302}

4.4.1.3 Dimethylzinc.1,4-dioxane

In the absence of X-ray crystallographic data [DMZn.1,4-dioxane] was originally proposed to be a monomeric molecule with a bidentate chelating 1,4-dioxane ligand.¹⁰⁵ **Figure 70**, shows it to be polymeric with repeating [Me₂Zn] moieties bridged by monodentate 1,4-dioxane ligands. The coordination at the Zn centre is a highly distorted tetrahedral.

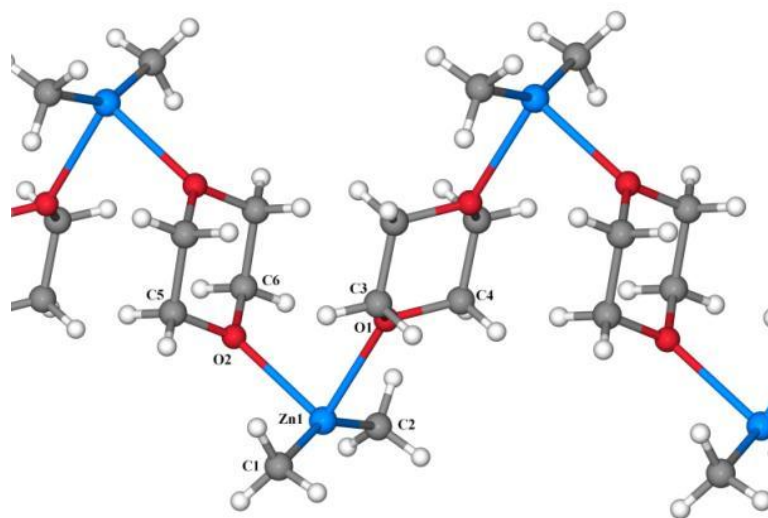


Figure 70 Crystal structure of [DMZn.1,4-dioxane].

There are few reported structures of dimethylzinc adducts with simple or cyclic ethers, but a comparison can be made with the structure of the parent alkyl [Me₂Zn]. The [C-Zn-C] bond in [DMZn.1,4-dioxane] distorts by 28° from the 180° linear angle in [Me₂Zn] to 152.0(3)°. The [Zn-C] bonds in [DMZn.1,4-dioxane] (Zn-C = 1.996Å, 2.000(7)Å) are longer than those in [Me₂Zn] (Zn-C = 1.930Å). It should be noted that although [DMZn.1,4-dioxane] is polymeric in the solid-state, the very long, weak [Zn-O] (2.399Å) bridging bonds may cleave during evaporation in the MOCVD process. This would give a monomeric gas-phase dimethylzinc complex containing a chelating 1,4-dioxane ligand. A bond angle of 152° shows this to be

very slightly more strongly bonded than the 1,2-dimethoxyethane adduct (**Figure 69**).

4.4.1.4 Dimethylzinc.1,4-thioxane

Remarkably, [DMZn.1,4-thioxane], has much weaker [Me₂Zn]-ligand interactions, as it has the largest Me₂Zn angle at 167.6°. The molecular structure, shown in **Figure 71** crystallises in space group *P2*₁/*m* with Zn, S and O atoms occupying crystallographic mirror planes.

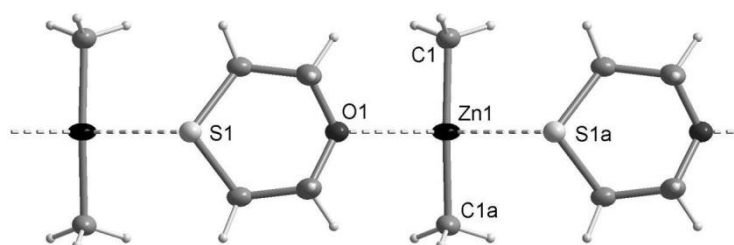


Figure 71 Crystal structure of [DMZn.1,4-thioxane].

The shortest contact between the Me₂Zn moiety and the ligand is a rather long Zn-O bond (2.592(5) Å). In addition, there is one exceptionally long Zn-S contact (Zn1-S1a 3.012(2) Å), which is substantially longer than dative Zn-S bonds of adducts of diorganozinc with thioethers. For example, a Zn-S distance of 2.50 Å was observed in the dimeric complex [Ph₂Zn(S(CH₂)₄)₂].³⁰³ **Figure 72** shows the loose packing chains formed via ZnO and ZnS contacts. These chains are packed loosely via very long Zn-S interactions of 3.280(2) Å to form a layered structure. As part of this rather loose arrangement, the [Me-Zn-Me] moiety is almost linear (167.6(3)°) and comparable to the 18-crown-6 complex of diethylzinc, which features a linear [C-Zn-C] moiety and six very long Zn-O contacts ranging from 2.83 to 2.89 Å.³⁰⁴ Comparing the valence-isoelectronic adducts [DMZn.1,4-dioxane] and [DMZn.1,4-thioxane] shows that the Zn-O/Zn-S distance is variable and strongly correlated to

the [Me-Zn-Me] angle. The solid state structure of [DMZn.1,4-thioxane] , with its loose Zn-ligand interactions, can be regarded as an intermediate between a coordination compound and a co-crystal. It appears that metal-donor interactions and crystal packing forces play an equally important role in the solid state assembly of these loose adducts.

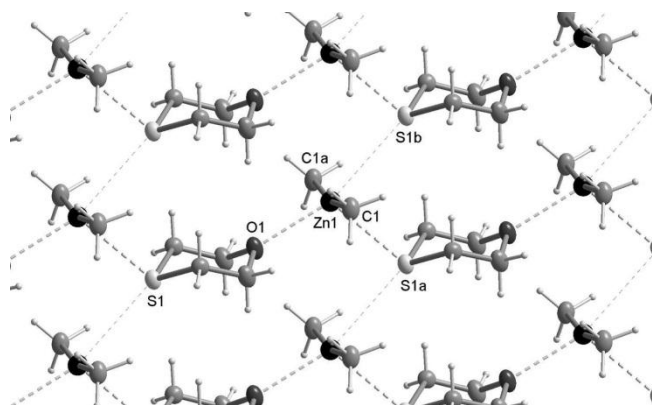


Figure 72 Loose packing chains formed via ZnO and ZnS contacts.

4.4.1.5 Summary

Table 17 highlights the crystallographic data from the DMZn.L crystal structures along with a summary of the most important bond lengths in **Table 18**.

Compound	[DMZn.DMOE]	[DMZn.1,4-dioxane]	[DMZn.1,4-thioxane]
Chemical formula	C ₆ H ₁₆ O ₂ Zn	C ₆ H ₁₄ O ₂ Zn	C ₆ H ₁₄ OSZn
Formula weight	185.56	183.54	199.6
Crystal system	orthorhombic	triclinic	monoclinic
Space group	Pbcn	P-1	P2 ₁ /m
<i>a</i> (Å)	12.348(5)	7.3530(15)	4.376(3)
<i>b</i> (Å)	6.895(3)	7.4055(15)	12.890(9)
<i>c</i> (Å)	90	8.9220(18)	7.595(5)
α (°)	90	88.57(3)	90
β (°)	90	87.26(3)	90.194(15)
γ (°)	107.718(7)	60.88(3)	90
<i>V</i> (Å³)	913.5(6)	423.92(15)	428.4(5)
<i>T</i>(K)	150	150	150
<i>Z</i>	4	2	2
μ(MoKα)/cm⁻¹	2.629	2.832	3.035
ρ(calc)/gcm⁻¹	1.349	1.438	1.547
Reflections, total	1904	5128	1000
Reflections, unique	645	1384	602
Parameter	44	84	48
R1 (F > 4σ(F))	0.0309	0.0548	0.0301
wR2 (all data)	0.0735	0.1548	0.0724

Table 17 Crystallographic data for DMZn.L where L=1,2-dimethoxyethane, 1,4-dioxane and 1,4-thioxane.

[DMZn.DMOE]	Zn1-C1	1.965(3) Å
	Zn1-O1	2.328(3) Å
	C1-Zn1-C1a	154.5(2) °
	O1-Zn1-O1a	71.64(12) °
[DMZn.1,4-dioxane]	Zn1-C1	1.999(6) Å
	Zn1-C2	2.000(7) Å
	Zn1-O1	2.399(4) Å
	Zn1-O2	2.333(5) Å
	C1-Zn1-C2	152.0(3) °
	O1-Zn1-O2	86.48(16) °
[DMZn.1,4-thioxane]	Zn1-C1	1.959(3) Å
	Zn1-O1	2.592(5) Å
	Zn1-S1a	3.012(2) Å
	Zn1-S1b	3.280(2) Å
	C1-Zn1-C1a	167.6(3) °
	O1-Zn1-S1a	110.07(17) °

Table 18 Selected bond lengths and angles for complexes of DMZn.L where L=1,2-dimethoxyethane, 1,4-dioxane and 1,4-thioxane.

4.4.2 TGA

TGA data for the DMZn adducts formed with the bidentate ligands is shown in **Figure 73**, along with the $[(\text{MeZn})_6\text{Zn}(\text{OMe})_8]$ species for comparison.

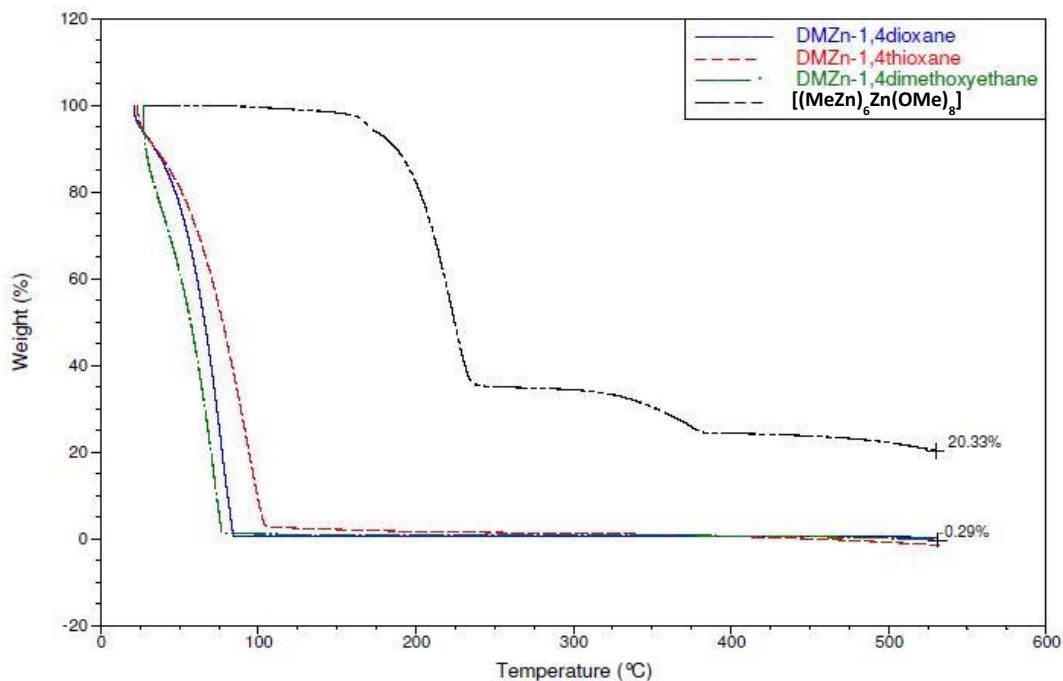


Figure 73 TGA data for DMZn.L and $[(\text{MeZn})_6\text{Zn}(\text{OMe})_8]$.

Dimethylzinc is an extremely volatile compound with a boiling point of 46°C . From looking at the TGA, the onset of volatilisation and weight loss for all three adducted species is observed at 50°C . $[\text{DMZn.DMOE}]$ is the most volatile compound, followed by $[\text{DMZn.1,4-dioxane}]$ and finally $[\text{DMZn.1,4-thioxane}]$. This can be rationalised by looking back to the crystal structures. The 1,2-dimethoxyethane ligand formed a monomeric structure. The difference in volatility for the cyclic 1,4-dioxane and 1,4-thioxane ligand can be attributed to the fact that the thioxane forms a larger network, with increased interactions between layers which could lead to it being slightly less volatile. The trace for $[(\text{MeZn})_6\text{Zn}(\text{OMe})_8]$ is more difficult to explain. As expected the temperature for volatilisation is much higher at approximately 200°C . It is difficult to suggest what the percentage mass loss relates

to. The $[(\text{MeZn})_6\text{Zn}(\text{OMe})_8]$ structure is formed as it is thermodynamically stable, but as this structure is heated, the thermal decomposition or restructuring to a more thermally stable structure could occur. The residue level is much higher indicating an zinc oxide based involatile species is formed.

4.5 Zinc Oxide Growth

The growth studies were performed by LI-MOCVD using an Aixtron AIX 200FE AVD reactor fitted with a modified liquid injection system (**Chapter 3**). The delivery of zinc precursor was achieved using 0.1M solutions of $[\text{DMZn.L}]$ in octane (experimental details in **section 4.8.2**). Research grade oxygen was introduced at the inlet of the reactor and controlled by a mass flow controller during deposition. Epi-ready Si (111) wafers, soda lime glass and F-doped tin oxide were used as substrates. Rotation of the substrates was used throughout deposition to help with film uniformity across the wafer. Full growth conditions are given in **Table 19**.

Substrate	Si(111) / F-doped SnO_2 /glass
Substrate temperature	350-550°C
Evaporator temperature	50°C
Reactor pressure	5 mbar
Solvent	Octane
Precursor solution concentration	0.1 M
Precursor solution injection rate	30 $\text{cm}^3\text{hr}^{-1}$
Argon flow rate	200 $\text{cm}^3\text{min}^{-1}$
Oxygen flow rate	100 $\text{cm}^3\text{min}^{-1}$
Run time	10 - 30 min
O_2/Zn precursor ratio	188:1 – 375:1

Table 19 Growth conditions used to deposit ZnO by LI- MOCVD using 0.1M n-octane solutions of $[\text{DMZn.L}]$.

The growth rate and morphology of the ZnO layers deposited using [DMZn.L] were investigated over the temperature range 350–550°C.^{106, 196} The effect of substrate temperature on the growth rate of the ZnO is shown in **Figure 74**.

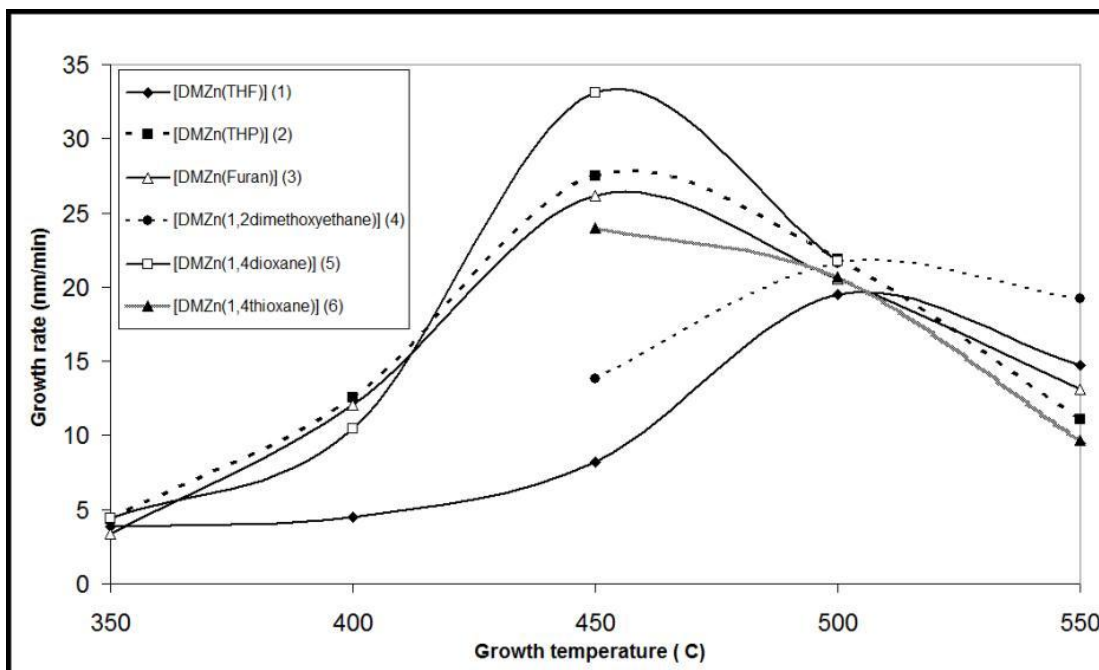


Figure 74 Variation of the ZnO growth rate with substrate temperature for [Me₂Zn(L)].

The growth rate of ZnO for compounds [DMZn.1,4-dioxane], [DMZn.THP] and [DMZn.furan], increases in the temperature range of 350°-450°C. This corresponds to the region of kinetic control where film growth is dominated by thermal decomposition of the precursor on the substrate. For [DMZn.THF], the region of kinetic control occurs at 500°C. This higher temperature is due to the relative base strengths of the oxygen donor ligands (THF>THP~Furan>dioxane) indicating its significant role in zinc oxide deposition.

Significantly, there is a complete suppression of the [Me₂Zn]/O₂ pre-reaction via the use of the [DMZn.L] species, which indicates the presence of the oxygen donor ligands in the gas-phase is a crucial factor. The crystal structures discussed earlier confirm that in the solid state they have only very weak [Me₂Zn]-ligand interactions.

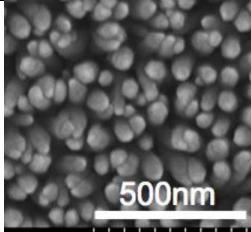
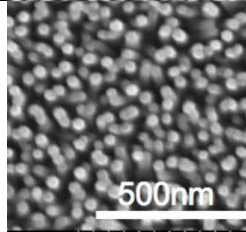
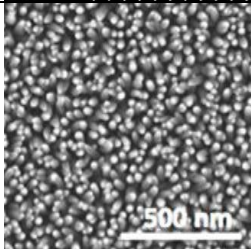
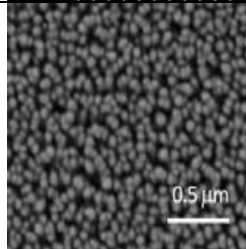
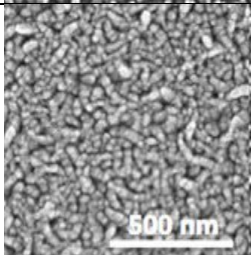
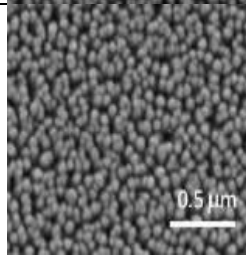
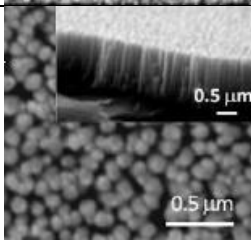
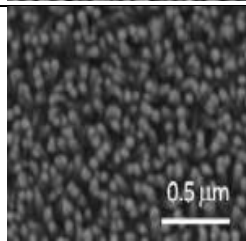
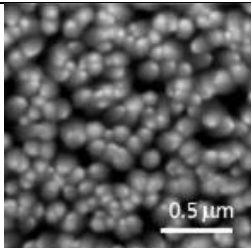
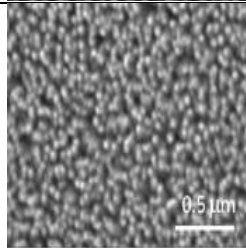
Precursor	Growth Temp. (°C)	ZnO nanowires SEM image	Precursor	Growth Temp. (°C)	ZnO nanowires SEM image
[DMZn. THF]	500		[DMZn. THP]	500	
[DMZn. furan]	500		[DMZn. 1,4-dioxane]	500	
[DMZn. furan]	450		[DMZn. 1,4-dioxane]	450	
[DMZn. DMOE]	500		[DMZn. 1,4-thioxane]	575	
[DMZn. DMOE]	450		[DMZn. 1,4-thioxane]	550	

Table 20 SEM images of temperature dependence of ZnO morphology using DMZn.L on Si(111) (O_2/Zn precursor ratio $\sim 188:1$).

The deposition of zinc oxide nanowires at more moderate temperatures ($\sim 450^\circ\text{C}$) on conducting substrates such as F-doped $\text{SnO}_2/\text{glass}$ is particularly important for solar cell applications, as it avoids crystallization and loss of conductivity of the F-doped SnO_2 coating. The deposition of ZnO nanowires did not occur at temperatures of 400°C or 350°C and continuous polycrystalline films were formed instead. On F-

doped SnO₂/glass substrates, only complex [DMZn.1,4-dioxane] gave vertically aligned nanowires at 450° and 500°C. However the nanowires were not as well ordered as those grown on Si(111), this is depicted in **Figure 76**

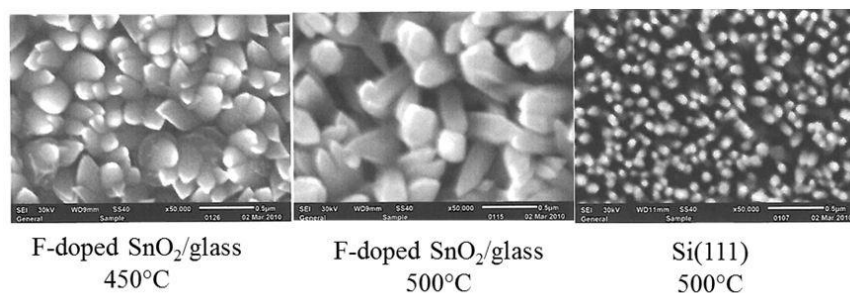


Figure 76 SEM images for ZnO nanowires deposited using [DMZn.1,4dioxane] on Si(111) and F-doped SnO₂/glass substrates at a O₂/Zn precursors ratio of 188:1.

[DMZn.1,4-thioxane] deposited continuous ZnO thin films, rather than nanowires, on F-doped SnO₂ coated glass or Si(100) substrates, however, at the slightly higher temperature of 550°C nanowires could be grown using Si(100). It is concluded that the formation of ZnO nanowires depends on the mobility and lifetime of species such as [MeZn(OMe)(L)] and/or [MeZn(OMe)] on the substrate surface. The data presented here suggests that at low substrate temperatures (eg. [DMZn.furan] at 450°C in **Table 20**) the alkylzinc alkoxide species has insufficient surface mobility for nanowire growth and thus, a polycrystalline morphology with randomly-orientated ZnO crystallites is yielded. At ~ 500°C, [DMZn.furan] has sufficient mobility and lifetime to allow efficient surface diffusion for the growth of ZnO nanowires. For nanowire growth, it is necessary for the Zn adsorbate to have sufficient surface lifetime to migrate to the ZnO nucleation sites and then to the tip of the growing nanowire, and this is achieved at temperatures of 450°C and 500°C. The slight difference in temperature required for ZnO nanowire growth suggest that the oxygen-donor ligand (L) influences the kinetics of ZnO nanowire growth, possibly due to differences in the surface stability, adsorption characteristics, and

mobility of precursor species such as $[\text{MeZn}(\text{OMe})(\text{L})]$. Further evidence of the influence of the oxygen-donor ligand on ZnO NW formation was provided by the observation that, under equivalent growth conditions ($T_g=500^\circ\text{C}$, O_2/Zn ratio 188:1), $[\text{DMZn.DMOE}]$ produced smaller diameter nanowires, approximately 49 nm, than those nanowires deposited using $[\text{DMZn.1,4-dioxane}]$, with a diameter of approximately 92nm. The diameter of the NWs was also influenced by the O_2/Zn precursor ratio, which is discussed in **section 4.6.1.2**.

It is significant that the use of $[\text{DMZn}(\text{L})]$ adducts avoids the necessity to use seed catalysts previously employed in the MOCVD of ZnO nanostructures. The precise nucleation mechanism for ZnO NW growth has not been identified, but previous studies indicate that the nucleation sites may be islands of ZnO. These may be formed by decomposition of $[\text{MeZn}(\text{OMe})]$ species which contain a strong $[\text{Zn-O}]$ bond. Looking to the composition data provided in **section 4.6.5**, the presence of sulfur in the oxide film indicates that the 1,4-thioxane ligand, and by extension, the 1,4-dioxane and 1,2-dimethoxyethane ligands, also play a role in the growth process. It is therefore possible that decomposition of $[\text{Zn-ether}]$ surface species may also lead to ZnO nucleation sites.

4.6.1.1 Influence of Deposition Time on Morphology

Using the DMZn.1,4-dioxane compound, an SEM study was undertaken to look at the impact of deposition time on the morphology of films formed. The images in **Figure 77** below show the SEM images recorded for deposition times ranging from 5 minutes to 30 minutes. All of the images were taken from ZnO samples deposited on Si(111) at 500°C and an oxygen flow rate of 100sccm. The approximate film thickness (based upon weight gain measurements) is given below each image.

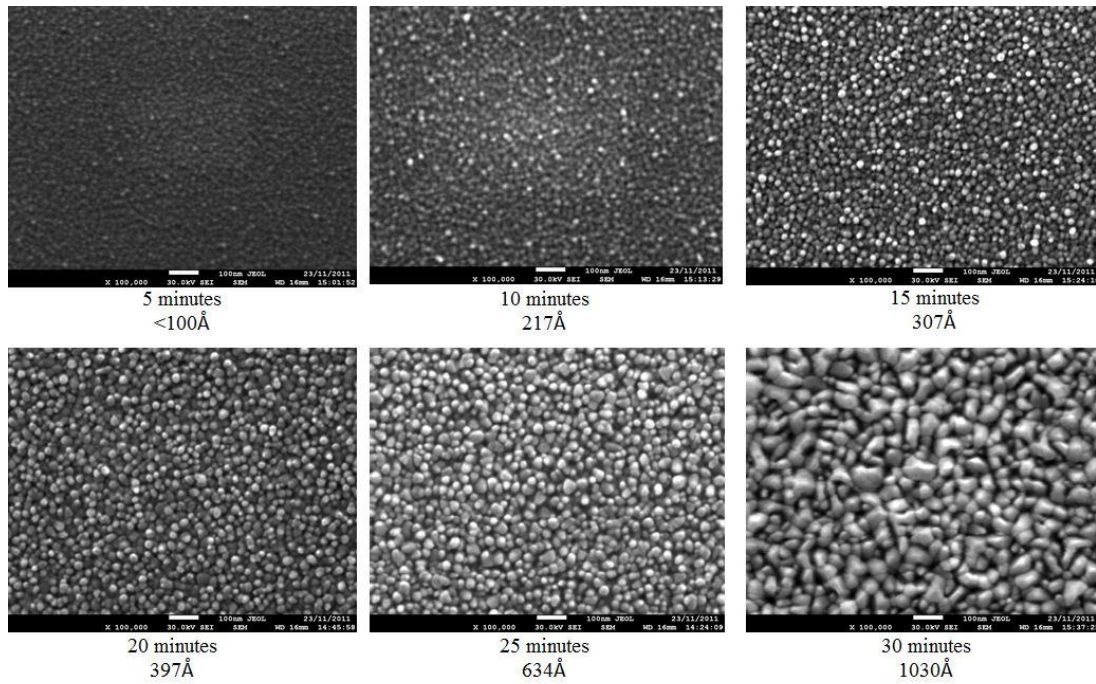


Figure 77 SEM images of the deposition time dependence on morphology of ZnO deposited on Si(111) at 500°C, oxygen flow rate 100sccm.

From looking at the images, as the deposition time increases there is a marked increase in size of the particles from 5 minutes to 30 minutes deposition time. After 5 minutes deposition, there is a high density of small spherical nanoparticles. There is a slight increase in the particle size from 5 to 15 minutes deposition. By 20 and 25 minutes deposition, the film morphology appears to be more 3D like. At 30 minutes there appears to be some coalescing resulting in the formation of larger particles. This is confirmation that by limiting the deposition time nanowires can be grown. As the deposition time is increases, coalescence would increase. Ultimately, this would be limiting in the target device. As ALD is a conformal process, the greater the surface area of ZnO present, the greater the area on which the copper oxide can be grown thus maximising the potential p-n junction.

4.6.1.2 Influence of Oxygen:Zinc Ratio

So far it has been shown that the formation of nanowires is dependant upon substrate temperature, deposition time and substrate. A further parameter investigated was the impact of the oxygen:zinc ratio. **Table 21** shows the oxygen flow rate used during deposition for the [DMZn.1,4-dioxane] compound, with the SEM images for these samples shown in **Figure 78**.

Substrate	Growth Temperature (°C)	O ₂ flow rate (sccm)	O ₂ :Zn ratio	ZnO morphology (SEM)	Average nanowire diameter (nm)
Si(111)	500	175	340:1	Nanowires	120
	500	150	276:1	Nanowires	120
	500	100	187:1	Nanowires	92

Table 21 Summary of oxygen flow rates and subsequent O₂:Zn ratio.

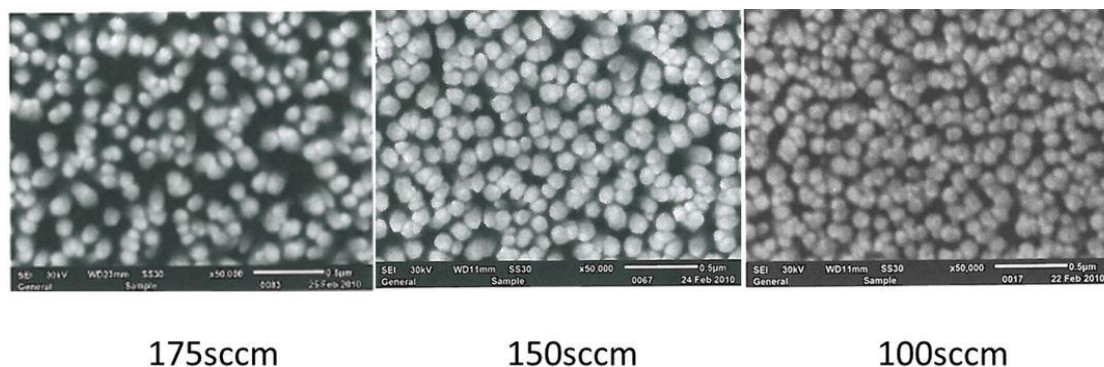


Figure 78 SEM images analysing the impact of oxygen flow rate on the morphology of ZnO on Si(111) at 500°C using [DMZn.1,4-dioxane].

The SEM images appear to show that as the oxygen decreases the packing density increases. With large VI/II precursor ratios, generally larger diameter ZnO nanowires were formed, as highlighted in **Table 21**.

4.6.1.3 Summary of Morphology

Table 22 summarizes the film morphology of ZnO deposited from DMZn.L and O₂ as discussed in this section

Precursor	Substrate	Growth Temp. (°C)	O ₂ :Zn ratio	ZnO morphology	Average nanowire diameter (nm)
[DMZn.1,4-dioxane]	Si(111)	500	188:1	Nanowires	92
		500	290:1	Nanowires	120
		450	188:1	Nanowires	108
		450	290:1	Nanowires	157
		400	188:1	Continuous Film	
		400	290:1	Continuous Film	
		400	375:1	Nanowires	
	F-doped SnO ₂ /glass	500	188:1/290:1	Nanowires	
		450	188:1/290:1	Nanowires	
		400	188:1/290:1	Continuous Film	
		400	375:1	Nanowires	
[DMZn.DMOE]	Si(111)	500	188:1	Nanowires	49
		500	290:1	Nanowires	75
		450	188:1/290:1	Nanowires	
		400	188:1/290:1	Continuous Film	
	F-doped SnO ₂ /glass	500	188:1/290:1	Platelets	
		450	188:1/290:1	Platelets	
		400	188:1/290:1	Continuous Film	
[DMZn.1,4-thioxane]	Si(111)	600	188:1/290:1	Nanowires	
		575	188:1/290:1	Nanowires	
		550	188:1/290:1	Nanowires	
		500	188:1/290:1	Continuous Film	
		450	188:1/290:1	Continuous Film	
	F-doped SnO ₂ /glass	500	188:1/290:1	Continuous Film	
		450	188:1/290:1	Continuous Film	

Table 22 Summary of the deposition conditions and ZnO film morphology from [DMZn.L] where L=1,4-dioxane, 1,2-dimethoxyethane and 1,4-thioxane.

4.6.2 XRD

X-ray diffraction was used to study the ZnO layers deposited. **Figure 79** is an example of the trace obtained when [DMZn.1,4-dioxane] was used as the precursor.

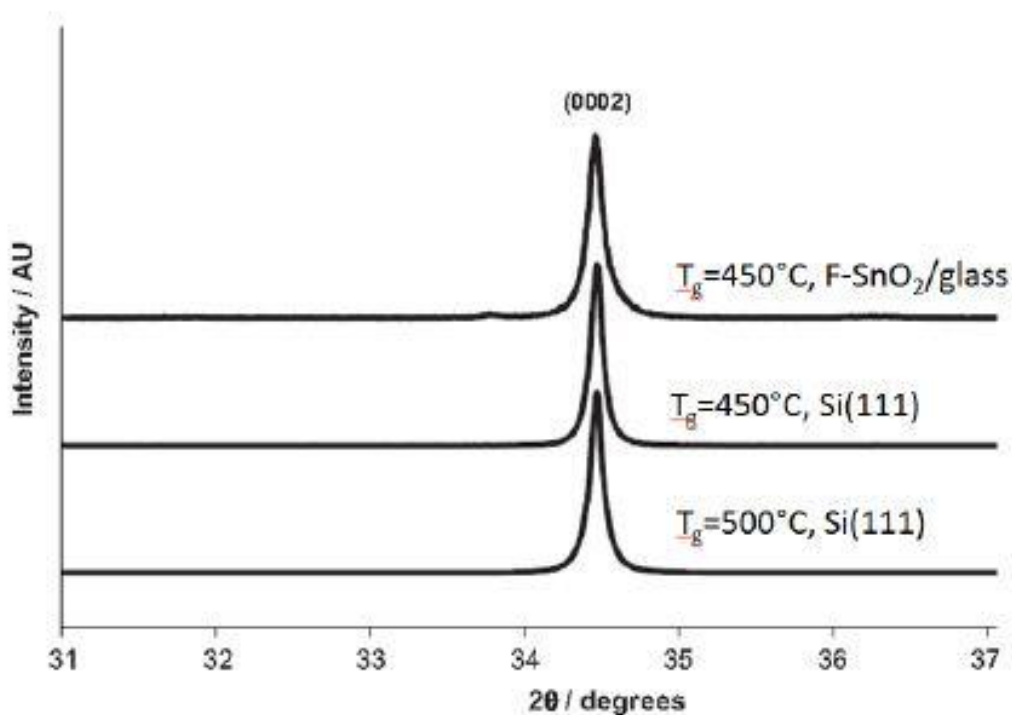


Figure 79 XRD data for the ZnO NWs deposited from [DMZn.1,4-dioxane].

The ZnO nanowires grown from all adducts on Si(111) and F-doped SnO₂/glass show diffraction patterns which are dominated by the (0002) reflection of the wurtzitic ZnO phase (P63mc) (JCPDS file No. 36-1451) observed at a 2θ value of 34.448. No significant intensity is apparent from any other ZnO reflections, which is consistent with the highly oriented fiber-texture-type growth of the ZnO nanowires with c-axis orientation. The XRD data correlates strongly with data reported for ZnO NWs grown by MOCVD on various substrates using [Et₂Zn] in the presence of O₂.

4.6.3 Raman

In single crystal wurtzite ZnO, there are four atoms per unit cell, giving rise to 12 phonon modes. These modes are important for understanding the thermal, electrical and optical properties of the crystal. The Raman data for a selection of the ZnO nanowires grown on Si(111) and F-doped SnO₂/glass are shown in **Figure 80**.

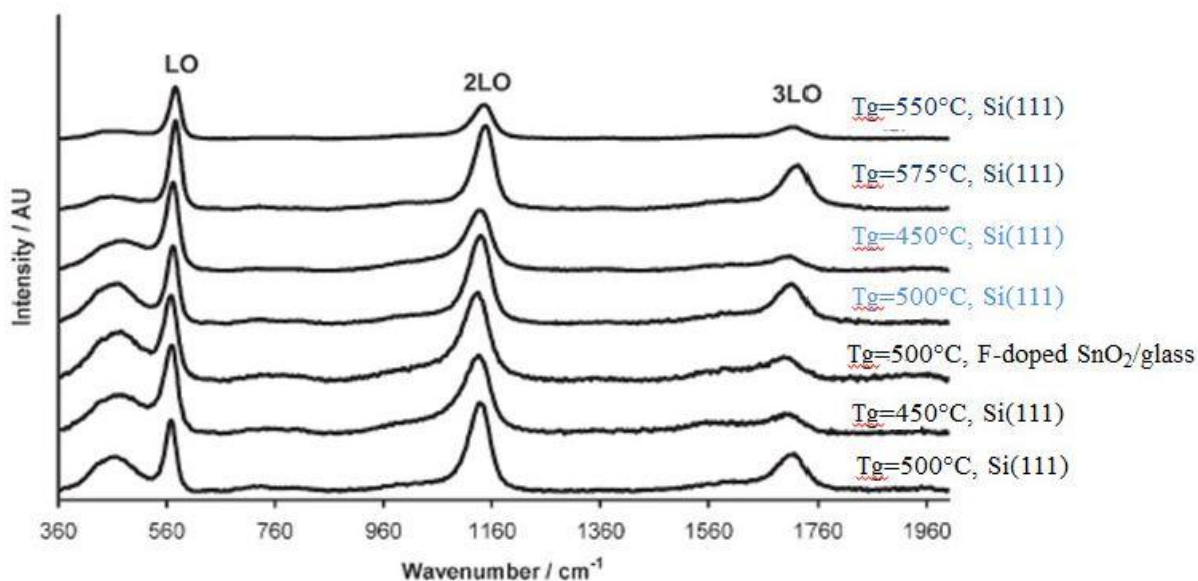


Figure 80 Raman spectra of the ZnO NWs grown [DMZn.1,4-dioxane], [DMZn.DMOE] and [DMZn.1,4-thioxane] where [DMZn.1,4-dioxane], [DMZn.DMOE] and [DMZn.1,4-thioxane] using (O₂/Zn188:1).

A 325nm UV Laser was used for excitation e.g. probing electronically coupled modes. Raman spectra of a selection of the ZnO NW samples were recorded using a confocal microscope. The instrument configuration dictates that both the incident laser illumination and the backscattered Raman optical paths are parallel to the ZnO nanowire c-axes. In this geometry and wavelength, the Raman selection rules only allow the longitudinal optic (LO) E₂ and A₁ modes to be observed. The UV-resonant Raman scattering process shows the first-, second-, and third-order LO features in the range 100–2000 cm⁻¹. The ratio of the 2-LO/LO intensities is a measure of electron-phonon coupling, and is sensitive to the ZnO domain size, which

corresponds to the ZnO nanowire diameter in this case. The intensity ratios were measured by fitting Gauss-Lorentzian functions to the two peaks to yield a range from 0.55 to 1.17 which corresponds to a range of average domain sizes between approximately 40 and 100nm when compared to previous measurements, relating to the growth of ZnO nanowires from zinc powder and air. The present Raman data are consistent with the nanowire diameters obtained from the SEM data shown in **Table 22**. The similarity between these results and other studies suggest that a common nucleation and growth mechanism exists where the most influential parameters on the NW morphology are the substrate temperature and the VI/II ratio.

4.6.4 Photoluminescence

The room temperature-PL data for the ZnO NWs grown on Si(111) using [DMZn.1,4-dioxane], [DMZn.1,2-dimethoxyethane] and [DMZn.1,4-thioxane] is shown in **Figure 81**

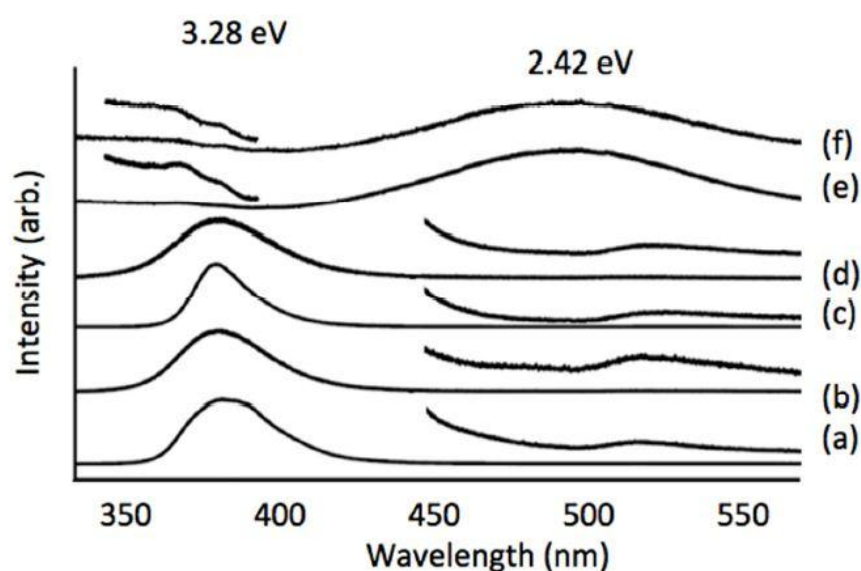


Figure 81 Room temperature photoluminescence data for ZnO NWs grown on Si(111) substrates using: [DMZn.1,4-dioxane] (a) $T_g = 500^\circ\text{C}$, (b) 450°C ; [DMZn.1,2-dimethoxyethane] (c) $T_g = 500^\circ\text{C}$, (d) $T_g = 450^\circ\text{C}$ and [DMZn.1,4-thioxane] (e) $T_g = 575^\circ\text{C}$, (f) $T_g = 550^\circ\text{C}$. (O_2 / Zn precursor ratio $\sim 188:1$).

The data for the ZnO NWs derived from [DMZn.1,4-dioxane] and [DMZn.1,2-dimethoxyethane], **Figure 81 a-d**, show an intense peak at 3.28 eV, attributable to near band-edge emission arising from the recombination of free excitons, with very low intensity green luminescence at 2.42 eV. This data also shows that the ZnO NWs grown from these compounds have a high degree of crystalline quality and are high purity with a low defect density. The PL data presented here is identical to the room temperature PL data for ZnO NWs grown at 500 °C on Si(111) substrates using [DMZn.L] (L=THF, THP, furan). The PL data shown in **Figure 81 a-d** are also very similar to PL data for high quality ZnO NWs grown by MOCVD using [Et₂Zn] and O₂ which is dominated by near band-edge emission with negligible defect-related green emission. The 2.42 eV defect-related emission peaks in the room temperature PL spectra for ZnO NWs grown using the [DMZn(bidentate ether)] adducts are significantly less intense than reported in PL data in some studies of ZnO NWs grown by other techniques, such as hydrothermal deposition. This demonstrates the excellent photonic properties of the ZnO NWs grown from the dimethylzinc adducts. In marked contrast, for [DMZn.1,4-thioxane] the room temperature PL data for the ZnO NWs grown at 550 °C and 575°C on Si(111), (**Figure 81e and f**), is dominated by defect-related emission at 2.42 eV, with the near band-edge emission peak at 3.28 eV being barely detectable above the background level. This suggests that the ZnO NWs grown from [DMZn.1,4-thioxane] contain a very high level of oxygen defects. In addition, the near band-edge emission peak has ‘blue-shifted’ to higher energy, which can be attributed to the Burstein–Moss effect and is explained by the filling of ZnO density of states, near the conduction-band minimum, with sulphur-induced excessive charge carriers.

This mechanism is confirmed by the presence of 1 at.-% of sulfur impurity detected by AES discussed in the next section.

4.6.5 Composition

The composition of selected ZnO films deposited on Si(111) substrates using [DMZn.L] (where L=THF, THP, furan, DMOE, 1,4-dioxane, 1,4-thioxane) were determined by Auger electron spectroscopy (AES) (see **Table 23**). The films were deposited at temperatures of 400°C and 500°C (O₂/Zn precursor ratio of 188:1) on Si(111) and F-doped SnO₂/glass substrates. The AES data showed that the films grown from DMOE and 1,4-dioxane were stoichiometric ZnO (O/Zn ratios=1.00–1.05) with no detectable carbon impurities (estd. detection limit 0.5 at.%). It is noteworthy that the ZnO films deposited by liquid injection MOCVD from the monodentate cyclic ether adducts [DMZn.L] (L=THF, THP, furan) were substoichiometric, whilst those with bidentate adduction (where the zinc coordination number is 4), were closer to the expected 1:1 ratio. The ZnO films deposited using [DMZn.1,4-thioxane] contained sulphur at a level of 1.1 at.% and the sulphur is clearly derived from thermal decomposition of the 1,4-thioxane ligand. This provides good evidence that the ether ligands play a role in the ZnO deposition process.

Precursor	Growth Temperature	Zn (at.%)	O (at.%)	Zn/O (at.%)
[DMZn.THf]	500	47.4	52.6	0.90
[DMZn.THP]	500	47.0	53.0	0.89
[DMZn.furan]	500	47.2	52.8	0.89
[DMZn.DMOE]	400	51.2	48.8	1.05
[DMZn.1,4-dioxane]	400	51.0	49.0	1.04
[DMZn.1,4-thioxane]	400	50.2	48.7	1.03

Table 23 The composition of ZnO nanowires deposited by MOCVD from DMZn.L at 500°C.

The data presented herein is further evidence for the crucial role played by oxygen-donor ligands in preventing the $[\text{Me}_2\text{Zn}]/\text{O}_2$ pre-reaction, and in facilitating ZnO NW growth. The crystal structures indicate that there are only very weak interactions between $[\text{Me}_2\text{Zn}]$ and the donor ligands. This strongly supports the proposal that prevention of pre-reaction is not due to simple blocking of the reactive Zn centre by associated gas-phase adducts of the type $[\text{Me}_2\text{Zn} \cdot \text{ether}]$. The weak $[\text{Me}_2\text{Zn}]$ -ether interactions suggest that the complexes may be only loosely associated in the gas phase during the MOCVD process. It is thus more probable that pre-reactions are prevented by formation of gas-phase intermediate species such as $[\text{MeZn}(\text{OMe})(\text{L})]_x$ which form stronger adducts with the donor ligand (L) than $[\text{Me}_2\text{Zn}]$. The crystal structure of the relatively oxygen-inert complex $[\text{tBuZn}(\text{O}^t\text{Bu})(\text{THF})]_2$ may serve as a model for the intermediate species $[\text{MeZn}(\text{OMe})(\text{L})]$. Its $[\text{Zn}-\text{THF}]$ bonds are shorter (2.239 Å) than the $[\text{Zn}-\text{ether}]$ bonds in the adducts THF, THP and furan, indicative of a higher $[\text{Zn}-\text{ether}]$ bond strength.

4.7 Conclusions

In summary, this chapter has highlighted the single crystal x-ray diffraction results for DEZn and DMZn. Single crystal XRD data for $[\text{DMZn} \cdot \text{L}]$ helps to show that $[\text{Me}_2\text{Zn}]$ forms weak adducts with ether ligands. The 1,4-dioxane complex is polymeric with repeating $[\text{Me}_2\text{Zn}]$ units bridged by 1,4-dioxane ligands. By contrast the 1,2-dimethoxyethane complex has a monomeric structure containing a bidentate and chelating ligands. The 1,4-thioxane precursor forms even weaker interactions with $[\text{Me}_2\text{Zn}]$ and the solid-state structure can be regarded as an intermediate between a coordination complex and a co-crystal. It has been demonstrated that the oxygen containing adducts $[\text{DMZn} \cdot \text{L}]$ (L = THF, THP, Furan, 1,2-dimethoxyethane,

1,4-dioxane and 1,4-thioxane) avoid the pre-reaction between [Me₂Zn] and oxygen. The suppression of gas-phase pre-reaction by the [DMZn.L] and the probable existence of alkylzinc alkoxide surface species, such as [MeZn(OMe)], allows the controlled growth of high-purity ZnO nanowires in a narrow growth temperature range centred on 500°C. Above and below this temperature, the precursors produced continuous polycrystalline ZnO films. The role of the heterocyclic oxygen donor molecules in mediating the reactivity of [Me₂Zn] in oxygen, has a critical influence on the morphology of the deposited ZnO nanowires. XRD data showed that the ZnO NWs grown from all six adduct precursors form in the wurtzitic ZnO phase. Room temperature PL data for the ZnO NWs grown using oxygen donor adducts showed an intense peak at 3.28 eV due to near band-edge emission with only a very low intensity of defect-related green luminescence at 2.42 eV. In contrast, room temperature-PL data for the ZnO nanowires deposited using [DMZn.1,4-thioxane] was dominated by deep centre, defect-related emission at 2.42 eV, related to a high level of oxygen vacancies.

4.8 Experimental Details

4.8.1 Dialkylzinc Adducts: Synthesis and Characterisation

Crystals of [DMZn.L] (where L=THF, DMOE, 1,4-dioxane, 1,4-thioxane) suitable for single crystal X-ray diffraction (XRD) were obtained by the slow dropwise addition of L (1 mol.equiv.) to [DMZn] (1mol.equiv.) in a glovebox. The mixture was allowed to cool back to room temperature from the heat generated by the exothermic reaction, and after being allowed to stand, colourless crystals of [DMZn.L] were formed. **Table 24** shows the ¹H NMR analysis obtained for the compounds.

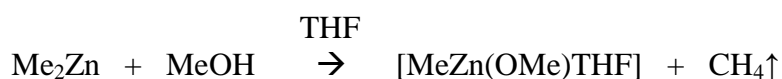
Zinc-Adducted Species	Chemical Shift ^1H NMR (d^6 -benzene) $\delta\text{H}(\text{ppm})$:
DMZn	-0.61 (s, 6H, CH_3)
DMZn.1,2-dimethoxyethane	-0.83 (s, 6H, CH_3), 3.04 (s, 6H, CH_3), 3.24 (t, 4H, CH_2CH_2)
DMZn.1,4-dioxane	-0.71 (s, 6H, Zn- CH_3), 3.35 (m, 8H, O- CH_2CH_2).
DMZn.1,4-thioxane	-0.73 (s, 6H, CH_3), 2.31 (t, 4H, CH_2), 3.63(t, 4H, CH_2).

Table 24 ^1H NMR characterisation data for [DMZn.L].

4.8.2 Solutions for MOCVD growth

All manipulations were carried out under an atmosphere of dry nitrogen using standard Schlenk line or dry box techniques. Dimethylzinc, $[\text{Me}_2\text{Zn}]$ (99.9999% purity on a metals basis) was supplied by SAFC Hitech. THF, THP, furan, 1,2-dimethoxyethane and 1,4-thioxane were supplied by Sigma Aldrich Ltd. The n-octane, and 1,4-dioxane were supplied by Romil. All were purified where necessary. For the liquid injection MOCVD studies the [DMZn.L] were synthesized in n-octane without isolation; $[\text{Me}_2\text{Zn}]$ (1mol.equiv.) was dissolved in anhydrous n-octane. Adduct L (1mol.equiv.) was then added dropwise. The concentration of the solution was adjusted to 0.1M by the addition of the required amount of n-octane. The concentration of the [DMZn.L]/n-octane solution was confirmed to be 0.1 M by ^1H NMR spectroscopy.

4.8.3 MeZnOMe Synthesis and Characterisation



Karl Fisher analysis was first performed on both methanol and THF, with average moisture content at 25ppm and 15ppm respectively. A room temperature reaction

was carried out using standard Schlenk line techniques. Me_2Zn (10.4g, 0.109mol) was solvated in THF (25ml) in glovebox. MeOH (5.3ml, 0.109mol) was solvated in THF (25ml). The MeOH/THF mixture was added to Me_2Zn /THF slowly with stirring, with a total addition time of 45mins. On addition, vigorous bubbling and strong exothermic reaction observed. As addition continued, white precipitate began to form. The clear solution was filtered away from the white precipitate.

This same method was repeated at a reduced temperature of approx. -40°C . This was to confirm that disproportionation doesn't occur at a higher temperature. Both reaction products were analysed by ^1H NMR using d^6 -benzene as a reference. :

-0.41 (s, 18 H; ZnCH_3), 3.37(s, 18 H; OCH_3), 3.40 ppm (s, 6H; OCH_3) .

Chapter 5 Copper Results and Discussion

5.1 Overview

This chapter examines the investigation into the deposition of Cu_2O . As discussed previously, Cu_2O is a p-type oxide and is the target material to form a p-n junction with ZnO . In addition, the scope of this investigation enabled the deposition of metallic copper to be studied. This is of interest in its own right as a metallisation layer for electronic devices and was highlighted in **section 2.2**.

For deposition work involving copper, two precursors were investigated, a Cu(I) β -diketonate, copper hexafluoroacetylacetonato cyclo-octadiene, $\text{Cu}(\text{hfac})(\text{COD})$ and a Cu(I) complex namely, cyclopentadienyl copper tertiary butyl isocyanide, $\text{CpCu}(\text{tBuNC})$. $\text{Cu}(\text{hfac})(\text{COD})$, shown in **Figure 82** was trialled first in a liquid injection method via thermal decomposition, CVD, and via ALD with both tertiary butyl hydrazine and ozone as co-reagents. With this precursor the deposition of Cu and CuO layers was achieved. Synthesis and the deposition parameters investigated are summarised in **section 5.6**.

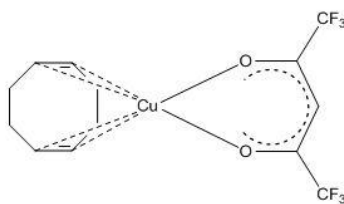


Figure 82 $\text{Cu}(\text{hfac})(\text{COD})$.

As the target layer for the PV device was Cu_2O , a further precursor, $\text{CpCu}(\text{tBuNC})$, was studied via conventional and plasma enhanced ALD. This target molecule was chosen as a potential ALD precursor due to its previous use in CVD.^{202, 305} **Figure 83** identifies the synthesis route, and the molecule^{306, 307} with further experimental details provided in **section 5.6**.

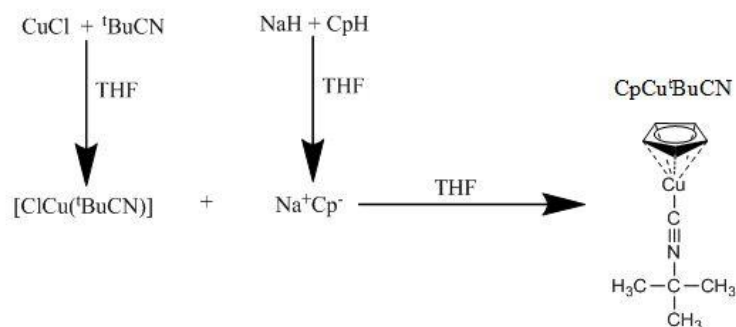


Figure 83 Reaction scheme for the synthesis of CpCu(^tBuNC).

The compound was characterised by ¹H NMR and the spectra is presented in **Figure 84**. The spectra (undertaken at an extended relaxation time of 25seconds), shows the expected singlet resonances at $\delta = 0.5\text{ppm}$ and $\delta = 6.2\text{ ppm}$ with the correct proton ratio of 9:5 respectively, indicating an η^5 -coordination mode of Cp to copper in the solution phase at room temperature.

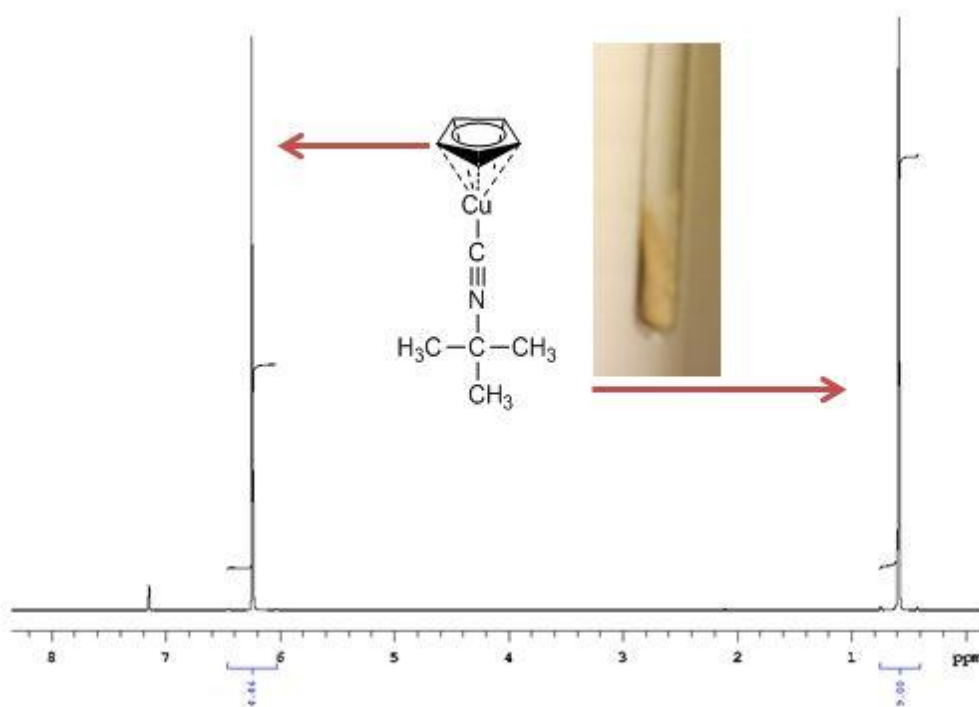


Figure 84 ¹H NMR with a photograph insert of CpCu(^tBuNC). ¹H NMR (C₆D₆): $\delta(\text{ppm})$: -0.6ppm (s,9H,N-C(H₃)₃), 6.2 (s, 5H, -C₅H₅)

The co-ordination mode of the Cp to the copper is further confirmed in the work undertaken by Willcocks²⁰² in which the molecular structure confirms a *pseudo* two-coordinate, half sandwich system. There is a slight deviation from full linearity to an angle of 173° between the Cp-Cu-C bond and an angle of 177° for the N-C-Cu bond. This deviation is thought to be due to crystal packing effects. The Cu-Cp_(centroid) distance is 1.849Å and Cu-C distance is 1.8152Å.

The TGA for CpCu(^tBuNC) is given in **Figure 85**. A mass drop begins at a temperature of 100°C and extends to 175°C relating to volatilisation of the precursor, with the mass loss being 76.3%. From 200°C onwards there is a much slower rate of mass loss as the species here is less volatile than the main precursor. The plateau weight of 21.5% is less than the expected 34% which would correlate to copper metal. This shows that volatilisation of the compound containing the copper metal is possible.

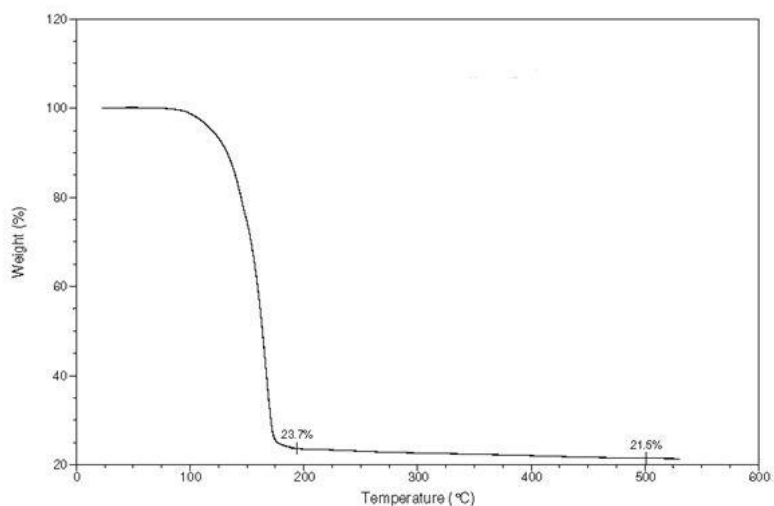


Figure 85 TGA of CpCu(^tBuNC).

The TGA curve provided an indication of the temperature required to transport the precursor.

Further information was gained from measuring the vapour pressure of $\text{CpCu}(\text{}^t\text{BuNC})$ various temperatures, **Figure 86**.

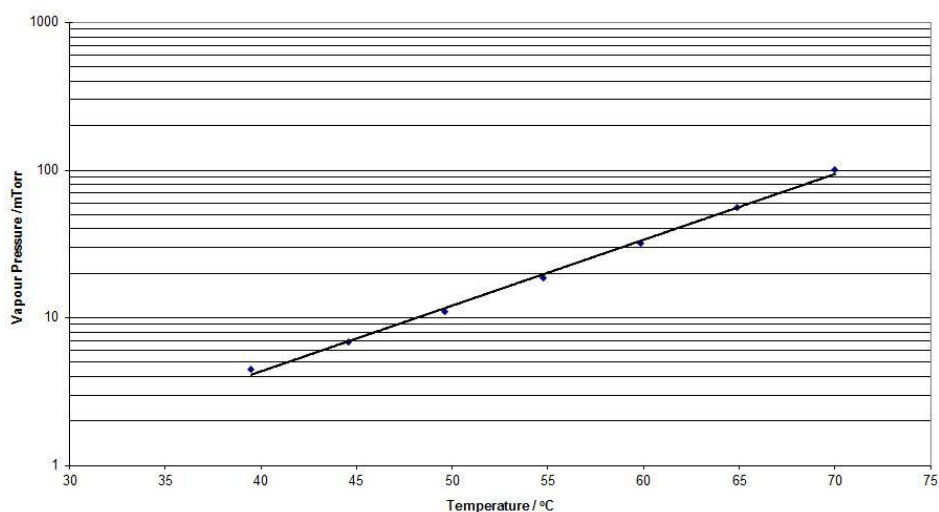


Figure 86 Vapour pressure of $\text{CpCu}(\text{}^t\text{BuNC})$.

The overall vapour pressure equation is:

$$\text{Log}_{10}P(\text{mTorr}) = -4772.5/T(\text{Kelvin}) + 15.863$$

For the deposition of this molecule, the precursor was held at a temperature of 100°C , giving a vapour pressure of 1.183T. This confirms the suitable volatility of the precursor for ALD and CVD processes.

To assess the thermal stability of the precursor, an isothermal TGA and ^1H NMR study was completed at 100°C (temperature the precursor was held at) and 140°C (the reported decomposition temperature)³⁰⁵. The isothermal TGA at 100°C is shown in **Figure 87**. For this method the precursor is charged into the pan, the temperature then jumps to the required temperature, then stabilises. The precursor is then held at this temperature for a specified length of time. For this case the temperature was 100°C and the run time 16 hours.

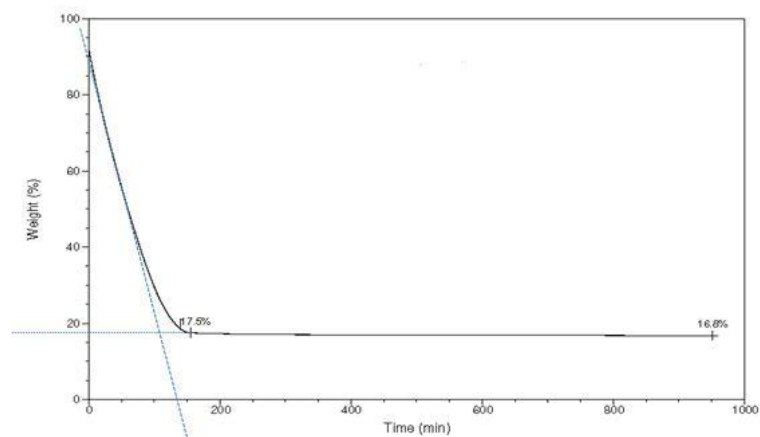


Figure 87 Isothermal TGA at 100°C.

The mass loss after 0 minutes is approximately 8%, this is attributed to volatilisation of the precursor before the 100°C temperature is reached. The rate of volatilisation is given by the gradient of the line. It is expected that this rate would remain constant, however in this case there is a slight change in rate just after 75 minutes. This change of rate can be explained by the physical changes in the TGA pan. As the mass decreases, the surface area also changes which has resulted in an apparent rate suppression. After 180 minutes the mass loss is extremely slow with the majority of the remaining material no longer volatile at 100°C. Again the final residue is less than pure copper suggesting vapourisation of the complete precursor molecule.

To try to gain an understanding of what the final residue could be, a sample of the material was charged into an NMR tube and subjected to 100°C for 16 hours. Deuterated benzene was added and ^1H NMR ran (**Figure 88**).

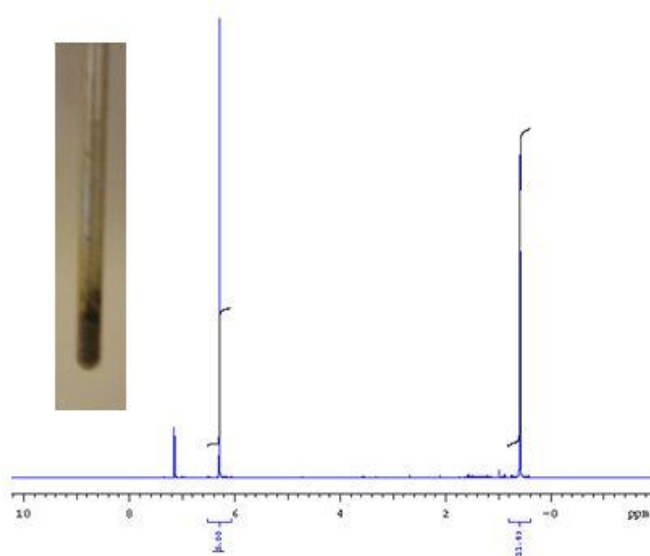


Figure 88 ^1H NMR for $\text{CpCu}(\text{tBuNC})$ after being held at 100°C for 16 hours.

From the photograph insert it is evident there is some colour change which must be attributed to thermal decomposition. Not all of the sample was soluble in the deuterated solvent, however, the spectra shows of that material that was soluble, the product still remains intact.

The isothermal TGA recorded at 140°C is shown in **Figure 89**.

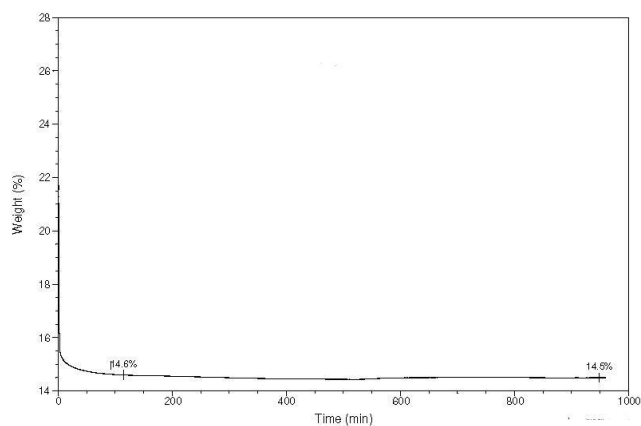


Figure 89 Isothermal TGA at 140°C for $\text{CpCu}(\text{tBuNC})$.

Note how the mass loss is $\sim 75\%$ before the sample has reached temperature. There is no further mass loss after 10 minutes. This indicates the rate of vapourisation is greater than the rate of decomposition. This is further confirmed by a lower final

residue of 14.5%. On completing a similar thermal NMR study to that at 100°C, the thermal decomposition was more evident with the sample much darker in colour. On running the NMR for this sample, very little was soluble. The 2% final residue difference for the isothermal samples at 100°C vs 140°C could account for the soluble material.

Thin film growth was trialled with $\text{CpCu}(\text{}^t\text{BuNC})$ in the following 5 schemes:

- Thermal decomposition with no co-reactant
- ALD with water co-reagent
- ALD with O_2 plasma co-reagent
- ALD with H_2 plasma co-reagent
- ALD with tertiary butyl hydrazine co-reagent

Both thermal decomposition and using H_2 plasma as a co-reagent gave metallic copper films, whilst, water and O_2 plasma gave Cu_2O and CuO respectively. With tertiary butyl hydrazine no growth was observed. In the following sections each growth regime will be discussed with regards to growth rates and temperature dependence, followed subsequently with characterisation, including comparisons, of the film and material characteristics achieved with each deposition system.

5.2 Deposition of Metallic Copper Films

5.2.1 Thermal Decomposition

In this section we compare the thermal decomposition of $\text{Cu}(\text{hfac})(\text{COD})$ and $\text{CpCu}(\text{}^t\text{BuNC})$ in the absence of a co-reagent. This approach will enable a baseline for the decomposition of both precursors to be established as a function of temperature and to highlight the onset of CVD-like growth. Copper films from both precursors were deposited onto silicon and borosilicate glass substrates. For the $\text{Cu}(\text{hfac})(\text{COD})$ precursor, a liquid injection methodology was employed. The copper compound was dissolved in toluene to give a solution of 0.65M. The

precursor was dosed in the reactor via a 2s pulse, followed by a 3s, 200sccm argon purge. A total volume of 20ml of Cu(hfac)(COD) was consumed.

Figure 90 shows the two temperatures recorded for thermal decomposition with Cu(hfac)(COD), with these data points included for reference only.

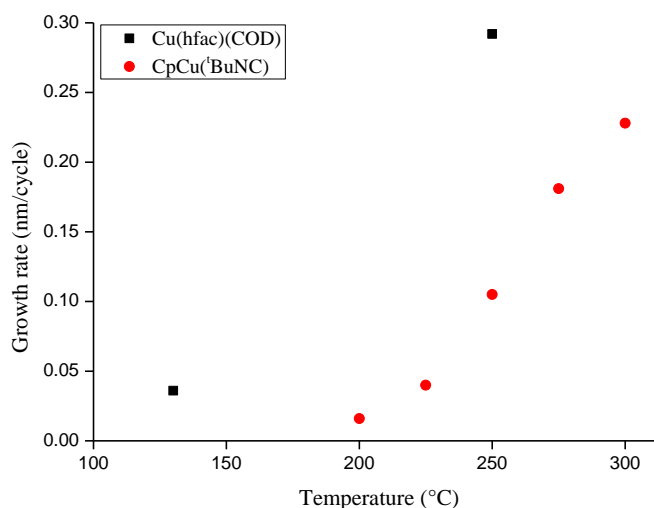


Figure 90 Thermal decomposition growth rates for Cu(hfac)(COD) and CpCu(tBuNC).

At room temperature, stored in the reactor vessel under an argon purge, decomposition of the precursor was observed, this is commented on further in **section 5.3.1**. In addition, due to the fact reflective films were deposited, weight gain was the method of choice over ellipsometry for determining film thickness. The stage of this reactor is a rotatable disc approximately 5cm in diameter. This size limitation resulted in small pieces of substrates with an unidentified surface area being used, leading to inaccuracies with film thickness. This calculation also involves the density of copper. The literature value of 8.92g/cm^3 was used which again adds inaccuracies as the copper films deposited are unlikely to be the most dense and highest purity. The data recorded helped to prove that at temperatures of 130°C and 250°C , a CVD component was observed, with growth rates of

0.04nm/cycle and 0.29nm/cycle respectively. The CVD component was further confirmed by visual inspection of the films after growth, with photographs of the deposited material shown in **Figure 91**.



Figure 91 Copper film deposited from Cu(hfac)(COD) on glass at 250°C with no co-reagent.

This experiment provided useful information. For previous growth runs, on opening the reactor to atmosphere when hot (250°C), the samples changed from a copper colour to a purple colouration, suggesting surface oxidation. This led to a change in approach when trying to deposit copper metal. The reactor was always cooled to below 100°C before exposing the samples to air to try to prevent thermal oxidation of the film. Deposition on silicon from CpCu(tBuNC) in the absence of a co-reagent was also trialled, and is again shown in **Figure 90**. Thermal decomposition was investigated using 2s doses and 3s purges. An Arrhenius – type increase in growth rate occurs with increasing substrate temperature. Although growth runs were completed between 100 and 175°C, the lowest temperature at which growth was detected was at 200°C, this was approximately 0.02nm/cycle. Due to the lack of co-reagent, this growth is attributed to decomposition of the molecule and indicates a CVD process. Temperatures below 200°C correspond to the region of kinetic control where there is insufficient energy for the molecule to be adsorbed onto the surface. The maximum growth rate of 0.23nm/cycle was observed at 300°C. Above this temperature, either pre-reaction of the precursor with the walls of the chamber or desorption from the substrate could explain the reduced growth rate. Comparing the thermal decomposition of the two precursors, for Cu(hfac)(COD) the onset of

growth is at 70°C lower than that of CpCu(^tBuNC). At 250°C the growth rate is higher for Cu(hfac)(COD) suggesting that this is the least thermally stable of the two precursors. The films deposited at 250°C from both precursors were characterised by XRD and are presented in **Figure 92**.

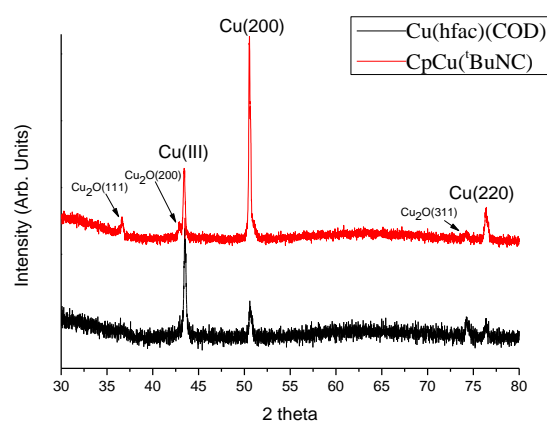


Figure 92 XRD for as-deposited films from CpCu(^tBuNC) and Cu(hfac)(COD) at 250°C on glass.

The as-deposited films were polycrystalline copper with films deposited from CpCu(^tBuNC) having preferential orientation in the (200) direction, and Cu(hfac)(COD) in the (111) direction. Looking at the CpCu(^tBuNC) trace, the peaks at approximately 36° and 74° correspond to Cu₂O (111) and (311) respectively and the shoulder at 47° could be from Cu₂O (200). Looking at the Cu(hfac)(COD) the Cu₂O (311) peak is evident. Although some of the smaller peaks could be attributed to CuO due to similar peak position, Cu₂O is more likely to be formed on surface oxidation. The surface morphology of the deposited films was examined by SEM and images for the as deposited samples from thermal decomposition of both precursors at 250°C are shown in **Table 25**. The scale of the images is not comparable for the two precursors, however, the difference in film morphology is instantly noticeable.

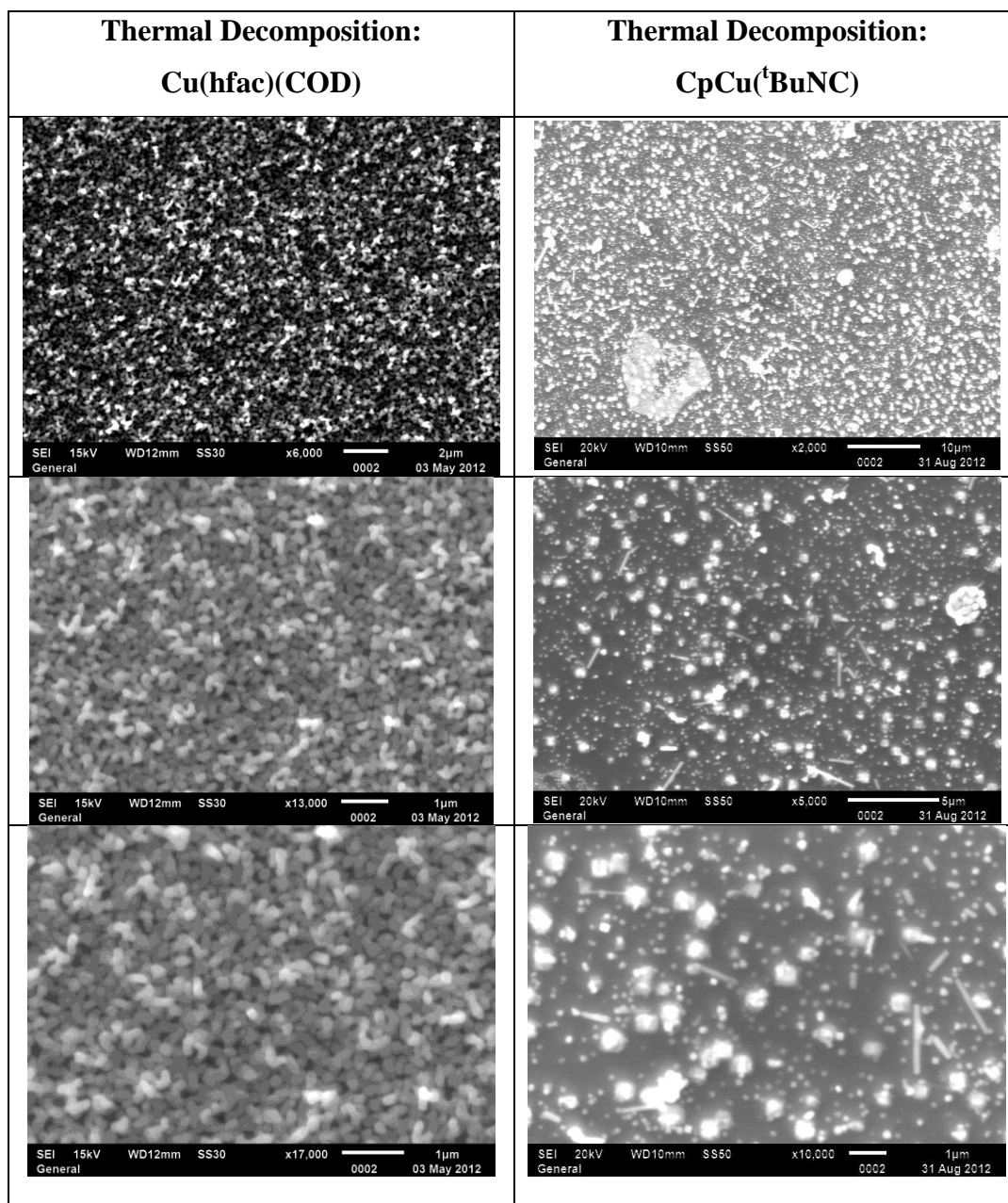


Table 25 SEM images for films deposited from Cu(hfac)(COD) and CpCu(^tBuNC) without co-reagent at 250°C.

The samples from Cu(hfac)(COD) deposition show dense films of long particles (with the longest approximately 500nm). There appears to be a tendency of agglomeration than the formation of a continuous film, with areas appearing more dense than others. CpCu(^tBuNC) deposited films are much more random. The nucleation density is much reduced, and small spherical particulates, cubic particle and rod structures are all observed. Four point probe measurements for the

Cu(hfac)(COD) gave a sheet resistance on glass of $0.826\Omega/\square$. CpCu(^tBuNC) samples on glass were tested but appeared non-conductive. The SEM images **Table 25** help to explain this result. The copper deposited in the case of Cu(hfac)(COD) although is non-uniform, covers the substrate. On bringing the four point probes to the surface, there is a network of copper crystalites which is able to carry the current and provide a measurement. Conversely, this is not the case for CpCu(^tBuNC), and to enable a conductive copper metal to be formed, surface reactions need to be analysed and a method employed to increase the density of nucleation sites.

5.2.2 TertiaryButyl Hydrazine

Due to the poor film coverage and uniformity of the copper layers grown via thermal decomposition of the two precursors, the next step was to analyse any improvements seen with the use of tertiary butyl hydrazine. This chemical is a stronger protonating agent than water and alcohol and also acts as a reducing agent. Typical pka values for hydrazines range from 6.56 for trimethyl hydrazine³⁰⁸ to 8.1 for tertiary butyl hydrazine.³⁰⁹ Water (pka value of 15.7) and alcohols (e.g. methanol and isopropanol with pka values of 15.5 and 16.5 respectively)³¹⁰, are less acidic than the hydrazines and are therefore less likely to donate protons. As discussed in **Chapter 3**, Cu(hfac)(COD) is quite unstable. At temperature in the reactor, the COD ligand dissociates from the copper. The hfac ligand system accepts the proton from the hydrazine, allowing a lower temperature, cleaner decomposition route. A prior project at the University of Liverpool had focused on the deposition of silver metal from Ag(hfac)(COD). Previously silver metal has been deposited using alcohol as co-reagent. It was proven that by using tertiary butyl hydrazine co-reagent, the deposition temperature was extended to a lower temperature from 130°C with alcohol to a temperature of 60°C with the tertiary butyl hydrazine³¹¹. For the silver

application, a conductive film of approximately 4nm was required. With alcohol, to overcome the formation of islands, thicker films were required to enable the islands to coalesce and form co-herent, conductive films. With hydrazine, a lower growth temperature, ensured the surface mobility of the silver species was reduced which led to an increase in density of smaller nuclei. At 80°C, conductive films were grown which fell within the specification. From reading the prior work conducted for copper metal deposition in chapter 2, it is apparent that copper too has a tendency to grow in islands. It was hoped that by using tertiary butyl hydrazine, the same benefits would be gained with the copper as for the silver. A further deposition study was carried out again using liquid injection ALD of Cu(hfac)(COD) and standard ALD for CpCu(^tBuNC). The method employed can be termed ALD as the cyclic alternate dosing of the copper reagent with the hydrazine ensured that the film deposited was dependent upon the saturative surface reactions. Although there was not an extensive study with the latter precursor, in all cases, no film growth was observed with CpCu(^tBuNC) and hydrazine. The growth conditions used in the case of Cu(hfac)(COD) are summarised in **Table 26**. The precursor was delivered to the chamber by liquid injection and subsequent flash evaporation, whereas the tertiary butyl hydrazine was delivered as neat precursor vapours by a vapour draw set-up.

Precursor	Cu(hfac)(COD) 0.65M toluene solution
Co-reagent	None/tertiary butyl hydrazine
Substrate Temperature (°C)	130 and 250
Substrate	Si(100), TaN and borosilicate glass
Flow rate through precursor (sccm)	30
Vapourisation Temperature (°C)	130
Flow rate of Argon through lines (sccm)	200
System pressure (mbar)	5
ALD recipe	2s/2s/0.1s/2s.
Run time (mins)	10-60
Film appearance	Reflective copper metal

Table 26 Conditions used for the thermal decomposition of Cu(hfac)(COD).

Analysis by XRD, **Figure 93**, of the sample deposited on glass at 250°C with tertiary butyl hydrazine confirms the growth of copper metal with a preferential Cu(111) orientation. Interestingly, when compared with the sample grown via thermal decomposition, both show polycrystalline copper with (111) and (200) orientation, although, note that for the hydrazine sample, the possible Cu₂O (311) peak is no longer visible. This could mean less surface oxidation has occurred due to the actual structure of the film formed, or the chemical reaction has terminated with and increased oxygen resistant surface.

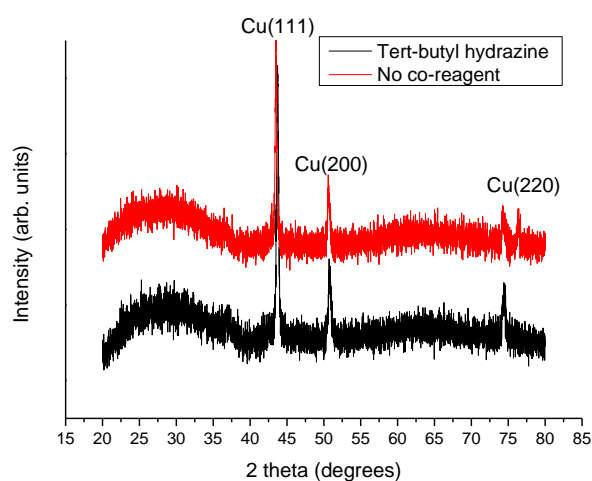


Figure 93 XRD trace of copper deposited from Cu(hfac)(COD) on glass via both thermal decomposition and with a tertiary butyl hydrazine coreagent at 250°C.

The film morphology was analysed by SEM. A photograph of the deposited films and a side-by-side comparison of films grown at 250°C without co-reagent (left hand column) and with tertiary butyl hydrazine (right hand column) for Cu(hfac)(COD) is shown in **Table 27**. Both of these samples appeared copper in colour on removing from the reactor, although the tertiary butyl hydrazine showed some pink colouration.



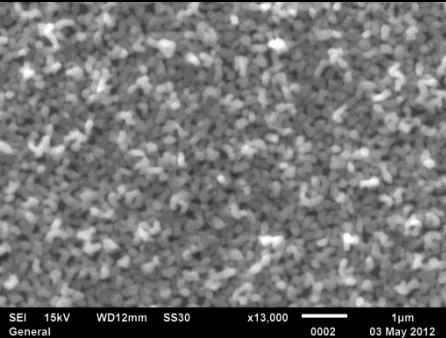
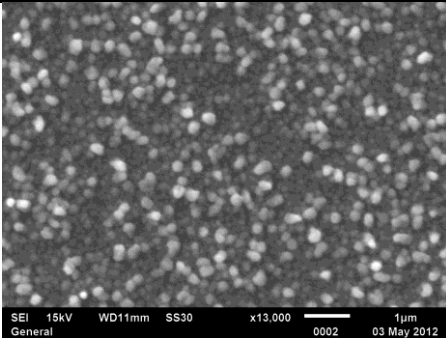
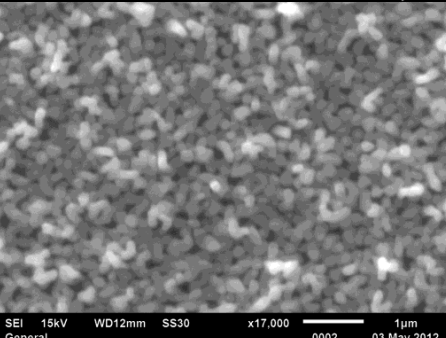
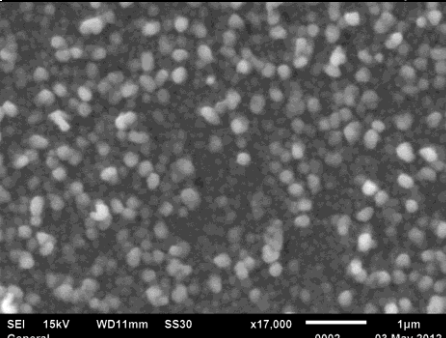
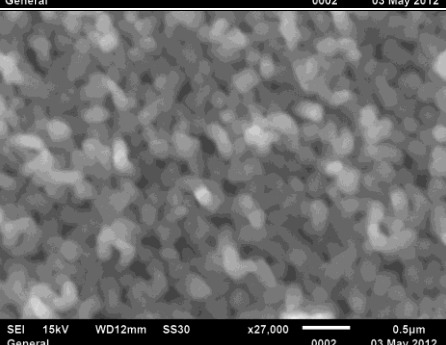
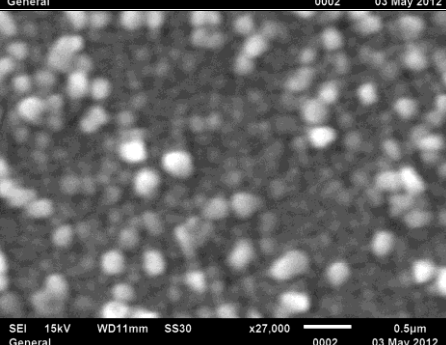
Thermal Decomposition	ALD with tertiary butyl hydrazine
250°C, 20ml precursor consumed, T=174Å	250°C, 20ml precursor consumed, 325cycles of 2s/2s/0.1s/2s. T=240 Å
	
	
	
	

Table 27 SEM images for films deposited using Cu(hfac)(COD) via thermal decomposition and with tertiary butyl hydrazine co-reagent on Si(100) at 250°C.

There is an increased growth rate observed when the more reactive tertiary butyl hydrazine is used. Note also that there is change in particle shape, for the thermal decomposition sample they appear more ‘worm-like’ whilst for the samples deposited with tertiary butyl hydrazine, they appear much more spherical. Looking more closely, the right hand side column also appears to show smaller particles

under a layer of larger, more randomly spaced larger particles. This phenomenon was highlighted in **Chapter 3**. From subsequent EDX studies, copper metal with limited oxygen seems to have been deposited in both cases. Interestingly on obtaining four point probe measurements, when no co-reagent was used, the glass sample recorded a sheet resistance of $0.826\Omega/\square$. When tertiary butyl hydrazine was used, conductivity measurements proved difficult to measure. This could be attributed too the potential of oxide formation but this is ruled out by XRD. Other reasons may be due to the formation of a non-continuous film or that a thin film has been deposited which is being punctured on undertaking four point probe measurements.

At a temperature of 130°C , with tertiary butyl hydrazine, a film with a target thickness of 3-5nm was deposited, but due to the limitations of analytical techniques, they are difficult to analyse by XRD and SEM. EDX data was collected which supported the growth of copper due to the lack of oxygen peak in the final spectra. A TEM sample was prepared during this growth run, with a holey carbon nickel mesh TEM grid used. **Figure 94a** is an image taken over a wide area at low magnification to show the deposited film and support. **Figure 94b** has a scale of 100nm and shows a large particle to the right of one of the holes of the support, by **Figure 94c**, it can be observed that the large particle is not spherical, and has a length of approximately 50nm. At this scale, the large particle appears to show some crystallinity, and a layer of much smaller particles are observed.

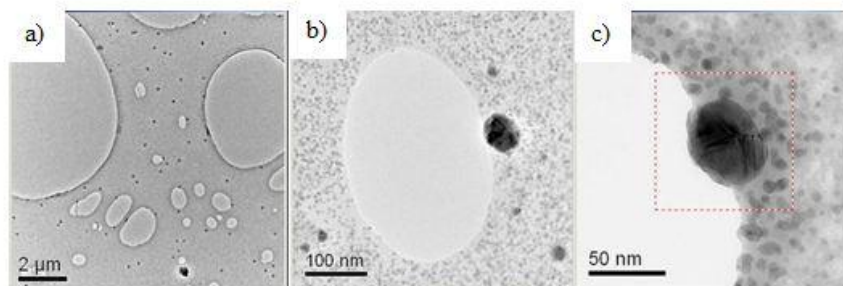


Figure 94 TEM images of the copper film grown with Cu(hfac)(COD) and tertiary butyl hydrazine(2s/2s/0.1s/2s) on a nickel mesh holey carbon grid.

To complete the TEM study, a diffraction pattern was collected over an area with smaller grains, these are shown in **Figure 95**

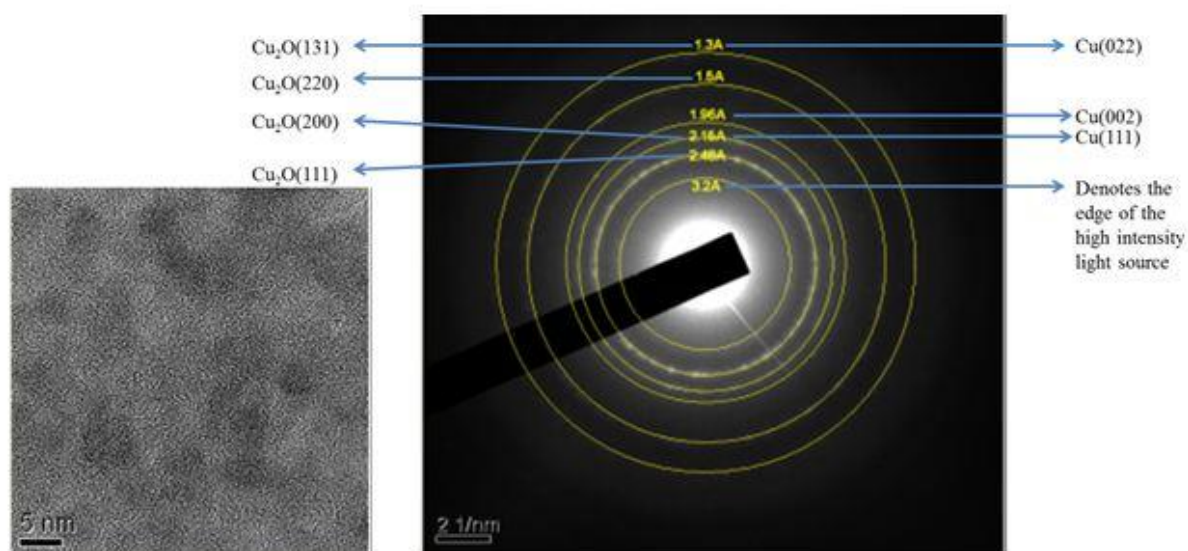


Figure 95 Diffraction pattern from TEM . The left hand side shows the image of the area from which a diffraction pattern was taken, with the characterised diffraction pattern on the right.

The diffraction patterns of copper and both oxides are difficult to analyse due to overlaps of d-spacings. It is easy to dismiss CuO. Cu₂O could have formed due to surface oxidation. Cu peaks are evident although due to the thin film, conductivity measurements proved elusive. From the TEM results, there is information to suggest that the tertiary butyl hydrazine is advantageous in the growth of continuous copper

films. However, the problems encountered with the stability of the Cu(hfac)(COD) was enough to direct the research to investigate a new copper precursor.

5.2.3 Hydrogen plasma

The Cu(hfac)(COD) with tertiary butyl hydrazine provided some encouraging results. With CpCu(^tBuNC) and tertiary butyl hydrazine, copper deposition remained elusive, so a stronger reducing agent, namely hydrogen plasma was trialled.

Table 28 shows a summary of the conditions used for the deposition of copper films from CpCu(^tBuNC) with a hydrogen plasma.

Parameter	Value
Precursor temperature	100°C
Substrate temperature range	75-200°C
Bubbler flow rate	300sccm argon
Hydrogen plasma conditions	300W, pulse 3s, purge 5s
Precursor conditions	pulse 2s, purge 3s

Table 28 Growth parameters used for copper metal deposition using CpCu(^tBuNC) and hydrogen plasma.

From results mentioned earlier when no co-reagent was employed, growth from below 200°C was unmeasurable. In this instance, when the substrate was exposed to a hydrogen plasma after the precursor pulse, growth below 200°C was recorded, the precursor is now behaving according to ALD with no measureable CVD component, this is shown in **Figure 96**.

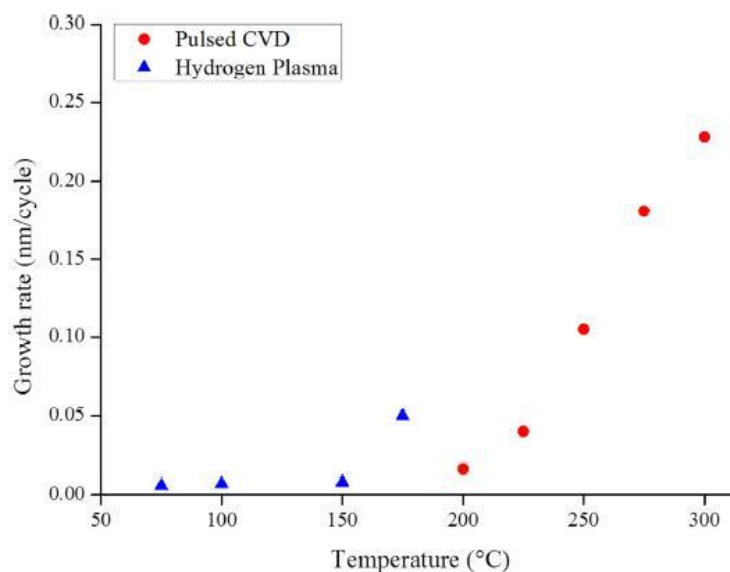


Figure 96 Variation of growth rate for $\text{CpCu}(\text{tBuNC})$ for pulsed CVD and hydrogen plasma-assisted ALD.

The growth rate recorded at a temperature of 75°C, 100°C, 150°C and 175°C were 0.006nm/cycle, 0.007nm/cycle, 0.008nm/cycle and 0.05nm/cycle respectively, based upon weight gain. The error in measurement can be attributed to the error in the balance (0.0001g), and the density of the film. The deposition was carried out on soda lime glass microscope slides (75mm x 25mm) to try to minimise discrepancies in the area. Further process optimization would be needed to enhance the growth rate. All films grown were metallic and highly reflective in appearance, this is shown in **Figure 97**. On visual inspection, all samples showed no colour grading indicating consistent growth across the substrates. The substrates were spread over the stage of the reactor, approximately 30cm diameter.



Figure 97 Photographs showing copper deposition on glass, silicon and TiN substrates. 10,000cycles, 100°C, H plasma, cooled under vacuum.

The hydrogen plasma ALD process was very slow, and a recipe time of 47 hours was required for these deposition runs. There would need to be process optimisation for this process to be used in industrial manufacturing. This section will discuss the deposition carried out at 75°C with 5000cycles. At this temperature Mellinex® 505 plastic was added as a substrate to see if low temperature deposition on a flexible substrate was possible, opening up the potential of many more applications. XRD data in **Figure 98** is recorded from the the as-deposited films which were shown to be predominantly orientated in the (111) direction for all substrates. For samples grown on Si, TiN and plastic some (200) direction is observed.

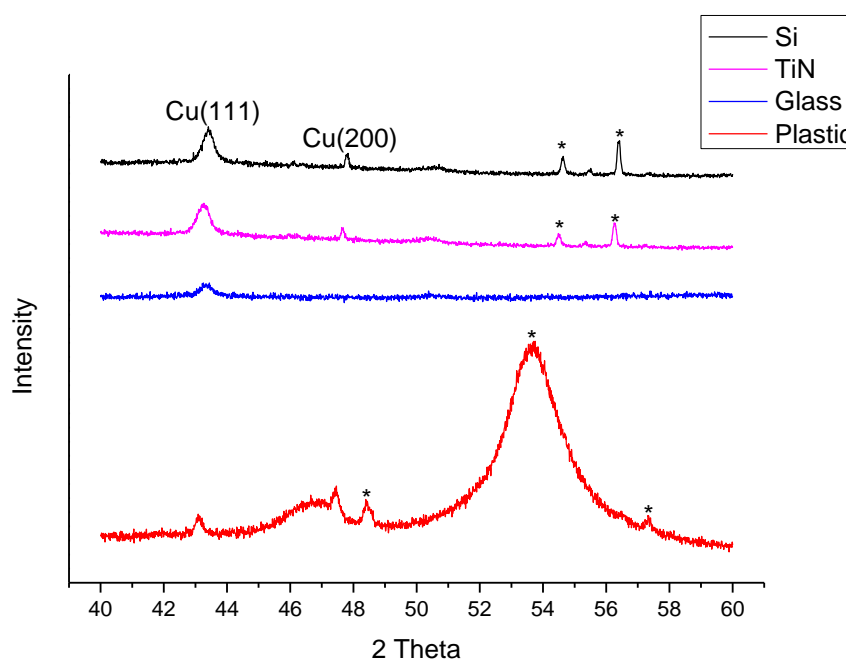


Figure 98 XRD for as-deposited samples from $\text{CpCu}(\text{tBuNC})$ and hydrogen plasma at 75°C. (* indicate substrate related features)

SEM was employed to study how the morphology of the films deposited at 75°C with H_2 plasma varied between substrates. **Figure 99** includes the images taken on all four substrates at a 50,000 magnification. The energies used for acquiring the images varied to optimise the quality of the images and reduce charging effects. Silicon and TiN were acquired with 15KV energy, Glass with 4KV and plastic at

2kV with a bias of 2000V. All working distances were 10mm except plastic, which was reduced to 3.5 mm to optimise resolution at this lower energy. Brightness and contrast levels have been changed.

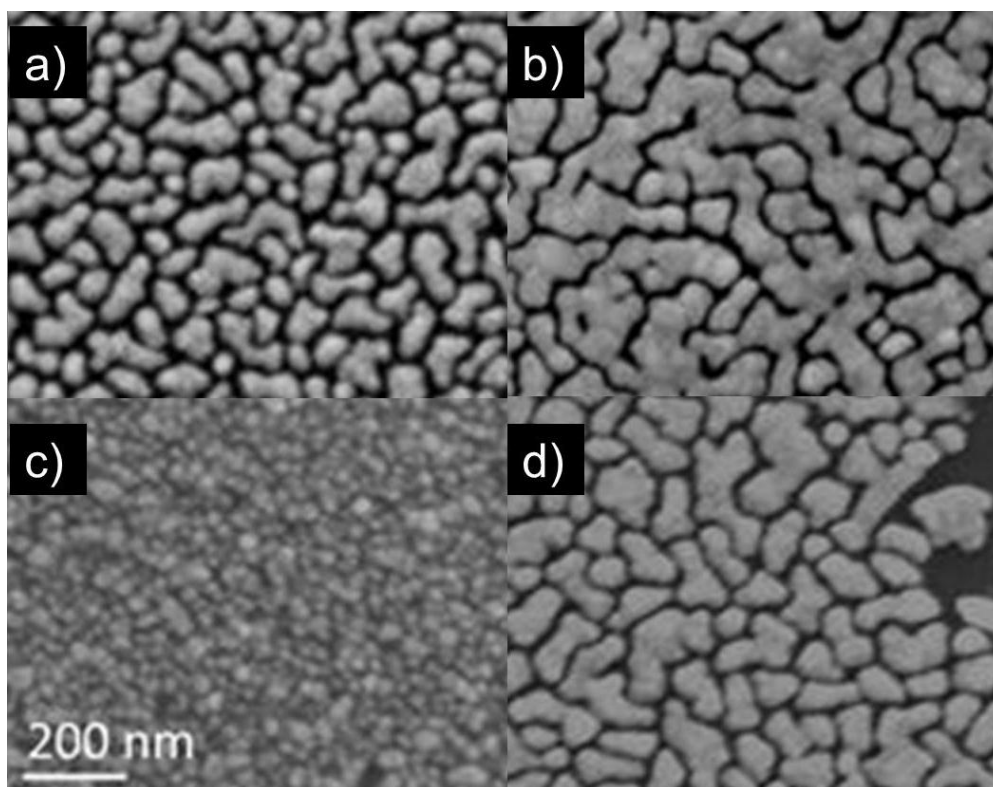


Figure 99 SEM study of the surface morphology of the Cu ALD film deposited on various substrates at 75°C at 10,000 magnification a) glass b) TiN c) Mellinex® 505 plastic and d) Si.

From inspection of the images, pin holes are observed for glass, TiN and Si surfaces. It is difficult to quantify average crystallite size due to the irregular shaping and connectivity of the crystallites. The image taken from the plastic substrate (c) is strikingly different. It reveals that the copper film is continuous and free of pin-holes and consists of small equiaxed grains. The average crystallite size appears much smaller, are more discrete and regularly spherical. There is an increase in density indicating improved nucleation or reduced surface mobility. The copper atoms preferential bond to each other rather than the substrate leading to island 3D growth.

This is typical of a Volmer-Weber growth mode. **Figure 99b** and **d** are images taken from TiN and silicon which show some agglomeration of the crystallites with TiN showing most coalesced material. This growth mode can be termed the Frank-van der Merwe method. The copper atoms are bound more strongly to the surface than each other, giving more 2D growth. The direction is along the surface due to increased surface mobility of the copper atoms. In the case of glass, the mode appears to be a cross between both 2D and 3D growth. The Stranski-Krastinov growth mode begins with 2D layer by layer growth, then a change in energetics of the surface can lead to 3D island growth. Some alluding to the growth mechanism has been reported previously by Li *et al.*²⁵² in which they used the Cu(aBu-amd)₂ (copper(I) N,N'-di-sec-butylacetactamidinate) precursor with hydrogen gas. They suggest that copper nucleates poorly on oxide surfaces and agglomerates leading to large copper nuclei and opening up access to additional reactive sites at which more copper precursor reacts. This could account for the appearance of the silicon and TiN samples as there are likely to have a small oxide layer at the interface with the copper film. Similarly, glass will have some –OH terminated groups for reaction, but overall, the surface mobility may be better or more nucleation sites available which are favourable in energy to grow rather than the copper growing on itself and forming islands. Previous literature indicates²⁵⁵ that by increasing the film thickness, connectivity between the crystallites is increased and likely to produce a dense network but with some voids leading to low resistivity films. From the images it can be concluded that the plastic substrate provides increased adhesion for the copper when compared to the other three substrates.

SEM was also used to look at the cross section of the copper film on silicon shown in **Figure 100**. Silicon was chosen as it was most easy to process (plastic is flexible,

glass much thicker) and image with little charging effects. To perform this technique a thin carbon and a thick platinum protection layer were used to cap the sample.

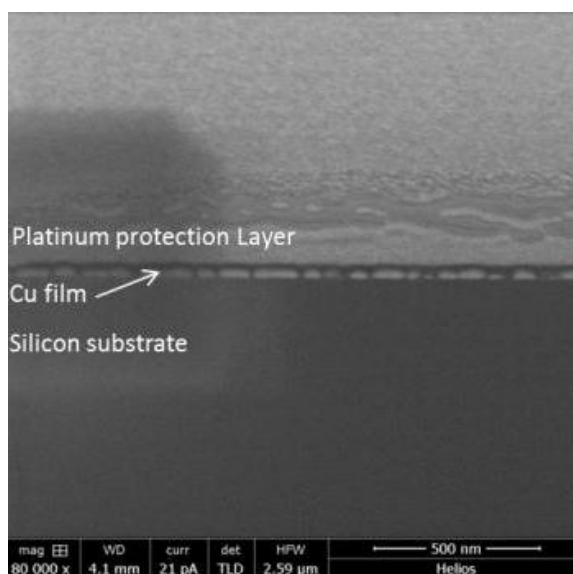


Figure 100 Cross section of a copper film grown at 75°C on silicon using $\text{CpCu}(\text{tBuNC})$ and a hydrogen plasma.

Figure 101 are the high tilt images acquired under an angle of 52° of the copper film on both silicon (left) and TiN (right). The film thickness was measured at 32nm, and some assumption is made in that the copper films deposited on all substrates at 75°C have a thickness of <50nm.

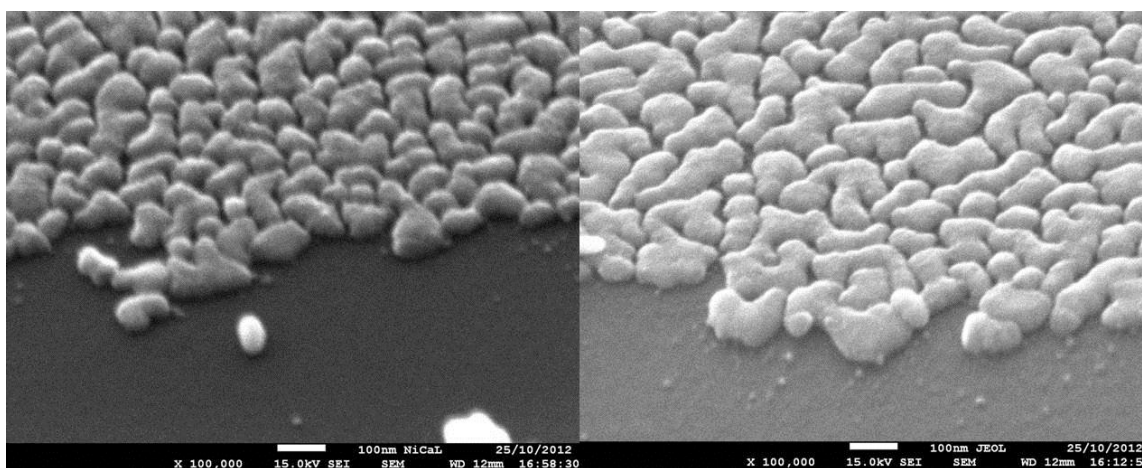


Figure 101 Copper films imaged at a high tilt angle on silicon and TiN (left and right respectively) deposited from $\text{CpCu}(\text{tBuNC})$ and hydrogen plasma.

A TEM study was also completed. **Figure 102a** is an image taken surveying a large area and showing the holey carbon grid. **Figure 102b** shows a distribution of densely packed clusters of nano-scale crystals forming a continuous film. **Figure 102c** and **d** shows overlapping, twinning crystals approximately 20nm in length. The presence of twins can be seen in several of the grains in the image. Twinning is observed where the lowest energy slip plane lies, and can be caused by stress in the film or the continuous in-situ annealing of underlying layers that takes place during long deposition runs.

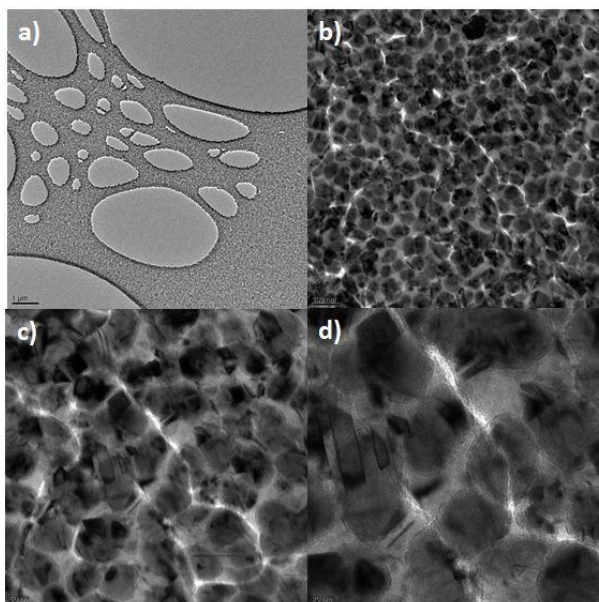


Figure 102 TEM of copper films deposited from $\text{CpCu}(\text{tBuNC})$ and hydrogen plasma at 75°C a) large area image showing the TEM support b) Brightfield micrograph taken at 200kV using a magnification of 20K c) showing twinned crystals d) greater magnification of area in c.

Looking at a higher magnification, **Figure 103**, atomic lattice imaging helps to show the crystalline properties of the material grown, and that the copper crystallites exhibit twinning. These films were confirmed by the diffraction pattern, **Figure 104** to be copper.

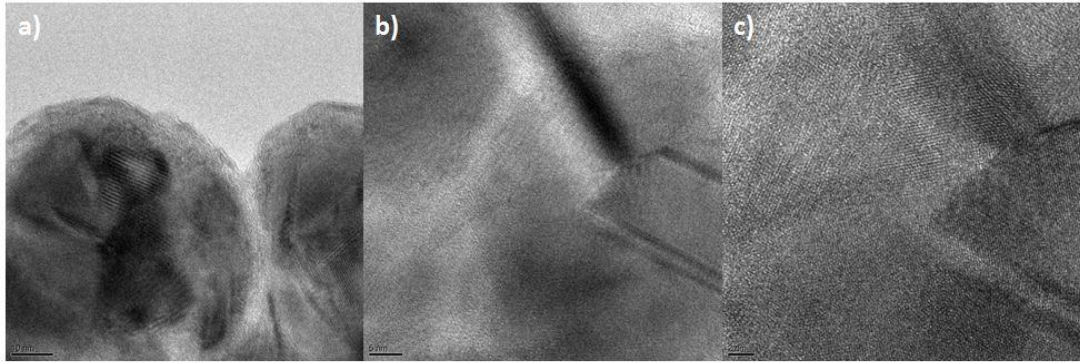


Figure 103 Atomic resolution TEM of copper films deposited from $\text{CpCu}(\text{}^t\text{BuNC})$ and hydrogen plasma. High resolution brightfield micrograph taken at 200kV using a magnification of a) 250K b) 400K c) 800K.

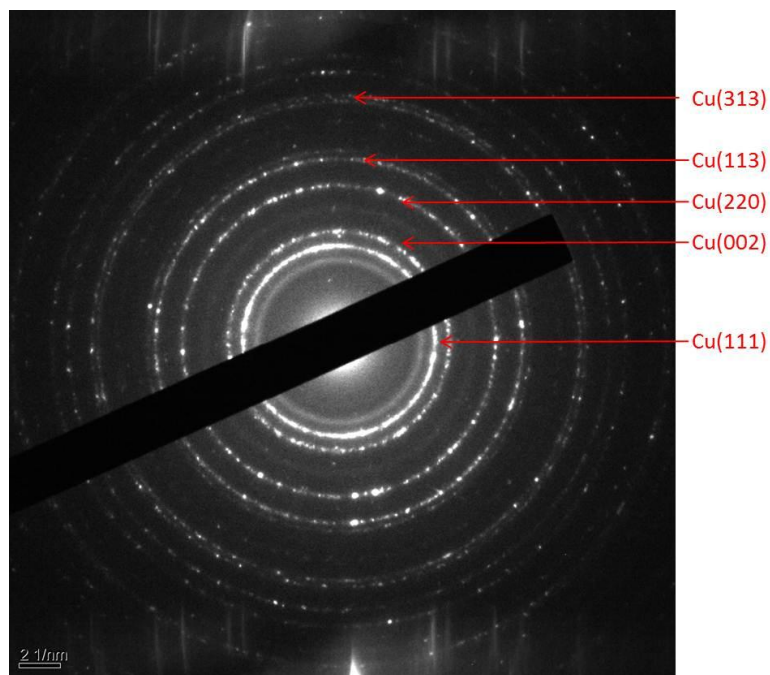


Figure 104 Diffraction pattern via TEM for the Copper film grown at 75°C using $\text{CpCu}(\text{}^t\text{BuNC})$ and hydrogen plasma.

EDX spectra together with electron energy loss spectroscopy (EELS) data presented here, shows that copper metal is deposited without significant oxygen content.

Figure 105 is the EELs spectra recorded for the sample grown at 75°C with a H₂ plasma.

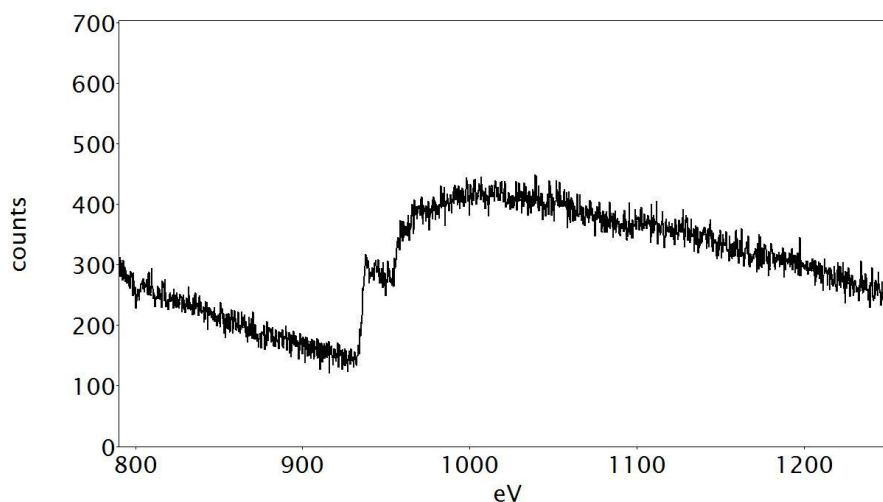


Figure 105 EELs spectra showing the characteristic copper metal peak at 925eV corresponding to the Cu-L2-3.

The EELs confirms the growth of high purity copper metal due to the characteristic trace and peak at approximately 925eV corresponding to the Cu-L2-3. The high purity of the film is further confirmed by **Figure 106** shows the lack of oxygen peak detected at the expected 530eV for oxygen.

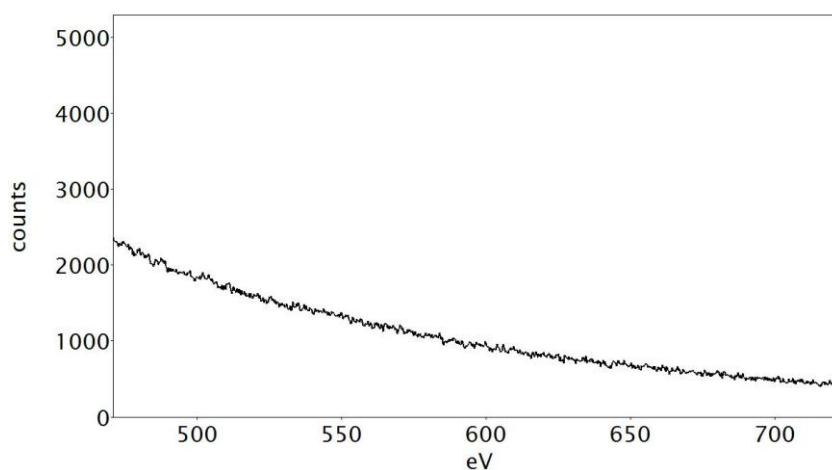


Figure 106 EELs spectra showing the lack of oxygen detected at 530eV.

The carbon and oxygen impurities were both low enough to give conductive copper films. The sheet resistance from the copper film grown on glass was measured using

a four point probe method. The sheet resistance was measured at numerous points over an area of 19.75cm^2 . All the results measured were consistent resulting in an average sheet resistance $0.55\Omega/\square$.

SEM and TEM methods were also used to investigate copper deposition at temperatures of 150°C and 175°C with hydrogen plasma. A selection of the data collected for 150°C will be discussed first. **Figure 107** shows the TEM images at 200nm, 50nm and 20nm scale.

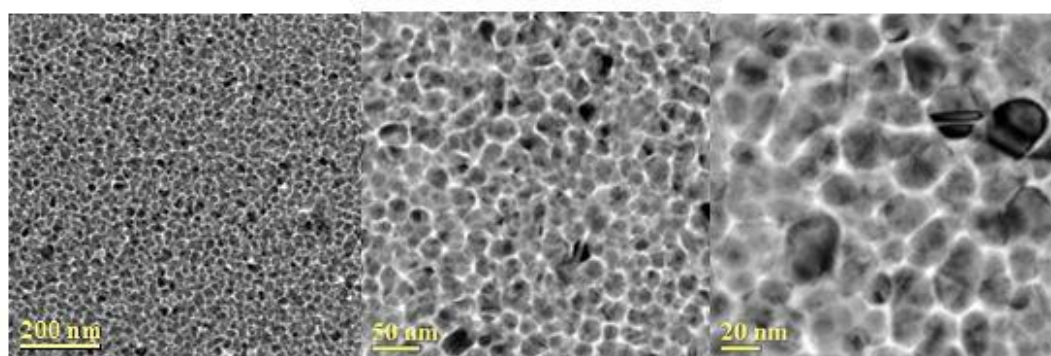


Figure 107 TEM images for copper film deposited at 150°C from 5000 cycles $\text{CpCu}(\text{tBuNC})$.

A continuous film is again observed. At the 20nm scale image, some twinning is shown. Overlapping grains are observed as the top and bottom of the TEM grid is being imaged simultaneously.

The diffraction pattern, **Figure 108**, confirms the growth of Cu metal with some Cu_2O . Although there is some overlap between the expected diffraction rings of CuO and Cu_2O , we can disregard CuO due to lack of bands at 1.4-1.6 which are all $>50\%$ intensity for CuO.

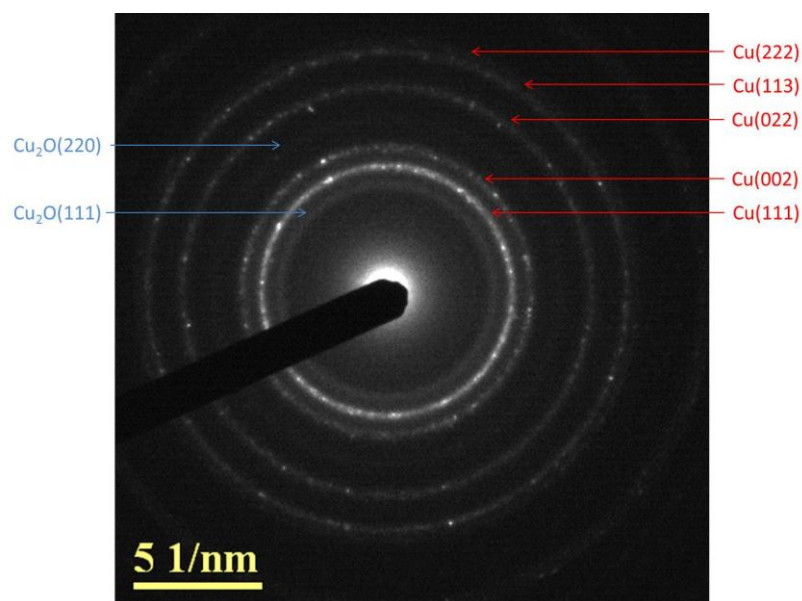


Figure 108 Diffraction pattern from the deposition at 150°C of CpCu(^tBuNC) and hydrogen plasma, 5000 cycles.

The TEM images generated from samples grown at 175°C are discussed next.

Figure 109 and **Figure 110** are 200nm and 20nm scale images respectively that show a distribution of densely packed clusters of nanoscale crystals which form a continuous film.

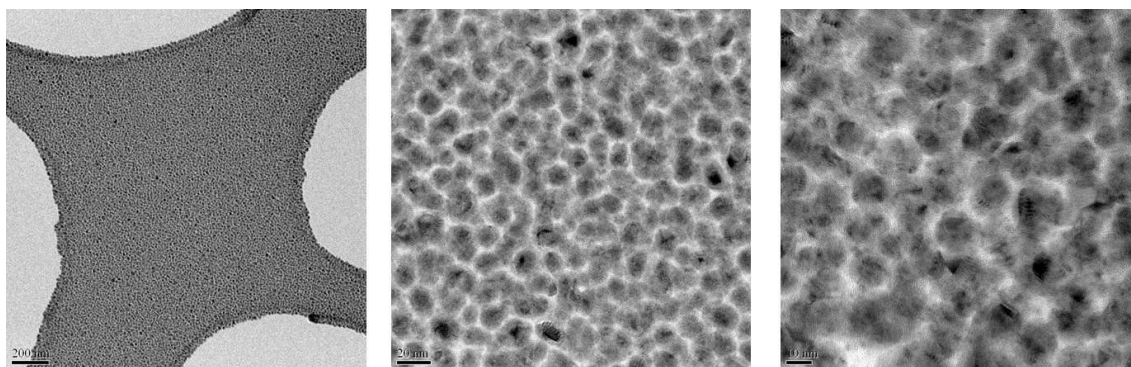


Figure 109 TEM images from the deposition of CpCu(^tBuNC) and hydrogen plasma at 175°C on a holey carbon grid at 200nm scale.

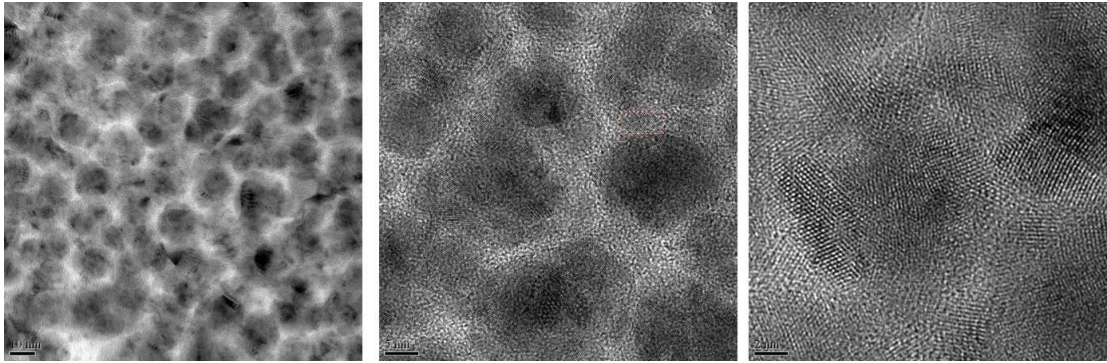


Figure 110 TEM images from the deposition of CpCu(tBuNC) and hydrogen plasma at 175°C on a holey carbon grid at 20nm scale.

Some basic statistical analysis was carried out. **Figure 111** shows the diameter of particles measured from a sample set of 114. The mean particle diameter was calculated to be 15nm.

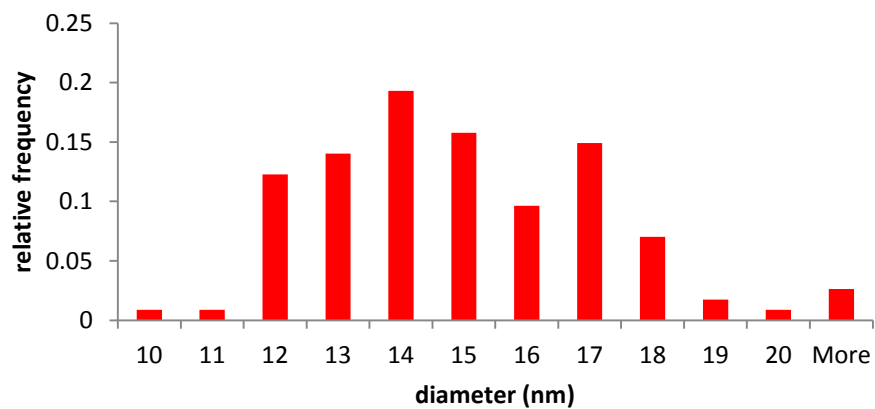


Figure 111 Statistical analysis of particle diameter.

Interestingly, at this temperature, the diffraction pattern, **Figure 112**, shows the d-spacings correlating to Cu₂O as well as Cu and this is further confirmed by the zone axis, **Figure 113**.

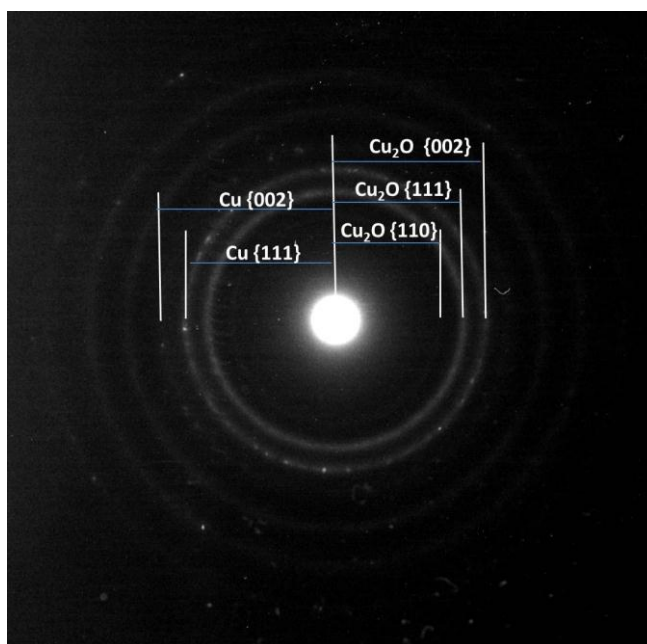


Figure 112 Diffraction pattern confirming both Cu and Cu₂O was deposited CpCu(^tBuNC) and hydrogen plasma at 175°C.

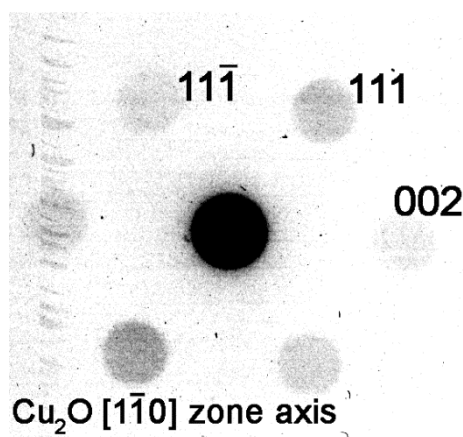


Figure 113 A spot pattern confirming the Cu₂O zone axis from the deposited CpCu(^tBuNC) and hydrogen plasma at 175°C.

The onset of the oxidation observed in the TEM by the characterisation of Cu₂O confirms the argument of the increased growth rate at 175°C shown in **Figure 96**.

5.3 Deposition of Cupric Oxide-CuO

5.3.1 Ozone

Figure 114 shows the film growth achieved from Cu(hfac)(COD) with ozone (2s precursor pulse /2s precursor purge/0.5s ozone pulse/2s ozone purge) for 500 cycles

over the temperature range from 100-350°C on silicon. Ozone was chosen as it is a more powerful oxidant than water or oxygen and it was hoped stoichiometric CuO would be formed.

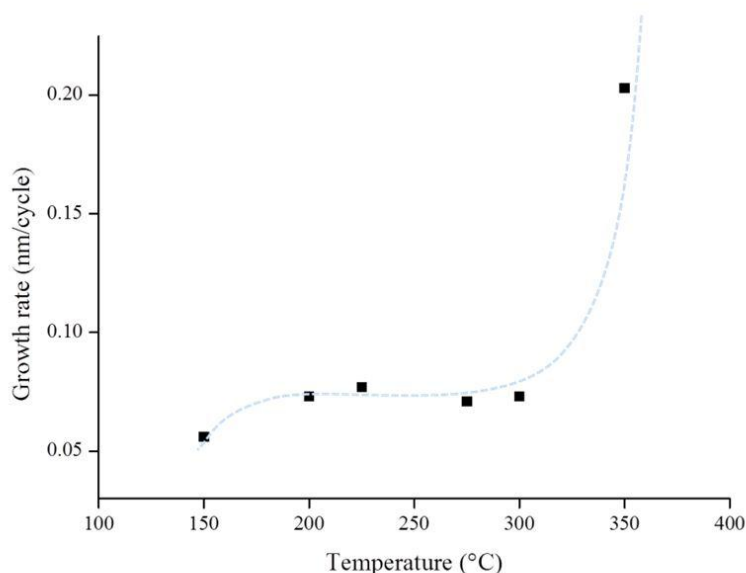
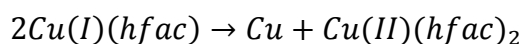
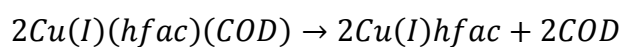


Figure 114 Growth curve for the ALD of Cu(hfac)(COD) with ozone.

The data here suggests a plateau in growth rate, the ALD window, between 200-300°C. At 150°C, there is limited energy for the precursor molecule to adhere to the silicon substrate, conversely, at 350°C there is a dramatic rise in growth rate and this can be attributed to thermal decomposition of the precursor. Although this precursor was handled and stored under nitrogen, its lifetime is limited. Should decomposition occur there is a drastic colour change from yellow Cu(I)(hfac)(COD) to green Cu(II)(hfac)₂. The change in oxidation state of the copper metal due to loss of ligands and is reported by Chi *et al.*³¹² where they propose the following decomposition route:



Analysis by XRD confirmed CuO was deposited for film deposition at all temperatures with Cu(hfac)(COD) and ozone, with characteristic peaks at 61° corresponding to CuO (113) and 69° CuO (113) observed. There is no obvious change in crystallinity with temperature.

The vibrational characteristics of the CuO layers were examined via Raman spectroscopy. The layers were excited with a 325nm UV laser (2 acquisitions of 30 seconds. 300 micron aperture size). The spectra taken from the CuO layers deposited on silicon for the range of temperatures is shown in **Figure 115**. Interestingly, there is an increase in the intensity of the CuO peaks at temperatures of 300°C and above. There is a lack of CuO peaks at 225°C and below. Silicon is denoted by the asterisks.

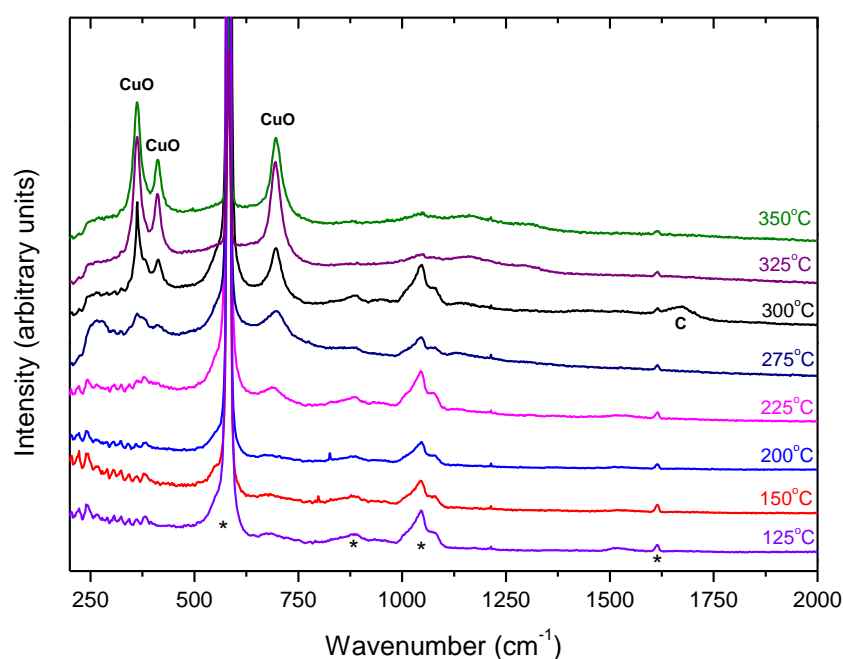


Figure 115 Raman spectra for as-deposited films from Cu(hfac)(COD) and ozone between 125°C and 350°C . (C is denoting the peak for carbon incorporation)

5.3.2 Oxygen Plasma

From the thermal decomposition study of $\text{CpCu}(\text{}^t\text{BuNC})$ (**Figure 96**), growth below 200°C and 175°C was unmeasurable, and the CVD component of growth was minimal, a stronger oxidant, namely O_2 plasma was then used to try to obtain film growth sub 200°C . At 150°C measurable growth ($0.012\text{nm}/\text{cycle}$) was observed.

The TEM images, given in **Figure 116**, show a dense continuous film with crystalline features visible on the 10nm scale.

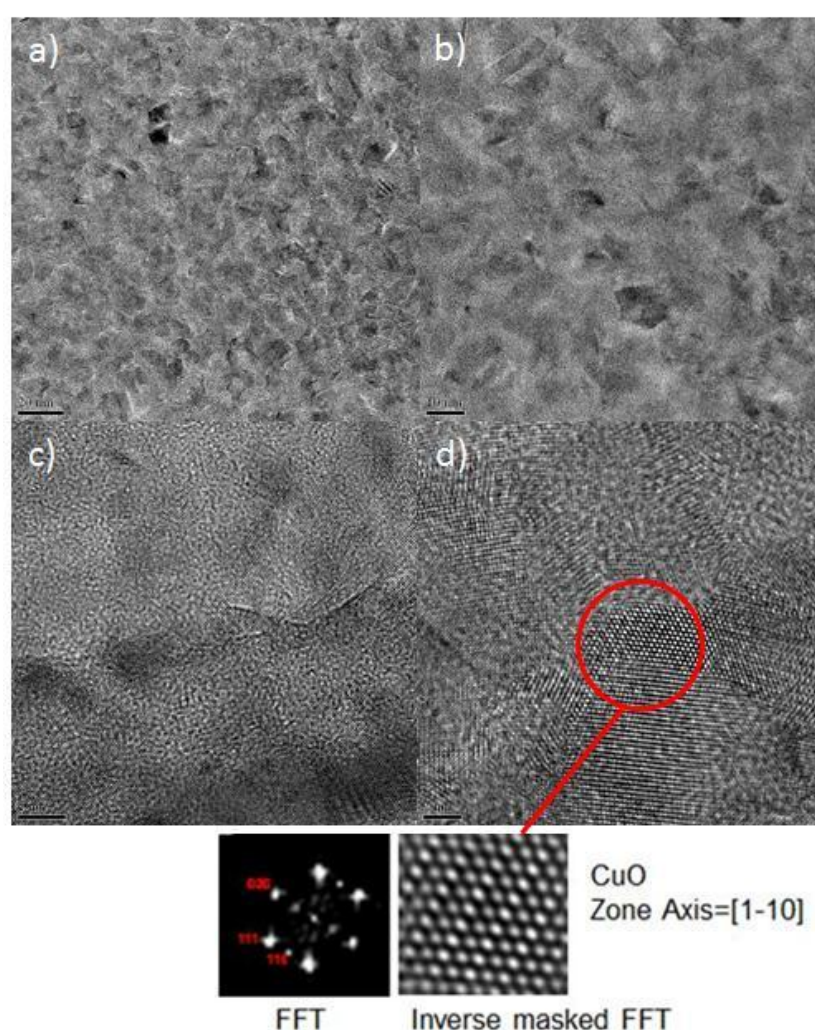


Figure 116 TEM images for the film deposited at 150°C with $\text{CpCu}(\text{}^t\text{BuNC})$ and oxygen plasma.

Atomic resolution was observed, **Figure 116d** and was further used to conduct analysis of the zone axis. The FFT is a process which deconstructs the periodic

features of an image into sine and cosine components. Each point in the transform represents a frequency in the image. An inverse FFT simply reverses this process and forms an image from the FFT pattern. If there is no processing of the FFT then you switch between the two images i.e. real image to spot pattern and back again. The reason we see discrete spots in the FFT is due to the periodic features (lattice planes and moiré fringes) in the original image. If the material contains no periodicity then the FFT does not either.

This data in addition to the diffraction pattern, **Figure 117**, confirms the CuO phase.

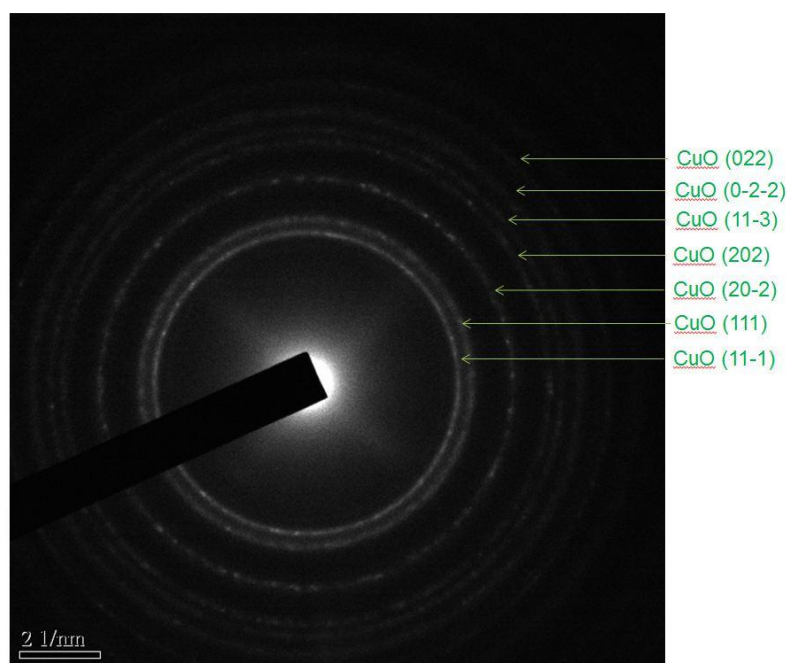


Figure 117 TEM diffraction pattern for the film deposited using CpCu(¹BuNC) and oxygen plasma at 150°C.

5.4 Deposition of Cuprous Oxide-Cu₂O

5.4.1 Water

On reaction of CpCu(¹BuNC) with water the growth rate/cycle was recorded over a temperature range of 150-350°C and is shown in **Figure 118**. The recipe followed a copper 2s pulse/3s purge, and a 0.02s water pulse/5s purge. The maximum growth rate of 0.156nm/cycle was achieved at a temperature of 275°C, a shift by 25°C when

compared to the thermal decomposition curve. The shift in deposition temperature, in addition to the altered growth rates indicated that the water was participating in the reaction.

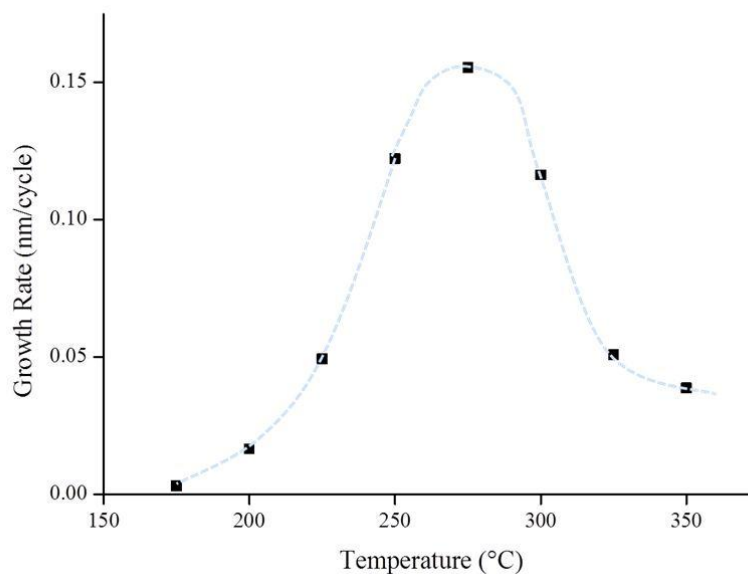


Figure 118 The growth rate for CpCu(^tBuNC) with water against the temperature range 175-350°C.

XRD for a sample grown with water at 175°C is shown in **Figure 119**. The characteristic peaks for Cu₂O were observed.

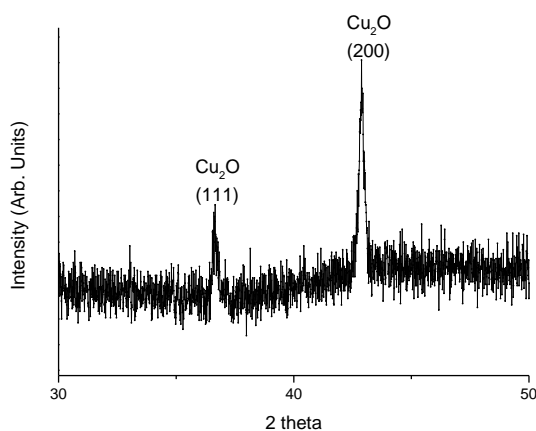


Figure 119 XRD for the film deposited with CpCu(^tBuNC) and water at 175°C.

TEM sample deposited at 175°C yielded the images in **Figure 120**.

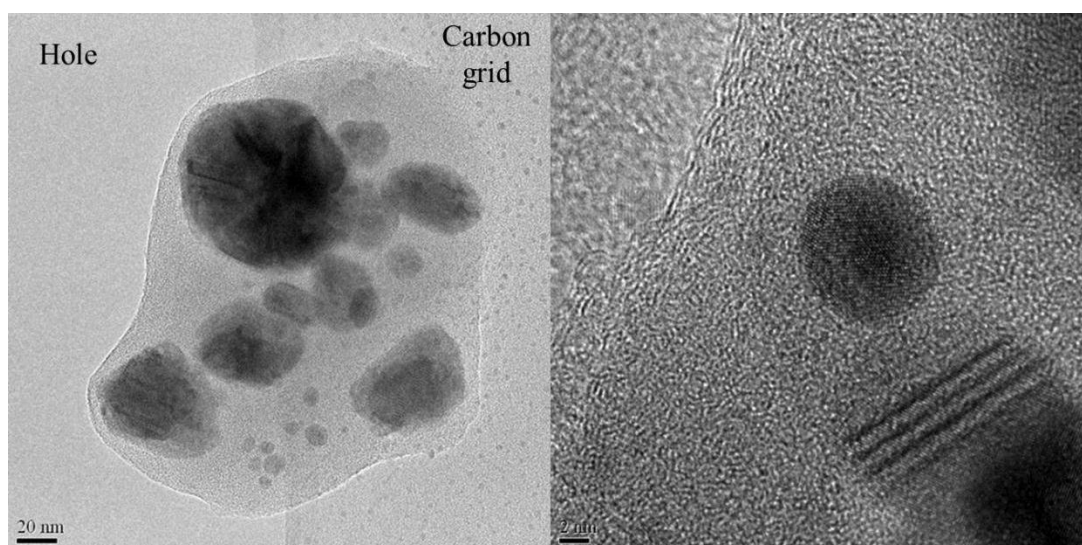


Figure 120 TEM images of deposited material from $\text{CpCu}(\text{}^t\text{BuNC})$ and water at 175°C.

Compared to the TEM images presented for all other co-reagents, the material deposited from $\text{CpCu}(\text{}^t\text{BuNC})$ appears strikingly different. There is no longer a continuous film. The image on the left hand side in **Figure 120** shows an amorphous material protruding from the mesh into one of the holes of the grid. Within the amorphous mass, there are distinct particles ranging in size from approximately 85nm in diameter, to just 5nm. The contrast of the particles help to show the increase in density of the material for the darker, and larger particles. The image on the right hand side of the figure, highlights that some crystalline material has been deposited, and twinning is observed. This image suggests a 2D type growth with some 3D islands. When FFT, **Figure 121**, was carried out on one of the particles, approximately 4nm in size, the Cu_2O zone axis was identified.

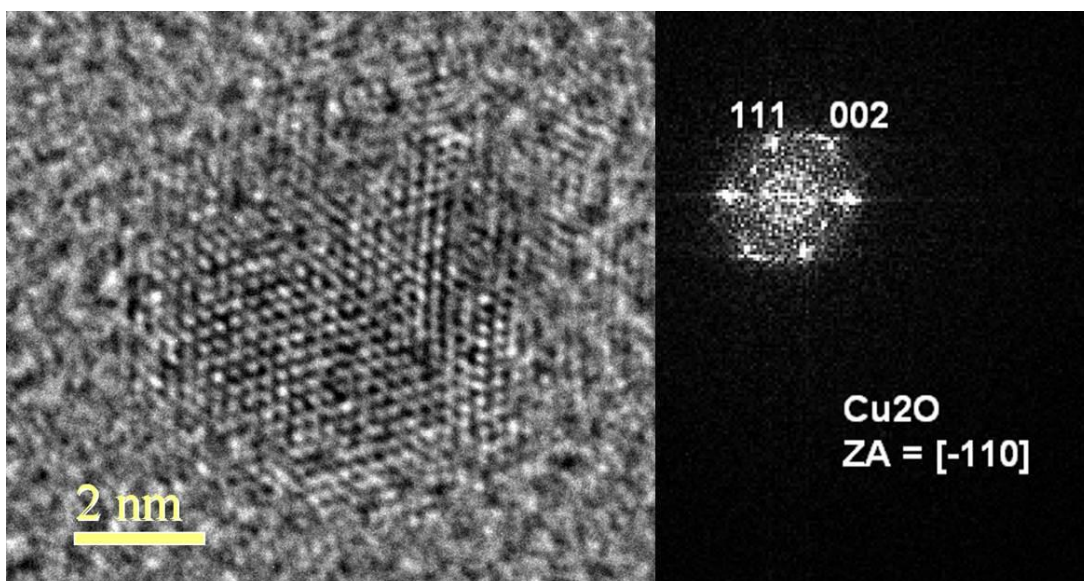


Figure 121 Identification of the Cu_2O zone axis from the FFT of a 4nm particle. For films deposited with $\text{CpCu}(\text{tBuNC})$ and water at 250°C SEM images were collected. Looking at the film morphology, **Figure 122a**, a 3D porous structure is observed. When the sample was cooled within the reaction chamber before exposure to air, **Figure 122b**, there are a few very dispersed particles.

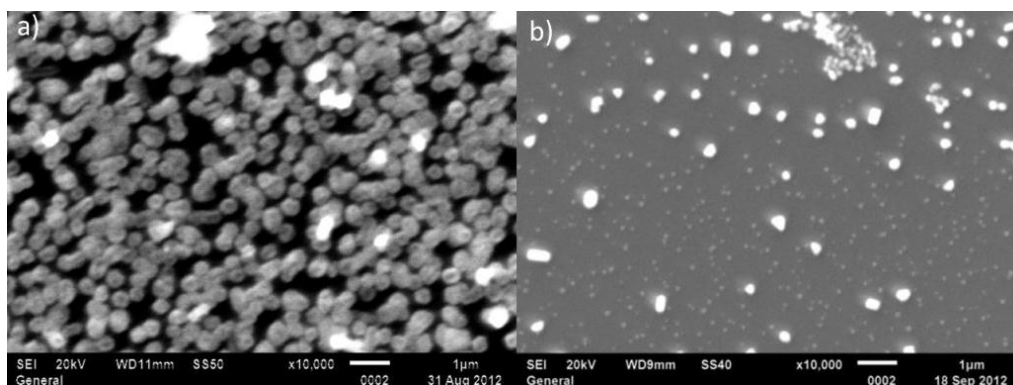


Figure 122 The morphology of a film deposited from $\text{CpCu}(\text{tBuNC})$ and water. Although this was the phase required, the growth for this process still contains a contribution of CVD. For solar cell fabrication, this would limit the efficiency of the device as not all of the ZnO nanowire surface would be coated.

5.5 Conclusions

The deposition conditions employed in this chapter are summarized in **Table 29**.

Co-reagent	LI-ALD of Cu(hfac)(COD)	ALD CpCu(^t BuNC)
Thermal Decomposition	Cu metal	Cu metal
Water	-	Cu ₂ O
Oxygen Plasma	-	CuO
Hydrogen Plasma	-	Cu metal
Tertiarybutylhydrazine	Cu metal	No growth
Ozone	CuO	-

Table 29 Copper and copper oxide deposition summary.

The use of Cu(hfac)(COD) was successfully used to deposit copper metal via thermal decomposition and with the use of tertiary butyl hydrazine as a co-reagent. Sheet resistance measurements for the thermally decomposed copper film was $0.826\Omega/\square$. Interestingly, a sheet resistance for the sample deposited via tertiary butyl hydrazine was not achieved. Looking to the film morphology and XRD analysis, the thermally decomposed sample shows a 'worm-like' particle formation but with polycrystalline copper with both (111) and (200) planes assigned. With the use of tertiary butyl hydrazine, the particles were more spherical in nature and were all of the Cu(111) form. When depositing copper using the second precursor CpCu(^tBuNC), with a H₂ plasma as a co-reagent for an ALD process, copper metal films have been deposited at temperatures as low as 75°C on Melinex® plastic, glass, silicon and titanium nitride and investigated by SEM, XRD and XPS. The results show that the substrate affects the surface morphology and that the copper grown was highly orientated in the (111) phase. The films were free from oxygen,

carbon and nitrogen contaminants. Sheet resistance measurements on glass show an average of $0.55\Omega/\square$.

Using ozone with $\text{Cu}(\text{hfac})(\text{COD})$ resulted in CuO (113) formation at all temperatures. To deposit CuO with the $\text{CpCu}(\text{}^t\text{BuNC})$ precursor via ALD, an oxygen plasma was needed, and TEM was used to gain a diffraction pattern to confirm CuO . For PV applications, Cu_2O would be the favoured choice for the p-type material. This was successfully deposited using $\text{CpCu}(\text{}^t\text{BuNC})$ with water. The film was a porous structure with some crystalline areas of Cu_2O observed.

5.6 Experimental

5.6.1 Precursor synthesis and characterisation

$\text{Cu}(\text{hfac})(\text{COD})$ shown in **Figure 82** was used as supplied by Sigma-Aldrich and dissolved in anhydrous toluene. The concentration of the solution was confirmed to be 0.65M via ^1H NMR. The $\text{CpCu}(\text{}^t\text{BuNC})$ precursor was synthesised using the methods of Cotton.^{306, 307} All reagents were bought commercially and used without further purification. The solvents used were anhydrous solvents which were subsequently passed through a solvent purification system. Standard Schlenk line techniques were employed with reactions carried out under a positive nitrogen flow. Freshly cracked cyclopentadiene (18.6g, 0.282 moles) was added to sodium hydride (11.3g, 0.282 moles) solvated in THF (100 ml). Separately, a mixture of ${}^t\text{BuNC}$ (23.4g, 0.282 moles) in anhydrous THF (100ml) was added to CuCl (27.9g, 0.282 moles) in THF (100ml). The NaCp salt was added dropwise to the $\text{ClCu}{}^t\text{BuNC}$. The THF was then removed and the product extracted in anhydrous toluene. As the volume of toluene was reduced, brown/yellow crystals began to precipitate. A further wash of the crystals with anhydrous hexane and drying under vacuo yielded a beige solid. Yield: 30g (50%)

5.6.2 Growth details

Liquid injection of 0.65M Cu(hfac)(COD) toluene solution held at room temperature was employed for pulsed CVD and ALD methods. For thermal decomposition studies, the precursor was injected for 2s, followed by a 2s purge. The overall reactor pressure was 5 mbar and 200sccm of argon was pushed through the precursor to aid transportation. The vapouriser and all pipes were maintained at 130°C. For the ALD mode, a 2s precursor pulse and purge was used, followed by either a 0.5s and 0.1s coreagent pulse in the case of ozone and tertiarybutyl hydrazine respectively. A 2s co-reagent purge was used in both cases. Due to size limitations of the stage in the Aixtron reactor, Si(100) and glass were the only substrates used.

Cyclopentadienyl copper tertiarybutyl isocyanide was held at 100°C for the growth study. A bubbling system was used with argon (flow rate of 300sccm) as the carrier gas. Depositions were carried out on an Oxford Instruments OpAL reactor complete with plasma unit. A pulsed CVD method was used for thermal depositions of copper metal from CpCu(^tBuNC) with no co-reagent. This followed a cyclic 2s precursor pulse length followed by a 3s purge. With CpCu(^tBuNC) and water the pulse purge train followed 2s Cu pulse/3s Cu purge/0.02s Water pulse/5s Water purge. An ALD method was employed when O₂ or H₂ plasma was used as the co-reagent with a 2s precursor pulse and a 3s precursor purge, followed by a 3s 300W O₂ or H₂ plasma exposure and then a 5s purge. Silicon (100) n-doped (2nm SiO₂ oxide layer) and glass substrates were used for the thermal, water and O₂ plasma depositions. For the low temperature plasma growth titanium nitride (TiN) and plastic substrates were used in addition to silicon and glass. Silicon, titanium nitride and Melinex® plastic

were used as purchased with no pre-treatment. Glass used was first cleansed from oil using isopropanol and then dried using acetone/N₂.

Chapter 6 Conclusions and Recommendations for Future Work

This thesis has demonstrated precursor development and investigated chemical vapour techniques for the deposition of n-type zinc oxide nanowires and p-type copper oxide thin films. The investigation of all oxide p-n junctions is of interest in the use of photovoltaic, with absorbing ZnO NWs offering an increased surface area for light harvesting, helping overall cell efficiency. Dialkylzinc precursors with oxygen co-reactant can be used to deposit ZnO, although pre-reaction can limit the control of the film grown. This research revisited the dialkylzinc precursors DEZn and DMZn and resulted in the successful determination of the solid-state crystal structures. All three structures contain linear diorganozinc molecules, which interact through weak intermolecular interactions with small covalent contributions. Interestingly, Me_2Zn undergoes a reversible solid–solid phase transition at 180 K; its high-temperature phase shows a two-dimensional disorder. DMZn was subsequently utilised in a series of adduct compounds, $[\text{DMZn.L}]$, (where L=1,2-dimethoxyethane, 1,4-dioxane, or 1,4-thioxane) . Single crystal XRD data for $[\text{DMZn.L}]$ helps to show that $[\text{Me}_2\text{Zn}]$ forms weak adducts with ether ligands. The 1,4-dioxane complex is polymeric with repeating $[\text{Me}_2\text{Zn}]$ units bridged by 1,4-dioxane ligands. By contrast the 1,2-dimethoxyethane complex has a monomeric structure containing both bidentate and chelating ligands. The 1,4-thioxane precursor forms even weaker interactions with $[\text{Me}_2\text{Zn}]$ and the solid-state structure can be regarded as an intermediate between a coordination complex and a co-crystal. By using the adducted compounds for ZnO deposition, the pre-reaction is avoided. LI-MOCVD was the technique employed and with careful selection of substrate temperature and the II:VI ratio of zinc to oxygen, the structure of the nanowires

could be controlled. Thin film analysis was carried out to characterise the morphology and electronic properties of the deposited material. SEM experiments enabled imaging of the microstructure helping to compare and contrast the density and size of the NWs and how this varies with the ligand system used, the substrate and the deposition time. For all the [DMZn.L] compounds with oxygen adducts at 500°C, all of the films showed nanowire formation, a slightly elevated temperature of 550°C was needed for NW formation from the thioxane adduct. All ZnO samples deposited were confirmed to be of the wurtzitic phase by XRD. Raman spectroscopy help to demonstrate NW diameters of between 40-100nm. The photoluminescence data in conjunction with the AES composition data helped to confirm the incorporation of sulphur into the final films, adding weight to the claim that the ligand system plays a part in the CVD reaction.

Copper oxide deposition was investigated both by LI-ALD using Cu(hfac)(COD) and by plasma-assisted ALD using CpCu(^tBuNC). In this thesis it is demonstrated that a pulsed Li-ALD approach can be exploited to deposit CuO with ozone as the co-reagent. Copper metal with a sheet resistance of 0.826Ω/□ was achieved following thermal decomposition. Although CpCu(^tBuNC) has previously been reported for CVD, this research is the first successful attempt to employ it as an ALD precursor. This work demonstrates that by tailoring the co-reagents, Cu, CuO and Cu₂O can be deposited with hydrogen plasma, oxygen plasma and water respectively. SEM and TEM techniques have proven invaluable in understanding film morphology, and to also gain crystal diffraction data for very thin films, enabling successful characterisation of the film grown. The metallic copper deposition was successful at temperatures as low as 75°C with a sheet resistance of 0.55Ω/□. It has been demonstrated that copper can be deposited on many substrates

(e.g. glass, Si, TiN and Melinex® plastic without the need for a seed layer. XPS and EDX have helped to confirm the high purity.

Recommendations for future work would include the process optimisation for the copper and copper oxide deposition. Work is currently underway to investigate the manufacture of thin film solar cells using CpCu(¹BuNC) to deposit Cu₂O on CdSe absorber layers. The wider scope would be to construct the target PV cell after fully characterising all constituents. A measurement on solar cell efficiency could help to determine if solar cell manufacture of this type would be suitable for industry.

Chapter 7 References

- 1 . Nelson, J.; *The Physics of Solar Cells*; Imperial College Press, 2003.
- 2 . <http://www.britannica.com/EBchecked/topic/183144/electrolyte> Encyclopedia Britanica Online, 2013.
- 3 . Zweibel, K.;Hersch, P.; *Basic Photovoltaic Principles and Methods, Solar Energy Research Institute*; Van Nostrand Reinhold, 1984.
- 4 . <http://pveducation.org/pvcdrom/manufacturing/czochralski-silicon> PV Education Organisation, 2013.
- 5 . <http://www.ise.fraunhofer.de/en/press-and-media/press-releases/presseinformationen-2013/world-record-solar-cell-with-44.7-efficiency> Fraunhofer ISE, October 2013.
- 6 . Green, M. A.;Emery, K.;Hishikawa, Y.; *Prog Photovoltaics Res Appl*, **2013**, 21 (1) p1-11.
- 7 . Olmsted,J.;Williams,G. M.; Band Theory of Solids in *Chemistry:The Molecular Science, 2nd Edition*; Wm. C. Brown, 1997.
- 8 . Whittaker,A. G.;Mount,A. R.; Semiconductors-bands in *Instant Notes:Physical Chemistry*; BIOS Scientific Publishers, 2000.
- 9 . Kittel, C.; *Introduction to Solid State Physics*; John Wiley, 2005.
- 10 . https://energypedia.info/wiki/Solar_Cells_and_Modules Energypedia, 2013.

- 11 . http://www.dur.ac.uk/renewable.energy/solarpower/pv-how_it_works/ Durham University, 2012.
- 12 . Parker, G.; *Introductory Semiconductor Device Physics*; Institute of Physics, 2004.
- 13 . Colinge, J. P.; Colinge, C. A.; *Physics of Semiconductor Devices*; Springer, 2002.
- 14 . www1.gantep.edu.tr/~bgonul/dersnotlari/sc/CHAPTER_2.ppt Gaziantep Universitesi, 2012.
- 15 . <http://www.students.tut.fi/~khamousk/semi.html> Tampere University of Technology, 2012.
- 16 . Shockley, W.; *Bell System Technical Journal*, **1949**, 28 (3) p435-489.
- 17 . Shockley, W.; *Electrons and Holes in Semiconductors*. Van Nostrand, 1950.
- 18 . Sah, C. T.; Noyce, R. N.; Shockley, W.; *Proceedings of the IRE*, **1957**, 45 (9) p1228-1243.
- 19 . Moll, J. L.; *Proceedings of the IRE*, **1958**, 46 (6) p1076-1082.
- 20 . http://www.electronics-tutorials.ws/diode/diode_3.html Electronic Tutorials, 2012.
- 21 . Green, M. A.; *Solar Cells: Operating Principles, Technology and System Applications*; Prentice-Hall, 1982.

- 22 . <http://chemistry.beloit.edu/edetc/SlideShow/slides/contents/pn.html> University of Wisconsin, 2012.
- 23 . Ginley, D. S.;Cahen, D.; *Fundamental of Materials for Energy and Environmental Sustainability*. Materials Research Society, Cambridge University Press, 2012.
- 24 . Van de Walle, C. G.;Neugebauer, J.; *Nature*, **2003**, 423 (6940) p626-628.
- 25 . Ichimura, M.;Song, Y.; *Jpn. J. Appl. Phys.*, **2011**, 50 p051002.
- 26 . Jeong, S.;Aydil, E. S.; *J. Cryst. Growth*, **2009**, 311 (17) p4188-4192.
- 27 . Shao,G.;Luo,J. University of Bolton. *Photovoltaic cell based on transition metal oxides of varied band gaps and p/n types*.30/06/2012**GB2466496**.
- 28 . Lv, P.;Zheng, W.;Lin, L.; *Physica B: Condensed Matter*, **2011**, 406 (6–7) p1253-1257.
- 29 . Chiang, C.;Aroh, K.;Franson, N.; *Int J Hydrogen Energy*, **2011**, 36 (24) p15519-15526.
- 30 . Caballero-Briones, F.;Artés, J. M.;Díez-Pérez, I.; *J. Phys. Chem. C*, **2009**, 113 (3) p1028-1036.
- 31 . Kramm, B.;Laufer, A.;Reppin, D.; *Appl. Phys. Lett.*, **2012**, 100 (9) p094102.
- 32 . Robertson, J.;Clark, S. J.; *Phys. Rev. B*, **2011**, 83 (7) p075205-075212.
- 33 . Wong, L. M.;Chiam, S. Y.;Wang, S. J.; *J. Appl. Phys.*, **2010**, 108 (3) p033702-033708.

- 34 . Hsueh, T.;Hsu, C.;Chang, S.; *Scr. Mater.*, **2007**, 57 (1) p53-56.
- 35 . Bu, I. Y. Y.; *Ceram. Int.*, **2013**, 39 (7) p8073-8078.
- 36 . Wang, P.;Zhao, X.;Li, B.; *Opt. Express*, **2011**, 19 (12) p11271-11279.
- 37 . Jeong, S. S.;Mittiga, A.;Salza, E.; *Electrochim. Acta*, **2008**, 53 (5) p2226-2231.
- 38 . Mittiga, A.;Salza, E.;Sarto, F.; *Appl. Phys. Lett.*, **2006**, 88 (16) p163502-163503.
- 39 . Hussain, S.;Cao, C.;Nabi, G.; *Electrochim. Acta*, **2011**, 56 (24) p8342-8346.
- 40 . Chen, J.;Perng, D.;Fang, J.; *Solar Energy Mater. Solar Cells*, **2011**, 95 (8) p2471-2477.
- 41 . Wang, Y.;She, G.;Xu, H.; *Mater Lett*, **2012**, 67 (1) p110-112.
- 42 . Wei, H.;Gong, H.;Wang, Y.; *CrystEngComm*, **2011**, 13 (20) p6065-6070.
- 43 . Kidowaki, H.;Oku, T.;Akiyama, T.; *IJRRAS*, **2012**, 13 (1) p67-72.
- 44 . Pilkington,A.;*Proceedings of the Royal Society of London Series A-Mathematical and Physical Sciences* , 16th December 1969, London, 314, (1516), 1-25.
- 45 . <http://asmcommunity.asminternational.org/portal/site/www/SubjectGuideItem/>;
ASM International, 2013.
- 46 . <http://www.beneq.com/transparent-conductive-oxide-tco.html> Beneq, 2013.

- 47 . Pakin, I. P.; Palgrave, R. G.; CVD of functional Coatings on Glass in *Chemical Vapour Deposition, Precursors, Processes and Applications*; Royal Society of Chemistry, 2009.
- 48 . Ban, T.; Ohya, Y.; Takahashi, Y.; *J. Appl. Phys.*, **1998**, 83 (5) p2631-2645.
- 49 . Edwards, P. P.; Porch, A.; Jones, M. O.; *Dalton Trans.*, **2004**, (19) p2995-3002.
- 50 . Hamberg, I.; Granqvist, C. G.; *J. Appl. Phys.*, **1986**, 60 (11) pR123-R160.
- 51 . Kamei, M.; Enomoto, H.; Yasui, I.; *Thin Solid Films*, **2001**, 392 (2) p265-268.
- 52 . Paine, D. C.; Whitson, T.; Janiac, D.; *J. Appl. Phys.*, **1999**, 85 (12) p8445-8450.
- 53 . Chen, C. H.; Chang, S. J.; Su, Y. -.; *Photonics Technology Letters, IEEE*, **2001**, 13 (8) p848-850.
- 54 . Sheu, J. K.; Su, Y. K.; Chi, G. C.; *Appl. Phys. Lett.*, **1998**, 72 (25) p3317-3319.
- 55 . Kim, S. T.; Lee, J. H.; Yang, J. Y.; *J. Korean Phys. Soc.*, **2007**, 50 (3) p662-665.
- 56 . Sittinger, V.; Ruske, F.; Werner, W.; *5th International Symposium on Transparent Oxide Thin Films for Electronics and Optics*, 7/1, 516, (17), 5847-5859.
- 57 . Horng, R.; Wu, D.; Lien, Y.; *Appl. Phys. Lett.*, **2001**, 79 (18) p2925-2927.
- 58 . Law, M.; Greene, L. E.; Johnson, J. C.; *Nat Mater*, **2005**, 4 (6) p455-459.
- 59 . Wu, J.; Chen, G.; Yang, H.; *Appl. Phys. Lett.*, **2007**, 90 (21) p213109.
- 60 . Baxter, J. B.; Aydil, E. S.; *Appl. Phys. Lett.*, **2005**, 86 (5) p053114.

- 61 . Colavita, P. E.;Sun, B.;Wang, X.; *J. Phys. Chem. C*, **2009**, 113 (4) p1526-1535.
- 62 . You, J. B.;Zhang, X. W.;Cai, P. F.; *Appl. Phys. Lett.*, **2009**, 94 (26) p262105.
- 63 . Gordon, R. G.; *MRS Bull*, **2000**, 25 (08) p52.
- 64 . Yang, F.;Forrest, S. R.; *Adv Mater*, **2006**, 18 (15) p2018-2022.
- 65 . Mondragón-Suárez, H.;Maldonado, A.;Olvera, M. d. l. L.; *Appl. Surf. Sci.*, **2002**, 193 (1–4) p52-59.
- 66 . Seeber, W. T.;Abou-Helal, M. O.;Barth, S.; *Materials Science in Semiconductor Processing*, **1999**, 2 (1) p45-55.
- 67 . Jiménez-González, A. E.;Soto Urueta, J. A.;Suárez-Parra, R.; *J. Cryst. Growth*, **1998**, 192 (3–4) p430-438.
- 68 . Schuler, T.;Aegerter, M. A.; *Thin Solid Films*, **1999**, 351 (1–2) p125-131.
- 69 . Musat, V.;Teixeira, B.;Fortunato, E.; *Surface and Coatings Technology*, **2004**, 180–181 (0) p659-662.
- 70 . Lin, S.;Huang, J.;Šajgalik, P.; *Surface and Coatings Technology*, **2005**, 190 (1) p39-47.
- 71 . Oh, B.;Jeong, M.;Lee, W.; *J. Cryst. Growth*, **2005**, 274 (3–4) p453-457.
- 72 . Zhang, D. H.;Yang, T. L.;Wang, Q. P.; *Mater. Chem. Phys.*, **2001**, 68 (1–3) p233-238.

- 73 . Fenske, F.;Fuhs, W.;Nebauer, E.; *Thin Solid Films*, **1999**, 343–344 (0) p130-133.
- 74 . Elam, J. W.;George, S. M.; *Chem. Mater.*, **2003**, 15 (4) p1020-1028.
- 75 . Kim, Y.;Kim, H.; *Mater Lett*, **1999**, 41 (4) p159-163.
- 76 . Groenen, R.;Löffler, J.;Sommeling, P. M.; *Thin Solid Films*, **2001**, 392 (2) p226-230.
- 77 . Lee, S.;Han, S.;Jung, H. S.; *J. Phys. Chem. C*, **2010**, 114 (15) p7185-7189.
- 78 . Saito, K.;Hiratsuka, Y.;Omata, A.; *Superlattices and Microstructures*, **2007**, 42 (1–6) p172-175.
- 79 . Chalker, P. R.;Marshall, P. A.;Romani, S.; *MRS Online Proceedings Library*, **2011**, 1315 .
- 80 . Chalker, P. R.;Marshall, P. A.;Roberts, J. W.; *J. Vac. Sci. Technol. A*, **2013**, 31 (1) p01A120.
- 81 . Irvine, S. J. C.;Barrioz, V.;Lamb, D.; *J. Cryst. Growth*, **2008**, 310 (23) p5198-5203.
- 82 . Krupanidhi, S. B.;Maffei, N.;Sayer, M.; *J. Appl. Phys.*, **1983**, 54 (11) p6601-6609.
- 83 . Sreenivas, K.;Sayer, M.;Baar, D. J.; *Appl. Phys. Lett.*, **1988**, 52 (9) p709-711.
- 84 . Ramesh, R.;Inam, A.;Chan, W. K.; *Appl. Phys. Lett.*, **1991**, 59 (27) p3542-3544.

- 85 . Manasevit, H. M.; *J. Cryst. Growth*, **1981**, 55 (1) p1-9.
- 86 . Shuster, G.; Kreinin, O.; Lakin, E.; *Thin Solid Films*, **2010**, 518 (16) p4658-4661.
- 87 . Jones, A. C.; Leedham, T. J.; Wright, P. J.; *Chemical Vapor Deposition*, **1998**, 4 (2) p46-49.
- 88 . Legrand, J.; Lhostis, S.; Chang, Y.; *Microelectronic Engineering*, **2004**, 72 (1-4) p310-314.
- 89 . Suntola, T.; *Materials Science Reports*, **1989**, 4 (5) p261-312.
- 90 . <http://www.picosun.com> Picosun, 2013.
- 91 . Ritala, M.; Niinisto, J.; *Chemical Vapour Deposition*; The Royal Society of Chemistry, 2009.
- 92 . Jones, A. C.; Aspinall, H. C.; Chalker, P. R.; *Chemical Vapor Deposition*, **2006**, 12 (2-3) p83-98.
- 93 . <http://www.zinc.org/> Zinc.Org, 2012.
- 94 . <http://minerals.usgs.gov/minerals/pubs/commodity/zinc/mcs-2011-zinc.pdf> US Gov, 2012.
- 95 . Knochel, P.; Singer, R. D.; *Chem. Rev.*, **1993**, 93 (6) p2117-2188.
- 96 . Frankland, E. Q.; *J. Chem. Soc*, **1850**, 2 p263.
- 97 . Frankland, E. Q.; *Liebigs Ann. Chem.*, **1949**, 71 p171.

- 98 . Haaland, A.;Green, J. C.;McGrady, G. S.; *Dalton Trans.*, **2003**, (22) p4356-4366.
- 99 . Seyferth, D.; *Organometallics*, **2001**, 20 (14) p2940-2955.
- 100 . Antes, I.;Frenking, G.; *Organometallics*, **1995**, 14 (9) p4263-4268.
- 101 . Almenningen, A.; *Acta Chem. Scand.*, **1982**, A36 p159.
- 102 . Bacsá, J.;Hanke, F.;Hindley, S.; *Angewandte Chemie International Edition*, **2011**, 50 (49) p11685-11687.
- 103 . O'Brien,P.; Cadmium and Zinc in *Comprehensive Organometallic Chemistry II: A Review od the Literature 1982-1994*; Elsevier Science Ltd., 1995.
- 104 . Van Der Kerk, G. J. M.; *Pure Appl. Chem.*, **1972**, 30 (3-4) p389-408.
- 105 . Thiele, K.; *Zeitschrift Für Anorganische Und Allgemeine Chemie*, **1963**, 322 (1-2) p71-80.
- 106 . Hindley, S.;Jones, A. C.;Ashraf, S.; *Journal of Nanoscience and Nanotechnology*, **2011**, 11 (9) p8294.
- 107 . O'Brien, P.;Walsh, J. R.;Jones, A. C.; *J. Mater. Chem.*, **1993**, 3 (7) p739-742.
- 108 . O'Brien, P.;Malik, M. A.;Walsh, J. R.; *Advanced Materials for Optics and Electronics*, **1997**, 7 (3) p117-121.
- 109 . Thiele, K.; *Zeitschrift Für Anorganische Und Allgemeine Chemie*, **1963**, 325 (3-4) p156-168.

- 110 . Coates, G. E.;Ridley, D.; *J. Chem. Soc.*, **1965**, 0 (0) p1870-1877.
- 111 . Butlerow, M. A.; *Jahresber.*, **1864**, 467 .
- 112 . Shearer, H. M. M.;Spencer, C. B.; *Chem. Commun. (London)*, **1966**, 0 (7)
p194a-194a.
- 113 . Jana, S.;Berger, R. J. F.;Fröhlich, R.; *Inorg. Chem.*, **2007**, 46 (10) p4293-4297.
- 114 . Bunn, C. W.; *Proceedings of the Physical Society*, **1935**, 47 (5) p835.
- 115 . Jagadish,C.;Coleman,V. A.; Basic properties and applications of ZnO in *Zinc oxide bulk, thin films and nanostructures : processing, properties and applications*; Elsevier, 2006.
- 116 . Ashrafi, A. B. M. A.;Ueta, A.;Avramescu, A.; *Appl. Phys. Lett.*, **2000**, 76 (5)
p550-552.
- 117 . Kim, S.;Jeong, S.;Cho, C.; *Appl. Phys. Lett.*, **2003**, 82 (4) p562-564.
- 118 . Bates, C. H.;White, W. B.; *Science*, **1962**, 137 (3534) p993-993.
- 119 . http://www.wiley-vch.de/books/sample/3527408134_c01.pdf) Wiley, 2012.
- 120 . Look,D. C.; Doping and defects in ZnO in *Zinc oxide bulk, thin films and nanostructures : processing, properties and applications*; Elsevier, 2006.
- 121 . Phillips, J. C.; *Bonds and Bands in Semiconductors*; Academic Press, 1973.
- 122 . Lide, D. R.; *CRC Handbook of Chemistry and Physics: 73rd Edition*; CRC Press, 1992.

- 123 . Özgür, Ü.;Alivov, Y.;Liu, C.; *J. Appl. Phys.*, **2005**, 98 (4) p041301.
- 124 . Himpsel, F. J.; *Advances in Physics*, **1983**, 32 p1-51.
- 125 . Rössler, U.; *Phys. Rev.*, **1969**, 184 (3) p733-738.
- 126 . Franklin, L.;Ekuma, C. E.;Zhao, G. L.; *Journal of Physics and Chemistry of Solids*, **2013**, 74 (5) p729-736.
- 127 . Vogel, D.;Kruger, P.;Johannes, P.; *Phys. Rev. B*, **1995**, 52 (20) pR14316-R14319.
- 128 . Wei, S. H.;Zunger, A.; *Phys. Rev. B*, **1988**, 37 (15) p8958-8981.
- 129 . Schröer, P.;Krüger, P.;Pollmann, J.; *Phys. Rev. B*, **1993**, 47 (12) p6971-6980.
- 130 . Xu, Y.;Ching, W. Y.; *Phys. Rev. B*, **1993**, 48 (7) p4335-4351.
- 131 . Schröer, P.;Krüger, P.;Pollmann, J.; *Phys. Rev. B*, **1994**, 49 (24) p17092-17101.
- 132 . Perdew, J. P.; *Phys. Rev. B*, **1981**, 23 (10) p5048-5079.
- 133 . Iwata, K.;Fons, P.;Niki, S.; *Physica Status Solidi (a)*, **2000**, 180 (1) p287-292.
- 134 . Kazuhiro, M.;Michihiro, S.;Hiroyuki, K.; *Jpn. J. Appl. Phys.*, **2002**, 41 (Part 2, No. 11A) pL1203-L1205.
- 135 . Miyamoto, K.;Sano, M.;Kato, H.; *J. Cryst. Growth*, **2004**, 265 (1–2) p34-40.
- 136 . Kaidashev, E. M.;Lorenz, M.;von Wenckstern, H.; *Appl. Phys. Lett.*, **2003**, 82 (22) p3901-3903.

- 137 . Albrecht, J. D.;Ruden, P. P.;Limpijumnong, S.; *J. Appl. Phys.*, **1999**, 86 (12) p6864-6867.
- 138 . Look, D. C.;Hemsky, J. W.;Sizelove, J. R.; *Phys. Rev. Lett.*, **1999**, 82 (12) p2552-2555.
- 139 . Look, D. C.;Reynolds, D. C.;Sizelove, J. R.; *Solid State Commun.*, **1998**, 105 (6) p399-401.
- 140 . Adachi,S.; Thermal Properties in *Properties of Semiconductor Alloys*; John Wiley & Sons, Ltd, 2009.
- 141 . Ibach, H.; *Physica Status Solidi (B)*, **1969**, 33 (1) p257-265.
- 142 . Klingshirn,C.; Intrinsic Linear Optical Properties Close to the Fundamental Absorption Edge in Springer Berlin Heidelberg, 2010.
- 143 . Florescu, D. I.;Mourokh, L. G.;Pollak, F. H.; *J. Appl. Phys.*, **2002**, 92 (2) p890-892.
- 144 . Chennupati, E. J.;Pearton, S. J.; *Zinc Oxide Bulk, Thin Films and Nanostructures : Processing, Properties and Applications*; Elsevier, 2006.
- 145 . Smith, F. T. J.; *Appl. Phys. Lett.*, **1983**, 43 (12) p1108-1110.
- 146 . Roth, A. P.;Williams, D. F.; *J. Appl. Phys.*, **1981**, 52 (11) p6685-6692.
- 147 . Kern, W.;Heim, R.; *J. Electrochem. Soc.*, **1970**, 117 (4) p562-568.
- 148 . Ghandhi, S. K.;Field, R. J.;Shealy, J. R.; *Appl. Phys. Lett.*, **1980**, 37 (5) p449-451.

- 149 . Park, W. I.;An, S.;Yi, G.; *J. Mater. Res.*, **2001**, 16 (05) p1358-1362.
- 150 . Park, W. I.;Yi, G.;Jang, H. M.; *Appl. Phys. Lett.*, **2001**, 79 (13) p2022-2024.
- 151 . Gorla, C. R.;Emanetoglu, N. W.;Liang, S.; *J. Appl. Phys.*, **1999**, 85 (5) p2595-2602.
- 152 . Zhang, B.;Manh, L.;Wakatsuki, K.; *Jpn. J. Appl. Phys.*, **2003**, 42 p2291-2295.
- 153 . Ma, Y.;Du, G. T.;Yang, T. P.; *J. Cryst. Growth*, **2003**, 255 (3–4) p303-307.
- 154 . Ma, Y.;Du, G. T.;Yang, S. R.; *J. Appl. Phys.*, **2004**, 95 (11) p6268-6272.
- 155 . Lau, C. K.;Tiku, S. K.;Lakin, K. M.; *J. Electrochem. Soc.*, **1980**, 127 (8) p1843-1847.
- 156 . Yasuda, T.;Segawa, Y.; *Physica Status Solidi (B)*, **2004**, 241 (3) p676-679.
- 157 . Solanki, R.;Collins, G. J.; *Appl. Phys. Lett.*, **1983**, 42 (8) p662-663.
- 158 . Ogata, K.;Kawanishi, T.;Maejima, K.; *J. Cryst. Growth*, **2002**, 237–239, Part 1 (0) p553-557.
- 159 . Ogata, K.;Maejima, K.;Fujita, S.; *J. Cryst. Growth*, **2003**, 248 (0) p25-30.
- 160 . Dadgar, A.;Oleynik, N.;Forster, D.; *J. Cryst. Growth*, **2004**, 267 (1–2) p140-144.
- 161 . Gruber, T.;Kirchner, C.;Thonke, K.; *Physica Status Solidi (a)*, **2002**, 192 (1) p166-170.

- 162 . Oleynik, N.;Adam, M.;Krtschil, A.; *J. Cryst. Growth*, **2003**, 248 (0) p14-19.
- 163 . Oda, S.;Tokunaga, H.;Kitajima, N.; *Jpn. J. Appl. Phys*, **1985**, 24 p1607-1610.
- 164 . Kirchner, C.;Gruber, T.;Reuß, F.; *J. Cryst. Growth*, **2003**, 248 (0) p20-24.
- 165 . Auld, J.;Houlton, D. J.;Jones, A. C.; *J. Mater. Chem.*, **1994**, 4 (8) p1249.
- 166 . Lad, R. J.;Funkenbusch, P. D.;Aita, C. R.; *J. Vac. Sci. Technol.*, **1980**, 17 (4) p808-811.
- 167 . Yamamoto, T.;Shiosaki, T.;Kawabata, A.; *J. Appl. Phys.*, **1980**, 51 (6) p3113-3120.
- 168 . Hwang, D.;Bang, K.;Jeong, M.; *J. Cryst. Growth*, **2003**, 254 (3–4) p449-455.
- 169 . Hachigo, A.;Nakahata, H.;Higaki, K.; *Appl. Phys. Lett.*, **1994**, 65 (20) p2556-2558.
- 170 . Mitsuyu, T.;Ono, S.;Wasa, K.; *J. Appl. Phys.*, **1980**, 51 (5) p2464-2470.
- 171 . Wright, P. J.;Cockayne, B.;Williams, A. J.; *J. Cryst. Growth*, **1987**, 84 (3) p552-554.
- 172 . Wright, P. J.;Cockayne, B.;Jones, A. C.; *Chemtronics*, **1988**, 3 p35.
- 173 . Cockayne, B.;Wright, P. J.;Armstrong, A. J.; *J. Cryst. Growth*, **1988**, 91 (1–2) p57-62.

- 174 . Wright, P. J.;Parbrook, P. J.;Cockayne, B.; *J. Cryst. Growth*, **1989**, 94 (2)
p441-447.
- 175 . Wright, P. J.;Cockayne, B.;Parbrook, P. J.; *J. Cryst. Growth*, **1990**, 104 (3)
p601-609.
- 176 . Yates, H. M.;Williams, J. O.; *J. Cryst. Growth*, **1991**, 107 (1-4) p386-389.
- 177 . Jensen, K. F.;Annapragada, A.;Ho, K. L.; *J. Phys. IV France*, **1991**, 02 (C2)
p243-252.
- 178 . Foster, D. F.;Patterson, I. L. J.;James, L. D.; *Advanced Materials for Optics
and Electronics*, **1994**, 3 (1-6) p163.
- 179 . Huh, J.;Patnaik, S.;Jensen, K.; *J Electron Mater*, **1993**, 22 (5) p509.
- 180 . Wright, P. J.;Cockayne, B.;Jones, A. C.; *J. Cryst. Growth*, **1988**, 91 (1-2) p63-
66.
- 181 . Jones, A. C.;Rushworth, S. A.;O'Brien, P.; *J. Cryst. Growth*, **1993**, 130 (1-2)
p295-299.
- 182 . Cloitre, T.;Briot, N.;Briot, O.; *Materials Science and Engineering: B*, **1993**, 21
(2-3) p169-173.
- 183 . Khan, O.;O'Brien, P.;Hamilton, P. A.; *Chemitronics*, **1989**, 4 (21) p412.
- 184 . Xu, J.;Pan, Q.;Shun, Y.; *Sensors Actuators B: Chem.*, **2000**, 66 (1-3) p277-
279.
- 185 . Huang, M. H.;Mao, S.;Feick, H.; *Science*, **2001**, 292 (5523) p1897-1899.

- 186 . Bao, J.;Zimmler, M.;Capasso, F.; *Nano Lett.*, **2006**, 6 (8) p1719-1722.
- 187 . Gonzalez-Valls, I.;Lira-Cantu, M.; *Energy Environ. Sci.*, **200**, 2 (1) p19-34.
- 188 . Yu, D.;Trad, T.;McLeskey, J.; *Nanoscale Research Letters*, **2010**, 5 (8) p1333-1339.
- 189 . Beek, W. J. E.;Wienk, M. M.;Janssen, R. A. J.; *Adv Mater*, **2004**, 16 (12) p1009-1013.
- 190 . Unalan, H. E.;-Hiralal, P.;Kuo, D.; *J. Mater. Chem.*, **2008**, 18 (48) p5909-5912.
- 191 . Zhang, Y.;Ram, M.;Stefanakos, E.; *Journal of Nanomaterials*, **2012**, 2012 p1-22.
- 192 . Park, W. I.;Kim, D. H.;Jung, S. W.; *Appl. Phys. Lett.*, **2002**, 80 (22) p4232-4234.
- 193 . Liu, X.;Wu, X.;Cao, H.; *J. Appl. Phys.*, **2004**, 95 (6) p3141-3147.
- 194 . Kwak, C. H.;Kim, B. H.;Park, S. H.; *J. Cryst. Growth*, **2009**, 311 (20) p4491-4494.
- 195 . Kaufmann, T.;Fuchs, G.;Webert, M.; *Crystal Research and Technology*, **1989**, 24 (3) p269-274.
- 196 . Black, K.;Chalker, P. R.;Jones, A. C.; *Chemical Vapor Deposition*, **2010**, 16 (1-3) p106-111.

- 197 . <http://www.chemistryexplained.com/elements/C-K/Copper.html#ixzz2BSQ7IPyp> Thompson Corporation, 2013.
- 198 . <http://www.uncp.edu/home/mcclurem/ptable/copper/cu.htm> University of North Carolina, Pembroke, 2013.
- 199 .
<http://asmcommunity.asminternational.org/portal/site/www/SubjectGuideItem/?vgnextoid=ad7cdc8cc359d210VgnVCM100000621e010aRCRD> ASM International, The Materials Information Society, 2013.
- 200 . Giancoli, D. C.; *Physics for Scientists & Engineers with Modern Physics / Douglas C. Giancoli*; Upper Saddle River, N.J. : Pearson Prentice Hall, 2009; 4th ed, 2009.
- 201 . Zant, P. V.; *Microchip Fabrication: A Practical Guide to Semiconductor Processing*; McGraw-Hill Education, 2004.
- 202 . Willcocks, A. M. *Development of Coinage Metal Precursor for Chemical Vapour Deposition (CVD) and Atomic Layer Deposition (ALD)*; **2011**, University of Bath, Department of Chemistry.
- 203 .
http://domino.research.ibm.com/comm/wvr_thinkresearch.nsf/pages/copper397.html
IBM, 2013.
- 204 . http://www.advanced-energy.com/upload/file/white_papers/sl-electroplating-270-01.pdf AnabellePratt, Advanced Energy, 2013.

- 205 . Andricacos, P., C.; *The Electrochemical Society Interface*, **1999**, p32-37.
- 206 . Campbell, S. A.; *The Science and Engineering of Microelectronic Fabrication*; New York: Oxford University Press, 2001.
- 207 .
- <http://www.matweb.com/search/DataSheet.aspx?MatGUID=859664f9f59f46bb958e99a063aec4b5> MatWeb LLC, 2013.
- 208 . Oku, T.;Motoyoshi, R.;Fujimoto, K.; *Journal of Physics and Chemistry of Solids*, **2011**, 72 (11) p1206-1211.
- 209 . Haukka,S.;Lakomaa,E. L.; Adsorption controlled preparation of heterogeneous catalysts in *Studies in Surface Science and Catalysis*; Elsevier, .
- 210 . Wagh, M. S.;Patil, L. A.;Seth, T.; *Mater. Chem. Phys.*, **2004**, 84 (2–3) p228-233.
- 211 . S Hüfner and M A Hossain and A Damascelli and,G.A.Sawatzky; *Reports on Progress in Physics*, **2008**, 71 (6) p062501.
- 212 . Bugarinović,S.;Rajčić-Vujasinović,M.; Cuprous Oxide as an Active Material for Solar Cells in *Solar Cells-New Aspects and Solutions*; InTech, 2011.
- 213 . Kim, D.;Wentorf, R. H.;Gill, W. N.; *Journal of the Electrochemical Society*, **1993**, 140 (11) p3267-3272.
- 214 . Lakshmanan, S. K.;Gill, W. N.; *J. Vac. Sci. Technol. A*, **1998**, 16 (4) p2187-2197.

- 215 . Juppo, M.;Ritala, M.;Leskela, M.; *J. Vac. Sci. Technol. A*, **1997**, 15 (4) p2330-2333.
- 216 . Hampden-Smith, M. J.;Kodas, T. T.; Chemical Vapor Deposition of Copper from Cu(I) Compounds in *The Chemistry of Metal CVD*; Wiley-VCH Verlag GmbH, 2007.
- 217 . Vertoprakhov, V.;Krupoder, S.; *Russ. Chem. Rev.*, **2000**, 69 (12) p1057-1082.
- 218 . Nguyen, T.;Charneski, L. J.;Hsu, S. T.; *Journal of the Electrochemical Society*, **1997**, 144 (8) p2829-2833.
- 219 . Lin, C.;Chen, P.;Lin, Y.; *Journal of the Electrochemical Society*, **2003**, 150 (7) pC451-C456.
- 220 . Jakob, A.;Shen, Y.;Wächtler, T.; *Zeitschrift Für Anorganische Und Allgemeine Chemie*, **2008**, 634 (12-13) p2226-2234.
- 221 . Mothes, R.;Ruffer, T.;Shen, Y.; *Dalton Trans.*, **2010**, 39 (46) p11235-11247.
- 222 . Van Hemert, R. L.;Spendlove, L. B.;Sievers, R. E.; *Journal of the Electrochemical Society*, **1965**, 112 (11) p1123-1126.
- 223 . Bertrand, J. A.;Kaplan, R. I.; *Inorg. Chem.*, **1966**, 5 (3) p489-491.
- 224 . Maverick, A. W.;Fronczek, F. R.;Maverick, E. F.; *Inorg. Chem.*, **2002**, 41 (24) p6488-6492.
- 225 . Lai, W. G.;Xie, Y.;Griffin, G. L.; *Journal of the Electrochemical Society*, **1991**, 138 (11) p3499-3504.

- 226 . Kim, D.;Wentorf, R. H.;Gill, W. N.; *Journal of the Electrochemical Society*, **1993**, 140 (11) p3273-3279.
- 227 . Girolami, G. S.;Jeffries, P. M.;Dubois, L. H.; *J. Am. Chem. Soc.*, **1993**, 115 (3) p1015-1024.
- 228 . Hanaoka, K.;Tachibana, K.;Ohnishi, H.; *Thin Solid Films*, **1995**, 262 (1–2) p209-217.
- 229 . Farkas, J.;Hampden-Smith, M. J.;Kodas, T. T.; *J. Phys. Chem.*, **1994**, 98 (27) p6763-6770.
- 230 . Temple, D.;Reisman, A.; *Journal of the Electrochemical Society*, **1989**, 136 (11) p3525-3529.
- 231 . Kim, J.;Lee, Y.;Park, H.; *Thin Solid Films*, **1998**, 330 (2) p190-195.
- 232 . Liu, X.;Wang, Q.;Wu, S.; *Chem. Vap. Dep.*, **2006**, 12 (11) p679-684.
- 233 . Liu, X.;Wang, Q.;Wu, S.; *Journal of the Electrochemical Society*, **2006**, 153 (3) pC142-C145.
- 234 . Momose, T.;Sugiyama, M.;Shimogaki, Y.; *Jpn. J. Appl. Phys.*, **2006**, 44 (38) pL1199-L1202.
- 235 . Kondoh, E.;Shigama, K.; *Thin Solid Films*, **2005**, 491 (1–2) p228-234.
- 236 . Rickerby, J.;Steinke, J. H. G.; *Chem. Rev.*, **2002**, 102 (5) p1525-1550.
- 237 . Hwang, S.;Choi, H.; *Chem. Mater.*, **1996**, 8 (5) p981-983.

- 238 . Hwang, S. T.;Shim, I.;Lee, K. O.; *J. Mater. Res.*, **1996**, 11 (05) p1051-1060.
- 239 . Pinkas, J.;Huffman, J. C.;Bollinger, J. C.; *Inorg. Chem.*, **1997**, 36 (14) p2930-2937.
- 240 . Gorbenko, O. Y.;Trojanov, S. I.;Meetsma, A.; *Polyhedron*, **1997**, 16 (12) p1999-2004.
- 241 . Trojanov, S. I.;Gorbenko, O. Y.;Bosak, A. A.; *Polyhedron*, **1997**, 16 (10) p1595-1598.
- 242 . Hsu, P. F.;Chi, Y.;Lin, T. W.; *Chemical Vapor Deposition*, **2001**, 7 (1) p28-31.
- 243 . Becker, R.;Weiß, J.;Devi, A.; *J. Phys. IV France*, **2001**, 11 (PR3) pPR3-569-PR3-575.
- 244 . Chi, Y.;Hsu, P.;Liu, C.; *J. Mater. Chem.*, **2002**, (12) p3541-3550.
- 245 . Becker, R.;Devi, A.;Weiß, J.; *Chemical Vapor Deposition*, **2003**, 9 (3) p149-156.
- 246 . Park, J. W.;Jang, H. S.;Kim, M.; *Inorganic Chemistry Communications*, **2004**, 7 (4) p463-466.
- 247 . Lay, E.;Song, Y. H.;Chiu, Y. C.; *Inorg. Chem.*, **2005**, 44 (20) p7226-7233.
- 248 . Mårtensson, P.;Carlsson, J.; *Chemical Vapor Deposition*, **1997**, 3 (1) p45-50.
- 249 . Mueller,S.;Waechtler,T.;Hofmann,L.;*Semiconductor Conference Dresden (SCD)*, **2011**, 1-4.

- 250 . Lim, B. S.;Rahtu, A.;Gordon, R. G.; *Nature Materials*, **2003**, 2 (11) p749-754.
- 251 . Lim, B. S.;Rahtu, A.;Park, J.; *Inorg. Chem.*, **2003**, 42 (24) p7951-7958.
- 252 . Li, Z.;Rahtu, A.;Gordon, R. G.; *Journal of the Electrochemical Society*, **2006**, 153 (11) pC787-C794.
- 253 . Dai, M.;Kwon, J.;Halls, M. D.; *Langmuir*, **2010**, 26 (6) p3911-3917.
- 254 . Maårtensson, P.;Carlsson, J.; *Journal of the Electrochemical Society*, **1998**, 145 (8) p2926-2931.
- 255 . Mane, A. U.;Shivashankar, S. A.; *Materials Science in Semiconductor Processing*, **2004**, 7 (4–6) p343-347.
- 256 . Niskanen, A.;Rahtu, A.;Sajavaara, T.; *Journal of the Electrochemical Society*, **2005**, 152 (1) pG25-G28.
- 257 . Solanki, R.;Pathangey, B.; *Electrochemical and Solid-State Letters*, **2000**, 3 (10) p479-480.
- 258 . Huoa, J.;Solankia, R.;McAndrew, J.; *J. Mater. Res.*, **2002**, 17 (9) p2394-2398.
- 259 . Lee, B. H.;Hwang, J. K.;Nam, J. W.; *Angew. Chem. Int. Ed.*, **2009**, 48 (25) p4536-4539.
- 260 . Knisley, T. J.;Ariyasena, T. C.;Sajavaara, T.; *Chem. Mater.*, **2011**, 23 (20) p4417-4419.
- 261 . Vidjayacoumar, B.;Emslie, D. J. H.;Blackwell, J. M.; *Chem. Mater.*, **2010**, 22 (17) p4854-4866.

- 262 . Szymańska, I.;Kucharek, R.;Szlyk, E.; *Mat. Sci.*, **2003**, 21 (2) p245-250.
- 263 . Jeffries, P. M.;Dubois, L. H.;Girolami, G. S.; *Chem. Mater.*, **1992**, 4 (6) p1169-1175.
- 264 . Uwai, K.; *J. Cryst. Growth*, **1991**, 112 (1) p298-301.
- 265 . Barreca, D.;Gasparotto, A.;Tondello, E.; *Surf. Sci. Spectra*, **2007**, 14 (1) p41-51.
- 266 . Comini, E.;Sberveglieri, G.;Barreca, D.; *IEEE SENSORS 2009 Conference*, **2009**, .
- 267 . Barreca, D.;Fornasiero, P.;Gasparotto, A.; *ChemSusChem*, **2009**, 2 p230-233.
- 268 . Hong, L.;Komiyama, H.; *J Am Ceram Soc*, **1991**, 74 (7) p1597-1604.
- 269 . Ottosson, M.;Carlsson, J.; *Surface and Coatings Technology*, **1996**, 78 (1–3) p263-273.
- 270 . Klippe, L.;Wahl, G.; *J. Alloys Compounds*, **1997**, 251 (1–2) p249-253.
- 271 . Koh, T.;O'Hara, E.;Gordon, M. J.; *J. Cryst. Growth*, **2013**, 363 (0) p69-75.
- 272 . Eisermann, S.;Kronenberger, A.;Laufer, A.; *Physica Status Solidi (a)*, **2012**, 209 (3) p531-536.
- 273 . Holzschuh, H.;Suhr, H.; *Appl. Phys. A*, **1990**, 51 (6) p486-490.
- 274 . Medina-Valtierra, J.;Ramírez-Ortiz, J.;Arroyo-Rojas, V. M.; *Thin Solid Films*, **2002**, 405 (1–2) p23-28.

- 275 . Maruyama, T.; *Solar Energy Mater. Solar Cells*, **1998**, 56 (1) p85-92.
- 276 . Yates, H. M.; Brook, L. A.; Sheel, D. W.; *Thin Solid Films*, **2008**, 517 (2) p517-521.
- 277 . Waechter, T.; Oswald, S.; Roth, N.; *Journal of the Electrochemical Society*, **2009**, 156 (6) p H453-H459.
- 278 . Shen, Y. Z.; Leschke, M.; Schulz, S. E.; *Chin. J. Inorg. Chem*, **2004**, 20 (11) p1257-1264.
- 279 . Munoz-Rojas, D.; Jordan, M.; Yeoh, C.; *AIP Advances*, **2012**, 2 (4) p042179-042186.
- 280 . Alnes, M. E.; Monakhov, E.; Fjellvag, H.; *Chemical Vapor Deposition*, **2012**, 18 (4-6) p173-173.
- 281 . Filipič, G.; Cvelbar, U.; *Nanotechnology*, **2012**, 23 (19) p194001.
- 282 . Ji, J.; Shih, P.; Yang, C. C.; *Nanotechnology*, **2010**, 21 (4) p045603.
- 283 . <http://www.mhhe.com/physsci/chemistry/carey/student/olc/ch13nmr.html>
Dushkin McGraw-Hill, 2013.
- 284 .
http://classconnection.s3.amazonaws.com/479/flashcards/788479/png/screen_shot_2012-03-18_at_45107_pm1332114720788.png Reddit, 2013.
- 285 . *Presentation entitled: ICP MS Theory and Hardware* Dr Simon Nelms,
Thermo-Fischer Scientific, 2013.

- 286 . Rushworth, S. A.;Smith, L. M.;Kingsley, A. J.; *Microelectronics Reliability*, **2005**, 45 (5–6) p1000-1002.
- 287 . Potter, R. J.;Chalker, P. R.;Manning, T. D.; *Chemical Vapor Deposition*, **2005**, 11 (3) p159-169.
- 288 . *Presentation entitled: Oxford Instruments ALD* Chris Hodson, Oxford Instruments, 2013.
- 289 . Fang,Z. *Atomic Layer Deposition of tantalum, hafnium and gadolinium nitrides*. **2011**, University of Liverpool.
- 290 . <http://mackenzie.chem.ox.ac.uk/teaching/Raman%20Scattering.pdf> University of Oxford, 2013.
- 291 . Wang, Y. G.;Liu, H. R.;Yang, Q. B.; *Chinese Phys. Lett.*, **2003**, 20 (6) p888.
- 292 . http://www.jawoollam.com/tutorial_2.html J.A. Woollam Company, 2013.
- 293 . Kanjolia, R.;Jones, A. C.;Ashraf, S.; *J. Cryst. Growth*, **2011**, 315 (1) p292-296.
- 294 . Ashraf, S.;Jones, A. C.;Bacsa, J.; *Chemical Vapor Deposition*, **2011**, 17 (1-3) p45-53.
- 295 . Shearer, H.;Spencer, C.; *Acta Cryst. B*, **(1980)**., 36 p2046-2050.
- 296 . Graham, D. V.;Hevia, E.;Kennedy, A. R.; *Organometallics*, **2006**, 25 (14) p3297-3300.
- 297 . Coward, K. M.;Jones, A. C.;Steiner, A.; *J. Chem. Soc. , Dalton Trans.*, **2000**, 0 (19) p3480-3482.

- 298 . O'Brien, P.;Hursthouse, M. B.;Motevalli, M.; *Journal of Organometallic Chemistry*, **1993**, 449 (1–2) p1-8.
- 299 . Hursthouse, M. B.;Motevalli, M.;O'Brien, P.; *J. Mater. Chem.*, **1991**, 1 (1) p139-140.
- 300 . Hursthouse, M. B.;Motevalli, M.;O'Brien, P.; *Organometallics*, **1991**, 10 (9) p3196-3200.
- 301 . Barnes, J. C.; *Acta Crystallographica Section E*, **2004**, 60 (7) pm971-m972.
- 302 . Stahl,L.; *Comprehensive Organometallic Chemistry*; Elsevier, 2006.
- 303 . Dickson, R. S.;Fallon, G. D.;Zhang, Q.; *J. Chem. Soc. , Dalton Trans.*, **2000**, 0 (13) p1973-1974.
- 304 . Pajerski, A. D.;BergStresser, G. L.;Parvez, M.; *J. Am. Chem. Soc.*, **1988**, 110 (14) p4844-4845.
- 305 . Blessmann, D.;Gräfe, A.;Heinen, R.; *Materials Science and Engineering: B*, **1993**, 17 (1–3) p104-107.
- 306 . Cotton, F. A.;Marks, T. J.; *J. Am. Chem. Soc.*, **1970**, 92 (17) p5114-5117.
- 307 . Kruck, T.;Terfloth, C.; *Chem. Ber.*, **1993**, 126 (5) p1101-1106.
- 308 . Hinman, R. L.; *J. Org. Chem.*, **1985**, 23 p1587.
- 309 . Acharya, S.;Neogi, G.;Panda, R. K.; *J. Chem. Soc. , Dalton Trans.*, **1984**, (8) p1477-1484.

310 . http://evans.harvard.edu/pdf/evans_pka_table.pdf Harvard University, 2014.

311 . Williams,P.;Rushworth,S. Sigma Aldrich Company. *Methods for preparing thin films by atomic layer deposition using hydrazines*.22nd Sept.

2011WO2011115878 A1.

312 . Chi, K. M.;Shin, H. -.;Hampden-Smith, M. J.; *Polyhedron*, **1991**, 10 (19)

p2293-2299.